Department of Materials

Conductive Behaviour of Carbon Nanotube Based Composites

By

Xinxin Sun

A doctoral thesis submitted in partial fulfillment of the requirement for the award of

Doctor of Philosophy of Loughborough University

2009

Supervisor: Dr. Mo Song

Department of Materials

Loughborough University

Abstract

This project was basically exploratory in the electrical properties of carbon nanotube (CNT) based materials. The direct current (DC) conductivity of CNT/polymer composites was computed by using equivalent circuit method and a three dimensional (3-D) numerical continuum model with the consideration of tunneling conduction. The effects of the potential barrier of polymer and the tortousity of CNTs on the conductivity were analyzed. It was found that both of percolation threshold and DC conductivity can be strongly affected by the potential barrier and the tortousity. The influence of contact resistance on DC conductivity was also computed, and the results revealed that contact resistance and tunneling resistance had significant influences on the conductivity, but did not affect the percolation threshold. The microstructure-dependent alternating current (AC) properties of CNT/polymer composites were investigated using the 3-D numerical continuum model. It was found that AC conductivity and critical frequency of CNT/polymer composites can be enhanced by increasing the curl ratio of CNTs. In the mid-range CNT mass fraction, with increasing curl ratio of CNTs, AC conductivity, interestingly, became frequency-dependent in low frequency range, which cannot be explained by reference to the percolation theory. A proper interpretation was given based on the linear circuit theory. It was also found that the critical frequency can also be affected by the size of CNT cluster. Series numerical formulas were derived by using a numerical capacitively and resistively junction model. In particular, this work introduced an equivalent resistor-capacitor (RC) circuit with simple definitions of the values of contact resistance and average mutual capacitance for CNT/polymer nanocomposites. Theoretical results were in good agreement with experimental data, and successfully predicted the effect of morphology on the AC properties of CNT/polymer composites.

DC and AC conductivities of multi-walled carbon nanotube (MWCNT)/graphene

oxide (GO) hybrid films were measured for selected MWCNT mass fractions of 10%, 33.3%, 50%, 66.7%, and 83.3% using four-probe method. The experimental results were fitted using scaling law, and relatively high percolation threshold was found. This high percolation threshold was understood in terms of the potential energy and intrinsic ripples and warping in the freestanding graphene sheets. The capacitance of these hybrid films were measured using the voltmeter-ammeter-wattmeter test circuit with different voltages and heat treatments. The MWCNT/GO film showed relatively high specific capacitance ($0.192 F/cm^3$ for the mass fraction of 83.3%) and power factor compared to conventional dielectric capacitors. Both of measured capacitance and power factor can be enhanced by increasing testing voltages. The capacitance of MWCNT/GO films rapidly decreased after heat treatments above 160℃. This decrease was caused by redox reaction in the GO sheets. The capacitive behaviour of MWCNT/GO hybrid films was also interpreted by using the equivalent circuit model.

Single-walled carbon nanotube (SWCNT) and SWCNT/Poly(vinyl alcohol) (PVA) films were used to form a piezoresistive strain sensor. Both of static and dynamic strain sensing behaviours of SWCNT and SWCNT/PVA films were measured. It was found that the sensitivities of these films decreased with increasing their thicknesses. The SWCNT film with a thickness of 1900 nm and SWCNT/PVA film exhibited 'viscoelastic' sensing behaviour, because van der Waals attraction force allowed axial slippages of the smooth surface of nanotubes. A numerical model was derived based on the dynamic strain sensing behaviour. This model could be useful for designing CNT strain sensors.

Finally, thermoelectric power (TEP) of deformed SWCNT films with various thicknesses was measured. It was observed that positive TEP of SWCNT films increased with increasing stain above the critical point. The experimental results were fitted by using a numerical model in terms of a variation of Nordheim-Gorter relation and fluctuation induced tunneling (FIT) model. From the numerical model, it was found that the increase of TEP above the critical strain resulted from the positive term

of the contribution from the barrier region, and the effect of barrier regions decreases with increasing the thickness of the film.

Key Words: Carbon Nanotube, Graphene-oxide, Strain Sensor, Thermoelectricity, Nanocomposites, Computer Modeling, Nanocapacitor.

Acknowledgement

I want to acknowledge the support of the Department of Materials at Loughborough University, in particular, my supervisor Dr. Mo Song for his fatherly help and guidance in both of professional and personal ways. His faith kept me going through the long, hard slog of writing up a thesis. Thanks are also due to Dr. Jie Jin for her helpful suggestions in both of research and life, to Dongyu Cai for his work on fabrication of graphene oxide films.

My thanks also go to the Dr. Zhimin Bai from National Computing Center China for his help on modeling.

Finally, I would like to thank all the members in Department of Materials. Their effective work and professional help gave a strong support for my research.

I want to dedicate this thesis to my great parents for their selfless support, and to my wife, Hongna Shi, who has always been there for me.

Content

List of Abbrevation

1-D	One dimensional
2-D	Two dimensional
3-D	Three dimensional
AC	Alternating current
AFM	Atomic force microscope
BZ	Brillouin zone
CNT	Carbon nanotubes
CVD	Chemical vapor deposition
DAQ	Data acquisition
DC	Direct current
DMF	N,N-dimethylformamide
DOS	Density of states
DWCNT	Double-walled carbon nanotube
DWCNT-OH	Double-walled carbon nanotube with hydroxyl group
ECJ	Equivalent circuit for a CNT junction
EG	Expandable graphite
EGO	Expandable graphite oxide
ES	Elementary segment
FIT	Fluctuation induced tunneling model
FTIR	Fourier transform infrared spectra
GO	Graphene oxide
GONP	Graphene oxide nanoplatelet
LJ	Lennard-Jones potential
MWCNT	Multi-walled carbon nanotube
MWCNT-OH	Multi-walled carbon nanotube with

	hydroxyl group
PC	Polycarbonate
PE	Polyethylene
PI	Polyimide
PMMA	Poly(methyl acrylate)
PmPV	Poly(m-phenylenevinylene-co-2, 5-di-octyloxy-p-phenylenevinylene)
PP	Polypropylene
PS	Polystyrene
PVA	Poly(vinyl alcohol)
PVAc	Poly(vinyl acetate)
SEM	Scanning electron microscopy
SNR	Signal to noise ratio
STM	Scanning tunneling microscopy
STs	Super carbon nanotubes
STS	Scanning tunneling spectroscopy
SWCNTs	Single-walled carbon nanotubes
TE	Thermoelectricity
TEM	Transmission electron microscopy
TEP	Thermoelectric power
XPS	X-ray photoelectron spectroscopy
VRH	Variable range hopping

List of Symbol

a_1, a_2	Lattice vector
C_h	Chiral vector
ϕ	Phase angle
p	Concentration of fillers
p_c	Percolation threshold
ω_0	Critical frequency
ξ	Correlation length
$\rho_{\parallel}$	Resistivity along to the axis of nanotubes
$\rho_{\perp}$	Resistivity normal to the axis of nanotubes
ε_0	Vacuum permittivity
ε_r	Relative permittivity
E_g	Bandgap
E_f	Fermi energy
σ_{AC}	AC conductivity
σ_{DC}	DC conductivity
τ	Curl ratio
θ	Chiral angle
κ	Constant of percolation model
$\bar{C}$	Mean capacitance
C_e	Equivalent Capacitor
C_x	Capacitance of the tested sample
J	Current density
k_1, k_2	Reciprocal vector of hexagon lattice
k_F	Fermi point
k_z	Reciprocal vector parallel to the axis

	direction
$k_{\perp}$	Reciprocal vector perpendicular to the axis direction
L_e	Equivalent inductance
n_c	Number of carbon atoms in unit cell
N_e	Number of elements contained in an ES
N_f	Number of fibers
PF%	Power factor
R_c	Contact resistance
R_e	Equivalent resistor
R_s	Radius of gyration
R_t	Tunneling resistance
Rl	Resistance of fibrous filler
S	Thermoelectric power
s	Laplace variable
S_g	Gage factor
S_d	Dynamic strain sensitivity
T	Temperature
T_0	Parameters in FIT and VRH models
V_0	Height of barrier
Y_m	Admittance
Z_J	Impedance of CNT junction

List of Figure and Tables

Chapter 1 Introduction

Creation of new materials with novel properties is the main driving force for the development of materials science and technology. Properties of materials are not only determined by the chemical bonding and composition, but also by the dimensions of materials. As the dimension of a material system reduces to the nm-scale, unique physical and chemical characteristics arise. Nano-materials have been mass fabricated by novel synthetic approaches, and have attracted a great deal interests from scientists and engineers. One interesting example of the nano-materials is carbon nanotubes (CNTs).

Since the discovery of CNTs by Iijima in 1991 [1], electronic structure [2-4], electrical and thermal transport properties [5-7], mechanical properties[8-10], and other novel properties [11-15] of CNTs have been extensively studied. Nowadays, CNTs can be mass produced mainly by three techniques: arc-discharges [16-19], laser-ablation [20-22] and catalytic growth [23,24], and have a Gaussian of diameter. Carbon atoms in CNTs bond together by sp^2 hybridization [25]. There are two types of CNTs according to carbon sheets consisted: single-walled carbon nanotubes (SWCNTs) and multi-walled carbon nanotubes (MWCNTs). A single-walled carbon nanotube (SWCNT), which only has a single shell, normally can be seen as a rolled-up graphene sheet. The CNT consists of up to tens of graphitic shells with a separation of approximately $0.34nm$ [26], which is referred to as a multi-walled carbon nanotube (MWCNT). Typically, two-dimensional (2-D) lattice vectors are employed to identify the types of SWCNTs [27]: $R = n_1a_1 + n_2a_2$, where a_1 and a_2 are primitive lattice vectors, R is chiral verctor, and $n_1 \geq n_2 \geq 0$. The physical properties of SWCNTs dramatically depend on the chiral vectors even for the SWCNTs with the same diameter. SWCNTs can be divided into three groups according to their energy gaps (E_g) [27]: (I) a metal with $n_1 = n_2$, (II) a narrow gap semiconductor with $n_1 \neq n_2$ and $2n_2 + n_1 = 3I$, where I is integer and (III) a

moderate-gap semiconductor with $2n_2 + n_1 \neq 3I$. This grouping can be understood by the zone folding approach [28]: in the case of $n_1 = n_2$ and $n_2 - n_1 = 3I$, Fermi points are on the allowed state lines [29], and there is no gap or small gap between the conduction band and valence band.

CNT based composites have generated a great deal of research interests owing to the potential of their multifunctional applications [30-36]. It is well known that the electrical conductivity of polymers can rise of 8-10 orders of the magnitude [37-40] by adding fairly low content of CNTs, which is at or above the percolation mass fraction (p_c), and most increase occurs around p_c. The most of the measured direct current (DC) conductivities of CNT/polymer composites range from 10^{-5} to 10^{-1} S/m [41-44], which are lower than the value expected. Relatively high electrical conductivities, which locate in the range of 0.01-480 S/m, were also reported [45, 46]. This large scattering may indicate the complex nature of the electrical conductivity of CNT/polymer composites due to the interactions of various factors, e.g. the waviness and geometric structure of CNTs, the dispersion of CNTs, and the properties of polymer matrix. The contact resistance is one of the most important factors. The contact resistance is induced by the unavoidable intertube gap, whose width is about 1nm, between CNTs, and the reported contact resistances are extremely high, from 100kΩ to 1 MΩ [47, 48]. As CNTs are dispersed in a polymer matrix, there is a thin layer of insulating polymer between neighboring CNTs, and the electrical transport is mainly by tunneling conduction, which is even more complex. However, the effects of contact resistance and the tunneling conduction are often completely ignored by researchers in both of experimental and theoretical studies.

The alternating current (AC) conductivity of CNT composites has also been studied by many research groups [49-51]. At low frequency, AC conductivity is frequency independent, which approaches to DC conductivity. As the applied frequency is over the critical frequency (ω_0), the AC conductivity of composites exponentially increases with increasing the frequency. The reported results reveal that the AC properties of

conductor/polymer composites are strongly influenced by the local morphology of the composites [40, 50]. However, these prior studies were restricted to the scaling law, and no considerations were given to the effect of local morphology on AC properties that might be of interest to improve the knowledge of CNT composites and design CNT composites with better properties. Another limitation of the existing literature is that the frequency dependent conductivity was understood by using the non-quantified method of correlation length ξ, in which critical frequency ω_0 is considered associating with the distance (ξ) between the connections in the system [52, 53]. As the frequency is lower than ω_0, charge carriers are considered to tunneling through at least one polymer barrier. In the case of the frequency higher than ω_0, the carriers are expected to travel within the continuous phase of conductor [53]. It is slightly idealized to consider electrons scanning a distance under AC field in the disorder polymer host, and the relationship between the travel distance and frequency is also strongly influenced by the polymer host and the morphology of the composites.

Strain sensors are important in the science and engineering fields. However, the existing strain sensors cannot be embedded in materials level and provide multidirectional sensibility. CNTs possess an extremely sensitive electronic structure to mechanical deformations due to the shift of Fermi point k_F away from the Brillouin zone (BZ) vertices [54]. This sensitive electronic structure makes the CNT as an attractive candidate to develop new strain sensors. To date, many efforts have been made to develop strain sensors based on CNT films and CNT/polymer composite films, and a nearly linear sensing behaviour has been observed [55, 56]. It was often considered that this linear response was resulted by the intrinsic sensing property of CNTs. However, there were small barriers between CNTs, and the contact resistance induced by the intertube barriers played a dominant role in the CNT based materials [47]. As strain is applied on the CNT films or CNT composite films, the intertube barriers could also be changed, and this change may result in the variation of the total resistance of CNT based materials. In order to reveal the variation of the resistance in deformed CNT films and composites does not result from an intrinsic

property of CNTs but rather is a consequence of the change of random oriented intertube barriers, it is necessary to understand the origin of the sensing behaviour in CNT and composite films.

Thermoelectric power (TEP) of a material is concerned with the amplitude of an induced thermoelectric voltages responding to the temperature difference in the material, and is extremely sensitive to the change of electronic structure at the Fermi energy [57]. TEP are widely used for developing power generator to convert thermal power to electricity [58]. There have been numbers of experimental efforts to measure TEP of individual CNT, CNT ropes and macroscopic CNT 'mat' [59-63]. In these measurements, CNTs may be subjected to various mechanical deformations, which may lead to the modification of their electronic structure and intertube barriers. However, the effect of mechanical deformations on the TEP of CNTs has not been explored yet.

Very recently, CNTs have strongly been challenged by graphene sheets, which have similar properties to CNTs [64]. It is difficult to strip graphene sheets from graphite due to the strong bonding between the graphene layers. The exfoliation of graphene oxide (GO) can be achieved by introduction of oxygenated groups [65], which reduce the interlay bonding. GO could be suitable to develop new electronic devices combining with CNTs.

The overall arm of this research is to improve the knowledge of CNT based materials and design CNT based materials with better electrical properties. The objectives of this Ph. D. project are summarized as follows:

(1) To investigate the roles of contact resistance, tunneling conduction, and local morphology in the DC electrical conductivity of CNT/polymer composites.
(2) To study the effect of microstructure on the AC properties of CNT/polymer composites.
(3) To understand and model the variation of the resistance in deformed CNT and

composite films.

(4) To investigate the variation of the TEP in CNT films induced by the mechanical deformation.

(5) To explore the electrical properties of capacitive CNT/GO films.

References

1. S. Iijima, Nature (London) 354, 56 (1991).
2. R. Satio, M. Fujita, G. Dresselhaus, and M. S. Dresselhaus, Phys. Rev. B, 46, 1804 (1992).
3. C. L. Kane, and E. J. Mele, Phys. Rev. Lett. 78, 1932 (1997).
4. J. W. Mintmire, B. I. Dunlap, and C. T. White, Phys. Rev. Lett. 68, 631 (1992).
5. S. J. Tans, M. H. Devoret, H. Dai, A. Thess, R. E. Smalley, and C. Dekker, Nature (London) 386, 474 (1997).
6. C. T. White, and T. N. Todorov, Nature (London) 393, 240 (1998).
7. S. Berber, Y. K. Kwon, and D. Tománek, Phys. Rev. Lett. 84, 4613 (2000).
8. J. P. Salvetat, J. M. Bonard, N. H. Thomson, A. J. Kulik, L. Forró, W. Benoit, and L. Zuppiroli, Appl. Phys. A, 69, 255 (1999).
9. J. P. Lu, Phys. Rev. Lett. 79, 1297 (1997).
10. M. F. Yu, B. S. Files, S. Arepalli, and R. S. Ruoff, Phy. Rev. Lett. 84, 5552 (2000).
11. J. Maultzsch, S. Reich, and C. Thomsen, Phys. Rev. B 64, 121407(R) (2001).
12. D. R. Wake, F. S. M. V. Klein, J. P. Rice, and D. M. Ginsbery, Phys. Rev. Lett. 67, 3728 (1991).
13. V. N. Popov, and L. Henrard, Phys. Rev. B 65, 235415 (2002).
14. E. W. Wong, P. E. Sheehan, and C. M. Lieber, Science, 277, 1971 (1997).
15. R. R. Bacsa, A. Peigney, C. Laurent, P. Puech, and W. S. Bacsa, Phys, Rev, B 65, 161404 (2002).
16. C. Journet, W. K. Maser, P. Bernier, A. Loiseau, M. L. Chapelle, S. Lefrant, P.

Deniard, R. Lee, and J. E. Fischer, Nature (London) 388, 756 (1997).

17. Y. Satio, and M. Inagaki, Jpn. J. Appl. Phys. 34, L954 (1993).
18. R. E. Smalley, Accounts Chem. Res. 25, 98 (1992).
19. T. W. Ebbesen, H. Hiura, J. Fujita, Y. Ochiai, S. Matsui, and K. Tanigaki, Chem. Phys. Lett. 209, 83 (1993).
20. A. Thess, R. Lee, P. Nikolaev, H. Dai, P. Petit, J. Robert, C. Xu, Y. H. Lee, S. G. Kim, A. G. Rinzler, D. T. Colbert, G. E. Scuseria, D. Tomanek, J. E. Fischer, and R. E. Smalley, Science 273, 483 (1996).
21. M. Yudasaka, T. Komatsu, T. Ichihashi, and S. Iijima, Chem. Phys. Lett. 278, 102 (1997).
22. W. Han, Y. Bando, K. Kurashima, and T Sato, Appl. Phys. Lett. 73, 3085 (1998).
23. M. J. Kim, T. Y. Lee, J. H. Choi, J. B. Park, J. S. Lee, S. K. Kim, J. B. Yoo, and C. Y. Park, Diamond & Related Materials 12, 870 (2003).
24. U. C. Chung, Y. H, Kim, D. B. Lee, Y. U. Jeong, W. S. Chung, Y. R. Cho, and I. M. Park, Bull, Korean. Chem. Sco. 26, 103 (2005).
25. O. Ozsoy, and N. Sunel, J. Phys. 54, 1495 (2004).
26. Y. Saito, T. Yoshikawa, S. Bandow, M. Tomita, and T. Hayashi, Phys. Rev. B 48, 1907 (1993).
27. N. Hamada, S. I. Sawada, and A. Oshiyama, Phys, Rev. Lett. 68, 1579 (1992).
28. C. T. White, and J. W. Mintmire, Nature (London) 394, 29 (1998).
29. S. Reich, C. Thomsen, and P. Ordejon, Phys. Rev. B 65, 155411 (2002).
30. M. J. Biercuk, M. C. Llaguno, M. Radosavljevic, J. K. Hyun, A. T. Johnson, and J. E. Fisher, Appl. Phys. Lett. 80, 2767 (2002).
31. G. D. Zhan, J. D. Kuntz, J. E. Garay and A. K. Mukherjee, Appl. Phys. Lett. 83, 1228 (2003).
32. P. Galvert, Nature (London) 399, 210 (1999).
33. A. Modi, N. Koratkar, E. Lass, B. Q. Wei, and P. M. Ajayan, Nature (London) 424, 171 (2003).
34. K. J. Loh, J. Kim, J. P. Lynch, N. W. S. Kam and N. A. Kotov, Smart. Mater. Struct. 16, 429 (2007).

35. J. N. Coleman, U. Khan, Y. K. Gun'ko, Adv. Mater. 18, 689 (2006).
36. R. H. Baughman, A. A. Zakhidov, W. A. De heer, Science 297, 787 (2002).
37. J. C. Grunlan, A. R. Mehrabi, M. V. Bannon, and J. L. Bahr, Adv. Mater. 16, 150 (2004).
38. Y. J. Kim, T. S. Shin, H. D. Choi, J. H. Kwon, Y. C. Chung, and H. G. Yoon, Carbon 43, 23 (2005).
39. Z. Ounaier, C. Park, K.E. Wise, E. J. Siochi, and J. S. Harrison, Composites Sci. and Tech. 63, 1637 (2003).
40. B.E. Kilbride, J.N. Coleman, J. Fraysse, P. Fournet, M. Cadek, A. Drury, and S. Hutzler, J. Appl. Phys. 92, 4024 (2002).
41. L Valentini, and JM Kenny, Polymer, 46, 6715 (2005).
42. F. H. Gojny, M. H. G. Wichmann, B. Fiedler, I. A. Kinloch, W. Bauhofer, A. H. Windle, and K. Schulte, Polymer 47, 2036 (2006).
43. E. Kymakis, and C. A. J. Amaratunga, J. Appl. Phys. 99, 084302 (2006).
44. M. S. Al-Haik, M. Y. Hussaini, H. Garmestani, D. Li, and K. Dahmen, J. Appl. Phys. 94, 6034 (2003).
45. R. Ramasubramaniam, J. Chen, and H. Y. Liu, Appl. Phys. Lett. 83, 2928 (2003).
46. E. S. Choi, J. S. Brooks, D. L. Eaton, M. S. Al-Haik, M. Y. Hussaini, H. Garmestani, D. Li, and K. Dahmen, J. Appl. Phys. 94, 6034 (2003).
47. M. S. Fuhrer, J. Nygard, L. Shih, M. Forero, Y. G. Yoon, M. S. C. Mazzoni, H. J. Choi, J. Ihm, S. G. Louie, A. Zettl, and P. L. McEuen, Science 288, 494 (2000).
48. A. Buldum and J. P. Lu, Phys. Rev. B 63, 161403 (2001).
49. D. S. McLanchlan, C. Chiteme, C. Park, K. E. Wise, S. E. Lowther, P. T. Lillehei, E. J. Siochi, and J. S. Harrison, J Polymer Sci. B 43, 3273 (2005).
50. B. Kim, J. Lee, and I. Yu, J Appl. Phys. 94, 6724 (2003).
51. M. T. Conner, S. Roy, T. A. Ezquerra, and F. J. B. Calleja, Phys. Rev. B 57, 2286 (1998).
52. J. C. Dyre, and T. B. Schroder, Rev. Mod. Phys. 72, 873 (2000).
53. M. Reghu, C. O. Yoon, C. Y. Yang, D. Moses, P. Smith, and A. J. Heeger, Phys. Rev. B 50, 13931 (1994).

54. L. Yang, and J. Han, Phys. Rev. Lett. 85, 154 (2000).
55. P. Dharap, Z. Li, S. Nagarajaiah, and E. V. Barrera, Nanotechnology 15, 379 (2004).
56. I. Kang, M. J. Schulz, J. H. Kim, V. Shanov, and D. Shi, Smart Mater. Struct. 15, 737 (2006).
57. G. Mahan, Solid State Phys. 51, 81 (1998).
58. F. J. DiSalvo, Science 285, 703 (1999).
59. K. Bradley, S. H. Jhi, G. Collins, J. Hone, M. L. Cohen, S. L. Louie, and A. Zettl, Phys. Rev. Lett. 85, 4361 (2000).
60. M. Baxendal, K. G. Kim, and G. A. J. Amaratunga, Phys. Rev. B 61, 12705 (2000).
61. G. U. Sumanasekera, B. K. Pradhan, H. E. Romero, K. W. Adu, and P. C. Eklund, Phys. Rev. Lett. 89, 166801 (2002).
62. H. E. Romero, G. U. Sumanasekera, G. D. Mahan, and P. C. Eklund, Phys. Rev. B 65, 205410 (2002).
63. J. P. Small, K. M. Perez, and P. Kim, Phys. Rev. Lett. 91, 256801 (2003).
64. A. K. Geim and K. S. Novoselov, Nature materials 6, 183 (2007).
65. D. Cai, M. Song, and C. Xu, Adv. Mater. 20, 1706 (2008).

Chapter 2 Fundamental of Carbon Nanotube and Its Composites

2.1 Introduction

During the past two decades, CNTs have received a lot of attentions from scientists due to their amazing physical properties. Significant progress in understanding the physical properties of CNTs and in identifying the potential applications has been made [1, 2]. CNTs possess a one-dimensional (1-D) electrical band structure, which gives rise to their unique electrical transport and thermal properties, and makes them as attractive candidates for great applications in many fields. Due to their high electrical conductivity, CNTs are widely employed as fillers to improve the electrical properties of polymers [3]. Their 1-D electronic structure can be modified by mechanical deformations due to the shift of Fermi point k_F away from Brillouin zone (BZ) vertices [4]. This sensitive electronic structure gives CNTs a great potential to develop new stain sensors [5]. In this chapter, we will describe the past progress and on-going efforts on the electronic properties of CNTs and their composites. Section 2.2 gave a brief overview on the geometric structure of CNTs. In section 2.3, the electrical and electronic properties of CNTs were summarized. The DC and AC properties of CNT/polymer composites were discussed in section 2.4. Section 2.5 briefly reviewed the on-going efforts for developing CNT based strain sensors. Lastly, section 2.6 provided a summary.

2.2 Geometric structure of CNTs

In order to understand the electronic properties of CNTs, it is necessary to know the geometric structure of CNTs. CNTs are often specified in terms of the graphite lattice vectors. Fig.2.1 shows the honeycomb structure in graphene. The unit vectors are constructed by connecting the second neighboring carbon atoms in CNTs, and the

length of unit vectors is 2.461Å [1]. The real space unit vectors a_1 and a_2 can be used to defined the chiral vector and translational vector. A SWCNT can be uniquely described by the chiral vector C_h, which can be expressed by using the lattice vector, namely

$$C_h = n_1 a_1 + n_2 a_2 \equiv (n_1, n_2) \tag{2.1}$$

where n_1 and n_2 are the length of elements of C_h in the direction of a_1 and a_2, respectively.

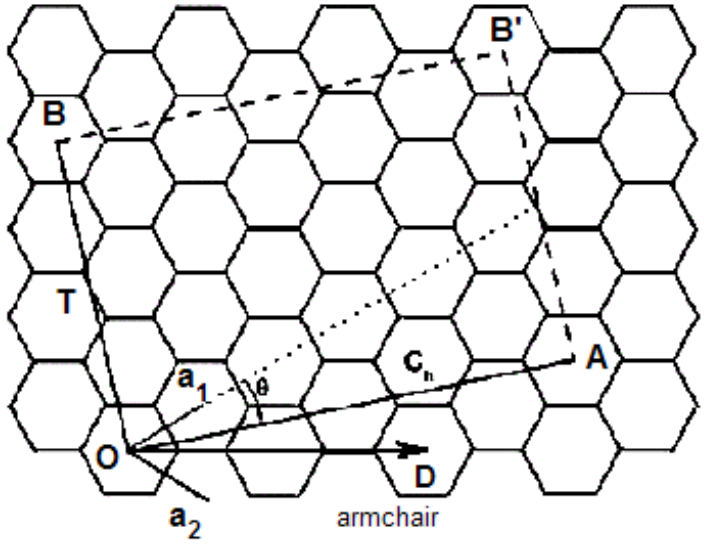

Figure 2.1 Honeycomb lattice of carbon nanotubes. $\overrightarrow{OB}$ is parallel to the direction of nanotube axis and $\overrightarrow{OA}$ is in the transverse direction of nanotube. O, A, B, B' are the crystallographically equivalent sites. When the graphene sheet is rolled, the points O and A coincide [1]. The CNT constructed by rolling the graphene sheet in the direction of OD is armchair nanotube, which is always metallic.

A SWCNT often can be seen as a graphene sheet rolled up in the way of the chiral vector as the circumference of the nanotube. Many physical properties of CNTs

strongly depend on the chiral vector, such as electronic band structure, thermal conductivity and elastic properties. The direction of chiral vector is described by the chiral angle (θ), which is defined as the angle between the vector C_h and lattice vector a_1. The chiral angle can be calculated by using the following equation [6],

$$\cos\theta = \frac{C_h \cdot a_1}{|C_h| \cdot |a_1|} = \frac{2n_1 + n_2}{2\sqrt{n_1^{\,2} + n_2^{\,2} + n_1 n_2}} \tag{2.2}$$

where $|C_h|$ is the length of chiral vector, and $|a_1|$ is the length of the lattice verctor a_1. The θ varies in the range from $0°$ to $30°$. The nanotubes with the chiral vector of (n, 0) ($\theta = 0°$) are called zigzag nanotubes due to the zigzag pattern along the chiral vector. The (n, n) CNTs are called armchair nanotubes with the chiral angle of $30°$. Other types of CNTs are called chiral nanotubes with chiral angles between $0°$ and $30°$. All the geometric parameters of CNTs, such as diameters, the dimension of unit cell and the number of carbon atoms in the unit cell, also can be determined by knowing the chiral vector. The diameter of nanotubes can be expressed by chiral vector [6] as follows:

$$d_t = \frac{L}{\pi} = \frac{|C_h|}{\pi} = \frac{\sqrt{C_h \cdot C_h}}{\pi} = \frac{a\sqrt{n_1^{\,2} + n_2^{\,2} + n_1 n_2}}{\pi} \tag{2.3}$$

where L is the circumference of the nanotube. The number of carbon atoms (n_c) in the unit cell can be calculated from the ratio of the area of the cylinder surface (S_t) to the area of the hexagonal unit cell (S_g) [1], namely

$$n_c = 2\frac{S_t}{S_g} = \frac{4\left(n_1^{\,2} + n_1 n_2 + n_2^{\,2}\right)}{n_d \cdot \zeta} \tag{2.4}$$

where $\zeta = 3$, if $(n_1 - n_2)/3d \cdot R$ is an integer and otherwise $\zeta = 1$. n_d is the greatest common divisor of n_1 and n_2. The translational vector (T) is defined as the length of the unit cell in the axial direction of CNTs. The translational vector also can be expressed by using real space unit vectors, namely [6]

$$T = t_1 a_1 + t_2 a_2 \equiv (t_1, t_2) \tag{2.5}$$

where t_1, t_2 are integers, a_1 and a_2 are real space unit vectors. t_1 and t_2 do not have a common divisor except for unity. The vector T is parallel to the axis of CNTs and perpendicular to the chiral vector [6]. Thus, the relationship between chiral and translational vector can be expressed mathematically as follows [6]

$$C_h \cdot T = |C_h| \cdot |T| \cdot \cos\theta = 0 \tag{2.6}$$

By using Eq. 2.6, Eq. 2.5 can be rewritten as [6]

$$T = \frac{2n_1 + n_2}{n_d \cdot \zeta} a_1 - \frac{2n_1 + n_2}{n_d \cdot \zeta} a_2 \tag{2.7}$$

Carbon atoms can be denoted within the unit cell of CNTs by the symmetry vector R times *i*, which is an integer. The expression of symmetry vector can be written as [6]

$$R = pa_1 + qa_2 \tag{2.8}$$

where p and q are integers, and they do not have a common divisor except for unity. $C_h \cdot R$ is normal to $T \times R$. Then, p and q can be determined by using this relationship. For the smallest unit cell (i=1), following equation can be obtained [6],

$$t_1 q - t_2 p = 1 \qquad (0 < n_1 p - n_2 q \le N) \tag{2.9}$$

where N is the number of hexagons in the unit cell. The p and q is uniquely identified by using Eq. 2.9 for the smallest unit cell, because there are no common divisors of p and q. The symmetry vector $(\phi|\tau)$ also can be denoted by using an angle ϕ and a translation τ, and displays the basic space group symmetry operation. The ϕ and τ can be determined by using following equations [6],

$$\tau = \frac{(n_1 p - n_2 q)\cdot T}{N} \tag{2.10}$$

$$\phi = \frac{2\pi}{N} \tag{2.11}$$

In summary, SWCNTs can be identified by just using chiral vector. All the geometric parameters of SWCNTs, such as diameter, chiral angle and unit cell, can be obtained from the chiral vector. Physical properties of CNTs dramatically depend on the chiral vector. Symmetry vector reflects the space symmetry operation in the unit cell of CNTs. All the sites of carbon atoms in the unit cell can be located by shifting the symmetry vector.

2.3 Electrical and Electronic properties of CNTs

Perhaps, CNTs are closest to an idea 1-D conductor with an extremely high aspect ratio. Their unique C-C bonding and 1-D structure give them many novel properties such as remarkable electron transport properties and band structure. A review of electrical and electronic properties will be given in this section as they have direct implications for the electronic applications of CNTs.

2.3.1 Band Structure of SWCNTs

Generally, electrical transport properties are determined by the electrons or holes near the Fermi level, since these electrons or holes have easy access to the conduction band. Thus, we only consider the band structure near the Fermi level. At present, electronic properties of SWCNTs are mainly studied within the central Brillouin zone (BZ) of SWCNTs by using zone-folding approximation [7-10]. The hexagonal BZ of a (7,7) SWCNT is presented in Fig. 2.2. A SWNCT can be constructed by rolling up a sheet of graphene, and the band structure of SWCNTs can be obtained from that of graphene by applying appropriate boundary conduction around the SWCNTs [11]. There are two reciprocal wave vectors associated with SWCNTs, and their expression can be obtained from the relation, $\mathrm{R_i} \cdot \mathrm{k_i} = 2\pi\delta_{ij}$. The vector $\mathrm{k_z}$ corresponds to the translational period defined by Eq. 2.7. The length of $\mathrm{k_z}$ is given by $\mathrm{k_z} = 2\pi/\mathrm{T}$ [11]. If we consider a SWCNT as an infinitely long cylinder, the wave vector $\mathrm{k_z}$ will be continuous. The first BZ in axial direction ranges from $-\pi/\mathrm{T}$ to π/T. $\mathrm{k_\perp}$ is the wave vector along the circumference *c* of the SWCNT. The $\mathrm{k_\perp}$ can be quantized by applying the following boundary condition [12]:

$$k_\perp = \frac{2\pi}{\lambda} = \frac{2\pi}{|c|} \cdot m = \frac{2}{d} \cdot m \tag{2.12}$$

where *c* is the circumference, *d* is the diameter of CNTs and m is an integer ($-n_c/2 \ldots\ldots 0 \ldots\ldots n_c/2$). This boundary condition can be associated with the stationary wave [12]. The wave of a quasi-particle around the circumference must have a phase shift of an integer multiple of 2π. Otherwise, the wave will vanish by the interference. Therefore, the wave with wave vector $\mathrm{k_\perp}$ has 2m nodes and the maximum of nodes is equal to the number of carbon atoms (n_c) in the unit cell. The 1D electronic structure of SWCNTs can be described by using these allowed $\mathrm{k_\perp}$ states that present as lines, and the number of allowed lines in the first BZ is n_c. Allowed lines are

parallel to the axis of nanotubes (shown in Fig. 2.2), and the spacing between allowed lines is $k_\perp = 2d$. The boundary condition for k_z and $k_\perp$ is that [11],

$$k_\perp \cdot c = 2\pi \qquad k_\perp \cdot T = 0 \tag{2.13}$$

$$k_z \cdot c = 0 \qquad k_z \cdot T = 2\pi \tag{2.14}$$

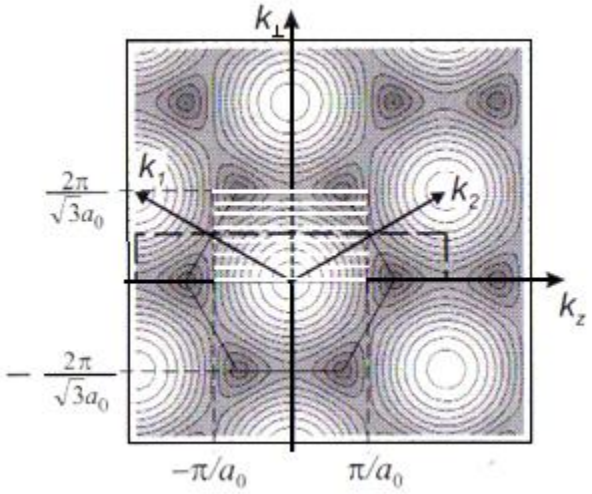

Figure 2.2 Illustration of BZ for a (7,7) armchair nanotube. The background is a contour plot of the electronic band structure. k_1 and k_2 is the reciprocal vector of hexagon lattice. k_z and $k_\perp$ are the reciprocal vectors parallel and perpendicular to the axis of nanotubes, respectively. The parallel lines present allowed states [1].

From Eqs. 2.13 and 2.14, the k_z and $k_\perp$ can be expressed as follows [13]:

$$k_\perp = \frac{2n_1 + n_2}{n_c \cdot n \cdot \zeta} k_1 + \frac{2n_2 + n_1}{n_c \cdot n \cdot \zeta} k_2 \tag{2.15}$$

$$k_z = -\frac{n_1}{n_c} k_1 + \frac{n_2}{n_c} k_2 \tag{2.16}$$

where n is integer, $\zeta = 3$, if $(n_1 - n_2)/3d \cdot R$ is an integer and otherwise $\zeta = 1$. By using Eqs. 2.15 and 2.16, a series of allowed lines can be drawn on the electronic

structure of the graphene sheet. The length and number of allowed lines depend on the chiral vector (n_1, n_2). The band structure of a SWCNT can be obtained from the energy dispersion of graphene by cross-sectional cutting with these allowed state lines as shown in Fig. 2.2. This is called zone-folding approximation of obtaining the band structure of SWCNTs.

Zone-folding approximation gives successful explanations of electrical types of SWCNTs [14]. Most SWCNTs are semiconducting and 1/3 of SWCNTs are metallic and quasi-metallic, which depend on the chiral vector. In zone-folding approximation, if the K points of the BZ locate in the allowed states, the SWCNT will be metallic, otherwise the SWCNT will be semiconducting. The first BZ with allowed state lines for a general (n_1, n_2) SWCNT is presented in Fig. 2.3. The reciprocal vector k_1 and k_2 must satisfy the Born-von Karman boundary condition, which can be expressed [12] as

$$k \cdot R = 2\pi m \tag{2.17}$$

where m is an integer. This is a very important relationship between reciprocal vector and real vector. The Fermi level of a SWCNT occurs at the vertices of the BZ hexagon. The Fermi points k_F can be located by reciprocal vectors, k_1 and k_2 [11], namely,

$$k_F = \pm(k_1 - k_2)/3, \pm(2k_1 + k_2)/3, \pm(k_1 + 2k_2)/3 \tag{2.18}$$

The position of the point k_F presented in Fig. 2.3 is $\frac{1}{3}(k_1 - k_2)$. If a SWCNT is metallic, the k_F will be on the allowed state lines [11], namely,

$$k \cdot R = 2\pi m = \frac{1}{3}(k_1 - k_2)(n_1 a_1 + n_2 a_2) = \frac{2\pi}{3}(n_1 - n_2) \tag{2.19}$$

Therefore, the following equation can be derived from Eq. 2.19,

$$m = \frac{n_1 - n_2}{3} \tag{2.20}$$

This equation, which was first derived by Saito et al. [15], can be used to characterize the metallic and semiconducting nanotubes. If $\frac{n_1 - n_2}{3}$ is an integer, the k_F pass through the allowed state, and these kinds of SWCNTs are metallic. Otherwise the SWCNT is semiconducting.

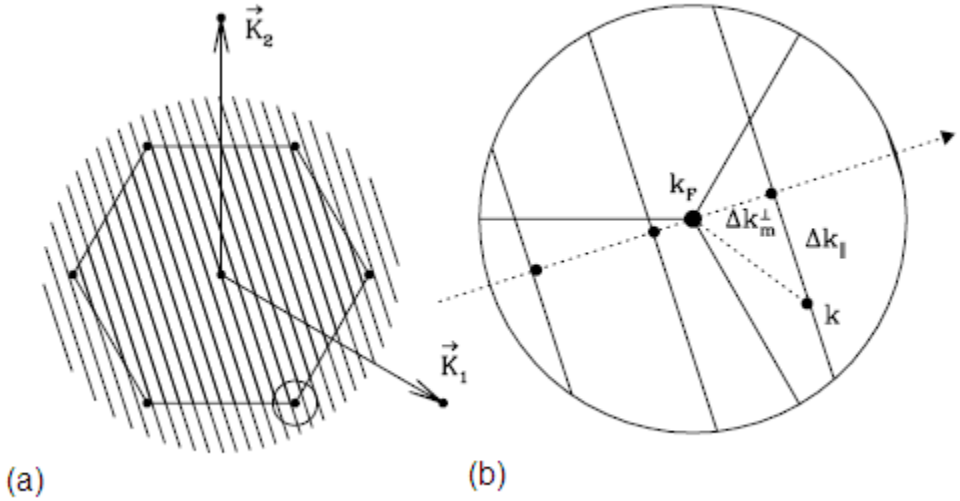

Figure 2.3 (a) Illustration of Brillouin zone of a graphene sheet. The circle at bottom right contains the region near the point k_F. (b) Enlarged depiction of allowed states near the Fermi point. k is the point on the allowed state line. $\Delta k_m^{\perp}$ and $\Delta k_m^{//}$ are the perpendicular and parallel components of the vector $k - k_F$ [11].

By using Eq. 2.17, the k_z, where the valence band crosses conduction band, can be calculated as [11],

$$k \cdot T = \frac{1}{3}(k_1 - k_2) \cdot \left(-\frac{2n_2 + n_1}{n_d \zeta} a_1 + \frac{2n_1 + n_2}{n_d \zeta} a_2 \right) = -2\pi \frac{n_1 + n_2}{n_d \zeta} = 2\pi k_z \tag{2.21}$$

Therefore,

$$k_z = \begin{cases} 0 \ \ if\ \zeta = 1 \\ 1/3 if\ \zeta = 3 \end{cases} \tag{2.22}$$

In summary, comparing with other methods, zone-folding approximation is simple for the calculation of the band structure of CNTs. However, it only has a good fit for SWCNTs with large enough diameters and the states are not too far away from Fermi level.

2.3.2 Density of States of SWCNTs

The density of states (DOS) is used for describing the how closed pack of the energy levels in a physical system. Generally, the electronic DOS is determined by the number of electrons in an energy interval or energy state. Saito et al. [15] first investigated the electronic structure of CNTs by using the tight-binding method. The expression of energy dispersion was derived and the instability of the Fermi level was discussed in their work. The electronic DOS of most metal and semiconductor rises as the square root of the energy. Some early work [16] predicted that CNTs also have $1/\sqrt{E}$ behaviour for DOS. However, this opinion changed when Mintmire et al. [11, 13] reported their derivation of the universal DOS for CNTs. An universal DOS expression was derived from the general DOS expression of 1-D band and the Fermi energy was calculated by Mintmire et al. [11] using the energy dispersion expression [12]. DOS, n(E), for 1D electronic subbands, can be expressed as [11],

$$n(E)=\frac{\partial N(E)}{\partial E}=\frac{2}{\ell}\sum_i dk\delta(k-k_i)\left|\frac{\partial\varepsilon}{\partial k}\right|^{-1} \tag{2.23}$$

where k_i is the root of the equation $E-\varepsilon(k_i)=0$ and ℓ is the length of BZ, and N(E) is the total number of electron states per unit cell at a given energy (E). In the low order of $|k-k_F|$, the electronic band of graphene can be approximately seen as a straight line close to the K point, and the dispersion relation of occupied states can be written as[11]

$$|\varepsilon(k)|\approx\frac{\sqrt{3}}{2}a|V_{pp\pi}||k-k_F| \tag{2.24}$$

where $V_{pp\pi}$ is the Slater-Koster parameter describing the nearest neighbor interactions. By using this linear approximation, the DOS in the vicinity of Fermi level can be expressed as [11]

$$\rho(E)=\frac{4}{\ell}\sum_{m=-\infty}^{\infty}\frac{2}{\sqrt{3}|V_{pp\pi}|a}g(E,\varepsilon_m)=\frac{\sqrt{3}}{\pi^2}\frac{1}{|V_{pp\pi}|}\frac{d}{r}\sum_{m=-\infty}^{\infty}g(E,\varepsilon_m) \tag{2.25}$$

where

$$g(E,\varepsilon_m)=\begin{cases}|E|/\sqrt{E^2-\varepsilon^2} & |E|>|\varepsilon_m|\\ 0 & |E|<|\varepsilon_m|\end{cases} \tag{2.26}$$

g(E, ε_m) becomes divergent at $|E|=|\varepsilon_m|$, which correlates to van Hove singularities, as $\varepsilon_m\neq 0$. Otherwise, the function $g(E,0)$ will be equal to one. The van Hove singularities in SWCNTs can be calculated as

$$\left|\varepsilon_m\right| = \frac{\sqrt{3}}{2}\left|V_{pp\pi}\right| a\Delta k_m^{//} = \frac{\left|3m - n_1 + n_2\right|}{2} \cdot \left|V_{pp\pi}\right| \cdot \frac{d}{r} \tag{2.25}$$

Fig. 2.4 depicts a comparison of DOS calculated from the Mintmire approximation with ab-initio calculation. From Fig. 2.4, it can be seen that the DOS from the Mintmire approximation are good agreed with that from ab-initio calculation for all types of SWCNTs near the Fermi level. Perhaps, first principle calculation is the most accurate way to determine the electronic structure of SWCNTs. However, it is difficult to operate in the system with a large number of atoms in the unit cell.

In summary, Mintmire approximation provides a simple and fast method for calculating the electronic structure of SWCNTs. However, the effects of curvature and trigonal warping still need to be considered to correct the Mintmire approximation.

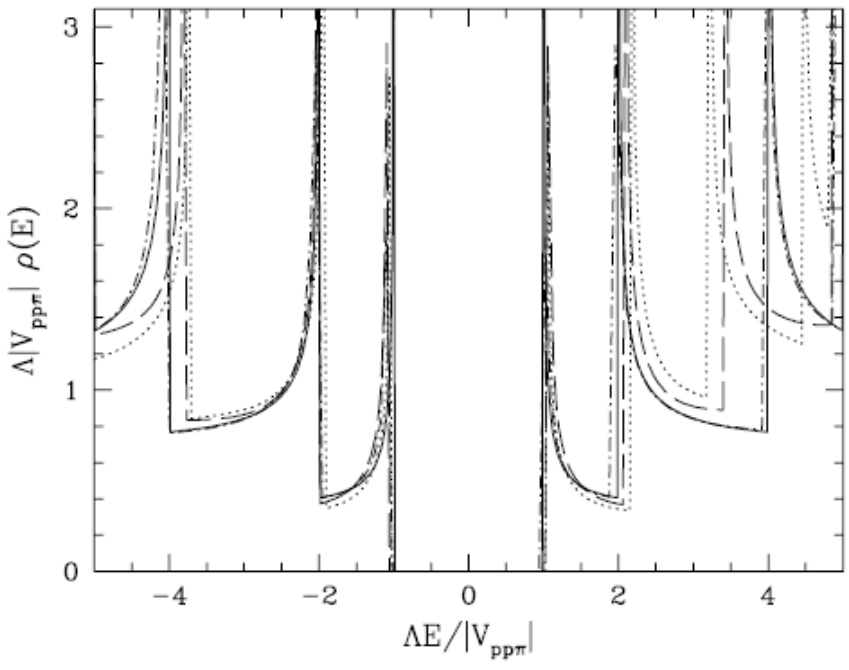

Figure 2.4 Comparison of DOS calculated from universal relationship from Eq. 2.30 (solid line) to ab-initio calculations for a (16, 0) (dot line) and dashed line for (13,6) and dot-dashed line for the (21,20) SWCNT. [11]

There are three methods for successfully measuring the electronic DOS of CNTs: scanning tunneling spectroscopy (STS) or STM [17, 18], resonant Raman scattering [19, 20], and optical absorption measurements [21, 22]. Here, we only reviewed the STM or STS measurements. In these experiments, the STM tip was placed over the CNT to record the tunneling current, which is the function of the voltage between the tip and sample. As the voltage between the sample and tip was applied, the Fermi level of sample was raised. Then, electrons, whose energy below the Fermi level of the sample but above the Fermi level of tip, could tunnel from the sample to the tip. With increasing the voltage, the number of electron tunneling into the tip increases. The differential conductance (dI/dV) is positively proportional to the DOS. In the high bias regime, I/V is often seen as a good approximation for DOS. Here are some results from STM measurement [23] presented in Fig.2.5 (a). From the measurement, the geometric parameters of the SWCNT can be directly obtained.

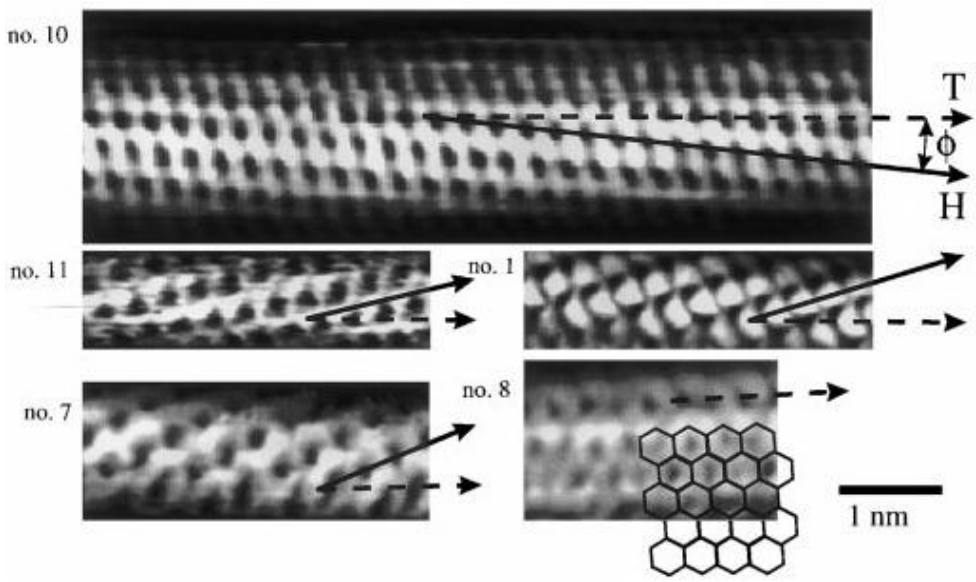

(a)

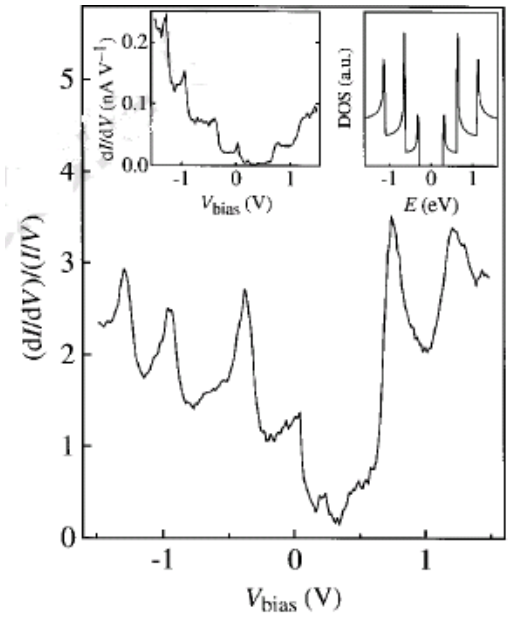

(b)

Figure 2.5 (a) Atomically resolved STM images of individual SWCNTs. Dashed arrows represent the axial direction of nanotubes and the solid arrows indicate the direction of the nearest-heighbour hexagon rows. Nanotubes of no. 10, 11 and 1 are chiral, and nanotubes of no. 7 and 8 are zigzag and armchair nanotubes, respectively. Nanotubes no. 10 has a chiral angle of 7° and a diameter of 1.3nm. (b) Local DOS from STM measurement for nanotubes of no. 9. The peaks correlate to van Hove singularities at the onset of 1D band structure of the nantubes. The left inset illustrates the raw dI/dV data. The right inset represents the DOS from calculation [23].

The STM or STS gives a direct probe of the electronic DOS near the Fermi level and van Hove singularities corresponding to peaks are easily found from the results (shown in Fig 2.5 (b)). The asymmetric peaks are broadened and have a finite height, which may be caused by the hybridization between nanotubes and substrate [24]. The overall shapes of peaks from measurement still have a good agreement with results calculated from Eq. 2.25. The van Hove singularities normally correspond to allowed states. The first van Hove singularities relate to the allowed state that is the closest line to Fermi points. The unoccupied DOS also yield peaks, because the dispersion relation is radically symmetric. Thus, from the results of STM or STS measurements, the dispersion relation can also be generally known.

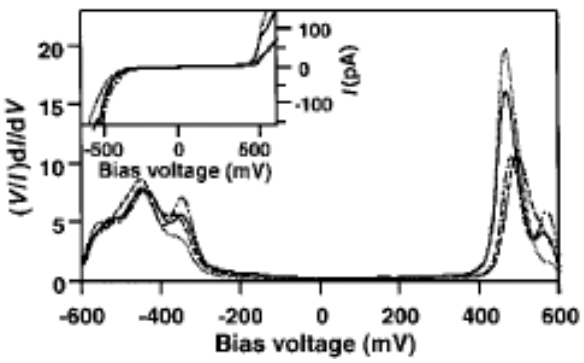

(a)

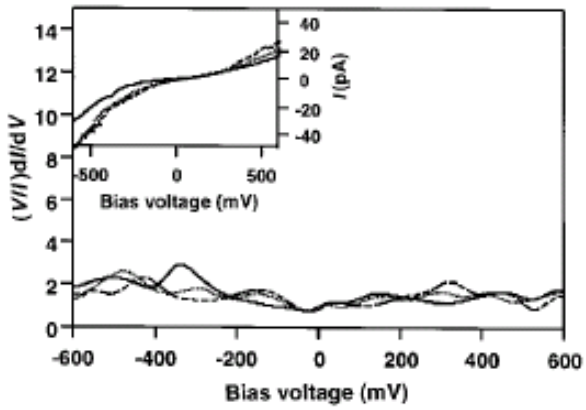

(b)

Figure 2.6 STS measurements of SWCNTs. (a) a semiconducting nanotube, (b) a metallic nanotube [24]. The inset is the measured I/V curves.

The electrical types of CNTs can also be determined from the STS measurements. There are two results [24] from STS measurements for two electrical types of isolated SWCNTs shown in Fig. 2.6. In Fig. 2.6 (a), the DOS of the semiconducting SWCNT is nearly zero when voltage ranges from -200mV to 400mV. Beyond that range, there are some peaks existing in the curve. In obtaining Fig. 2.6 (b) for a metallic SWCNT, the DOS gently increased near Fermi level, and no peaks were detected in the measurement. It should note that the STM results may vary with substrates used in the measurement.

In summary, STS or STM measurement is an effective mean to determine the

geometric parameters, van Hove singularities, the electrical types and band gap of SWCNTs. The STM or STS measurements also confirm the theoretical prediction in Eq. 2.25.

2.3.3 Modification to Band Structure

As reviewed in section 2.3.1, the 1-D electronic structure of SWCNTs can be described by the zone-fold approximation with parallel allowed lines and linear energy dispersion near the Fermi level. Displacements between the allowed states and Fermi points can be induced by external perturbations, such as mechanical deformation and electrical field. As a result, the band structure of SWCNTs will change. In this section, we will examine the effect of mechanical deformation on the electronic structure of SWCNTs.

Various mechanical deformations, such as tensile and compressive strains, can lead to the change of the unit cell of SWCNTs. Depending on Eq. 2.17, the positions of Fermi points are also changed, which gives rise to the modification of the electronic structure of SWCNTs. Yang et al. [4] gave an analytic solution to predict the effect of the mechanical deformation on the electronic structure of SWCNT based on the Mintmire approximation [11]. The key point of their work is "how to describe the electronic states near the Fermi level in the deformed SWCNTs" [11]. A deformed SWCNT under axial and torsional strain was described by using the uniform 2-D strain tensor for the graphene sheet. In the deformed graphene sheet, the real lattice vector is given by,

$$r = (I + \varepsilon) r_0 \tag{2.26}$$

where I is the unit matrix, which describes undeformed states and ε is the tensor matrix. By using the k spacing transformation, $k \cdot R_0 = k_0 \cdot R = 2\pi m$, it was proved

that the BZ and allowed state lines were invariant. Therefore, only the variation of k_F (Δk_F) was considered, and it was obtained by expanding the Hamiltonian to the first term of Δk_F, namely [4]

$$\Delta k_F^c r_0 = (1+\upsilon)\varepsilon_{//}\cos 3\theta + \varepsilon_{\perp}\sin 3\theta \tag{2.27}$$

$$\Delta k_F^t r_0 = -(1+\upsilon)\varepsilon_{//}\sin 3\theta + \varepsilon_{\perp}\cos 3\theta \tag{2.28}$$

where θ is chiral angle, $\varepsilon_{//}$ is the strain along the axial direction, $\varepsilon_{\perp}$ is the strain around the circumference, υ is the Poisson's ratio, and Δk_F^t and Δk_F^c are the components of Δk_F in the transitional and circumference direction, respectively. From Eqs. 2.27 and 2.28, it can be found that the Fermi point is driven away long the direction of 3θ to the direction of applied strain. For armchair nanotubes with θ of 30°, Fermi points move along the allowed states, which are perpendicular to the axial direction. For zigzag nanotubes with θ of 0°, the Fermi points move along the axial direction. The expression of DOS for deformed SWCNTs was derived from Eq. 2.25 as [4]

$$\rho(E) = \frac{4}{\ell}\sum_{m=-\infty}^{\infty}\frac{2}{3t_0 r_0}g(E,\varepsilon_m) \tag{2.29}$$

where

$$g(E,\varepsilon_m) = \begin{cases} |E|/\sqrt{E^2-\varepsilon^2} & |E| > |\varepsilon_m| \\ 0 & |E| < |\varepsilon_m| \end{cases} \tag{2.30}$$

and

$$l = \left(\frac{1 - v\varepsilon_{//}}{1 + \varepsilon_{//}} \right) \left(\frac{2}{3}\sqrt{3} \right) D / r_0^2 \tag{2.31}$$

$$\left| \varepsilon_m \right| = \frac{3}{2} t_0 r_0 \Delta k_m^c \tag{2.32}$$

$$\Delta k_m^c = \left| \frac{2}{3D} \left[3m - (3q + p) \right] - \Delta k_F^c \right| \tag{2.33}$$

where D is the diameter of the SWCNT, p and q is the given parameter, which depends on the geometric structure of SWCNTs with p=0 for metallic nanotubes and ± 1 for the semiconducting nanotubes. The general formula of bandgap variation (ΔE_{gap}) for uniaxial and torsional strain was derived from Eqs. 2.28 and 2.32 as [4]

$$\Delta E_{gap} = \mathrm{sgn}(2q + 1) 3 t_0 [(1 + \nu)\sigma \cos 3\theta + \gamma \sin 3\theta] \tag{2.34}$$

where σ is the uniaxial strain and γ is the torsional strain. It can be found that the bandgap modulation due to the uniaxial strain is largest for zigzag SWCNTs and zero for armchair SWCNTs, whereas the changes due to the torsional strain is largest for armchair SWCNTs and zero for zigzag SWCNTs. Because, as armchair nanotubes are stretched, the Fermi points are driven along the allowed lines. As a result, the bandgap is not changed. For the other types of nanotubes, the Fermi points are moved towards or apart to allow lines, and the change of bandgap will be induced.

Yang et al. have mentioned that "Brillouin zone and k lines remain invariant" [4]. However, in the deformed SWCNTs, both of bond lengths and angles between C-C bonds are changed. By using the relationship between the reciprocal lattice vector and real lattice vector, the reciprocal lattice can be expressed as [25]

$$k_i = \frac{2\pi}{r_i} = \frac{2\pi}{(I+\varepsilon)r_0} = \frac{2\pi}{r_0}(I+\varepsilon)^T \tag{2.35}$$

Thus, it can be reached that the both of |k| and BZ are changed in deformed CNTs. For the k line, if only the |k| changes, the conditions ($k \cdot R_0 = k_0 \cdot R = 2\pi\delta_{ij}$) they mentioned, are still satisfied, because k remains perpendicular to R_0. If the real lattice vectors rotate, k will not be perpendicular to R_0 any more, and $k \cdot R_0 = |k| \cdot |R_0| \cdot \cos\vartheta \neq 0$. Therefore, some corrections to their work are necessary as the applied strain is high.

Lots of efforts have been made to investigate the effect of radial and squeezing deformation on the electronic structure of SWCNTs. Gulseren et al. [26] gave an accurate prediction, in which the first principle total energy and electronic structure were calculated within the periodically repeating supercell by using the pseudo-potential plane wave method and periodic boundary condition. The radial deformations were induced by applying a uniaxial compressive stress on a narrow strip on the side wall of SWCNTs. Consequently, SWCNTs were squeezed in the direction of stress and elongated in the perpendicular direction of stress. The strain in the radial direction was calculated as [26]

$$\varepsilon = \frac{R_0 - a}{R_0}. \tag{2.36}$$

where R_0 is the radius of undeformed nanotubes and a is the major or minor axis of the elliptical cross-section of deformed nanotubes. From their calculation of the geometric structure of deformed SWCNTs, it can be found that the first and second neighboring distances are not noticeably affected by the radial deformation. It also can be seen that the bandgap of zigzag nanotubes decreases with increasing strain and

finally, the bandgap becomes zero. The reason is that the π^* conduction band shifts down with increasing strain and eventually crosses with π valence band at K point. For the armchair nanotubes, a bandgap is induced by the radial strain, because the π^* conduction band and π valence band move apart from each other, and consequently a pseudo-gap is induced. As the radial strain increases, charge moves from the regions with low curvature to the regions with high curvature. The chemical activity also varies with the radial deformation. The electronic structure of radially deformed SWCNTs also was investigated by Chen et al. [27] using numerical calculation. They reported that different dimensions of the area, which compressive stress was applied on, affected the electronic structure differently.

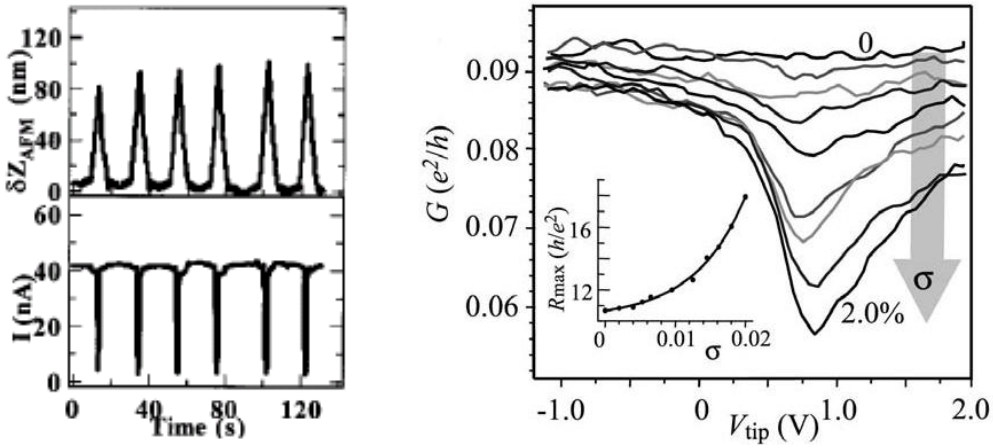

(a) (b)

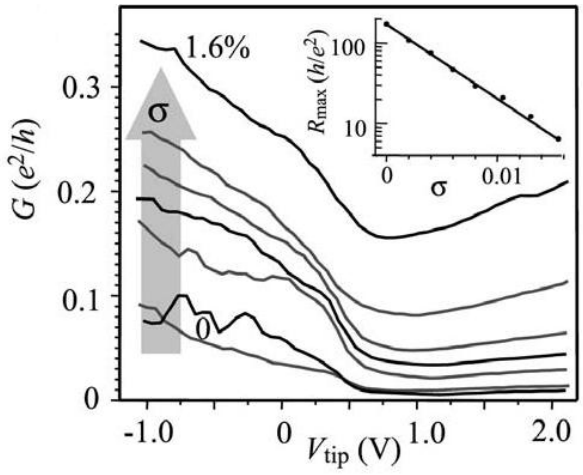

(c)

Figure 2.7 The effect of mechanical deformation on the transport properties of

SWCNTs. The mechanical deformation is induced by an AFM tip. (a) The decrease of current is caused by the AFM tip pushing. (b) Bandgap is enhanced by strain. (c) Bandgap decreases with applied strain. [28, 29]

Some experimental efforts have been made to investigate the change in the transport properties caused by mechanical deformations [28-30]. In these experiments, the tensile strain was normally induced by using the atomic force microscope (AFM) tip directly pushing on suspended SWCNTs. The electrical conductance of the SWCNTs was found to change with the applied strain (shown in Fig. 2.7). This change is caused by modification of band structure due to the stretching. Perhaps, the change can also be induced by the strong local bonding deformation due to an AFM tip or the contribution from other electromechanical deformations [28]. Cao et al. observed that a bandgap was opened in metallic SWCNTs (presented in Fig 2.7 (b)) [29]. Minot et al. reported that the bandgap of semiconducting nanotubes became narrow with increasing applied strain, which is shown in Fig. 2.7 (c) [30]. These measurements confirm the theoretical prediction in Eq. 2.35. The local bonding deformation, such as the area under the AFM tip and near the contact electrodes, can also cause the variation of conductance, which may induce some discrepancies in experiments. The variation of conductance with strain can also be observed from STM [31].

In summary, the band structure can be modified by mechanical deformations such as stretching, squeezing, and twisting. The bandgap can be either enhanced or decreased by the mechanical deformation, which is dependent on the chiral vector of CNTs. A formula derived by Yang et al. [4] can give a good prediction of the DOS of SWCNTs with low strain. This prediction is confirmed by the results from AFM measurements, in which the strain was induced by the AFM tip pushing on the sidewall of SWCNTs.

2.3.4 Electrical Conductivity of CNTs

The amazing transport properties of CNTs relate to their 1-D band structure and unique C-C bond. The extremely high electrical conductivity of CNTs gives them great potential for many important applications in various fields, such as used as nanowires for quantum conduction in electronic devices and as fillers for improving the electrical properties of matrix materials, e.g. polymers and ceramics. In order to well use the CNTs in these applications, fundamental understanding of the electrical properties of CNTs is necessary. In this section, the electrical conductivity of CNTs will be reviewed.

Table 2.1 Summary of electrical resistivities for CNTs [32, 33].

Results reported by Ebbesen et al.		Results reported by Dai et al.	
Radius (nm)	Resistivities (Ω. cm)	Radius (nm)	Resistivities (Ω. cm)
3.6	$> 4.0 \times 10^{-3}$	8.5	0.195 ± 0.02
6.1	9.8×10^{-4}	9.5	1.17 ± 0.19
7.4	2.0×10^{-4}	12.4	0.46 ± 0.018
9.1	5.1×10^{-6}	13.9	0.078 ± 0.01
10.2	1.2×10^{-4}	15.0	0.376 ± 0.01

Dai et al. probed the conductivity of individual CNTs using a general approach [32]. In their measurement, CNTs were dispersed in ethanol with assistance of ultrasonic treatment, and deposited on a SiO_2 substrate. Then, Au layer was coated on the substrate, and a striped pattern was made on the Au layer. The conducting tip was placed on the CNT samples. Then, a voltage was applied between the Au layer and a conducting tip of force microscope, and the resistance of the CNT was determined by measuring the current flow through the CNT. They reported that the resistivity of CNTs ranged from 7.8 to 117 ohm.m (listed in Tab. 2.1), and the resistivity of CNTs increased with increasing the density of structural defects. Because CNTs possess 1-D

band structure, and charge carriers in the 1-D system can only forward and backward scatter. The increase in structural defects will enhance the number of electrons scattering backward. They also reported that the resistance of a CNT (diameter of 13.9 nm) could increase by more than one order of the magnitude around the bend at the end of this nanotube.

A four-probe measurement on an individual SWCNT was performed by Ebbesen et al. [33] at room temperature. In the measurement, the 80-nm-wide tungsten leads were patterned on the nanotubes as electrodes, and these small electrodes were connected to four surrounding gold pads. The electrical resistivity of SWCNTs reported by them ranged from 5.1×10^{-6} to $4.0 \times 10^{-3}\,\Omega.\mathrm{cm}$, which are listed in Tab 2.1. They also stated that the resistivity of SWCNTs was temperature dependent, and the various SWCNTs exhibited different temperature dependent behaviours. Resistivity of the SWCNT with a diameter of 7.4 nm linearly decreased with increasing temperature(shown in Fig. 2.8 (a)), however, the SWCNT with a diameter of 6.1 nm exhibited a large transition with a strong decrease in resistivity as temperature is lowered past 220K (presented in Fig. 2.8 (b)). This large transition might be caused by the Peierls transition. A slight positive magneto-resistance was also observed.

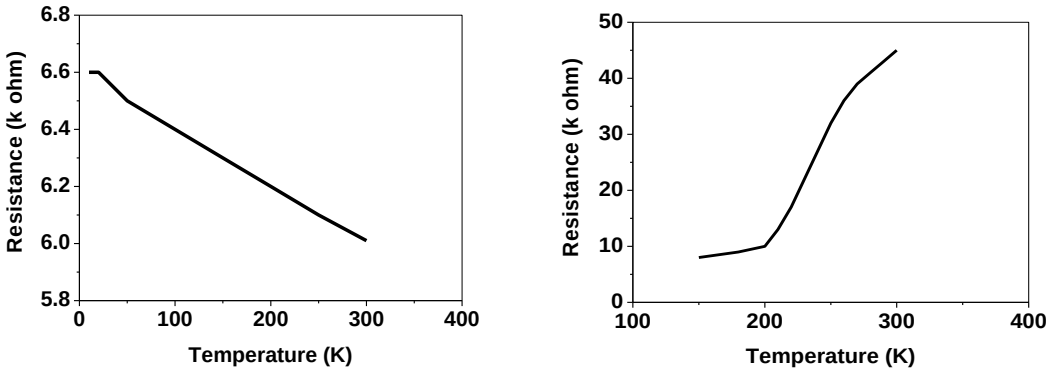

(a) (b)

Figure 2.8 Temperature dependent resistance of SWCNTs: (a) with a diameter of 7.4 nm, and (b) with a diameter of 6.1 nm.

From the resistivities of CNTs listed in Tab. 2.1, it can be found that the resistivity reported by Dai et al. [32] is two orders higher in magnitude than that reported by Ebbesen et al. [33]. This difference might be partly caused by the different methods employed in these two measurements. Ebbesen et al. used four-probe method, which can avoid the possible ambiguities due to the poor electrical contacts comparing to two termination method employed by Dai et al. The difference also can be caused by the different contact resistance between CNTs and various types of electrodes.

De Heer et al. [34] measured the resistivity of an oriented CNT film (thinner than 1μm) using four-probe method both along ($\rho_{\parallel}$) and normal ($\rho_{\perp}$) to the axis of nanotubes, and the anisotropic resistivity of the CNT film was found. They reported that $\rho_{\parallel}$ was about 20mΩ.cm at 300K, and gradually decreased with increasing temperature (shown in Fig. 2.9). $\rho_{\perp}$ was much higher than $\rho_{\parallel}$, and decreased rapidly with increasing temperature (shown in Fig. 2.9). The anisotropy of resistivity was explained on the basis of a simple geometrical consideration, in which it was considered that fewer intertube contacts had to be crossed for a given size of sample in $\rho_{\parallel}$ direction than in $\rho_{\perp}$ direction. This measurement provided the first determination of the resistivity along the axial direction, and revealed the key role of contact resistance in the conduction of CNT films or bundles.

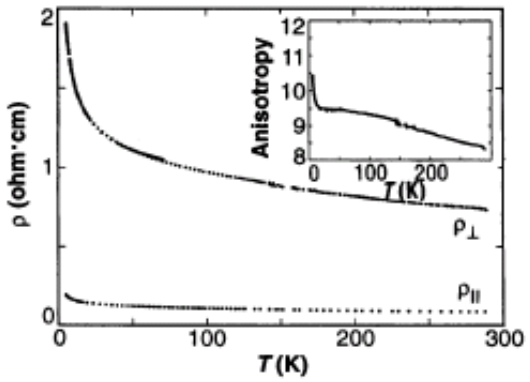

Figure 2.9. Temperature dependent resistivity of an oriented nanotube film (5mm square and approximately 1μm thick). The right inset illustrates the variation of

anisotropy ($\rho_{\perp}/\rho_{\parallel}$) with temperature [34].

The resistivity of crystalline ropes of SWCNTs was measured by Fisher et al.[35], and they reported that $\rho_{\parallel}$ of the ropes was in the range of 0.03 to 0.1mΩ.cm at 300K. In contrast to the temperature dependent behaviour of oriented film, $\rho_{\parallel}$ of the rope gradually increased with increasing temperature. They also found that the unoriented bulk SWCNT mat had a much higher resistivity than that of ropes. Two probe magneto-conductivity measurements on individual MWCNTs at low temperature were performed by Langer et al. [36]. They stated that the conductance of MWCNTs exhibited logarithmic temperature dependence and saturated at low temperature. The magnetic field normal to the axial direction increased the electrical conductance and gave rise to an aperiodic fluctuation. The electrical conductivity of CNTs can be decreased by heat treatment such as annealing. Hone et al. [37] reported that the conductivity of SWCNTs could decrease from 10^4 to 10^3 S/cm after heat treatment. This decease may associate with improvement of the crystallinity , and the remove of the residual acid.

In summary, the electrical conductivity of CNTs was measured by many research groups. Normally, the electrical conductivity of individual CNTs is in the order of 10^3-10^6 S/cm. The defects in CNTs reduce the conductivity of CNTs due to the growth of backward scattering. The temperature can affect the conductance of CNTs but various temperature dependent behaviours were reported. None of MWCNTs show the positive $d\rho/dT$ characteristic of a metal. CNT films possess anisotropic resistivities, and $\rho_{\perp}$ is much higher than $\rho_{\parallel}$ due to the contact resistance between CNTs. The electrical conductivity of CNTs can also be affected by magnetic field and heat treatment.

2.3.5 Contact Resistance between CNTs

CNTs can not really connect with each other, and there is a small gap between neighboring CNTs, which induces the large contact resistance. Contact resistance between CNTs plays key role in the electrical conductance of disorder CNT systems such as CNT mat and CNT percolation network. As mentioned in previous section, the anisotopic resistivity of CNT films is resulted by the contact resistance, and the large resistance in the random oriented CNT mat is also induced by the contact resistance. In this section, we will review the experimental and theoretical work on the contact resistance between CNTs.

Fuhrer et al. [38] measured the contact resistance between two crossed SWCNTs. In their experiment, the SWCNT-SWCNT junction was formed by two crossed individual SWCNTs or small bundles (diameter <3nm), and the four-terminal conductance was measured. They reported that the contact resistance strongly depended on the electrical types of SWCNTs in the junction. In the case of the junction formed by the same electrical types of SWCNTs, there are good tunneling contacts in the junction and the electrical resistance is in order of $10^5 - 10^6\Omega$. In the case of the junction formed by different electrical types of SWCNTs, the doping of the semiconducting SWCNT are depleted by metallic SWCNTs at the junction. As a result, the tunneling barrier between the two SWCNTs is enhanced, and the electrical resistance is much higher than that of the junction formed by the same electrical types of SWCNTs.

The contact resistance between CNTs was theoretically predicted by Buldum et al. [39] by using the Landauer-Buttiker formalism to calculate the conductance with the surface Green's function method. They stated that the contact resistance strongly depended on contact lengths and the angles between CNTs in the contact region, and atomic scale movement could induce the contact resistance varying several orders of magnitudes. The dependence of conductance on the contact length was nonlinear and

quasiperiodic (shown in Fig. 2.10 (a)), and the periods of the zigzag-zigzag and armchair-armchair tube junction were a_z and $3a_z$, respectively. In the case of rotation dependence, the lowest resistance values was found as junction was in-registry configuration. For (18,0)-(10,10) nanotubes junction, electrical resistance was lowest at $\Theta = 30°, 90°, 150°$ (presented in Fig. 2.10 (b)). The contact resistance could be significantly reduced by the structural relaxation and applying a pressure on the junction, which is shown in Fig 2.10 (c). The contact resistance predicted varies from $100k\Omega$ to $3.4M\Omega$.

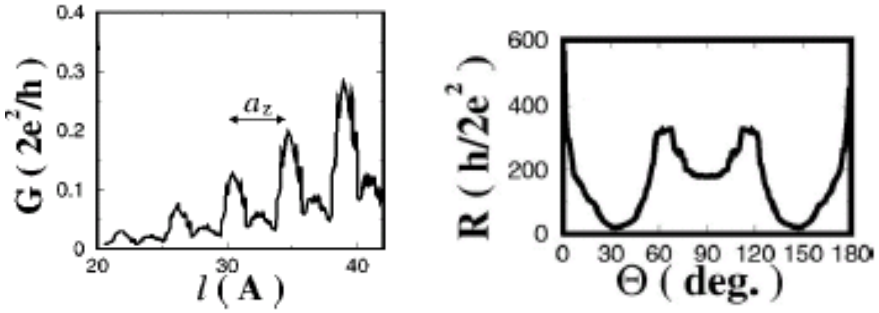

(a) (b)

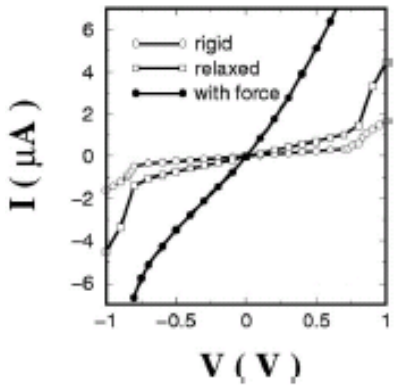

(c)

Figure 2.10 (a) Variation of conductance with contact length for the (18,0)-(18,0) junction. The period (a_z) of the oscillation is the unit cell length of the nanotubes. (b) Variation of the contact resistance of the (18,0)-(10,10) junction with rotation angle θ. (c) I-V curve of a (18,0)-(10,10) junction. The contact resistance of the rigid nanotubes ($3.36M\Omega$) reduces to $3.21\ M\Omega$ caused by relaxation and to $1.66M\Omega$

induced by applied force. [39]

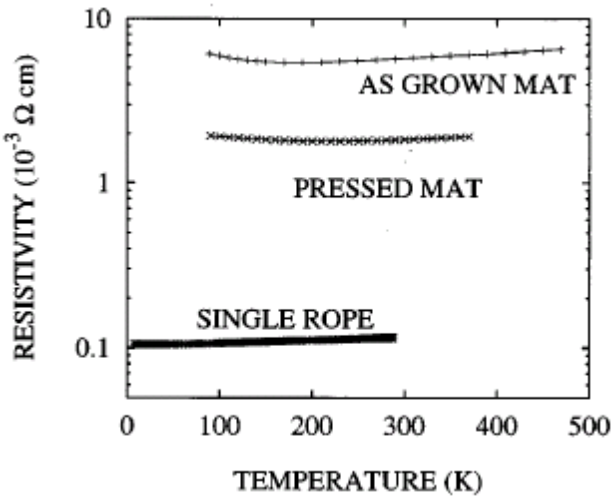

(a)

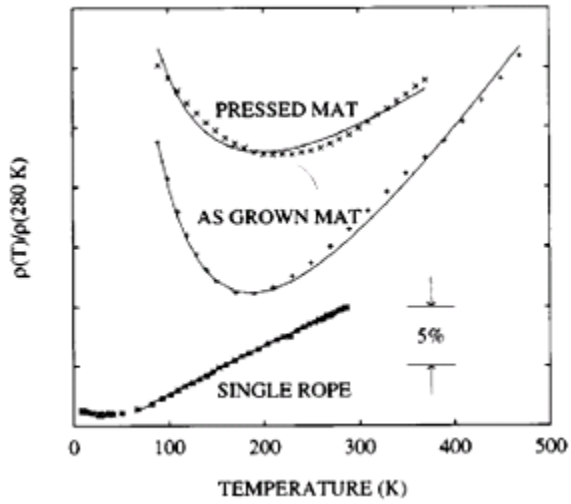

(b)

Figure 2.11 (a) Variation of resistivity with temperature for as-grown and pressed SWCNT mats, and single SWCNT rope. (b) Variation of reduced resistivity with temperature for as-grown and pressed SWCNT mats and single SWCNT rope. [35]

As discussed in previous section, the anisotropic resistivities of the CNT films are resulted from the contact resistance and geometric difference in axial and normal direction [35]. The curves of resistivity versus temperature for different SWCNT materials (as grown and lightly pressed randomly oriented mat, and single-rope) are

presented in Fig. 2.11 (a). As grown mat, in which SWCNTs and intertube barrier are randomly oriented in the mat, possesses the highest resistivity in these three samples. However, it can be observed that the average resistivity ($\langle\rho\rangle$) of as grown mat is only 50 times higher than $\rho_{\parallel}$ of the single SWCNT rope. This small difference was explained by the extreme aspect ratio of the ropes contained in the mat, which reduced the number of rope-rope contacts. As the pressure was applied on the mat, the resistivity reduced by a factor 5, which is partly due to the decrease of the contact resistance under the pressure. The single rope has the lowest resistivity in these samples, because the orientation of intertube barriers is perpendicular to the axial direction, therefore, intertube barriers only have a little effect on the electrical resistivity of the rope. The temperature dependence behaviour can be more clearly seen in an expanded relative scale, which is presented in Fig 2.11 (b). It can be observed that the temperature dependent behaviours of SWCNTs samples are different from each other. This difference is also caused by the intertube gaps.

In summary, the extremely high contact resistance is induced by the small intertube barriers. Measured contact resistance of the same electrical types of SWCNTs junction ranges from $100\text{k}\Omega$ to $400\text{k}\Omega$, and two order higher for the junction consisted of two different types of SWCNTs. Theoretical calculations predicted the contact resistance between CNTs was in the range of $100\text{k}\Omega - 3.4\text{M}\Omega$. The contact resistance plays a dominant role in the resistance of disorder CNT systems. The contact resistance can be reduced by structural relaxation and applying pressure, and can be enhanced by heat treatments.

2.3.6 Thermoelectricity of CNTs

The thermoelectricity (TE) is concerned with the direct generation of electromotive force by thermal means, and this involves subjecting a conductor to a temperature gradient. The electrons in the hot region intend to diffuse to the cold region due to the

lower energy states in the cold region. As a result, an electric potential between the hot and cold regions is induced. Thermoelectric power (TEP) of a material is concerned with the amplitude of an induced thermoelectric voltage responding to the temperature difference in the material. For an one-band system in a 1-D conductor, TEP can be expressed as [41],

$$S = -\frac{k}{e}\left(\frac{3F_{1/2}}{F_{-1/2}} - \zeta\right) \tag{2.37}$$

where F_i is the Fermi-Dirac function, and ζ is the reduced Fermi level relative to the band edge for electrons and holes. The Fermi-Dirac function F_i is given by,

$$F_i = \int_0^\infty \frac{x^i}{e^{(x-\zeta)}+1}\,dx \tag{2.38}$$

A general equation of TEP for a homogeneous system was derived from the Mot and Jones theory [42] as,

$$S = \frac{\pi^2 k^2 T}{3e}\frac{d\ln\sigma(E)}{dE}\Big|_{E_F} \tag{2.39}$$

where *k* is the Boltzman constant, T is temperature, e is the electronic charge, and σ(E) is a conductivity-like function of electronic energy E. For the heterogeneous CNT systems, which comprise two parallel electrical paths, the total TEP can be expressed by a two-band model,

$$S = \frac{\sigma_1}{\sigma}S_1 + \frac{\sigma_2}{\sigma}S_2 \tag{2.40}$$

where S_1 and S_2 are the TEP for two electrical pathways, and the total conductance is the sum of the conductance of two paths, $\sigma = \sigma_1 + \sigma_2$. Hone et al. [43] measured the temperature-dependent TEP of crystalline ropes of SWCNTs. Large and positive

TEP of SWCNTs ropes at high temperature were reported. The total TEP decreased with lowering temperature, and approached to zero as $T \to 0$, which is presented in Fig. 2.12. The temperature-dependent TEP was well fitted by the equations derived from the two-band model,

$$S_{tot} = AT + (B\lambda + CT)\exp(\frac{-\lambda}{T}) \quad \text{for a constant metallic conductivity} \quad (2.41)$$

or

$$S_{tot} = AT + (\frac{B\lambda}{T} + CT)\exp(\frac{-\lambda}{T}) \quad \text{for a } 1/T \text{ metallic conductivity} \quad (2.42)$$

where A-C are constants and λ is gap temperature. In both cases, the first term represents the TEP of metallic path, and second term indicates the TEP of semiconducting path. The measured TEP was fitted by adjusting the values of A, B, C, and λ.

Small et al. [44] measured the TEP of individual SWCNTs in mesoscopic scales. They found that the TEP could be affected by the gate voltage. The smooth variation of the conductance with applied gate voltage was observed at 300K (shown in Fig. 2.13 (a)). This voltage dependent behaviour attributes to the resonant electron scattering by the defects in metallic SWCNTs, and multiple scattering sites are created by these defects as temperature decreases. Therefore, TEP exhibits more complicated voltage dependent behaviour at lower temperature, which is presented in Fig. 2.13 (b). It can be observed that TEP has periodic oscillations as a function of gate voltages in the Coulomb blockade regime. The amplitude of oscillations decreases with increasing temperature, and the oscillations finally disappear as temperature above 30K.

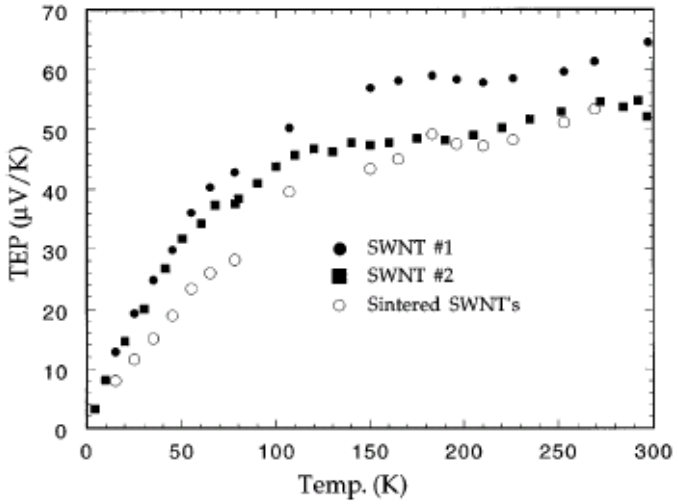

Figure 2.12 TEP of three SWCNTs samples [43]. The contacts between nanotubes have been improved in sintered samples by pressing and heating.

The effect of the randomly oriented intertube barriers on TEP was explored by Baxendale et al. [45]. A strong positive TEP was observed for mats with randomly oriented CNTs, by contrast, a macroscopic bundle of MWCNTs only gave a weakly negative TEP. They stated that the positive TEP was not an intrinsic characteristic of CNTs but rather was a consequence of the random intertube barriers. This positive TEP was explained by using two band model and variable range hopping (VRH) conduction, and a model with the consideration of intertube barriers was given to qualitatively describe the temperature dependent behaviour of TEP. At the room temperature, the model was expressed as [45],

$$S = A'T\exp(\frac{-T}{T_0})^{1/4} + B'\exp\left(\frac{-\lambda}{T}\right) \times \exp\left(\frac{-T}{T_0}\right)^{\frac{1}{4}}\left[\frac{C'\lambda}{T} + D\right] + ET^{1/2} \qquad (2.43)$$

where T_0 is the parameter in VRH conduction, and A'-E are constants. The first, second, and third terms in Eq. 2.43 represent the contributions from metallic and semiconducting CNTs, and barrier regions, respectively. The change of the sign of TEP is induced by the hopping factor, $\exp(\frac{-T}{T_0})^{1/4}$, and the contribution of barrier regions, $ET^{1/2}$.

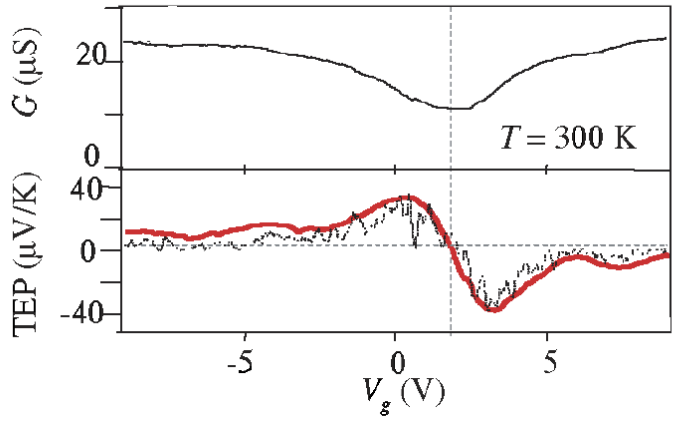

(a)

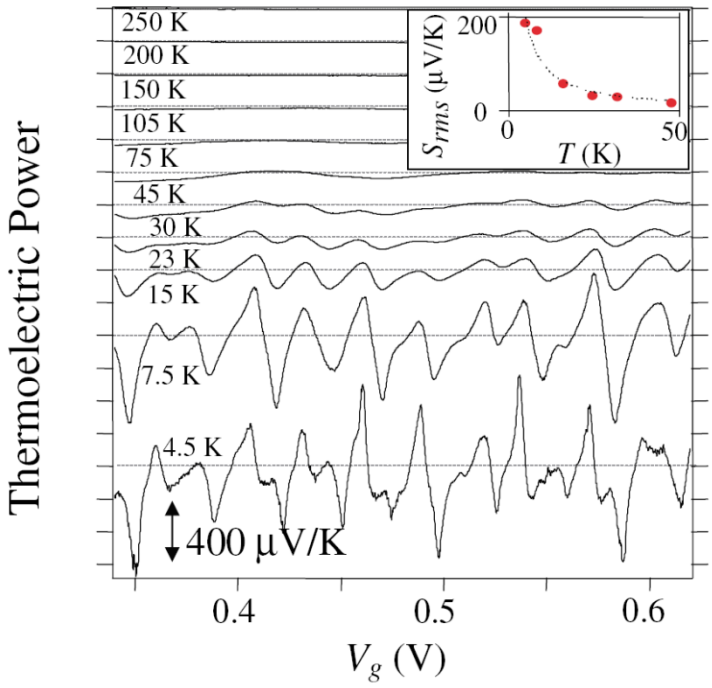

(b)

Figure 2.13 Variation of TEP with applied gate voltage at (a) 300K, and (b) lower temperature range (4.5K-250K). [44]

The sensitivity of TEP to gas exposure history was discovered by Bradley et al. [46]. It was reported that CNTs exposed to oxygen always had a positive TEP. The TEP of deoxygenated CNTs was strongly negative, and it was enhanced with increasing temperature. Interestingly, they also found that the temperature dependent behaviour of fully oxygenated and deoxygenated SWCNTs appeared to be 'mirror images' of

each other. As O_2 molecules are attracted on SWCNTs, the electronic states are generated at the Fermi level by the strong oxygen interaction. Two-fold degenerate valence bands split and two peaks near the Fermi level are resulted. This increase of DOS near the Fermi level gives the positive TEP of oxygenated SWCNTs. Here, we give another possible interpretation that an ionized impurity scattering is induced by the oxygen molecules doping on SWCNTs, which enhances the TEP of the SWCNTs. This interpretation is confirmed by the experiment performed by Sumanasekera et al. [46], in which the TEP of SWCNT films during the adsorption of cyclic hydrocarbons C_6H_{2n} (n=3-6) was measured. They found that the enhancement of TEP was maximum for benzene (C_6H_6; 6 π electrons) and decreased to zero for cyclohexane (C_6H_{12}; no π electrons). The benzene on the sidewall can be seen as an ionized impurity due to the interaction between π electrons in benzene and SWCNTs. As a result, a new scattering channel was created, and the TEP of the SWCNTs was enhanced.

In summary, the TEP of CNTs is very sensitive to the change of electronic structure. A modulation of TEP can be induced by applying a gate voltage, and the positive TEP of CNTs is caused by the absorption of oxygen molecules. The strongly positive TEP of CNT mats or films can be attributed to the randomly oriented intertube barriers. In these measurements, the CNT samples may subject to various mechanical deformations, which may correlate to the changes in the electronic structure of CNTs and intertube barriers between CNTs, and a variation of TEP can be induced. However, the mechanical deformation induced the variation of the TEP of CNTs have not been explored yet.

2.4 Electrical Properties of CNT/Polymer Composites

Electrically conductive polymeric materials are important in many applications, in which electrostatic dissipative and electromagnetic shielding are required. CNTs, due

to their high electrical conductivity and high aspect ratio, have attracted growing interests in the materials community in recent years as a conducting filler in the development of conducting polymer composites. It is well known that the electrical conductivity of polymers can be dramatically enhanced by 8-10 orders of magnitude by adding very low content of CNTs. In this section, the DC and AC electrical properties of CNT/polymer composites will be reviewed.

2.4.1 DC Conductivity of CNT/Polymer Composites

Electrical conduction in a conductive polymer composite comprised of the conducting filler and the polymer insulated phase is mainly described by three means: percolation theory, hopping conduction, and temperature fluctuation induced tunneling between the conductors. Kirkpatrick [48] and Stauffer [49] solved the electrical conductivity of a conductor-insulator system by percolation theory, which describes the behaviour of connected clusters in a random graph. In the percolation theory, it is considered that the continuous phase of conducting filler is the only pathway for electron transporting, and the electrical conductivity , σ, can be described as follows [49]:

$$\sigma_{dc} = \alpha \cdot (p - p_c)^t \tag{2.44}$$

where α is a constant, p_c is the percolation threshold, p is the concentration of conducting component and t is a corresponding critical exponent. This equation is only valid as $p > p_c$ or $p \sim p_c$. As the concentration increases around the p_c, the electrical conductivity of the composites sharply increases with increasing the mass fraction. Because the continuous pathways through the composites begin to form as $p > p_c$. The exponent t depends on the dimensionality of the system with calculated values of $t \sim 1.33$ and $t \sim 2.0$ in two and three dimensions, respectively [49]. The value of t may vary due to the various methods of simulation employed. The value of α can be determined by fitting Eq. 2.44 to experimental results.

In percolation theory, it is considered that the electrons only transport through the continuous network of conductor. However, in the real conductor-insulator composites, the electrons are allowed to tunnel between conductors through the thin insulating layer. For disordered materials, in which large conducting regions separated by small insulating barriers, the electrical conduction can be described by fluctuation-induced tunneling (FIT) model [50], in which the thermally activated voltage fluctuations across insulating gaps play an important role in determining the temperature and field dependences of the conductivity. By regarding the modulating effects induced by voltage fluctuation on either an image-force corrected potential barrier, the tunneling conductivity was derived as follows:

$$\begin{aligned} \sigma &= \sigma_0 \exp[-T_1/(T+T_0)] \\ T_1 &= wA\varepsilon_0^2/8\pi k \\ T_0 &= A\varepsilon_0^2/4\pi^2\chi k \end{aligned} \tag{2.45}$$

where σ is conductivity, σ_0 is constant, w is the width of the tunneling gap, A is the area of the capacitance formed by the tunneling junction, V_0 is the height of barrier, m is the mass of electrons, $\varepsilon_0 = 4V_0/ew$, and $\chi = (2mV_0/h^2)^{1/2}$. It can be easily seen that electrical conductivity depends on the width of barriers at a given temperature, and Eq. 2.45 can be rewritten as

$$\sigma_{dc} \propto \exp(-w) \tag{2.46}$$

The width of gaps between conductors is proportional to $p^{-1/3}$ in a homogenous system [49]. Thus, scaling law can be derived from Eq. 2.46 for a homogenous CNT/polymer system, namely

$$\ln\sigma_{dc} = -p^{-1/3} \tag{2.47}$$

The tunneling of electrons from occupied to unoccupied states involves one or more phonons, and is called hopping. When both number of phonons and the energy decreases, the hopping between states that are closer in energy becomes more preferable than that between the nearest neighbors whose energies differ substantially [51]. This mechanism is known as variable range hopping (VRH). The electrical conductivity of CNT/polymer composites is often described by VRH model as [51],

$$\sigma_{dc} = \sigma_0 \exp[-(T_0/T)^{\gamma}] \tag{2.48}$$

where T_0 is the parameter depending on the DOS at the Fermi level, and γ is the exponent. For 3-D Mott VRH model, the value of γ is 1/4. When Coulomb effects are important, the γ is proposed to be 1/2 [52].

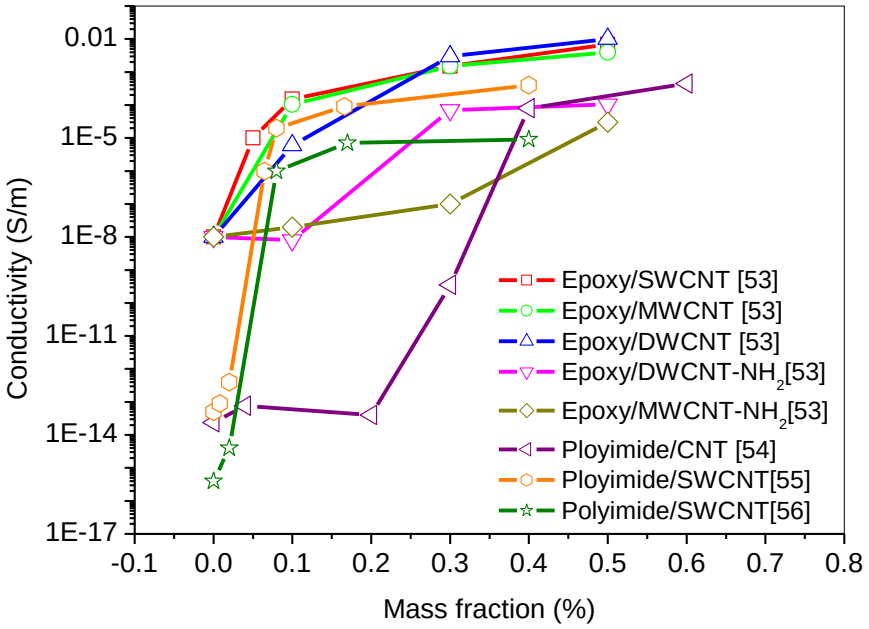

Figure 2.14 Summary of DC experimental conductivity for CNT/epoxy and CNT/Polyimide composites. DWCNT is double walled carbon nanotube.

Table 2.2 Summary of measured electrical conductivity and p_c for various CNT/polymer composites.

Polymer matrix	Types of CNTs	Processing	p_c (wt%)	Conductivity (S/m)
Epoxy [53]	SWCNTs	In-situ polymerization	0.05	0.01
Epoxy [53]	MWCNTs	In-situ polymerization	0.075	0.0065
Epoxy [53]	DWCNTs	In-situ polymerization	0.1	0.01
Epoxy [53]	MWCNTs-NH_2	In-situ polymerization	0.3-0.5	7×10^{-4}
Epoxy [53]	DWCNTs-NH_2	In-situ polymerization	0.1-0.3	3×10^{-4}
Epoxy [54]	CNTs	Solution casting	0.4	1.3×10^{-4}
Polyimide [55]	SWCNTs	Solution casting	0.04	0.005
Polyimide [56]	SWCNTs	Solution casting	0.43	1×10^{-5}
PE [57]	MWCNTs	Melting mixing	7-8	10^{-4}
PP [58]	MWCNTs	Melting mixing	1-2	10^{-3}
PC [59]	MWCNTs	Melting mixing	5-6	10^{-6}
PVA [60]	MWCNTs	Solution casting	0.04-0.05	10^{-4}
PMMA [61]	MWCNTs	In-situ polymerization	0.4-0.6	3.2×10^{-2}

Extensive efforts have been made to develop high perform CNT/polymer composites with low percolation thresholds and high electrical conductivities. Most measured electrical conductivities range from 10^{-5} to 10^{-2} S/m, and p_c varies from 7 wt% to 0.05 wt %. Measured conductivities and p_c of various CNT/polymer composites

are summaried in Tab 2.2, and the variations of conductivity as a function of mass fraction is plotted in Fig. 2.14.

Large scattering can be found from reported DC conductivities. This large scattering indicates the complex nature of the electrical conductivity in CNT/polymer composites due to various factors, such as the waviness and geometric structure of CNTs, the dispersion of CNTs, and polymer matrices. The excluded volume (V_{ex}) of an object is defined as the volume associated to that object which is not accessible by the center of mass of another object [49]. Generally, it is considered that p_c is inversely proportional to the object excluded volume. For a straight fiber system, V_{ex} is the function of aspect ratio (ζ), and the relationship between them was given by Balberg et al. [62] as

$$V_{ex} = \frac{4\pi}{3} d^3 \left[1 + \frac{3}{8}\zeta + \frac{3}{128}\zeta^2\right] \tag{2.49}$$

Yi et al. [63] reported that p_c significantly increased with fiber waviness (simulated by a sinusoidal shape of fibers in 2-D systems). Dalmas et al. [64] investigated the p_c in wavy fibers system by using a discretization method, and they showed that p_c increased with increasing the waviness of fiber in a 3-D system. Li et al. [65] presented that contact resistance between CNTs played a dominant role in the electrical conductivity of CNT based composites by Monte Carlo simulation, and they predicted that both of p_c and exponent were strongly affected by the contact resistance. Foygel et al. [66] estimated that the contact resistance between CNTs in composites was in the order of $10^{13}\Omega$, and they stated that this high contact resistance was induced by tunneling conduction in the CNT percolation cluster.

CNT based composites with extremely high electrical conductivities and low p_c have also been reported. Homogeneous CNT/polymer composites were fabricated by Ramasubramaniam et al. [67] using noncovalently functionalized, soluble SWCNTs.

The electrical conductivity of the composites was dramatically improved with very low percolation threshold ($p_c \sim 0.05 - 0.1\%$ wt). CNTs can be aligned by applying a magnetic field [68] due to their anisotropic magnetic susceptibilities [69]. Choi et al. presented that the electrical properties of SWCNT/polymer composites can be significantly enhanced by magnetic alignment during processing [70]. They found that the electrical conductivity of composites processed under magnetic field can be increased by six orders of magnitude at the same mass fraction. Recently, a novel cellular structure of CNTs in polymeric matrix has been created to achieve low p_c. Grunlan et al. [71] reported that p_c based on PVAc latex (105nm) was found to be 0.04%wt. During the film formation of the polymer latex, CNTs were pushed to the interstitial space between spherical particles to form the cellular structure. As a result, the free volume for CNTs to construct percolation network was dramatically reduced, and low p_c was achieved.

In summary, the conductive CNT/polymer composites have been extensively studied. Most of measured electrical conductivity was in the range of 10^{-7} to 10^{-2}S/m, and the p_c ranged from 8% to 0.1%. However, the p_c tailored to the range of 0.02%wt-0.05%wt has also been reported. The large scattering in the reported results indicates the complex nature of the electrical conductivity in CNT/polymer composites due to various factors. However, some questions still remain unanswered, especially for the effect of local morphology and tunneling conduction. Due to the relatively low conductivity of CNT/polymer composites, it may be doubted whether CNTs can be effective conductive fillers for improving the electrical conductivity of polymers.

2.4.2 AC Properties of CNT/Polymer Composites

The AC admittance (Y_m) of CNT/polymer composites is consisted of the real (Y_{mr}) and imaginary (Y_{mi}) terms. The AC admittance (Y_i) of polymer also can be expressed

by the sum of real and imaginary part: $Y_i = Y_{ir} + Y_{ii}$ with $Y_{ii} = \omega\varepsilon_0\varepsilon_{ir}$, where ω is the applied frequency, $\varepsilon_0$and ε_{ir} are the dielectric constant of vacuum and polymer matrix, respectively. The AC percolative Y_m, as a function of volume fraction and frequency, has been investigated by series of studies [72-74], which was often regarded in three regions: Ⅰ where $p > p_c$, the admittance can be described by the expression: $Y_m = A(p - p_c)^t - iB\omega\varepsilon_0\varepsilon_{ir}(p - p_c)^{-s}$, where A and B are arbitrary constants. Ⅱ where $p < p_c$, the admittance can be expressed as $Y_m = A(p_c - p)^t - iB\omega^2\varepsilon_0^2\varepsilon_{ir}^2(p_c - p)^{t-2s}$ Ⅲ called the crossover where $p \sim p_c$, the admittance Y_m and dielectric constant $\varepsilon_m$are proportional to $\omega^{t/(s+t)}$ [75]. Recently, series of studies [73, 74, 76] have shown that the equation

$$(1-p)\left(\sigma_i^{\frac{1}{s}} - \sigma_m^{\frac{1}{s}}\right)\left(\sigma_i^{\frac{1}{s}} + A\sigma_m^{\frac{1}{s}}\right) + p\left(\sigma_c^{1/t} - \sigma_m^{1/t}\right)\left(\sigma_c^{1/t} + A\sigma_m^{1/t}\right) = 0 \qquad (2.50)$$

with $A = (1 - p_c)/p_c$ and s, t as exponents for permittivity and conductivity, have the best fit with experimental results for percolation systems. Two limits were yielded from Eq. 2.50 as

$$\sigma_m \to \infty:\ \sigma_m = \sigma_i\left(\frac{p_c}{(p_c - p)}\right)^s \qquad p<p_c \qquad (2.51)$$

$$\sigma_i \to 0:\ \sigma_m = \sigma_c\left(\frac{(p - p_c)}{(1-p)}\right)^s \qquad p>p_c \qquad (2.52)$$

These equations have a similar form to the scale law of DC conductivity of CNT/polymer composites, and are normalized standard percolation results [77]. In the crossover region, the AC conductivity can be expressed as

$$\sigma_m = \sigma_c^{s/(s+t)}(\omega\varepsilon_0\varepsilon_i)^{t/(s+t)} \qquad (2.53)$$

Normally, the conductivities of polymers linearly grow with increasing the applied

frequency, and CNT/polymer composites with $p<p_c$ exhibit the same frequency dependent behaviour as polymers. In the case of $p>p_c$, electrical conductivities exhibit a frequency independent behaviour as applied frequency (ω) is below the critical frequency (ω_0), and will increase linearly with applied frequency as $\omega > \omega_0$. The measured frequency dependent behaviours of CNT/polymer composites with various mass fractions are presented in Fig. 2.15 (a). Various approaches have been proposed to interpret this frequency dependent conductivity at the frequencies higher than ω_0. An explanation based on the percolation theory is often used for understanding the frequency dependent behaviour [78]. A characteristic length scale known as correlation length ξ can be defined in a percolation system [79]. ξ associates with the largest size of conductors in the systems [80]. The charge carriers are considered scanning a distance under applied AC voltage, and the scanning distance can be scaled with the period of the perturbing wave. If a charge carrier scans a distance l at a frequency of ω_l, it will travel a larger distance at the frequencies smaller than ω_l, and vice versa. In the case of the frequencies lower than ω_0, it is expected that the charge carriers tunneling at least one intertube gap between CNTs. In the case of $\omega > \omega_0$, charge carriers would be expected to travel within CNTs. The ω_0 is related with ξ of the percolation system and the relationship between them is given by [81]

$$\omega_0 = \xi^{-1/\alpha} \tag{2.54}$$

where α is in the range of 0.5-1. $\alpha = 0.5$ corresponds to the random walk along the percolation network, and $\alpha = 1$ correlates to the trajectory under strong electrical fields. Previous simulations [81] based on the random walk indicated that the simulated results were strongly affected by the presence of loops in the system, leading to reduce electrical properties under electrical filed. In percolation system, the correlation length decreases as the mass fraction increases, and it can be expressed in a scaling law form as,

$$\xi \propto (p - p_c)^{-\nu} \tag{2.55}$$

where the exponent ν depends on the dimension of system. Therefore, Eq. 2.54 can be rewritten as,

$$\xi \propto (p - p_c)^{-\nu/\alpha} \tag{2.56}$$

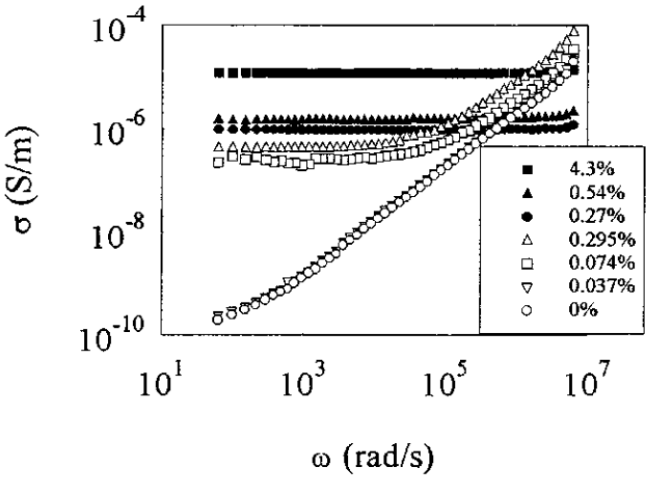

(a)

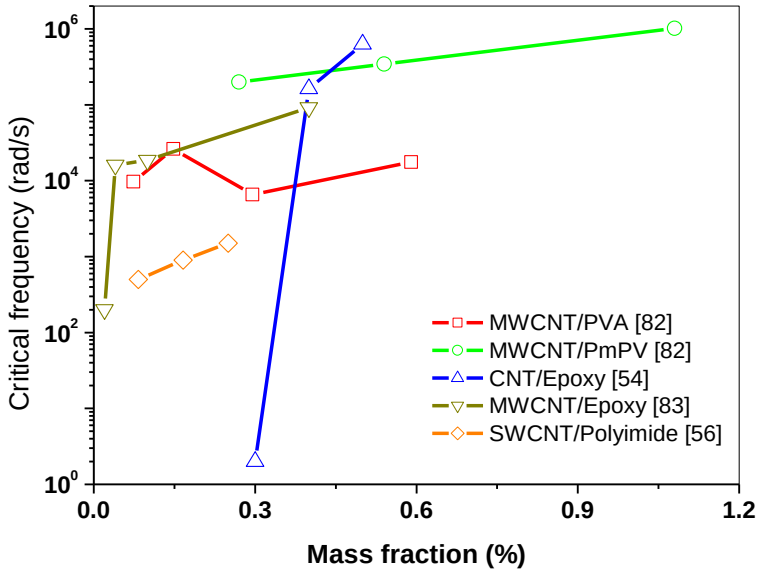

(b)

Figure 2.15 (a) Frequency dependent conductivity for MWCNT/PVA with various mass fractions. [82] (b) Summary of measured critical frequencies as a function of

mass fraction for various CNT/polymer composites.

Table 2.3 Summary of measured AC properties of CNT/polymer compostes. σ_0 is independent conductivity, and s is exponent.

p (wt%)	Types of CNTs	Polymer matrix	σ_0 (S/m)	ω_0 (rad/s)	s
0.590	MWCNTs	PVA [82]	9.68×10^{-7}	1.76×10^{4}	0.93
0.295	MWCNTs	PVA [82]	4.01×10^{-7}	6.56×10^{3}	0.91
0.148	MWCNTs	PVA [82]	4.46×10^{-7}	2.63×10^{4}	0.91
0.074	MWCNTs	PVA [82]	2.41×10^{-7}	9.68×10^{4}	0.94
0.04	CNTs	Epoxy [54]	2.4×10^{-16}	Fully dependent	1.04 ± 0.01
0.3	CNTs	Epoxy [54]	3.5×10^{-12}	2	0.81 ± 0.01
0.4	CNTs	Epoxy [54]	7.9×10^{-7}	1.63×10^{5}	0.84 ± 0.02
0.6	CNTs	Epoxy [54]	4.4×10^{-6}	6.28×10^{5}	0.65 ± 0.08
0.27	MWCNTs	PmPV [82]	9.42×10^{-7}	1.19×10^{5}	-
0.54	MWCNTs	PmPV [82]	1.44×10^{-6}	3.45×10^{5}	-
1.08	MWCNTs	PmPV [82]	2.32×10^{-6}	1.02×10^{6}	-
2.15	MWCNTs	PmPV [82]	4.88×10^{-6}	3.01×10^{6}	-
0.02	MWCNTs	Epoxy [83]	8.3×10^{-9}	2.01×10^{2}	0.88
0.04	MWCNTs	Epoxy [83]	4×10^{-7}	1.61×10^{4}	0.86
0.1	MWCNTs	Epoxy [83]	5.3×10^{-6}	1.86×10^{4}	0.86

The AC properties have been measured by many research groups. Measured ω_0 and exponents are summarized in Tab. 2.3, and the measured frequency-dependent behaviour versus mass fraction is presented in Fig. 2.15 (b). From the listed results, it

can be found that ω_0 varies with mass fraction, types of CNTs comprised in composites, and the types of polymer hosts. For p=0.1%, ω_0 ranges from 1.86×10^4 to 1×10^6 rad/s. From Fig 2.15 (b), it can be clearly seen that CNT based composites behaves differently from each other.

The large scattering can be found from the reported results even for CNTs in the same polymer matrix. This large scattering indicates that the AC properties of conductor/polymer composites are strongly influenced by the local morphology of the composites. However, prior studies were only restricted to interpret the frequency dependent behaviour by the scaling law, and no considerations have been given to the influence of local morphology on the AC properties that might be of interest to improve the knowledge of composites and design composites with better properties. Another limitation of the existing literature is that the frequency dependent conductivity was understood by only using the non-quantified method based on the percolation theory. It is slightly idealized to consider electrons scanning a distance under AC field in the disorder polymer hosts, and previous simulation indicated that correlation length was strongly influenced by the polymer host and the morphology of the composites.

2.5 Strain Sensors Applications

Strain sensors are important in the science and engineering field. However, there are many limits for the existing strain sensors, e.g. existing sensors can not be embedded in materials level and provide multidirectional sensibility. A new sensor, which has multidirectional sensibility, and can be embedded into the material, is needed to develop. The electronic structure of CNTs is extremely sensitive to the mechanical deformations due to the shift of Fermi point k_F away from the vertices of BZ [4] as reviewed in section 2.3.3. This sensitive 1D electronic structure gives CNTs great potential to be used to develop a new strain sensor. Furthermore, their small size

allowed CNTs to be able to fabricate extremely small sensors, which are sensitive to the mechanical environments around the CNTs. In this section, the past progress and on-going efforts on the development of CNT strain sensor will be reviewed.

To date, most studies directly relate the modification of electronic structure to the change in electrical properties of CNT films or composites. Dharap et al. [84] investigated the CNT strain sensor based on the randomly oriented CNT film. The resistance of the film was measured by using four-probe method. They observed a linear change in the resistance as the CNT film was subjected to tension and compression (presented in Fig. 2.16). The deviation from the linear trend was also found, and they stated that this deviation might be caused by the change of local temperature and the gas exposure history. A 'neuron sensor' was created by Kang et al.[85, 86] using SWCNT/PMMA composites. The neuron sensor is a long continuous strain sensor, which has a low cost, and is simple to install. They examined static and dynamic sensing behaviour, and suggested that the neuron system can be attached to the surface of a structure to build a sensor network for monitoring the structural health. They also stated that the deviation from the linear trend was caused by axial slipping of smooth sidewalls of CNTs, and the repeatability and linearity of the CNT based strain sensor can be improved by blending CNTs with polymers, which enhance the interfacial bonding between nanotubes. The linear sensing behaviours of SWCNT/PMMA were also observed by them. Zhang et al. [87] reported the sensing behaviour of MWCNT based composites, and the sensitivity of CNT composites was 3.5 times higher than conventional strain sensors. They suggested that MWCNT composites could be used for self-diagnostics and real-time health monitoring. Loh et al. [88] fabricated layer-by-layer CNT/poly(electrolyte) film for strain sensing. A linear sensing behaviour was also reported by them. They stated that the resistance in deformed CNT films exponentially decayed during sampling of resistance due to the joule heat generated by current.

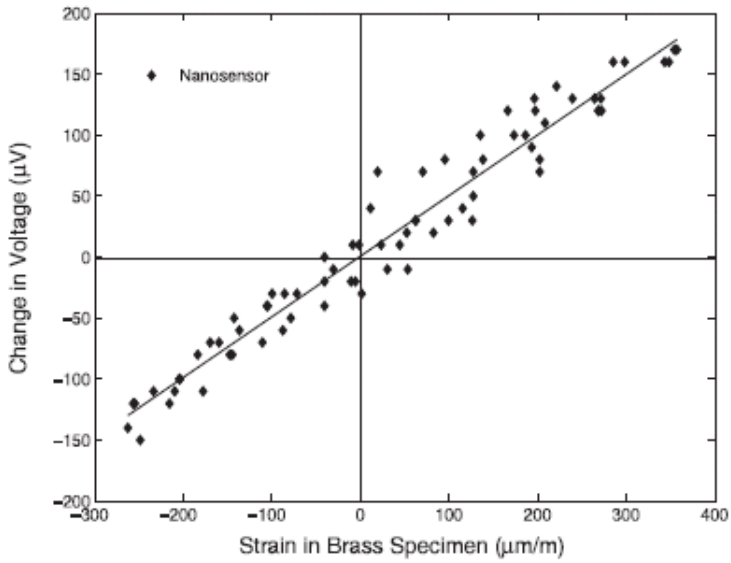

Figure 2.16. Measured variation of voltage as a function of tensile strain. [84]

Many groups related the modification of band structure to the change of the position of the D* Raman band, which strongly depends on the strain of the CNTs. Zhao et al. [89] measured the wavenumber shift in deformed SWCNT/polymer composites by using unpolarized Raman spectrum. Hadjiev et al. [90] presented results about the Raman shift at 1590 cm^{-1}, called the G band shift. However, it is difficult to implement Raman spectroscopy for strain measurements in field applications.

Recently, the ultra-high sensitivity of super CNTs (STs) based strain sensor was reported by Li et al. [91]. The resonant frequency of STs and their geometric structure will be changed under mechanical deformation. Thus, frequency shift was observed. They found that the STs based strain sensors possessed extremely high sensitivity, 887Hz/nanostrain, which is much higher than that of SWCNT based strain sensors. They suggested that STs could be used to design the new generation of strain sensors due to its high sensitivity and low density.

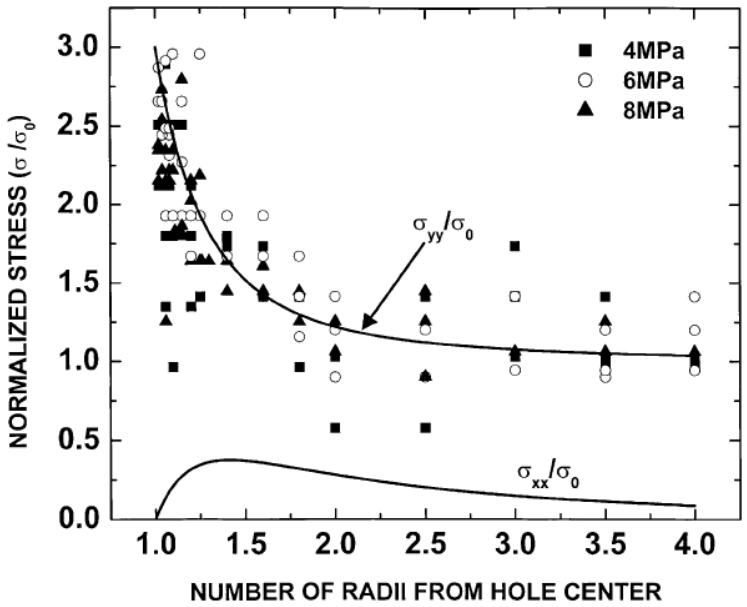

Figure 2.17. Unpolarized Raman results for SWCNTs in UV cured urethane-acrylate polymer with various applied stress levels. The solid lines are the linear elastic solution of Inglis for normal stresses (σ_{xx}, σ_{yy}) in x and y directions.

The common feature among these reports of the strain sensing is that the variations of the resistance with strain approximately behaved linearly. However, there is a small gap between CNTs [92], and a very large contact resistance between CNTs is induced by the small intertube barriers [93]. The electrical conductivity of CNT films or CNTs composites is dominated by the contact resistance [93]. As CNT based material is deformed, the barrier regions are also modified, and contact resistance may also change with deformation. Therefore, it is proposed that the variation of the resistance of CNT films and composites with strain may be not resulted from an intrinsic property of the CNTs but rather is a consequence of the modification of intertube barrier regions. The deviation from the linear trend also might be due to the variation of the barrier regions.

2.6 Summary

In this chapter, we reviewed the fundamental of CNTs and associated applications. CNTs possess 1-D electronic band structure, and the essential feature of the CNTs band structure can be obtained by zone folding approximation from graphene due to the 1-D structure. Singularities known as van Hove singularities are formed in DOS, which appear as peaks in STM measurement. The electronic structure of CNTs is very sensitive to the mechanical deformation. As a CNT is deformed, the Fermi point is driven away from the vertices of BZ, and this modification can strongly affect the transport properties of the CNT. Although CNTs possess extremely high electrical conductivity that is in the order of 10^3-10^6 S/cm, the electrical conductivity of CNT films and CNT composites is dominated by the large contact resistance, which is induced by the intertube gaps. TEP of CNTs is also very sensitive to the change of electronic structure. The modulations of TEP induced by applying a gate voltage and the absorption of oxygen molecules have been studied. In previous measurements, the CNT samples may subject to various mechanical deformations, which may induce the changes in the electronic structure of CNTs and barriers between CNTs, and a variation of TEP can be resulted. However, the mechanical deformation induced the variation of the TEP of CNTs have not been explored yet. CNTs are widely employed for improving the electrical conductivity of polymers. Large scattering in the reported results can be found from literature. This large scattering indicates the complex nature of the electrical conduce in CNT/polymer composites due to various factors. However, some questions still remain unanswered, especially for the effect of local morphology and tunneling conduction. Due to the sensitive electronic structure, CNTs can be used to develop new strain sensors. The linear sensing behaviour has been reported by several research groups. Dose this sensing behaviour result from an intrinsic property of CNTs? This thesis will address the efforts and contribution from dealing with these issues.

References

1. R. Saito, G. Dresselhaus, and M. S. Dresselhaus, Physical Properties of Carbon Nanotubes, Imperial College Press, 1998.
2. R. H. Baughman, A. A. Zakhidov, and W. A. de Heer, Science 297, 787 (2002).
3. E. Kymakis, I. Alexandou, and G. A. J. Amaratunga, Synthetic Metals 127, 59 (2002).
4. L. Yang, and J. Han, Phys. Rev. Lett. 85, 154 (2000).
5. P. Dharap, Z. Li, S. Nagarajaiah, and E. V. Barrera, Nanotechnology 15, 379 (2004).
6. P. J. F. Harris, Carbon nanotubes and related structure: new material for 21st century, Cambridge University Press, 1999.
7. S. Reich, and C. Thomsen, Phys. Rev. B 62, 4272 (2000).
8. M. Damnjanovic, T. Vukovic, and I. Milosevic, Solid state comm. 116, 265 (2000).
9. C. L. Kane, and E. J. Mele, Phys. Rev. Lett. 68, 631 (1997).
10. J. C. Charlier, X. Blasé, and S. Roche, Rev. Mod. Phys. 79, 677 (2007).
11. J .W. Mintmire and C. T. White, Phys. Rev. Lett. 81, 2506 (1997).
12. L. Kantorovich, Quantum Theory of the Solid State: An Introduction, Kluwer Academic Publisher, 2004.
13. C. T. White, and J. W. Mintmire, Nature (London) 394, 29 (1998).
14. S. Reich, C. Thomsen, and P. Ordejon, Phys. Rev. B 65, 155411 (2002).
15. R. Satio, M. Fujita, G. Dresselhaus, and M. S. Dresselhaus, Phys. Rev. B, 46, 1804 (1992).
16. A. M. Rao, E. Richter, S. Bandow, B. Chase, and P. C. Eklund, Science 275, 187 (1997).
17. L. C. Venema, J. W. Janssen, M. R. Buitelaar, J. W. G. Wildoer, S. G. Lemay, L. P. Kouwenhoven, and C. Dekker, Phys. Rev. B 62, 5238 (2000).
18. P. Kim, T. W. Odom, J. L. Huang, and C. M. Liever, Phys. Rev. Lett. 82, 1225 (1999).

19. M. S. Strano, S. K. Doorn, E. H. Haroz, C. Kittrell, R. H. Hauge, and R. E. Smalley, Nano Lett. 3, 1091 (2003).
20. Z. Yu, and L. E. Brus, J. Phys. Chem. B 105, 6831 (2001).
21. S. M. Bachilo, M. S. Strano, C. Kittrell, R. H. Hauge, R. E. Smalley, and R. B. Weisman, Science 298, 2361 (2002).
22. M. J. O'Connell, S. M. Bachilo, C. B. Huffman, V. C. Moore, and M. S. Strano, Science 297, 593 (2002).
23. J. W. G. Wildoer, L. C. Venema, A. G. Rinzler, R. E. Smalley, and C. Dekker, Nature 391, 59 (1998).
24. T. W. Odom, J. L. Huang, P. Kim, and C. M. Lieber, Nature (London) 391, 62 (1998).
25. A. M. Samsonov, strain soliton in solids and how to construct it, London: Chapman&Hall, 2001.
26. O. Gulseren, T. Yildirim, S. Ciraci, and C. Kilic, Phys. Rev. B 65, 155410 (2002).
27. J. W. Chen, X. P. Yang, L. F. Yang, H. T. Yang, and J. M. Dong, Phys. Lett. A 325, 149 (2004).
28. T. W. Tombler, C. Zhou, L. Alexseyev, J. Kong, H. Dai, L. Liu, C. S. Jayanthi, M. Tang, and S. Y. Wu, Nature (London) 405, 769 (2000).
29. J. Cao, Q. Wang, and H. Dai, Phys. Rev. Lett. 90, 157601 (2003).
30. E. D. Minot, Y. Yaish, V. Sazonova, J. Y. Park, M. Brink, and P. L. McEuen, Phys. Rev. Lett. 90, 156401 (2003).
31. J. Lee, H. Kim, S. J. Kahng, G. Kim, Y. W. Son, J. Ihm, H. Kato, Z. W. Wang, T. Okazaki, H. Shinohara, and Y. Kuk, Nature (London) 415, 1005 (2002).
32. H. Dai, E. W. Wong, and C. M. Lieber, Science 272, 523 (1996).
33. T. W. Ebbesen, H. J. Lezec, H. Hiura, J. W. Bennett, H. F. Ghaemi, and T. Thio, Nature (London) 382, 54 (1996).
34. W. A. deHeer, W. S. Bacsa, A. Chatelain, T. Gerfin, R. Humphrey-Baker, L. Forro, and D. Ugatre, Science 268, 845 (1995).
35. J. E. Fischer, H. Dai, A. Thess, R. Lee, N. M. Hanjani, D. L. Dehaas, and R. E. Smalley, Phys. Rev. B 55, R4921 (1997).

36. L. Langer, V. Bayot, E. Grivel, J. P. Issi, J. P. Heremans, C. H. Oik, L. Stockman, C. Van Haesendonck, and Y. Bruynseraede, Phys. Rev. Lett. 76, 479 (1996).
37. J. Hone, M. C. Liaguno, N. M. Nemes, A. T. Johnson, J. E. Fisher, D. A. Walters, M. J. Casavant, J. Schmidt, and R. E. Smalley, Appl. Phys. Lett. 77, 666 (2000).
38. M. S. Fuhrer, J. Nygard, L.shih, M. Forero, Young-Gui Yoon, M. S. C. Mazzoni, H. J. Choi, J. Ihm, S. G. Louie, A. Zettl, and P. L. McEuen, Science 288, 494 (2000).
39. A. Buldum and J. P. Lu, Phys. Rev. B 63, 161403 (2001).
40. C. Li, E. T. Thostenson, and T. W. Chou, Appl. Phys. Lett. 91, 223114 (2007).
41. D. D. Pollock, Thermoelectricity Theory, Thermometry, Tool, ASTM Special Technical Publication 852, 1985.
42. M. Cutler and N. F. Mott, Phys. Rev. 181, 1336 (1969).
43. J. Hone, I. Ellwood, M. Muno, A. Mizel, M. L. Cohen, A. Zettl, A. G. Rinzler, and R. E. Smalley, Phys. Rev. Lett. 80, 1042 (1998).
44. J. P. Small, K. M. Perez, and P. Kim, Phys. Rev. Lett. 91, 256801 (2003).
45. M. Baxendal, K. G. Kim, and G. A. J. Amaratunga, Phys. Rev. B 61, 12705 (2000).
46. K. Bradley, S. H. Jhi, G. Collins, J. Hone, M. L. Cohen, S. L. Louie, and A. Zettl, Phys. Rev. Lett. 85, 4361 (2000).
47. G. U. Sumanasekera, B. K. Pradhan, H. E. Romero, K. W. Adu, and P. C. Eklund, Phys. Rev. Lett. 89, 166801 (2002).
48. S. Kirkpatrick, Rev. Mod. Phys. 45, 574 (1973).
49. D. Stauffer, Introduction to Percolation Theory, Taylor&Francis London, 1987.
50. P. Sheng, Phys. Rev. B 21, 2180 (1980).
51. N. F. Mott, Philos. Mag. 19, 835 (1969).
52. A. L. Efros and B. I. Shklovskii, J. Phys. C 8, 49 (1975).
53. F. h. Gojny, M. H. G. Wichmann, B. Fiedler, I. A. Kinloch, W. Bauhofer, A. H. Windle, and K. Schulte, Polymer 47, 2036 (2006).
54. S. Barrau, P. Demont, A. Peigney, C. Laurent, and C. Lacabanne, Macromolecules 36, 5187 (2003).

55. Z. Ounaier, C. Park, K.E. Wise, E. J. Siochi, and J. S. Harrison, Composites Sci. and Tech. 63, 1637 (2003).
56. D. S. Mclanlan, C. Chiteme, C. Park, K. E. Wise, S. E. Lowther, P. T. Lillehei, E. J. Siochi, and J. S. Harrison, J Polymer Scien. B, 43, 3237 (2005).
57. T. McNally, P. Potschke, P. Halley, M. Murphy, D. Martin, and S. E. J. Bell Polymer 46, 8222 (2005).
58. M. K. Seo, and S. J. Park, Chem. Phys. Lett. 395, 44 (2004).
59. L. Chen, X. J. Pang, Z. L. Yu, Mater. Sci. Eng. A 457, 287 (2007).
60. P. Xue, K. H. Park, X. M. Tao, W. Chen, and X. Y. Cheng, Comp. Struct. 78, 271 (2007).
61. X. Yao, H. Wu, J. Wang, S. Qu, and G. Chen, Chem. Euro. 13, 846 (2006).
62. I. Balberg, C. H. Anderson, S. Alexander, and N. Wagner, Phys Rev. B 30, 3933 (1984).
63. Y. B. Yi, L. Berhan, and A. M. Sastry, J. Appl. Phys. 96, 1318 (2004).
64. F. Dalmas, R. Dendievel, L. Chazeau, J.Y. Cavaille, and C. Gauthier, Acta Materialia, 54, 2923 (2006).
65. C. Li, E. Thostenson, and T. W. Chou, Appl. Phys. Lett. 91, 223114 (2007).
66. M. Foygel, R. D. Morris, D. Anez, S. French, and V. L. Sobolev, Phys. Rev. B 71, 104201 (2005).
67. R. Ramasubramaniam, J. Chen, and H. Liu, Appl. Phys. Lett. 83, 2928 (2003).
68. T. Kimura, H. Ago, M. Tobita, S. Oshima, M. Kyotani and M. Yumura, Adv. Mater. 14, 1380 (2002).
69. F. Tsui, L. Jin, and O. Zhou, Appl. Phys. Lett. 76, 1452 (2000).
70. E. S. Choi, J. S. Brooks, D. L. Eaton, M. S. Al-Haik, M. Y. Hussaini, H. Garmestani, and K. Dahmen, J. Appl. Phys. 94, 6034 (2003).
71. J. C. Grunlan, A. R. Mehrabi, M. V. Bannon, J. L. Bahr, Adv. Mater. 16, 150 (2004).
72. J. Wu, and D. S. Mclachlan, Phys Rev. B, 58, 14880 (1998).
73. J. Wu, and D. S. Mclachlan, Phys Rev. B, 56, 1238 (1997)
74. C. Chiteme, and D. S. Mclachlan, Phys Rev. B, 67, 024206 (2003).

75. D. S. Mclachlan, C. Chireme, W. D. Heiss, J. Wu, J. Phys B: Condens. Matter. 338, 256 (2003).

76. D. S. Mclachlan, C. Chiteme, W. D. Heiss, J. Wu, J. Phys. B Condens. Matter. 338, 261 (2003).

77. J. P. Clerc, G. Girand, J. M. Langier, J. M. Luck, Adv. Phys. 39, 191 (1999).

78. M. T. Connor, S. Roy, T. A. Ezquerra, and F. J. Balta Calleja. Phys. Rev. B 57, 2286 (1998).

79. M. Reghu, C. O. Yoon, C. Y. Yang, D. Moses, P. Smith, and A. J. Heerger, Phys. Rev. B 50, 13931 (1994).

80. J. C. Dyre and T. B. Schroder, Rev. Mod. Phys. 72, 873 (2000).

81. A. Bunde, J. Drager, and M. Porto, in Computational Physics, edited by K. H. Hoffman and M. Schreiber, Springer Berlin (1984).

82. B. E. Kilbride, J. N. Coleman, J. Frayese, P. Fournet, M. Cadek, A. Drury, S. Hutzler, S. Roth, and J. Wu, J Appl. Phys, 92, 4024 (2002).

83. S. Barrau, P. Demont, A. Peigney, C. Laurent, and C. Lacabanne, Macromolecules 36, 5187 (2003).

84. P. Dharap, Z. Li, S. Nagarajaiah, and E. V. Barrera, Nanotechnology 15, 379 (2004).

85. I. P. Kang, M. J. Schulz, and N. Korathkar, Smart Mater. Struct. 15, 737 (2006).

86. I. P. Kang, J. W. Lee, G. R. Choi, J. Y. Jung, S. H. Hwang, Y. S. Choi, et al. Key Eng Mater: Adv. Nondestructive Evail 32, 321 (2006).

87. W. Zhang, J. Suhr, S. Nagarajaiah, and E. V. Barrera, Nanotechnology 15, 379 (2004).

88. K. J. Loh, J. Kim, J. P. Lynch, N. W. S. Kam and N. A. Kotov, Smart Mater. Struct. 16, 429 (2007).

89. Q. Zhao, M. D. Frogley, and H. D. Wagner, Comp. Sci. Tech. 62, 147 (2002).

90. V. G. Hadjiev, M. N. Lliev, S. Arepalli, P. Nikolaev, and B. S. Files, Appl. Phys. Lett. 78, 3193 (2001).

91. Y. Li, X. Qiu, F. Yang, X. Wang and Y. Yin, Nanotechnology 19, 165502 (2008).

92. M. Baxendal, K. G. Kim, and G. A. J. Amaratunga, Phys. Rev. B 61, 12705,

(2000).

93. A. Buldum and J. P. Lu, Phys. Rev. B 63, 161403 (2001).

Chapter 3 Electrical Properties of CNT/Polymer Composites

3.1 Introduction

CNTs, due to their high electrical conductivity, have attracted growing interests in the materials community in recent years as a conducting filler in the development of conductive polymer composites. As reviewed in section 2.3.4, the electrical conductivity of a single CNT is in the order of $10^3 - 10^7 \mathrm{S/m}$ [1, 2]. Although intensive efforts have been made to investigate the electrical properties of CNT/polymer composites, there are still some questions unanswered: how do the poor contacts between CNTs affect bulk conductivity of CNT based composites? How dose the local morphology influence the electrical properties of CNT/polymer composites? Due to the relatively low conductivity of CNT/polymer composites, it may be doubted whether CNTs can be effective conductive fillers for improving the electrical conductivity of polymers. The intent of this chapter is to improve the knowledge of CNT/polymer composites and design better CNT composites by using the morphology dependent properties. In order to investigate these issues mentioned above, a 3-D numerical simulation system was built to determine the electrical properties of CNT/polymer composites and the effect of microstructure on the electrical properties of composites, and a numerical formula was derived for predicting the AC properties of CNT/polymer composites with consideration of the effect of microstructure. The rest of the chapter was organized as follows. In section 3.2, we discussed the DC properties of CNT/polymer composites based on a 3-D continuum model. In section 3.3, we investigated AC properties using the 3-D numerical model. In section 3.4, we derived series numerical formulas using the capacitively and resistively junction model for predicting AC properties. Lastly, a brief summary was given in section 3.5.

3.2 DC conductivity of CNT/polymer composites

3.2.1 Introduction

Electrical conduction in a conductive polymer composite comprised of the conducting filler and the polymer insulating phases is mainly described by the percolation theory [3-5], in which the electrical conductivity of the composite, σ, can be expressed as follows [6]:

$$\sigma \propto (p - p_c)^t \tag{3.1}$$

where p_c is the percolation threshold, p is the concentration of conductive component and t is a corresponding critical exponent. This equation is only valid as $p > p_c$ or $p \sim p_c$. As the mass fraction increases around p_c, the continuous pathways through the composites begin to form. As a result, the electrical conductivity of the composites sharply increases with increasing mass fraction. When the content of the conducting phase is below the percolation threshold, considerable conductivity, which is the result of tunneling through the thin layer insulating phases between two neighboring conductive fillers, was also observed [7-9].

The percolation approach has also been employed mainly for investigating the electrical conductivity of CNT/polymer composites [10-12]. Kilbride et al. [13] observed experimentally that the conductivity of MWCNT/poly(vinyl alcohol) composites obeyed the percolation theory with p_c=0.053 vol.% and t=1.36. Ounaies et al. [14] reported experimentally that p_c was in the range from 0.02 vol.% to 0.1 vol.% and t=1.5 for SWCNT/polyimide. Dalmas et al. [15] simulated the electrical conductivity of entangled MWCNTs in a perfect insulating medium system, and reported that the percolation threshold for MWCNTs in poly (styrene-co-butyl acrylate) was 0.2vol.% with t=1.6. In percolation theory, it is considered that the electrons only transport through the continuous network of conductors in the

insulating matrix. However, in the real conductor/insulator composites, electrons are allowed to tunnel between conductors through the thin insulating layer. These researches, however, completely ignored the tunneling mechanism. The contribution of tunneling to conductivity is also significant [7, 16, 17] even after the formation of the percolation threshold.

Due to the low conductivity of CNT/polymer composites, it may be doubted whether CNTs can be an effective conductive filler for improving the electrical conductivity of polymers. In order to further investigate this issue, a 3-D numerical simulation system was built and tunneling conduction was introduced into CNT networks to determine the electrical conductivity of CNT/polymer composites. An attempt was made to justify the phenomenological percolation approach, and to understand the effects of polymer matrix and of CNT's tortousity, aspect ratio, diameter and contact resistance on the electrical conductivity and percolation threshold of the CNT/polymer composites.

3.2.2 Model and Modelling

The modeling of the DC properties of CNT/polymer nanocomposites was performed in three steps: (1) the generation of the microstructure of nanocomposites; (2) the creation of a pure resistor circuit corresponding to this microstructure; and (3) the computation of the resistance of the system.

Generation of microstructure

As the first step in the modeling, curly CNTs were generated in a polymer matrix within a given volume (V). The given volume can be described by a 3-D cubic matrix $(c \times c \times c)$. The size of the cubic matrix can be calculated from V: $c = 10 \times \sqrt[3]{V}$. In the matrix, the value of elements representing polymers were set to 0, and the elements occupied by CNTs were set to integers. The integer was used to identify

CNTs for constructing multidimensional connecting matrix, which will be introduced in the following section. A continuum model was built to allocate CNTs in a polymer matrix. A curved CNT can be approximated by straight segments with infinitesimal sizes. Thus, each CNT was constructed by *N* elementary segments (ESs), which were defined as one layer comprised by a number of 0.1 x 0.1 x 0.1 nm^3 elements (see Fig. 3.1). The number (N_e) of elements contained in an ES was equal to $(10 \times d)^2$, where d is the diameter of a CNT. The position of an element in an ES can be identified by shifting the starting element (only one) along the *i* and *j* axes, which can be expressed mathematically as (i+a, j+b, k), where *a* and *b* are integers between 0 and d/0.1. It follows that any one ES can be constructed by knowing the index of the starting element, which determines the position of the constructed CNT in the matrix. The position of the first ES was randomly allocated with the index (i, j, k). The second ES was generated with the index $(i \pm 1, j, k)$ or $(i, j \pm 1)$ or $(i, j, k \pm 1)$ and so on. One limit for the generation of CNTs is that the elements cannot be located in the sites occupied by other CNTs or itself. For an example, as a site (i+1, j, k) have been occupied by another CNT, the following ES can only be generated with the index of $(i-1, j, k)$ or $(i, j \pm 1)$or $(i, j, k \pm 1)$. If all the sites of the following ES are occupied, the starting ES will be relocated. The core programmes of generating 2-D and 3-D microstructure were presented in appendix A.

The inter-nanotube interactions were detected from the calculation of the distance $(d_c = 0.1 \times \sqrt{(i-i')^2 + (j-j')^2 + (k-k')^2})$ between each pair ESs in different CNTs. If $d_c \leq d + 0.1 \times \sqrt{3}$, an interaction can be established between the two ESs (i, j, k) and (i', j', k'). The interaction does not mean the exact contact of two CNTs. There is van der Waals separation between two neighboring CNTs, which results in a contact resistance [18].

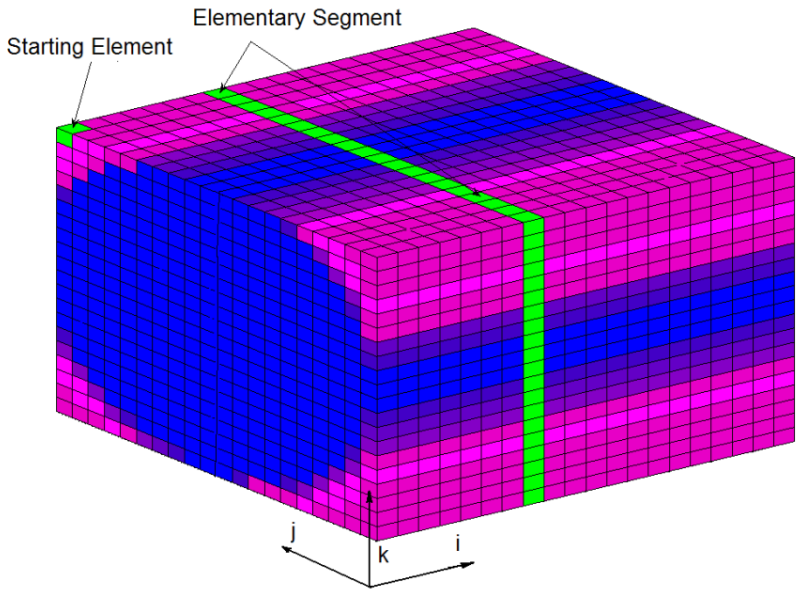

Figure 3.1 Schematic of continuum model for CNTs in a polymer matrix. Blue and purple elements represent CNTs and polymer matrix, respectively.

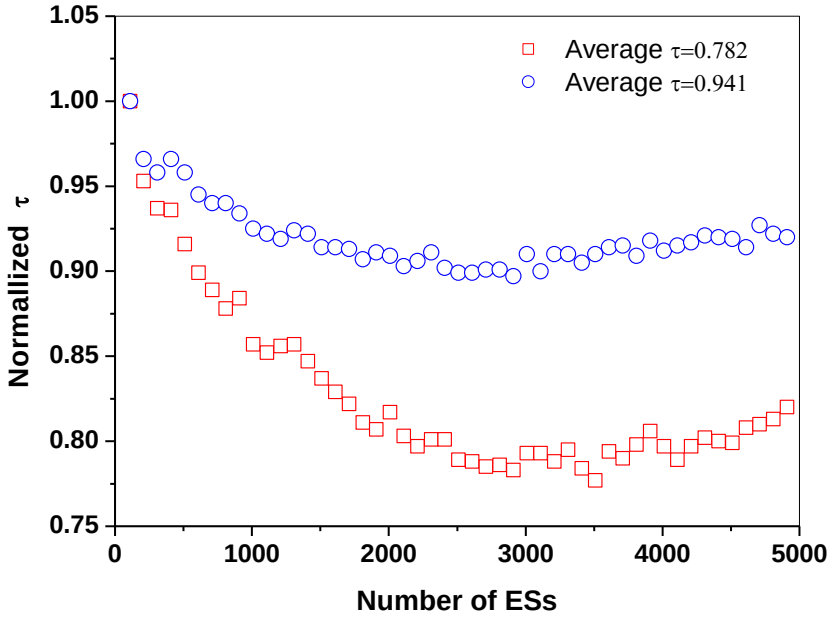

Figure 3.2 Effect of calculation scale (number of ESs) on the calculated τ for SWCNTs with various average τ, which was computed in every 1000 ESs. Reduced τ is the ratio of τ calculated in N ESs to the one calculated in 110 ESs.

The number, N, of ESs in a CNT can be calculated by knowing length (L) of the CNT, $N = L/0.1$. CNT volume fraction (ψ) can be established from the number of CNTs (N_f) in the given volume, $\psi = N_f \cdot N \cdot N_e \cdot \pi/\left(4c^3\right)$. Generally, CNTs well-dispersed in polymers can be straight, twisted and even looped. The curliness of CNTs was described by the curl ratio, τ, which was defined as the ratio of the end distances to CNTs running length in present work. A CNT can be considered as a straight stick at a curl ratio of 1, and can be seen as a spherical particle at a curl ratio ~0. As the curl ratio increases, a CNT straightens. The curl ratio was calculated in every 500 segments length (the calculation scale is 500), and the average was considered as the curl ratio of the whole system. The calculated τ can vary with the selected calculation scale. The effect of the calculation scale on the average τ was plotted in Fig.3.2. It can be found that the effect of calculation scale becomes weak as increasing the average curl ratio. The average τ calculated at the same calculation scale is reliable for the comparison of the tortuosities of CNTs.

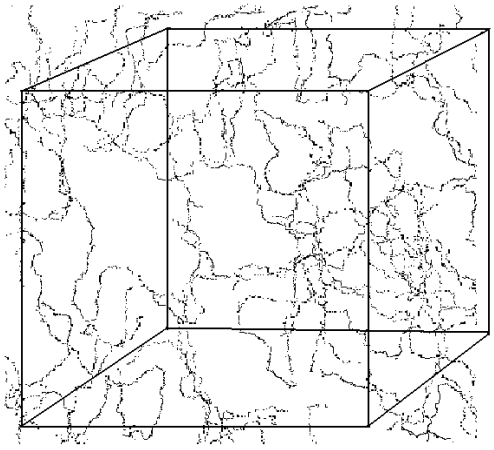

Figure 3.3. Illustration of a 3-D microstructure of SWCNT/polymer composites, composed by 50 SWCNTs. The volume fraction of SWCNTs was set to 5.3%. The number of overlapping points was obtained as 87 and the τ was calculated to be 0.684. The equivalent circuit of the microstructure is presented in appendix B.

Fig. 3.3 illustrates a 3-D microstructure of SWCNT/polymer composites, composed

by 50 SWCNTs. Once the microstructure is built up, the corresponding parameters, such as volume fraction, curl ratio, and equivalent circuits can be obtained.

Equivalent resistor circuit

To create an equivalent resistor circuit, the effective tunneling distance must be worked out first. The effective tunneling distance is defined as the thickness of the polymer layer between two neighboring SWCNTs (CNT-polymer layer-CNT junction, N-P-N) with the significant non-zero tunneling conduction. To be injected into another nanotube, the charge carriers must overcome the N-P-N potential barrier. For a small barrier, a large number of charge carriers can cross the N-P-N by thermionic emission. It is well-known polymers possess high potential barriers, and the injection can only happen via tunneling through the barrier under the applied voltages.

For non-conjugated polymers, the potential barrier is the difference between the Fermi energy (E_F) and the free particle level of the polymer due to the low polaron level [19]. The tunneling conduction for a non-conjugated polymer can be described as follows [19]

$$J = \left(6.2\times10^{10}/l^2\right)\cdot\left\{\varphi_I \exp(-1.025\cdot l\cdot\varphi_I^{1/2}) - \left(\varphi_I + V\right)\cdot\exp\left[-1.025\cdot l\cdot\left(\varphi_I + V\right)^{1/2}\right]\right\} \tag{3.2}$$

where l is the distance between two ESs showing tunneling behaviour, V is the voltage applied on the N-P-N, and φ_I is the average barrier height.

Resistor network approach [20] was employed to calculate the electrical conductivity of the composite by constructing an equivalent circuit, which was based on an array of series or parallel-CNT segments in the simulated structure. The general equation to scale the resistance of the fibrous filler is that,

$$R_i = \frac{\rho_f L_i}{A_i} \tag{3.3}$$

where ρ_f and L_i are the resistivity and the length of the segment *i*, respectively, and A_i is the cross-sectional area of the fibrous filler. As mentioned in chapter 2, the electrical conductivity ($1/\rho_f$) of CNTs is in the order of $10^3 - 10^7 S/m$ [1]. Consequently, CNTs are almost zero resistance ($R_i \approx 0$) compared to polymers. CNTs, therefore, can be considered as 'wires' in the equivalent circuit, and resistors were mainly attributed to the contact resistance and tunneling resistance of CNT bundles. The contact resistance can vary, theoretically, from $100K\Omega$ to $3.4M\Omega$ [21] and, experimentally, from $100\,K\Omega$ to $360\,K\Omega$ [18]. The equivalent tunneling resistance can be calculated using Eq. 3.2. In the real CNT/polymer composites, the tunneling conduction can occur in an area (illustrated in Fig. 3.3 (a)), and the ESs in the tunneling area can be seen parallel connecting with each other. The resistance of the tunneling areas is equal to the resistance arising from the parallel connection of single tunneling resistors and can be calculated by:

$$R_t = 1/\sum_1^i I_i / V_i \tag{3.4}$$

where I_i is the current through the elementary segment *i*. The variation of voltage, V_i, in the tunneling area is very small due to the high conductivity of CNTs and the small dimension of the tunneling junctions. It follows that V_i can be considered as a constant and equivalent tunneling resistance can be rewritten, $R_t = V^*/\sum_1^i I_i$, where V^* is the average voltage applied on the tunneling conduction area. After identifying the contact and tunneling resistances, the resistor elements in the equivalent circuit

were identified and the equivalent circuit can be constructed.

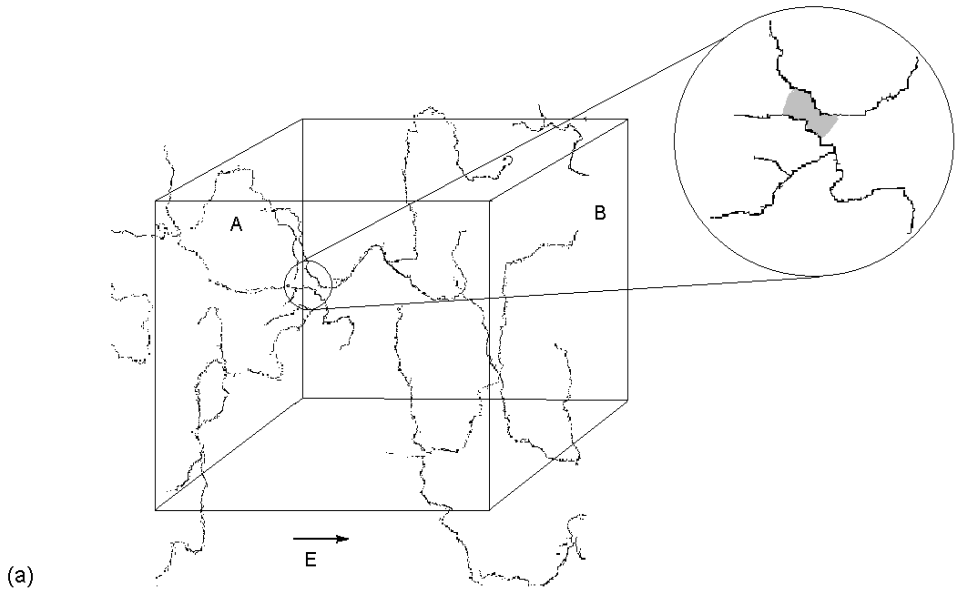

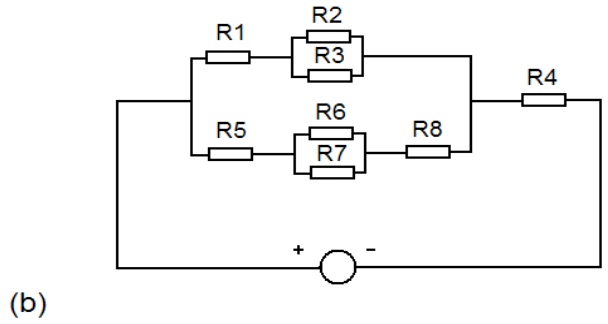

Figure 3.4 (a) Schematic of a 3-D microstructure of CNT/polymer composites. An electrical field, E, was applied between two opposite faces A and B. The amplified schematic represents the tunneling conduction area (highlight in grey). (b) Illustration of the equivalent resistor circuit based on microstructure presented in (a). Resistors R3 and R8 were determined by the tunneling resistance and the remainder resistors represented the contact resistances between CNTs.

In order to simplify the calculation, we assumed that each MWCNT has an electrical relationship with its M surrounding neighbours. The M can be estimated as the

average coordination number of the 3-D Voronoi tesselltion z_s, which was calculated to be 15.54 by Meijering [22]. The number of the nearest neighbours was, therefore, set to 16. The resistor circuit was created based on the ESs of CNTs. Between a pair of the closest neighbouring ESs, either a contact resistor or tunneling resistor was added to the equivalent circuit depending on the geometrical contacts between the ESs.

A multidimensional connecting matrix was constructed to describe the resistor circuit, and each resistor element was determined by Eq. 2.2 or the value of contact resistance. The example of connecting matrix was presented in appendix B. The corresponding units and standard symbols (such as "R" for resistor) were suffixed to the element value to denote the types of elements between the nodes. CNTs were seen as zero-resistance wires, therefore, the number of nodes is equal to the number of CNTs contained in the percolation network [23]. Here, the equivalent circuit was pure resistor network. In order to simplify the modeling processes, no symbols were suffixed to the element value. Then, the SPICE [23] input file was created from the connecting matrix, and resistor circuit was analysed by using the PSpice software, developed by Cadence Design Systems [23]. Fig. 3.4 (a) shows a schematic for a 3-D microstructure of CNT/polymer composites and Fig. 3.4 (b) presents the corresponding resistor circuit.

3.2.3 Results and Discussion

In order to calculate the tunneling resistance in a CNT/polymer composite, it is necessary to know the barrier height of the polymer. In present work, CNT/polyethylene (PE), CNT/polyimide (PI) and CNT/poly(vinyl alcohol) (PVA) were used as examples. The barrier heights of these examples were calculated by using Liang's method [24]. The *I-V* characteristics of PE, PI and PVA were measured using Al electrodes, and modified Norde function method [25] was employed to

determine the barrier heights of PE, PI and PVA. The barrier heights of PE, PI and PVA were found to be 4.43 *eV* , 4.56 *eV* and 2.58*eV,* respectively. The difference of the work function between CNT (5.00 *eV*) and Al (4.28*eV*) is 0.72 *eV*. Then, it follows that the barrier heights of CNT/PE, CNT/PI and CNT/PVA composites were 3.71*eV,* 3.84*eV* and 1.86 *eV*, respectively.

The characteristics of the tunneling conduction of two neighboring CNTs were analyzed using Eq.3.2. The variation of tunneling resistivity with the distance between two neighboring CNTs is presented in Fig. 3.5 for SWCNT/PE, SWCNT/PI and SWCNT/PVA composites, respectively. It is well-known that CNTs cannot exactly contact each other, and there is always a margin of about *1.0nm* [26] between two 'connecting' CNTs. The results shown in Fig. 3.5 revealed that for a given tunneling distance, the resistivity of the tunneling junction was higher for the composite, in which the polymer host has a high potential barrier, than that with a low potential barrier.

Here, we define effective tunneling distance as the point, at which tunneling conduction becomes zero. When the distance is below this point, the tunneling conduction is a significant contributor to the electrical conductivity of the composite, and can be considered as a resistor in the equivalent circuit. The effective tunneling distance in SWCNT/PE, SWCNT/PI and SWCNT/PVA composites was found to be 2.00 *nm*, 2.50*nm* and 2.27 *nm*, respectively.

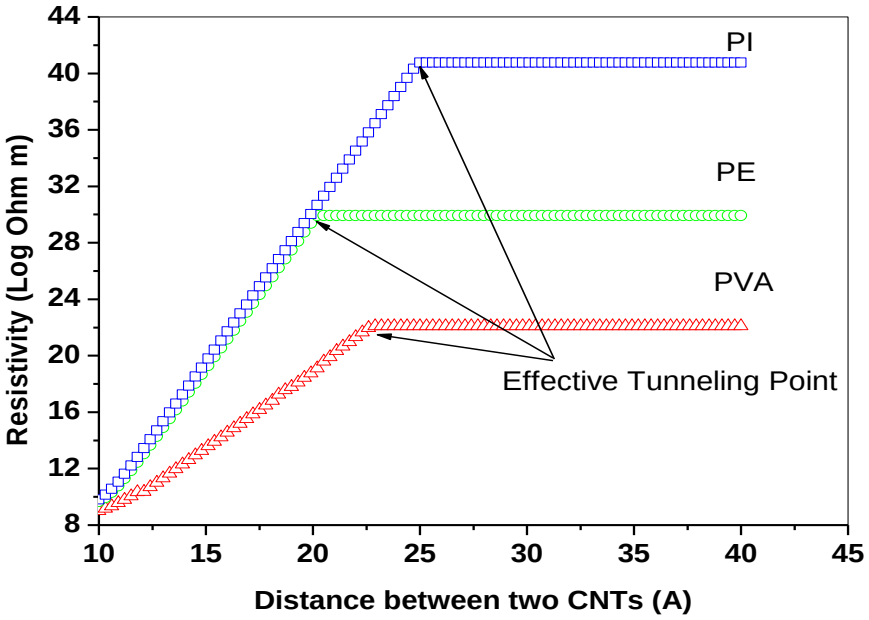

Figure 3.5 Illustration of the resistivity of tunneling junctions versus distance between two nearest SWCNTs in SWCNT/PE, SWCNT/PI and SWCNT/PVA composites.

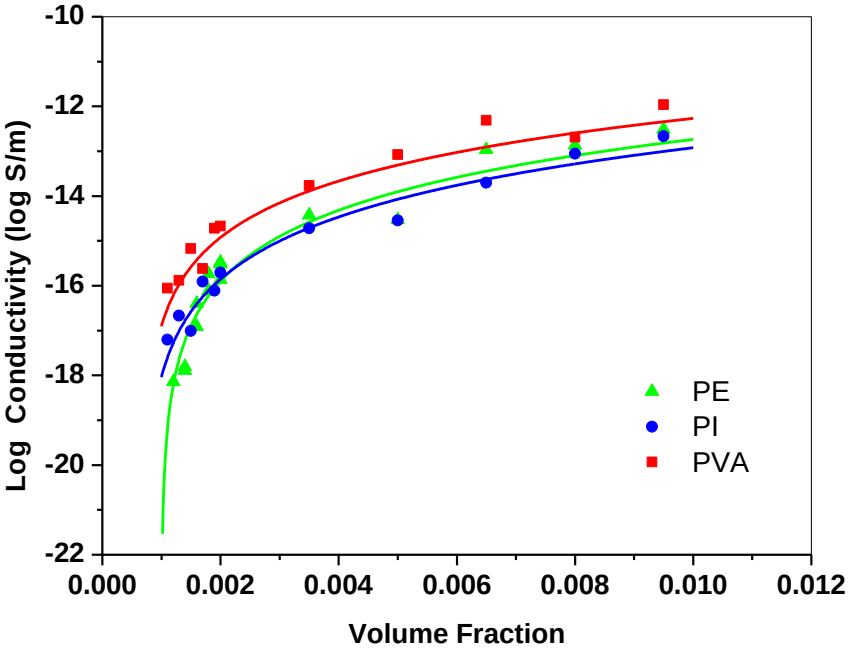

Figure 3.6 Illustration of conductivity versus volume fraction of SWCNTs for SWCNT/PE, SWCNT/PI and SWCNT/PVA composites with $\tau = 0.8$ (ignoring the

effect of crystallinity), and the length of the SWCNT was 5 μm. Here it was assumed that SWCNTs can be homogenously dispersed in these polymers.

Table 3.1 Simulated results for SWCNT/PVA, SWCNT/PE and SWCNT/PI composites with and without the consideration of tunneling conduction.

Matrix	p_c (vol.%)		t	
	Tunneling	No Tunneling	Tunneling	No Tunneling
PE	0.11	0.14	1.44	1.46
PVA	0.07	0.14	1.49	1.46
PI	0.07	0.14	1.31	1.46

Compared to that of the equivalent resistor network, the contribution of the polymer matrix to the bulk conductivity can be ignored. By integrating the network using PSpice software, the bulk conductivity of CNT/polymer composites can be obtained. The conductivities of SWCNT/PE, SWCNT/PI and SWCNT/PVA composites versus the volume fraction of SWCNTs are shown in Fig. 3.6. The p_c in this simulation was defined as the volume fraction of SWCNTs, where the conductivity of composites begins to increase shapely. The modeling data were fitted using the percolation law (Eq. 3.1) (solid lines in Fig. 3.6), and the values of p_c and t are listed in Tab. 3.1. It is clear that the percolation threshold obtained with consideration of tunneling conduction is lower than that without consideration of tunneling conduction. A continuous equivalent circuit can be constructed by introducing the tunneling conduction in the model before the real percolation CNT network is formed. The number of the pathway for electrical conduction is also increased with consideration of tunneling conduction. In the case of without tunneling conduction, the percolation threshold is not affected by the polymer matrix. In the case of considering tunneling conduction, the percolation threshold depends on the polymer matrix. It is clear that the threshold of the PE matrix is a little bit higher than that of the PVA and PI matrices. Because CNTs in PVA and PI matrix have larger effective tunneling

distances than in PE matrix, and consequently CNTs possess larger tunneling conduction areas in PVA and PI matrices than in the PE matrix, which increases possible pathways for electron transport.

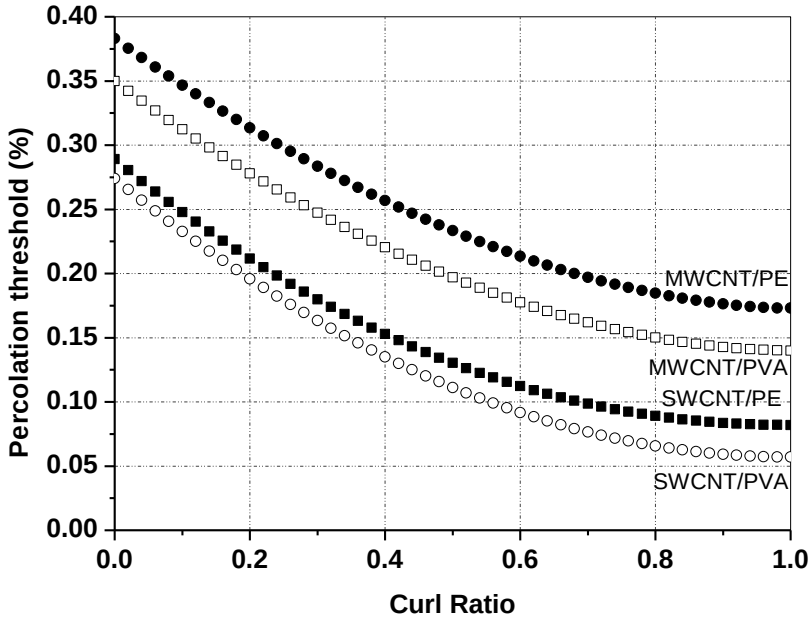

Figure 3.7 Percolation threshold vs. curl ratio for SWCNTs and MWCNTs in PE and PVA matrix. The diameter and length used here were 8nm and 5 μm for MWCNTs and 1nm and 5 μm for SWCNTs, respectively.

Fig.3.7 shows the effect of CNT curliness on percolation threshold. It can be seen that the tortuosity has a strong influence on the percolation threshold. As the curl ratio increased from 0 to 1, the percolation threshold decreased from 0.28vol.% to 0.08vol.% for PE matrix, and from 0.273vol.% to 0.06vol.% for the PVA matrix. From Fig. 3.7, it also can be seen that the curves for MWCNT and SWCNT systems have the same shape, but the thresholds in MWCNT systems are higher than that in SWCNT systems. At the curl ratio of 0.6, the threshold of the MWCNT/PVA composite is 0.18% and the threshold is only 0.096% for the SWCNT/PVA. This observation revealed the CNTs with high aspect ratio had lower percolation threshold than that with low aspect

ratio. These results indicated that the both of tortousity and aspect ratio had significant influences on the percolation threshold.

As reviewed in section 2.3.5, the contact resistance, ranging from $100K\Omega$ to $3.4M\Omega$, depends on the types of CNTs. Fig. 3.8 illustrates the effect of contact resistance on the electrical conductivity of SWCNT/PVA composites. It can be seen that the conductivity increases with decreasing contact resistance. The conductivity of CNTs with contact resistance of $100K\Omega$ at 2vol.% is approximately 8 times higher than CNTs with $1M\Omega$ contact resistance. However, the percolation threshold is nearly the same for these composites. The contact resistance only influences the electrical conductivity, and not the percolation threshold.

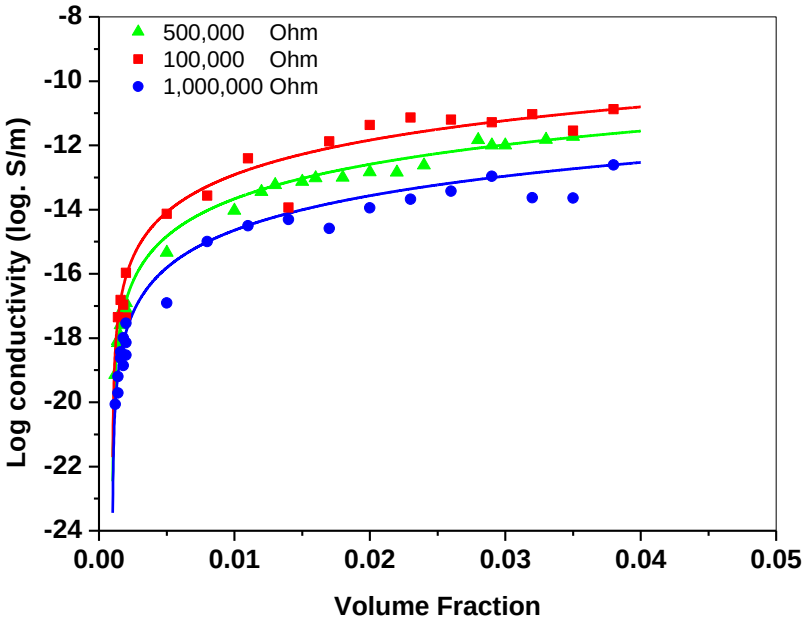

Figure 3.8 Illustration of conductivity of SWCNT/PE as a function of contact resistance ($100K\Omega$, $500K\Omega$, and $1M\Omega$).

Fig. 3.9 (a) gives a comparison of the modeling results with experimental data obtained by Kilbride et al.[13] on the conductivity of MWCNT/PVA composites. The modelling threshold ($p_c = 0.091$wt.%) is slightly higher than Kilbride's result and

critical exponent ($\alpha = 1.33$) is in good agreement with Kilbride's result. However, the deviation is still in the range of variation caused by tortuosity, contact resistance (R_c) and aspect ratio. Fig.3.9 (b) presents experimental [14] and our modeling results of the conductivity of SWCNT/PI composites. The effect of contact resistance on the conductivity of SWCNT/PI nanocomposite is also given in Fig. 3.9(b). The upper boundary corresponds to the CNTs with high aspect ratio and curl ratio in the composites, and low boundary related to the CNT fillers with low aspect ratio and curl ratio. The experimental result locates in the region of $R_c = 10^4 \Omega$. The low contact resistance might be partly due to the conducting impurities in the composites.

Dalmas et al.[15] have also simulated the electrical conductivity of MWCNT/polymer composites. In their work, the influence of contact resistance on bulk resistivity was ignored. It was found from Damas' results that the threshold is 0.12vol% higher than that of the present simulation. The reason could be that the tunneling behaviour was not taken into account. The tunneling conduction makes also a significant contribution to the electrical conduction around the percolation threshold.

From experimental [10-14] and the present work, the conductivity of CNT/polymer composites is maximally around about 10^{-4} S/m with low CNT content (less than 1vol%) due to the high contact resistance between CNTs. There is no doubt that the application of CNTs to improving the electrical conductivity of polymers will be limited. CNTs cannot be considered as a valuable conductive filler for improving the electrical conductivity of polymers unless the contact and tunneling resistances are reduced significantly.

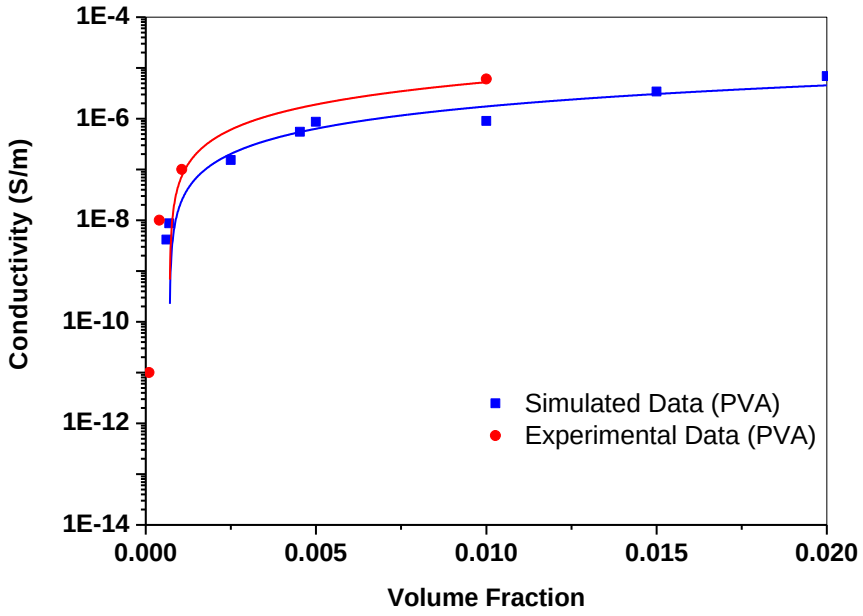

(a)

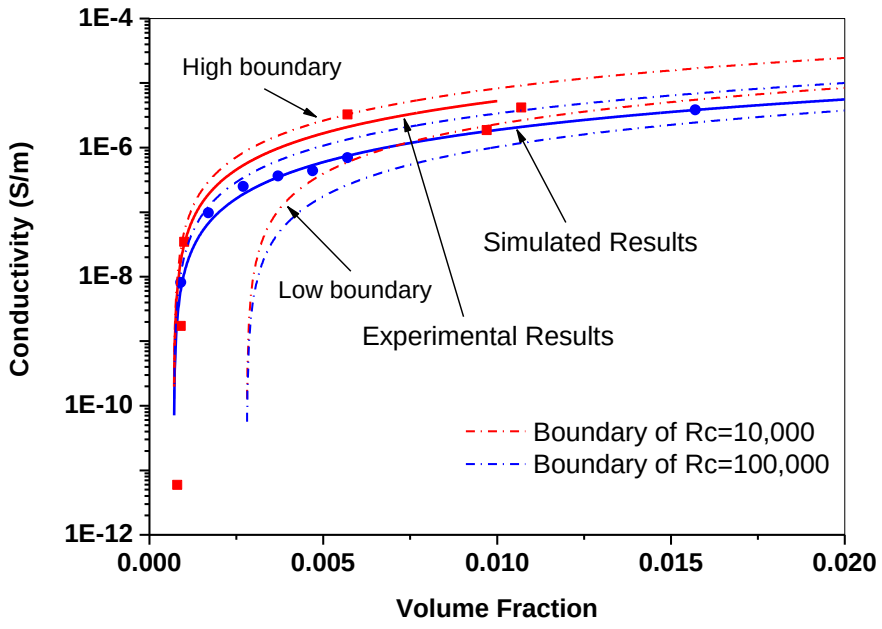

(b)

Figure 3.9 Comparison of simulated conductivity with experimental data, the high boundary represents the composites with curl ratio = 1, and the low boundary represents curl ratio ≈ 0. (a) MWCNT/PVA and (b) SWCNT/PI composites.

3.2.4 Conclusions

A continuum model was constructed to investigate the DC properties of CNT/polymer composites. Based on this model, the effect of the microstructure of CNT/polymer composites on the electrical conductivity was predicted. As examples, the percolation threshold and critical exponent of CNT/polyethylene, CNT/polyimide and CNT/poly(vinyl alcohol) were simulated. In the case of considering tunneling conduction, the percolation threshold depends on the polymer matrix. The contact resistance and tunneling resistance between CNTs have significant influences on conductivity but not on the percolation threshold. The effects of the tortousity of SWCNTs on the conductivity were also analyzed. The percolation threshold increases with decreasing the curl ratio. CNTs cannot be considered as valuable conductive fillers for improving the electrical conductivity of polymers unless the contact and tunneling resistances are reduced significantly.

3.3 Numerical Simulation of AC Conductivity for CNT/Polymer Composites

3.3.1 Introduction

The AC percolative Y_m, as a function of volume fraction and frequency, is normally expressed in the form of power law. Generally, the conductivity of polymers linearly increases with increasing applied frequency. As $p<p_c$, CNT/polymer composites exhibit the same frequency dependent behaviour as polymers. In the case of $p>p_c$, the electrical conductivity of CNT/polymer composites exhibits a frequency independent behaviour as applied frequency (ω) is below the critical frequency (ω_0), and will increase linearly with applied frequency as $\omega > \omega_0$. As reviewed in section 2.4.2, the AC behaviour of CNT/polymer composites is often understood by using the notion of correlation length ξ, which associates with the distance between the largest size of

conductors in the systems.

The AC properties of CNT/polymer composites have been measured by many research groups. Kilbride et al. [13] reported that the critical frequency, ω_0, of MWCNT/PVA thin films was in the range of 6 x 10^3 to 3 x 10^4 rad/s, and the exponent, t/(s + t) (t ≈1), varied from 0.91 to 0.94. They also indicated that the critical frequency and exponent for various polymer hosts displayed different values. In the investigation of SWCNT/PI nanocomposites, Mclachlan et al.[27] found that the exponent, t/(s + t), was 0.75, and ω_0 was found to be 3.5KHz. They also reported that for $p > p_c$, at low frequency, the real AC dielectric constant slowly decreased with increasing frequency, and the AC dielectric constant rapidly decreased at around the critical frequency ω_0. In Kim et al.'s study of the AC electrical behaviour of SWCNT/expoxy nanocomposites [28], the exponent, t/(s + t), was estimated to be 1.3 ± 0.2, p_c was found to be 0.0074wt% and ω_0 was found to be at the level of 10^2 Hz. The AC dielectric constant strongly decreased with increasing frequency from a very low frequency.

The preceding review of the reported measurements of the AC properties of CNT/polymer nanocomposites suggests that the conductivity can be described by Eq.2.50. However, the fact that the measured AC properties are quite different, even for the same polymer host nanocomposites, indicates that AC properties are sensitive to the local morphology, which cannot be interpreted using the scaling theory [6]. This section will focus on understanding the effect of the microstructure on the AC properties of MWCNT/polymer nanocomposites using the linear circuit theory [29]. To this end, a 3-D numerical simulation system was built to determine the electrical properties of MWCNT/polymer nanocomposites and the effect of microstructure on the AC properties of nanocomposites, especially in the region of $p \sim p_c$. Due to the failure of correlation length as an explanation of the effect of curl ratio on the critical frequency, an interpretation based on the linear circuit theory will also be given in the section.

3.3.2 Model and Modelling

The modeling of the AC properties of CNT/polymer nanocomposites was also conducted in three steps: (1) the generation of the microstructure of the nanocomposite; (2) the creation of a resistor-capacitor circuit corresponding to this microstructure; and (3) the computation of the AC properties. The first step was the same as the microstructure generation step in the simulation of DC properties as the description in section 3.2.2, and AC properties was also calculated by using PSpice software.

Equivalent resistor-capacity circuit

In contrast to the pure resistor equivalent circuit in DC simulation, the equivalent circuit for analyzing the AC properties is a resistor-capacitor (RC) circuit. In order to simplify the calculation, the number of the nearest neighbours was also set to 16 [22]. The RC circuit was created based on the ESs of CNTs. Between a pair of the nearest neighbouring ESs, either a resistor or a capacitor was added to the circuit depending on the geometrical contact between the ESs. The contact between two ESs can be modeled by adding a resistor in the circuit. The value of the contact resistance between CNTs was found to vary from 100KΩ to 3.4MΩ[21]. Here, 400KΩ was used as the value of the contact resistance. The CNT itself possesses extremely high electrical conductivity [1] and, comparing to the given contact resistance and the insulating polymer host, the resistance of CNTs can be neglected.

Two isolated CNTs can be seen as the 'plates' of a capacitor and the mutual capacitance can be estimated by the well known equation $\varepsilon_0\varepsilon_r\frac{A_c}{s}$, where ε_0 is the vacuum permittivity, ε_r is the relative permittivity, and A_c is the area of the conductors. The capacitance of two neighbouring short fibres was proposed by Flandin et al. [30]. It was assumed that the local electrical field line were segments on

the surface of CNTs, which can be divided into parallel and perpendicular elements to the direction of ESs. Here, we also employed $\vec{V}_i(k)$ to describe the local electrical field of ESs. The total capacitance between two CNTs i and j is a sum of capacitance of ESs, which can be expressed by [23]:

$$C_{ij} = \varepsilon_0 \varepsilon_r . \sum_1^{L/0.1} \frac{0.1 \times d \cdot \|\vec{U} \times \vec{V}_i(k)\| \cdot \|\vec{U} \times \vec{V}_j(k)\|}{|\vec{x}_i(k) - \vec{x}_j(k)| - d} \quad (3.5)$$

where ε_r is the relative permittivity of the polymer host, $\vec{U}$ is the vector for external electrical field, $\vec{x}_{ij}(k)$ is the vector of ESs. In order to simplify the calculation, the capacitance was calculated in every 100 ESs, and 'plates' approximated to be a straight rod with the diameter of simulated CNTs between the starting and ending ESs. The effect of the calculation scale on the simulated capacitance is shown in Fig.3.10. It can be observed that the effect of calculation scale on the simulated capacitance becomes weak as increasing curl ratio. The capacitance computed at the calculation scale of 100 ESs is less than 1% deviated from the capacitance calculated per ES. Thus, capacitance computed at the calculation scale of 100 ESs is reliable for the simulation of AC properties.

A multidimensional connecting matrix was constructed to describe the RC circuit, and each passive element was determined by the branch between two nodes. The corresponding units and standard symbol (such as "C" for capacitor) were suffixed to the element value to denote the type of elements between the nodes. It can be noticed that the mutual capacitance is in the order of 10^{-9}C, and the contact resistance is in the order of $10^5\Omega$. Therefore, in order to simplify the modeling process, the standard symbol R was directly suffixed to the elements with the value higher than 0.1, and standard symbol C was suffixed to the elements with the value lower than 0.1. Then, the SPICE [23] input file was created from the connecting matrix, and RC circuit was also analysed by using the PSpice software, developed by Cadence Design Systems.

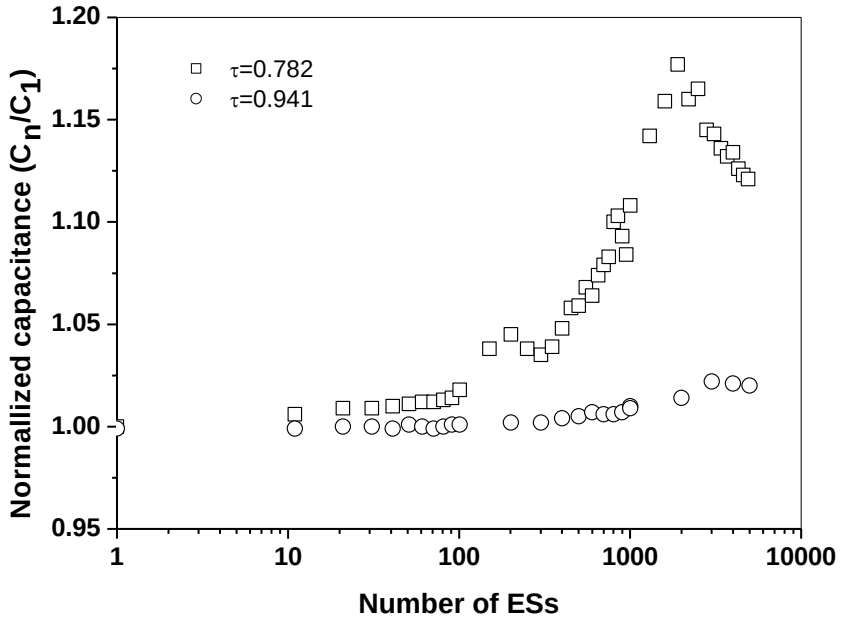

Figure 3.10 Effect of calculation scale (number of ESs) on the calculated τ for CNT with various average τ, which was computed in every 1000 ESs.

3.3.3 Results and Discussion

In the simulation, a MWCNT/PVA nanocomposite film with a thickness of 80 nm was created, and MWCNT with a diameter of 5 nm and length of 5 μm was arbitrarily dispersed in the PVA host. The curl ratio of the MWCNT is set as 0.852 for the good fitting to the experimental results. The simulation was carried out over a frequency range of 10^2 to 10^6 rad/s with the amplitude of 1V, and the contact resistance was set at $10^4\Omega$. The critical frequency ω_0 was marked as the frequency, at which the admittance reached 110% of the frequency-independent admittance. Fig. 3.11 presents the comparison of the simulated frequency-dependent conductivity with the experimental results for the thin MWCNT/PVA film. It can be seen that the simulated results and the experimental data are in good agreement.

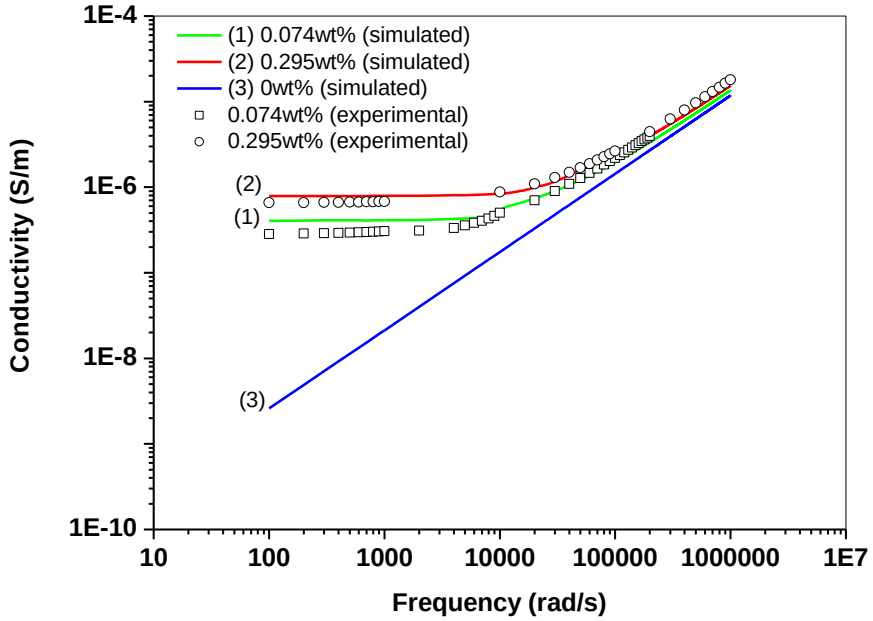

Figure 3.11 Illustration of the frequency-dependent conductivities for the MWCNT/PVA nanocomposites (filled with 0%, 0.074%, and 0.295% by volume) from the simulated results in present work and the experimental data of Kilbride et al. [13]. The frequency-dependent conductivity can be clearly observed at above 10^5 rad/s.

The critical frequency ω_0 and exponent s from the present work and experimental work of Kilbride et al. [13] are listed in Tab. 3.2. It was found that there is a slight difference for the critical frequency ω_0 at the mass fraction of 0.148% and 0.295%. The simulated ω_0 increases with increasing mass fraction, which is in agreement with the percolation theory. In all network systems described by the percolation theory, the correlation length ξ is normally used to understand the AC properties. The critical frequency ω_0 has a power law relationship with ξ [13], which is associated with the largest size of MWCNT clusters in MWCNT/PVA composites. Kilbride et al. [13] stated that the AC properties can be sensitive to the local morphology. It is, therefore, possible that, due to the different local morphologies, some experimental data differ from the simulated results.

The frequency dependence of the phase angle were determined in the range of 10 rad/s to 1M rad/s, and the curves of phase angle against applied frequency for the MWCNT/PVA composites were plotted in Fig. 3.12. It can be observed that the frequency-dependent phase angle appears as the frequency is above ω_0. The frequency-dependent behaviour of phase angle becomes weak, and ω_0 increases with increasing MWCNT mass fraction.

Table 3.2 Summary of the numerical values from simulation and experiment.

p (%)	ω_0 (rad/s)		s	
	Experimental	Present	Experimental	Present
0.074	9.86×10^3	7.32×10^3	0.94	0.92
0.148	2.64×10^4	9.22×10^3	0.91	0.93
0.295	6.56×10^3	1.17×10^4	0.91	0.94
0.590	1.76×10^4	1.77×10^4	0.93	0.94

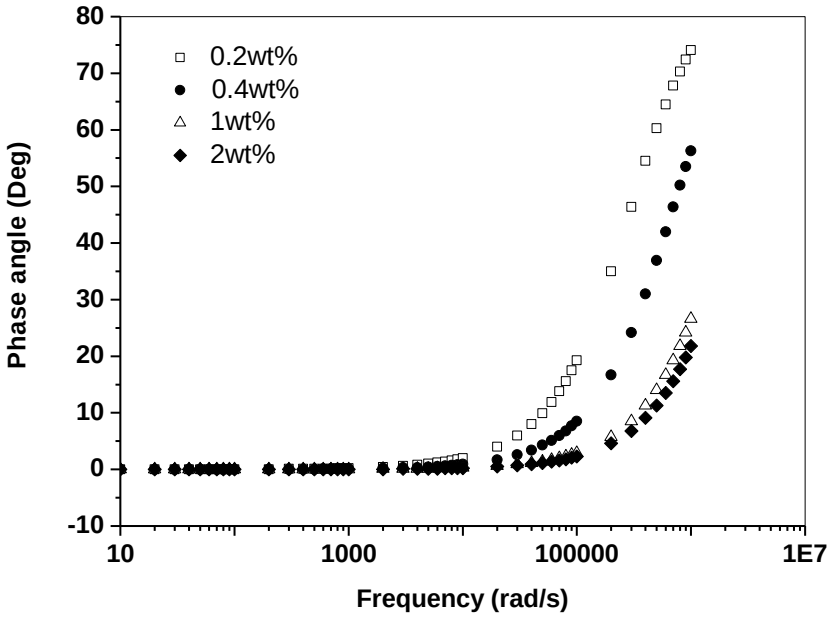

Figure 3.12. Illustration of frequency-dependent phase angle for MWCNT/PVA composites (filled with 0.2%, 0.4%, 1%, and 2% by weight).

At low frequencies, the AC conductivity of CNT/polymer nanocomposites is frequency independent, and approaches to DC conductivity. With increasing frequency, the AC conductivity will switch to being frequency-dependent at the critical frequency ω_0. The ω_0 is often related to the correlation length ξ. Charge carriers are expected to scan a distance, which can be determined by the frequency of the perturbing wave, driven by the AC field [31]. Assuming that a charger carrier scans a distance of ξ at a frequency of ω_ξ, the mean distance scanned at frequencies larger than ω_ξ will be smaller than ξ. Conversely, where $\omega < \omega_\xi$, the mean distance scanned will be larger than ξ. In MWCNT/polymer nanocomposites, it was expected that the charge carriers would tunnel between MWCNTs at frequencies of $\omega < \omega_\xi$. In case of $\omega > \omega_\xi$, it was expected that only the charge carriers in MWCNTs would contribute to the admittance of the composite. Connor et al. [32] have interpreted ω_0 as a function of the correlation length. They considered a power law governed the frequency, which was given by $\omega_\xi \propto \xi^{-\frac{1}{\alpha}}$ with$0.5 < \alpha < 1$. This means that the distance between CNT clusters could also affect ω_0. Thus, the microstructure of the nanocomposites could have an influence on the critical frequency ω_0.

The AC conductivity of MWCNT/PVA nanocomposites with various curl ratios at the mass fractions of 0.4wt% and 1wt% against frequency is shown in Fig. 3.13 (a). It can be seen that the AC conductivity of the nanocomposites is enhanced with increasing curl ratio. In present work, the AC properties are classified into three categories: low-mass fraction ($p \ll p_c$), mass fraction around the threshold ($p \sim p_c$), and high-range mass fraction ($p \gg p_c$). In respect of nanocomposites with high-range mass fraction(the simulation with 1wt% in Fig.3.13 (a)), the curliness of MWCNTs has a weak effect on their AC conductivity. In the nanocomposites with mid-range mass fraction (the simulation with 0.4wt% in Fig.3.13 (a)), with decreasing curl ratio, frequency-dependent AC conductivity appears in the low frequency range. AC

conductivity rapidly increases with increasing frequency until the conductivity is close to the frequency-independent value. This behaviour cannot be explained by reference to correlation length mentioned above. Here, the linear circuit theory was employed to understand the effect of curl ratio on the AC properties. For the composites with a given p, the number of parallel branches in the equivalent circuit decreases with the decrease of curl ratio due to the reduce of interactions between MWCNTs. For the composites with p just above p_c, the percolating network can even become discontinuous with decreasing curl ratio. Thus, it also can be equivalently seen that some disconnections of the MWCNT network can be induced by a decrease in the curl ratio, which can be simulated by introducing capacitors connected in series into the equivalent circuit. Consequently, the conductivity exhibits a capacitive behaviour.

Curl ratio dependent ω_0 is illustrated in Fig. 3.13 (b). It can be seen that ω_0 for the composites with high mass fraction increases linearly with increasing curl ratio. In the case of mid-range mass fraction, with increasing curl ratio, the ω_0 decreases initially and then increases. This behaviour also cannot be explained by reference to correlation length. It was revealed [33] that the threshold decreases with increasing curl ratio, which means that more fillers are needed to reach continuous network using low curl ratio fillers than using high curl ratio ones. The average distance between the fillers regimes in high curl ratio system is lower than that in the low curl ratio system at a given mass fraction in mid-range. According to percolation theory, the critical frequency ω_0 should increase with increasing curl ratio. However, from the simulated results, it can be seen that the critical frequency ω_0 behaves in the opposite manner, which can be well understood using the linear circuit theory. In the case of mass fraction in mid-range, the corresponding equivalent circuit is mainly constructed by combining the branches in series. With increasing curl ratio, disconnections in the circuit become connected due to the increase of the interactions between MWCNTs, and the number capacitors connected in series decreases. As a result, the mutual capacitance in the circuit increases, and ω_0 decreases according to

the relationship, $\omega_0 \sim \log\left(\frac{1}{C}\right)$ [34]. As the curl ratio continues to increase, percolation network is formed, and there are no capacitors connected in series any more. Then, the mutual capacitance between MWCNTs decreases with increasing curl ratio due to the decrease of the isolated 'plates' in the composites. In the case of high-range mass fraction, disconnections will not be induced by decreasing curl ratio, and the mutual capacitance between MWCNTs always decreases with increasing curl ratio.

Generally, MWCNTs can aggregate together as MWCNT bundles in polymers. The dispersion of MWCNTs in the composites can also affect ω_0, as depicted in Fig. 3.14. It can be seen that the shape of the curve depends on the mass fraction. The number of parallel connections increases as the size of MWCNT clusters increases, which leads to an increase in ω_0. As the size of MWCNT continues to increase, the number of parallel connections starts to decline, and, consequently ω_0 decreases with increasing the size of MWCNT clusters. At a certain level in the cluster size, disconnections are induced in the network. As a result, the circuit becomes capacitive, and the critical frequency gently rises as the size of the clusters increases. It also can be observed that the position of the turning points strongly depends on the mass fraction of the composites. The position of the first turning point moves towards high mass fraction with increasing the size of MWCNT clusters. For the composites with high-mass fractions, there was only one turning point in the selected range, but it can be expected that there will be other turning points outside this range.

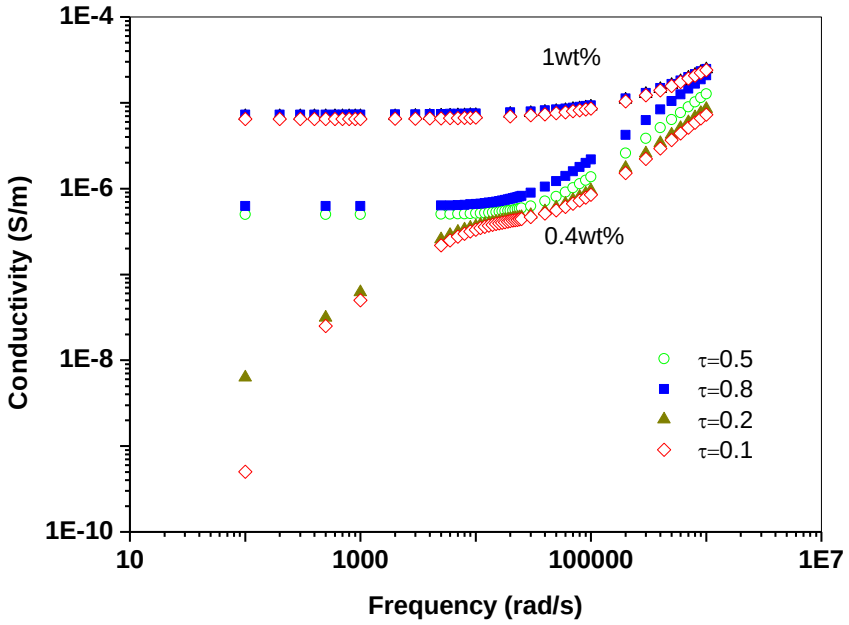

(a)

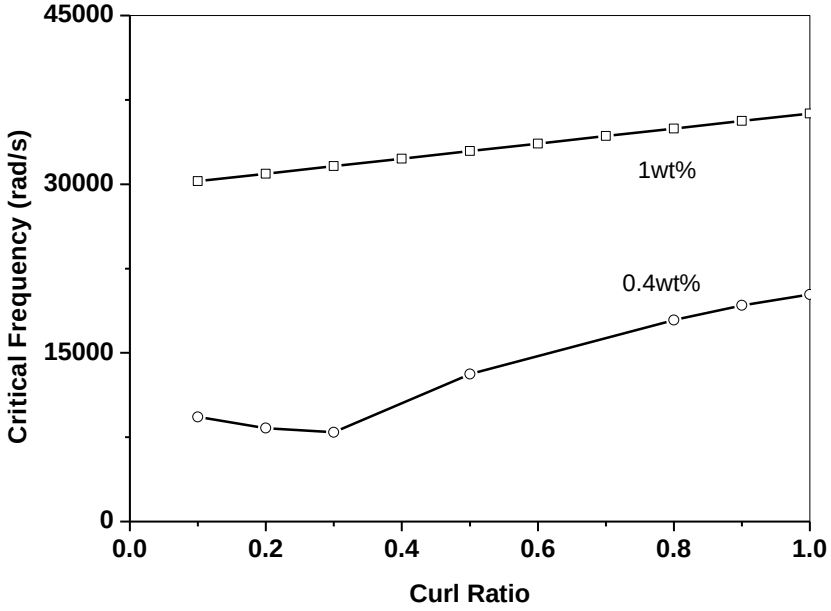

(b)

Figure 3.13 (a) Frequency-dependent conductivity for the nanocomposites with different curl ratios (0.1, 0.2, 0.5, and 0.8) in the high-mass fraction region (1wt%) and in mid-mass fraction region (0.4wt%). (b) Plot of critical frequency against curl ratio for the nanocomposites with mass fraction of 1wt% and 0.4wt%, respectively.

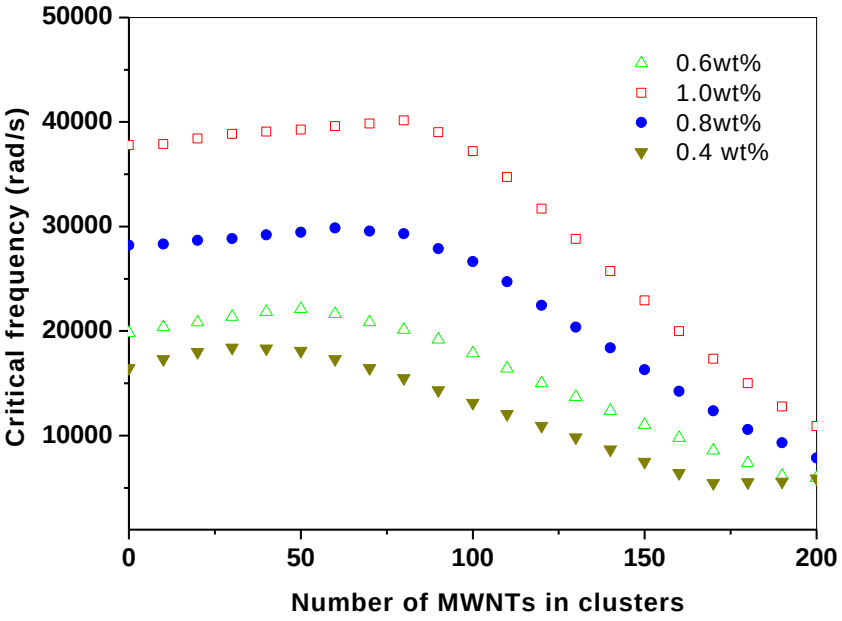

Figure 3.14. Illustration for the influence of MWCNTs dispersion on the critical frequency ω_0 of the MWCNT/PVA nanocomposites.

3.3.4. Conclusions

In this section, research into the effect of the microstructure on the AC conductivity of CNT/polymer nanocomposites was carried out. A continuum model was built for investigating the microstructure dependent AC properties of MWCNT/polymer composites. As frequency increases above ω_0, the AC conductivity switches to a frequency-dependent region. Both of AC conductivity and ω_0 of MWCNT/polymer composites can be enhanced by increasing the curl ratio of MWCNTs. The curliness of MWCNTs has a weak influence on the AC conductivity for the nanocomposites with high-mass MWCNT fraction. In the mid-range mass fraction, with decreasing the curl ratio of MWCNTs, AC conductivity become frequency-dependent in low frequency range, which cannot be explained by reference to correlation length. A proper explanation based on the linear circuit theory was given. As the size of

MWCNT clusters increased, ω_0 increased, peaked and decreased.

3.4 A Theoretical Analysis on AC Conduction of Carbon Nanotube /Polymer Nanocomposites

3.4.1 Introduction

The AC properties of conductive polymer nanocomposites have received many experimental attentions in the recent years [13,14]. However, the frequency dependent conductivity was understood only based on the non-quantified method of correlation length ξ [35]. As frequency is lower than ω_0, the charge carriers were considered to tunnel through at least one polymer barrier because the travel distance is larger than the size of conductors, while for frequency higher than ω_0, the carriers were expected to travel within the continuously conductive phases. It is slightly idealized to consider that electrons scan a distance in AC field in the disorder polymer host. However, it is not clear whether the relationship between the travel distance and frequency is strongly influenced by the polymer host and the morphology of the nanocomposites.

In this section, an attempt was made to reveal the conductivity vs. frequency characteristics of CNT/polymer nanocomposites with various microstructures. Since the pioneer work of Kirpatrick [35], the numerical method used for modeling the electrical properties has been improved, and equivalent circuit model has been widely employed to explain frequency-dependent conductivity of conductive polymer nanocomposites. The theoretical analysis performed in this report was based on the capacitively and resistively junction model (CRJ) [36], in which the junctions between conductors in the polymer matrix can be viewed as an equivalent circuit with an Ohmic resistance R and a capacitance C in parallel. The equivalent circuit of the conductive nanocomposites can be constructed by connecting CRJ in parallel or series, and electrical properties can be obtained by analyzing the circuit. A series numerical

formula were produced for predicting the effect of the microstructure of the AC properties.

3.4.2 Development of theoretical analysis

Firstly, we analyzed the AC behaviour of the equivalent circuit for a junction between two CNTs in the polymer matrix, which is schematized in Fig. 3.15. The current (I_J) through the junction is the sum of the current, I_r, through resistor R_t and the current, I_C, through the capacitor C. The value of R_t is equal to the DC resistance of the junction, which can be equal to the contact resistance or modeled by the tunneling mechanism [19],

$$1/R_t = \frac{A\cdot\left(6.2\times10^{10}/l^2\right)\cdot\left\{\varphi_I \exp(-1.025\cdot l\cdot\varphi_I^{1/2}) - \left(\varphi_I + V\right)\cdot\exp\left[-1.025\cdot l\cdot\left(\varphi_I + V\right)^{1/2}\right]\right\}}{V} \tag{3.6}$$

where V is the voltage across the junction, A is the area of the tunneling junction, l is the distance between two elementary segments showing tunneling behaviour, and φ_I is the average barrier height. The area of the junction in a fibrous network is given by Kallmes et al. [37], $A = \frac{\pi}{2}d^2$, where d is the diameter of the fiber. The current $I_r(t)$ can be obtained following Ohm's law, $1/R_t \cdot V_m \sin(\omega t)$, and current $I_C(t)$ through the capacitor is equal to $C\cdot\frac{d}{dt}(V_m \sin(\omega t))$. When two isolated conductors are not in contact, the two conductors can be seen as the 'plates' of a capacitor, and the mutual capacitance can be estimated by the well known equation $\varepsilon_0\varepsilon_r\frac{A_c}{s}$, where ε_0 is the vacuum permittivity, ε_r is the relative permittivity, and A_c is the area of the conductors. R_l is given by $\rho\cdot\frac{4l_c}{\pi\cdot d^2}$, where l_c is the length between two crossing points, ρ is the resistivity of the fiber, and d is the diameter of the fiber. The mean

segment length of the fibrous network is given by Yi et al.[39], $l_c = \frac{\pi S \sum_{i=1}^{N_f} \lambda_i}{2[\left(\sum_{i=1}^{N_f} \lambda_i\right)^2 - \sum_{i=1}^{N_f} \lambda_i^2]}$, where S is the domain area in interest, N_f is the number of fibres, and λ is the length of the segment. Here, the length of fiber was chosen to be the average length $\bar{\lambda}$, and the domain area to be $\bar{\lambda}^2$, then $l_c = \frac{\pi\bar{\lambda}}{2(N_f-1)}$.

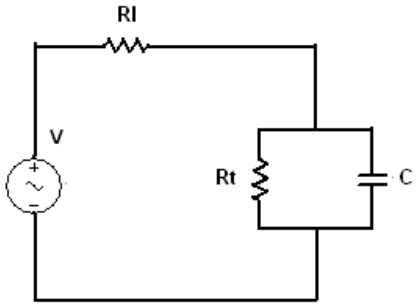

Figure 3.15 Schematic of the equivalent circuit for a junction (ECJ) between two CNTs in the polymer matrix. R_l represents the resistance of the conductors, R_t is the resistance of the tunneling junction, and C is the mutual capacitance between conductors.

The impedance of the ECJ can be written as $Z_J = Rl + \frac{Rt}{Rt \cdot j\omega C + 1}$. The equivalent circuit of the conductive nanocomposites can be synthesized by connecting numbers of ECJ in series and parallel. Here, we used a approximating function [34], which is the function of the Laplace variable s instead of $j\omega$ to represent the given network as closely as possible. In the case of series connection of ECJs, the impedance of the synthesized circuit can be calculated by adding Z_J parameters algebraically, namely

$$Z(s) = \sum_{i=1}^{a} Rl_i + \sum_{i=1}^{a} \frac{Rt_i}{Rt_i C_i s + 1} \quad (3.7)$$

where a represents the number of ECJ in the synthesized series connection. In the case

of parallel connection of ECJs, the admittance can be computed by adding $1/Z_J$ algebraically, namely

$$Y(s) = \frac{1}{Z(s)} = \sum_{i=1}^{n} \frac{1}{Rl_i + \frac{Rt_i}{Rt_i C_i s+1}} \tag{3.8}$$

where n is the number of ECJ in the synthesized circuit. Here, we also classified the conductive nanocomposite into three categories according to the mass fraction of CNTs, i.e., high-mass fraction ($p \gg p_c$), mid-range mass fraction ($p \sim p_c$) and low-mass fraction ($p \ll p_c$). In the range of high-mass fraction, the most of CNTs form a continuous network by connecting each other in parallel, and there are numbers of pathways, which can be seen as parallel branches in the equivalent circuit. The resistance of the junction in the percolating network can be considered to be the contact resistance (R_c), $Rt_i = R_c$, and the Rl_i can be neglected due to the extremely high conductivity of CNTs. Therefore, we have the following results.

For series,

$$Z(s) = \sum_{i=1}^{a} \frac{R_c}{R_c C_i s+1} \tag{3.9}$$

For parallel,

$$Z(s) = \frac{R_c/n}{\frac{R_c}{n}\sum_{i=1}^{n}(C_i s)+1} \tag{3.10}$$

In order to obtain a more readable equation, we made all terms in Eq. 3.9 have the same value of denominator by multiplying a coefficient k_i on both sides of the fraction. Then, Eq. 3.9 can be rewritten as

$$Z(s) = \sum_{i=1}^{a} \frac{R_c k_i}{k_i (R_c C_i s+1)} = \frac{R_c \sum_{i=1}^{a} k_i}{R_c \bar{C} s+1} \tag{3.11}$$

where k_i can be expressed by using the mean capacitance $\bar{C}$, $k_i = \frac{\bar{C}s+\frac{1}{R_C}}{C_i s+\frac{1}{R_C}}$. k_i now is the ratio of the admittance of ECJ with a capacitor of average capacitance to that of ECJ with a capacitor of mutual capacitance of junction i. As mentioned previously, the mutual capacitance is positively proportional to the area of the junction between CNTs, and negatively proportional to the distance between CNTs. If assuming CNTs have the same geometric parameters, we can write k_i as a function of $\bar{l}/l_i$. Eq. 3.9 can be expressed in term of $\bar{C}$, namely

$$Z(s) = \frac{R_c/n}{R_c\bar{C}s+1} \tag{3.12}$$

The equivalent circuit of the composite can be finally boiled down to a single equivalent ECJ, which just consists of equivalent resistor (R_e) and equivalent capacitor (C_e). $R_c\bar{C}s$ is the only term related to frequency in both of Eqs. 3.11 and 3.12. The frequency-responding term does not vary with the complexity of topology of the circuit, and it is a function of the mean capacitance of the equivalent circuit. Eq. 3.11 can be rewritten to describe a single pathway by using R_C instead of R_i as follows:

$$Z(s) = \sum_{i=1}^{a} \frac{R_i k_i}{k_i (R_i C_i s+1)} = \frac{R_C \sum_{i=1}^{a} \nu \cdot k_i}{R_c\bar{C}s+1} \tag{3.13}$$

where $k_i = \frac{\bar{C}s+\frac{1}{R_C}}{C_i s+\frac{1}{R_i}}$, $\nu = \frac{R_C}{R_i}$, R_i is the linear combination of R_C, $\alpha \cdot R_C$, α is the parameter related to the topology of the equivalent circuit. i.e. $k_i = 3 \cdot \frac{\bar{C}s+\frac{1}{R_C}}{C_i s+\frac{3}{R_C}}$ for three ECJ connected in parallel.

Eq.3.12 can be rewritten as follows representing the impendance of the equivalent

circuit for the CNT composite.

$$Z(s) = \frac{1}{\sum_{i=1}^{n}(C_i s + \frac{1}{Rt_i})} = \frac{1}{\sum_{i=1}^{n} k_i} \cdot \frac{1}{Cs + \frac{1}{R_C}} \tag{3.14}$$

From mid-range to low-mass fraction, the number of continuous pathways in the nanocomposite reduces, and discontinuous phases exist in the network. For the discontinuous phase, the tunneling conduction is so small that it can be neglected, and the capacitance of the discontinuous phase can be modeled by only using a capacitor. The impedance of synthesized series connection can be obtained by adding the ECJ and the capacitance of discontinuous phases, namely

$$Z(s) = \sum_{i=1}^{a} \frac{Rt_i}{Rt_i C_i s + 1} + \sum_{j=1}^{b} \frac{1}{C''_j s} \tag{3.15}$$

where a represents the number of continuous phases and b represents the number of discontinuous phases in a single pathway, respectively. C''_j is the capacitance for a discontinuous phase j. For the composites with high and mid-range mass fractions, there is a small amount of discontinuous phases existing in the pathway. Then, Eq. 3.15 can be rewritten as follows.

$$Z(s) = \sum_{i=1}^{a} \frac{R_c k_i}{k_i (R_c C_i s + 1)} = \frac{R_c \sum_{i=1}^{a} k_i}{R_c C s + 1} + \frac{1}{C_s s} \tag{3.16}$$

where C_S is the sum of capacitance for the discontinuous phases in a single pathway. For parallel connecting pathways, the admittance can be computed by adding 1/Z(s) algebraically, namely

$$Y(s) = \frac{1}{Z(s)} = \sum_{i=1}^{n} \frac{1}{Rl_i + \frac{Rt_i}{Rt_i C_i s + 1}} + \sum_{j=1}^{m} \frac{1}{Rl_j + \frac{Rt_j}{Rt_j C_j s + 1} + \frac{1}{C''_j s}} \tag{3.17}$$

where n is the number of continuous pathways and m is the number of discontinuous

pathways in the equivalent circuit, respectively. Here, we introduce a transfer coefficient φ, defined as $\varphi_i \cdot \frac{1}{C''_i s} = \frac{Rt_i}{Rt_i C_i s+1}$. Then, Eq. 3.17 can be rewritten as

$$Z(s) = \frac{1}{\sum_{i=1}^{n}(1/k_i)+\sum_{j=1}^{m}\frac{1}{(1+\frac{1}{\varphi_j})\cdot k_j}} \cdot \frac{1}{Cs+\frac{1}{R_C}} \tag{3.18}$$

In the case of low-mass fraction, there are no continuous pathways in the composite. The impedance of the synthesized circuit will have the same form as Eqs.3.12 and 3.16. Tunneling conduction through the discontinuous phases can be neglected. Therefore, in the low-mass fraction range, $n = 0$, and $\varphi_j = 1$. Then, the equation for the impedance of the synthesized circuit in a general form can be written as follows.

For series,

$$Z(s) = \sum_{i=0}^{a}\frac{R_c k_i}{k_i (R_c C_i s+1)} + \sum_{j=1}^{b}\frac{1}{C''_j s} = \frac{R_c \sum_{i=1}^{a} k_i}{R_c Cs+1} + \frac{1}{C_s s} \tag{3.19}$$

For parallel,

$$Z(s) = \frac{1}{\sum_{i=1}^{n}(\frac{1}{k_i})+\sum_{j=1}^{m}\frac{1}{\left(1+\frac{1}{\varphi_j}\right)\cdot k_j}} \cdot \frac{1}{Cs+\frac{1}{R_C}} \tag{3.20}$$

with the constraint of

$$\begin{cases} n \gg m & \text{high mass fraction} \\ n \sim m m & \text{midrange} \\ n = 0, \varphi_j = 1 & \text{low mass fraction} \end{cases}$$

In the high-mass range, the constraint is that $n \gg m$ and $a \gg b$. As the mass fraction decreases, the number of discontinuous phases increases. In the mid-range mass fraction, the number of continuous pathways is comparable to the number of

discontinuous pathways. As the mass fraction further decreases below the threshold, there are no continuous pathways in the nanocomposite and n consequently reduces to 0. The number of contacts between CNTs also decreases with decreasing the mass fraction, and eventually falls down to zero, when CNTs are isolated in the polymer host.

From the general equations, it can be seen that the equivalent circuit with complex topology eventually can be boiled down to a network with equivalent resistance and mean capacitance. In the case of series connection, the equivalent circuit consists of a resistor of $R_c \sum_{i=1}^{n} k_i$ connecting with a capacitor of $\frac{\overline{C}}{\sum_{i=1}^{n} k_i}$ in parallel. In the case of parallel connection, the final equivalent circuit contains a resistor of R_c linking with a capacitor of $\frac{1}{\sum_{i=1}^{n}(\frac{1}{k_i})+\sum_{j=1}^{m}\frac{1}{\left(1+\frac{1}{\varphi_j}\right)\cdot k_j}} \cdot \overline{C}$. There are multi-pathways in the composite with mass fraction above p_c, and these pathways can be treated as branches connected in parallel. Therefore, the equation of impedance for the composite has the same form as Eq.3.18, namely

$$Z(s) = \frac{1}{\sum_{i=1}^{n}(\frac{1}{k_i})+\sum_{j=1}^{m}\frac{1}{\left(1+\frac{1}{\varphi_j}\right)\cdot k_j}} \cdot \frac{R_C}{R_C \overline{C} s+\delta} \tag{3.21}$$

where $\delta = \frac{\sum_{i=0}^{m+n}\frac{R_c}{R_t}}{m+n}$, and $\frac{1}{\sum_{i=1}^{n}(\frac{1}{k_i})+\sum_{j=1}^{m}\frac{1}{\left(1+\frac{1}{\varphi_j}\right)\cdot k_j}} \cdot \overline{C}s$ is the term related to frequency. In the case of mid-range mass fraction, the pathways can be considered to be formed by connecting CNTs in series. Therefore, δ can be approximated to 1. In the case of $p > p_c$, $\delta = \kappa' \cdot (p - p_c)^{-t}$. When DC voltage is applied on the composite, the Z(s) could be equal to the DC resistance of the composite. It is well known that the DC conductivity of conductive composites obeys the scaling law [17], i.e. $\sigma \propto (p - p_c)^t$. For DC source, $\omega = 0$. Then, we have the following results.

For mid-range mass fraction,

$$Z(s) = \frac{R_c}{\sum_{i=1}^{n}\left(\frac{1}{k_i}\right)+\sum_{j=1}^{m}\frac{1}{\left(1+\frac{1}{\varphi_j}\right)\cdot k_j}} \propto (p - p_c)^{-t} \tag{3.22}$$

For high-mass fraction,

$$Z(s) = \frac{R_c}{\sum_{i=1}^{n}\left(\frac{1}{k_i}\right)+\sum_{j=1}^{m}\frac{1}{\left(1+\frac{1}{\varphi_j}\right)\cdot k_j}} \propto (p - p_c)^{-2t} \tag{3.23}$$

For the nanocomposite with high-mass fraction, CNTs strongly entangle each other. As a result, the R_t is closed to R_C, and the mutual capacitance will be very low. The term of $R_C\bar{C}s$ can be neglected and the parameter $k_{i,j}$ is equal to 1. The resistivity of the composite can be computed by Eq. 3.23. Therefore, the AC conductivity of the nanocomposite with high-mass fraction depends only on the topology of the equivalent circuit and the contact resistance between CNTs.

As the mass fraction decreases, the distance between CNTs increases and the mutual capacitance increases due to the decrease of the crossing points between CNTs. The conductivity turns to frequency-dependent mode until $R_C\bar{C}s$ is comparable to 1. The value of $R_C\bar{C}s$ increases with decreasing the mass fraction. In the case of mid-range mass fraction, Eq. 3.21 can be rewritten as

$$Z(s) = \kappa^{-1} \cdot (p - p_c)^{-t}\frac{R_C}{R_C\bar{C}s+1} \tag{3.24}$$

Eventually, as the mass fraction further drops down to the low-mass fraction range, there are no continuous pathways, and the tunneling conductivity ($\frac{1}{R_t}$) is much lower than $\bar{C}s$. Then, Eq. 3.21 turns to the form of $Z(s)\sim\frac{1}{\bar{C}s}$. The AC conductivity of the

nanocomposite with low mass fraction possesses the same frequency-dependent behaviour as a capacitor. In the case of low-mass fraction, Eq. 3.21 can be rewritten as

$$Z(s) = \kappa^{-1} \cdot (p - p_c)^{-t} \cdot \frac{1}{\bar{C}s} \tag{3.25}$$

Exponent, t, has the value of 1.33 in a 2-D model and 2 in a three-dimensional one [6]. κ can be obtained by fitting Eq. 3.21 to the DC conductivity ($\omega = 0$). $\bar{C}$ can be calculated from the slope of the AC conductivity versus frequency. By known $\bar{C}_0$ with the given mass fraction (p), $\bar{C}$ and the function of mass fraction can be identified by $\bar{C}_0 \left(1 + \frac{p' - p}{p - p_c}\right)^t$ for the composites with mid-range mass fraction. After computing these parameters from one single measurement, Eqs. 3.23 and 3.24 can be used for predicting the AC properties of the CNT/polymer nanocomposites.

3.4.3 Results and Discussion

Fig. 3.16 shows for a comparison of theoretical results of the frequency-dependent conductivity obtained from Eqs. 3.23 and 3.24 with experimental data for MWCNT/poly(vinyl alcohol) (PVA) nanocomposites [13]. It can be seen that present results are in good agreement with the experimental data. In the case of low-mass fraction, the AC properties of the composites can be described by Eq. 3.25, and it shows typical dielectric behaviour, i.e. the AC conductivity linearly increases with frequency. As the mass fraction increases, continuous pathways in the nanocomposite start to form, and the number of isolated CNTs begins to decrease, which causes the decrease of mutual capacitance. A result intermediate between a resistor (frequency-independent) and a capacitor (frequency-dependent) can be observed. The plateau in the curve corresponds to the electrical properties of resistive percolating networks. As frequency increases, the admittance of local 'capacitor' increases, and when $\bar{C}s$ is comparable to or even larger than the conductivity of 'resistor network', the conductivity becomes capacitor-like. In the case of high mass fraction, CNTs

strongly entangle each other, and the mutual capacitance is, therefore, extremely small. Macroscopic conductivity of the nanocomposite will strongly depends on the conductivity of the resistor network, and it exhibits resistor-like behaviour. Critical frequency ω_0 and exponent s from the present work and Kilbride et al. [13] are listed in Tab. 3.3. There is slightly different for the critical frequency ω_0 at mass fractions of 0.074wt% and 0.148wt%. As discussed in section 3.3.3, this difference is caused by the different morphology. The calculated ω_0 increases with increasing mass fraction, which is in good agreement with the percolation theory. In all network systems described by percolation theory, the correlation length ξ is used for understanding the AC properties. The critical frequency ω_0 has power law relationship with ξ.

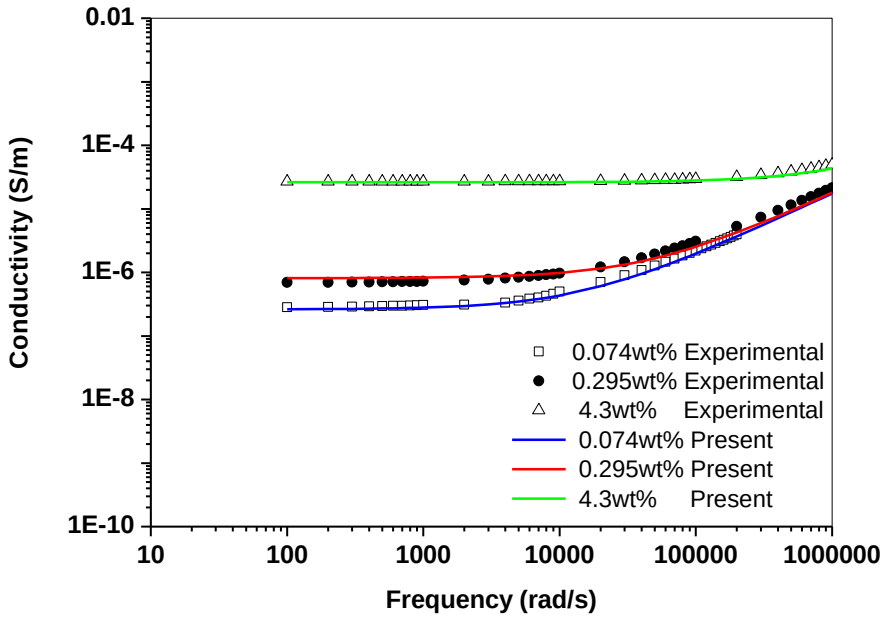

Figure 3.16 Comparison of the frequency-dependent conductivity from the present work to experimental data [13].The geometric parameters of MWCNTs used in the present calculation are as follows: length = 1.5 µm and diameter = 17.5nm.

By applying the kirchhoff's rules on the equivalent circuit, an ordinary differential equation (ODE) with constant coefficients can be obtained as follows.

For high-mass fraction,

$$\kappa^{-1}(p - p_c)^{-2t} \cdot \bar{C}\frac{d}{dt}U(t) + \frac{U(t)}{R_c} = i(t) \tag{3.26}$$

For mid-range mass fraction,

$$\kappa^{-1}(p - p_c)^{-t} \cdot \bar{C}\frac{d}{dt}U(t) + \frac{U(t)}{R_c} = i(t) \tag{3.27}$$

where U(t) is a sinusoid. After solving the ODE, the equation of phase angle (ϕ) can be obtained as follows.

For high-mass fraction,

$$\phi = \tan^{-1}[\omega \cdot \kappa^{-1}(p - p_c)^{-2t} \cdot \bar{C} \cdot R_c] \tag{3.28}$$

For mid-mass fraction,

$$\phi = \tan^{-1}[\omega \cdot \kappa^{-1}(p - p_c)^{-t} \cdot \bar{C} \cdot R_c] \tag{3.29}$$

Table 3.3 Summary of the numerical values from present work and Kilbride et al. experiment [8].

p(%)	ω_0 (rad/s)		s	
	Experimental	Present	Experimental	Present
0.074	9.86×10^3	2.03×10^3	0.94	1
0.148	2.64×10^4	3.83×10^3	0.91	1
0.295	6.56×10^3	5.14×10^3	0.91	1
0.590	1.76×10^4	1.62×10^4	0.93	1

Fig. 3.17 shows the plot of the phase angle against frequency for MWCNT/PVA nanocomposites. The frequency-dependent phase angle appears at above 10^4rad/s. The frequency-dependent behaviour becomes weak and the critical frequency increases with increasing MWCNT mass fraction. In the range of low frequency, the AC properties exhibit pure resistor behaviour, and the phase angle is close to zero. As frequency increases, the phase angle increases due to the decrease of the impedance of the local 'capacitors'.

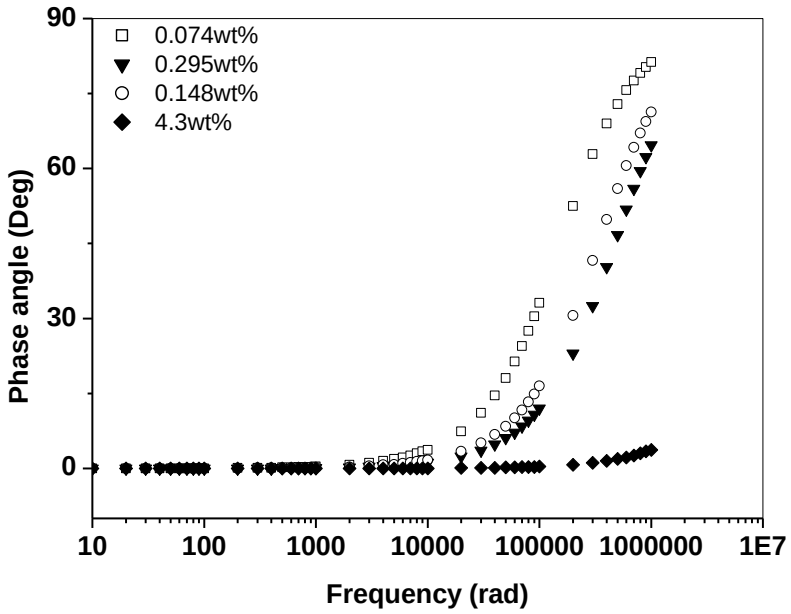

Figure 3.17 Illustration of frequency-dependent phase angle for the MWCNT/PVA nanocomposites (filled with 0.074wt%, 0.148wt %, 0.295wt%, and 4.3wt%).

In the realistic case of a finite system with complicated object, the 'surface' of the object is difficult to define. The 'radius of gyration' (R_s) is often employed to describe the dimension of objects in percolation theory. We now use the same definition to estimate the 'surface' of CNTs and the average distance between two CNT sites. Generally, CNTs are neither parallel nor perpendicular to the applied electrical field. As a result, the capacitance cannot be calculated using the conventional definition of 'area of the plate' and 'distance between plates'. In order to estimate the mutual capacitance, an assumption on the effective area of CNTs was introduced. The more

realistic way is assumed to use the circle with radius R_s as the 'plate', which is centered on the mass centre of CNTs and perpendicular to the axis of the electrical field. The area of the circle is πR_s^2, and the average of the squared R_s is proportional to $(p - p_c)^{-2v}$ [6], where v=4/3 for a 2-D system, and $v \approx 0.9$ for a 3-D system. The average distance between the two sites of CNTs is proportional to $B \cdot (p - p_c)^{-v}$ [6]. Then, Eq. 3.24 can be modified to the following equation, which only has one variable of $(p - p_c)$, namely

For high-mass fraction,

$$Y(s) = \varepsilon_0 \varepsilon_r \cdot B \cdot \kappa \cdot (p - p_c)^{2t-v} \cdot s + \frac{\kappa \cdot (p-p_c)^t}{R_c} \tag{3.30}$$

For mid-range mass fraction,

$$Y(s) = \varepsilon_0 \varepsilon_r \cdot B \cdot \kappa \cdot (p - p_c)^{t-v} \cdot s + \frac{\kappa \cdot (p-p_c)^t}{R_c} \tag{3.31}$$

where $\frac{\kappa \cdot (p-p_c)^t}{R_c}$ is the DC conductivity of the composite, and parameter B can be calculated by fitting experimental results. Fig. 3.18 presents a comparison of results obtained from Eqs. 3.30 and 3.31 with the experimental data, which is relatively good in agreement with experimental data [13].

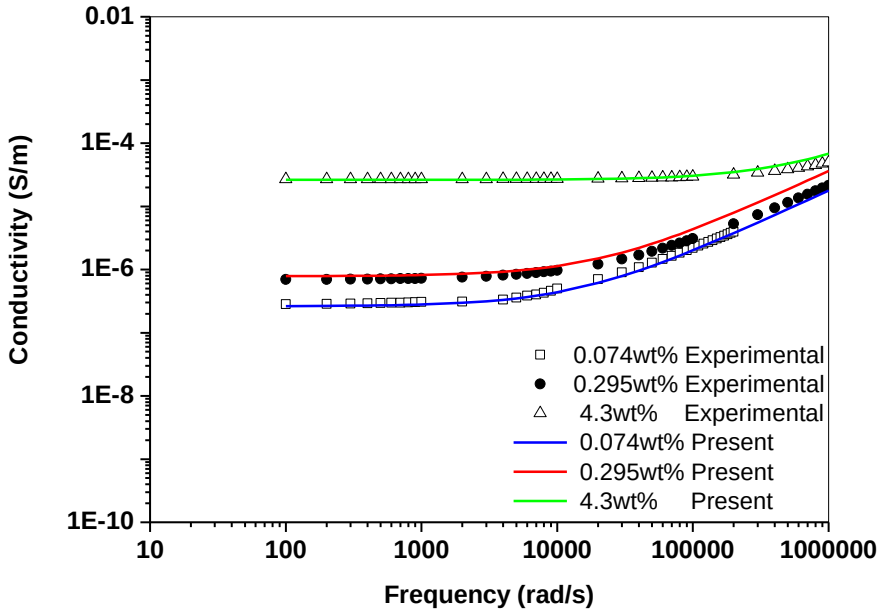

Figure 3.18 Comparison of theoretical frequency-dependent conductivity with experimental results [13].

Now we consider the critical frequency of the nanocomposite with mid-range mass fraction. The critical frequency ω_0 is defined as the frequency at which the conductivity reached 110% of the frequency-independent conductivity. From Eqs. 3.30 and 3.31, the following equation can be derived,

$$\omega_0 = \frac{B\cdot(p-p_c)^v}{10R_c\varepsilon_0\varepsilon_r} \tag{3.32}$$

For straight fibers, the percolation threshold is a function of aspect ratio (ζ) of CNTs, and the relationship between them was given by Balberg et al. [37]. In their analytical percolation model, the percolation threshold is inversely proportional to the object excluded volume, which was expressed by a second order polynomial of ζ for the random distribution as follows [6].

$$V_{ex} = \frac{4\pi}{3}d^3\left[1+\frac{3}{8}\zeta+\frac{3}{128}\zeta^2\right] \tag{3.33}$$

Then, the effect of the aspect ratio on the critical frequency can be plotted, shown in Fig.3.19. It can be found that critical frequency increases with increasing aspect ratio of CNTs at a given mass fraction. In the case of mass fraction around threshold, the aspect ratio strongly affects critical frequency, and this effect becomes weak with increasing mass fraction. It also can be found that the percolation threshold increases with decreasing the aspect ratio.

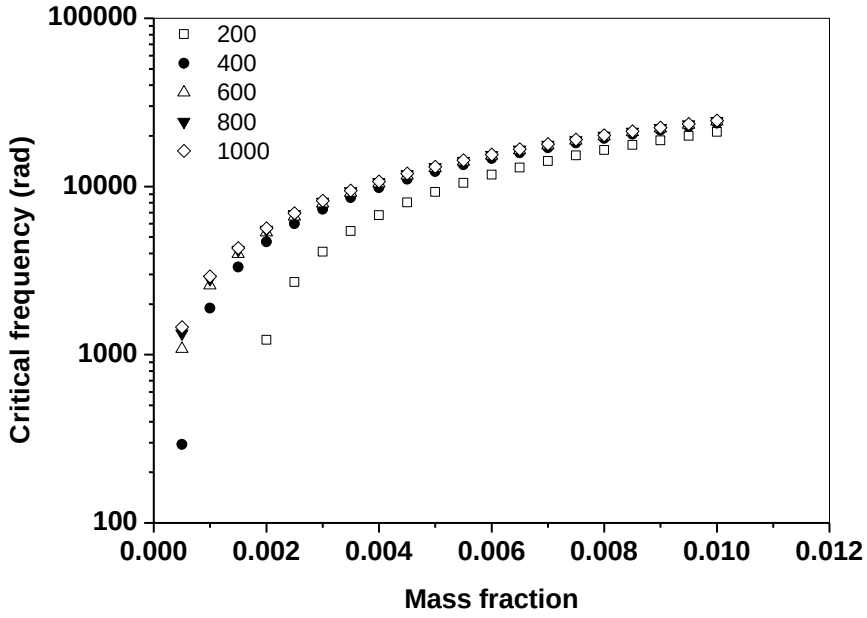

Figure 3.19 Illustration of critical frequency vs. mass fraction for the MWCNT/PVA nanocomposite with different aspect ratios (200, 400, 600, 800 and 1000). The diameter of MWCNTs used in calculation was 8 nm.

We now turn to investigate the effect of waviness on the AC properties of CNT/polymer nanocomposites. The excluded volume of a wavy fiber can be identified by using hard-core model [38], which is expressed as follows.

$$V_{ex} = \frac{32\pi}{3} R^3 \left[(1 - t^3) + a_1 (1 - t^2) (\frac{L'}{R}) + a_2 \left(\frac{L'}{R} \right)^2 (1 - t) \right] \quad (3.34)$$

where t is the ratio of the radius of the core to the outer radius of soft shell, L' is the running length of the fiber, $a_{1,2}$ is constants, and R is the radius of the fiber. We introduce the quantity $\bar{q}$ that serves as a description of the average waviness, $\bar{q} = \frac{L}{L'}$, and wavy fiber can be equivalent to a straight one, which runs between the two extremities of the wavy fiber. Eq. 3.34 can be rewritten as follows

$$V_{ex} = \frac{32\pi}{3} R^3 \left[(1 - t^3) + \frac{3}{8} \cdot (1 - t^2) \cdot \bar{q} \cdot \zeta + \frac{3}{128} \cdot \zeta^2 \cdot \bar{q}^2 \cdot (1 - t) \right] \quad (3.35)$$

The effect of the waviness of CNTs on the critical frequency is presented in Fig.3.20. It can be seen that the nanocomposite with more tortuous CNTs has a lower critical frequency than with straighter CNTs. In the case of mid-range mass fraction, the critical frequency rapidly increases with decreasing the waviness of CNTs. In the case of high-mass fraction, the waviness of CNTs has a weak influence on the critical frequency. As the waviness of CNTs increases, the percolation threshold also increases. The isolated probability is inversely proportional to the waviness of CNTs [16] at the same mass fraction above the threshold due to the strong decrease of the crossing points between CNTs.

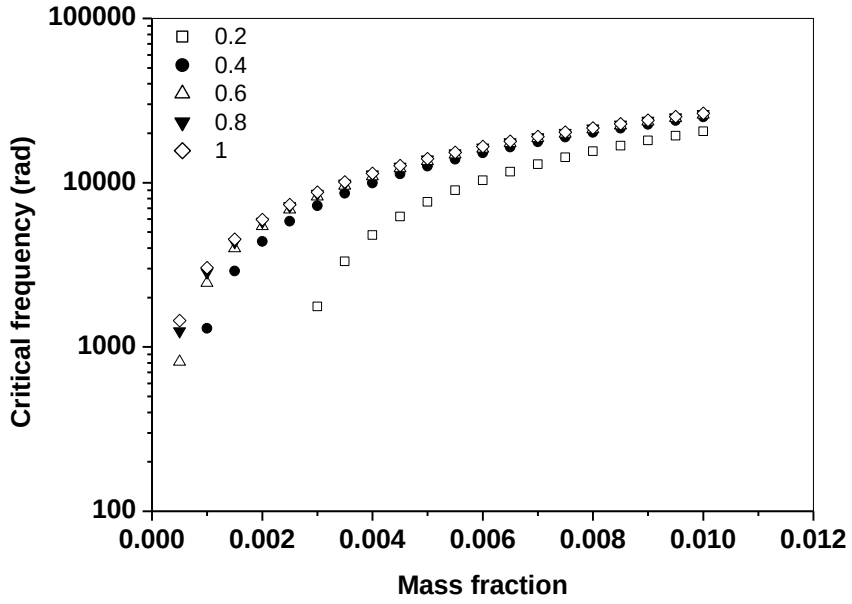

Figure 3.20 Illustration of critical frequency vs mass fraction for MWCNT/PVA nanocomposites with different $\bar{q}$ (0.2, 0.4, 0.6, 0.8 and 1.0). The aspect ratio of the MWCNTs was 1000, and the diameter of MWCNTs was 8nm.

The effect of the contact resistance on the AC conductivity and critical frequency are presented in Fig. 3.21. It can be seen that the frequency-independent resistance drops down with increasing contact resistance. The frequency-independent resistance mainly depends on the resistive percolating network. As the contact resistance increases, the resistance of the percolating network increases. Consequently, the frequency-independent resistance also increases. The critical frequency decreases, because the frequency, which makes $\bar{C}s$ be comparable to $\frac{1}{R_C}$, becomes low due to the decrease in $\frac{1}{R_C}$. Therefore, the critical frequency decreases, and the width of plateau narrows down with increasing the contact resistance.

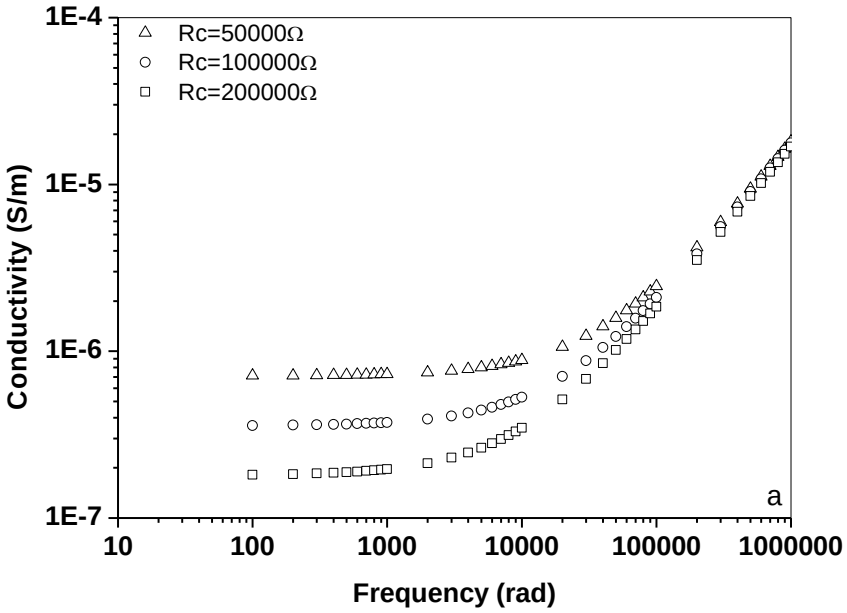

(a)

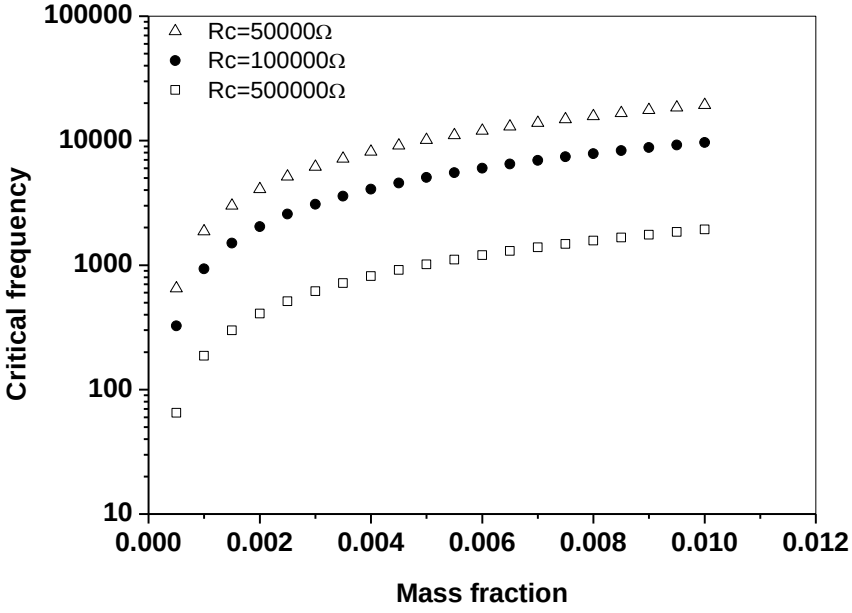

(b)

Figure 3.21. (a) Illustration of the AC conductivity of MWCNT/PVA nanocomposites vs. frequency for different contact resistance ($R_c = 5 \times 10^4$, $R_c = 1 \times 10^5$ and $R_c = 2 \times 10^5$). The aspect ratio of MWCNTs was 500, and the diameter of MWCNTs was 8 nm. (b) Illustration of critical frequency vs. mass fraction for different contact

resistances.

3.4.4 Conclusions

The AC properties of CNT/polymer composites was evaluated using the capacitively and resistively junction model. A series numerical formulas were derived for predicting AC properties with consideration of the effect of microstructure. Theoretical results are in good agreement with experimental data. The numerical formulas developed in the present work provide a new and easy way for understanding of the frequency-dependent AC properties of CNT/polymer nanocomposites based on linear circuit theory. In particular, this work introduced an equivalent RC circuit with simple definition of the values of contact resistance and average mutual capacitance for CNT/polymer nanocomposites. The effect of the local morphology and the contact resistance also can be predicted by equations given in present work. The critical frequency is enhanced by increasing the aspect ratio and curl ratio, and declines with increasing the contact resistance. As the contact resistance increases, the critical frequency decreases.

3.5 Summary

In this chapter, we investigated the DC and AC properties of CNT/polymer composites based on the equivalent circuit model. A 3-D continuum model was constructed by introducing effective tunneling conduction for predicting DC conductivity of CNT/polymer composites. The effect of the microstructure of CNT/polymer composites on DC conductivity was assessed particularly for CNT/PE, CNT/PI and CNT/PVA composites. CNT contact resistance and tunneling resistance have significant influences on the conductivity but do not affect the percolation threshold. The effects of the potential barrier of polymer and the tortousity of CNTs on the conductivity were also analyzed, and both of percolation threshold and DC conductivity can be affected by them. CNTs might not be an effective filler to

improve the conductivity of polymers unless the contact resistance can be significantly reduced.

The continuum model was also employed to investigate the microstructure -dependent AC properties of CNT/polymer nanocomposites. With increasing frequency, the AC conductivity switches to a frequency-dependent behaviour. The curliness dependent AC conductivity in low frequency range, which cannot be explained by reference to correlation length, was first reported by us. The AC conductivity of the composite can be enhanced with increasing curl ratio of MWCNTs. In the case of composites with high-mass fraction, the curliness of MWCNTs only has a weak influence on the AC conductivity of the nanocomposite. In the mid-range mass fraction, with increasing curl ratio of MWCNTs, the AC conductivity, interestingly, became frequency-dependent in low frequency range, which cannot be explained by reference to correlation length. A proper interpretation based on the linear circuit theory was given. Both of AC conductivity and critical frequency can be significantly affected by the size of CNTs clusters.

In order to develop a more reasonable and quantified method for understanding AC conductivity, a series numerical formulas were derived by using a numerical capacitively and resistively junction model. In particular, this work introduced an equivalent RC circuit with simple definition of the values of contact resistance and average mutual capacitance for CNT/polymer nanocomposites. Theoretical results were in good agreement with experimental data, and successfully predict the effect of the morphology on the AC properties. The critical frequency is enhanced by increasing the aspect ratio and curl ratio of CNTs, which is agreed with present simulated results.

References

1. T. W. Ebbessen, H. J. Lezec, H. Hiura, J. W. Bennett, H. F. Ghaemi, and T. Thio, Nature 382, 54 (1996).
2. H. Dai, E. W. Wong, and C. M. Lieber, Science 272, 523 (1996).
3. B. Abeles, H. L. Pinch, and J. J. Gittleman, Phys. Rev. Lett. 35, 247 (1975).
4. S. Feng, B.I. Halperin, and P.N. Sen, Phys. Rev. B *35*, 197 (1987).
5. S. Kirkpatrick, Rev. Mod. Phys. 45, 574 (1973).
6. D. Stauffer, A. Aharony, Introduction to Percolation Theory, Taylor and Francis, London, 1992.
7. P. Sheng, E.K. Sichel, and J.I. Gittleman, Phys. Rev. B 40, 1197 (1978).
8. Q. F. Huang, S. F. Yoon, Rusli, H. Yang, B. Gan, Kerlit Chew, and J. Ahn, J. Appl. Phys. 88, 4191 (2000).
9. S. T. Chui, Phys. Rev. B 43, R14276 (1991).
10. K. Ahmad, W. Pan, and S. Shi, Appl. Phys. Lett. *89*, 133122 (2006).
11. Y. Zou, Y. Feng, L. Wang, and X. Liu, Carbon *42*, 271 (2004).
12. Z. Rubin, S. A. Sunshine, M. B. Heaney, I. Bloom, and I. Balberg, Phys. Rev. B 59, 12196 (1999).
13. B.E. Kilbride, J. N. Coleman, J. Fraysse, P. Fournet, M. Cadek, A. Drury, and S. Hutzler, J. Appl. Phys. *92*, 4024 (2002).
14. Z. Ounaier, C. Park, K.E. Wise, E. J. Siochi, and J. S. Harrison, Composites Sci. and Tech. 63, 1637 (2003).
15. F. Dalmas, R. Dendievel, L. Chazeau, J.Y. Cavaille, and C. Gauthier, Acta Materialia 54, 2923 (2006).
16. P. Sheng, B. Abeles, and Y. Arie. Phys. Rev. Lett. 31, 44 (1973).
17. I. Balberg, Phys. Rev. Lett. 59, 1305 (1987).
18. M. S. Fuhrer, J. Nygard, L.shih, M. Forero, Young-Gui Yoon, M. S. C. Mazzoni, H. J. Choi, J. Ihm, S. G. Louie, A. Zettl, and P. L. McEuen, Science 288, 494 (2000).
19. J. G. Simmons, J. Appl. Phys. 34, 1793 (1963).

20. R. Fisch and A. B. Harris, Phys. Rev. B 18, 416 (1978).
21. A. Buldum and J. P. Lu, Phys. Rev. B 63, 161403 (2001).
22. J. L. Meijering, Philips Res. Rep., 8, 270 (1953).
23. A. H. Robbins, and W. C. Miller, Circuit Analysis Theory and Practice, Thomson Delmar Learning, 2004.
24. G. Liang, T. Cui, K. Varahramyan, Solid-State Electronics 47, 691 (2003).
25. H. Norde, J. Appl. Phys. 50, 5052 (1979).
26. J. H. Walther, R. Jaffe, T. Halicioglu and P. Koumoutsakos, Center for Turbulence Research, Proceeding of the Summer Program (2000).
27. D. S. Mclanlan, C. Chiteme, C. Park, K. E. Wise, S. E. Lowther, P. T. Lillehei, E. J. Siochi, and J. S. Harrison, J Polymer Scien. B 43, 3237 (2005).
28. B. Kim, J. Lee, and I. Yu, J Appl. Phys., 94, 6724 (2003).
29. L Moura, I Darwazeh, Introduction to Linear Circuit Analysis and Modeling, Newnes, 2005.
30. L. Flandin, M. Verdier, B. Boutherin, Y. Brechet, and J. Y. Cavaille, J Polymer Science B, 37, 805 (1998).
31. J. C. Dyre, and T. B. Schroder, Rev. Mod. Phys. 72, 873 (2000).
32. M. T. Connor, S. Roy, T. A. Ezquerra, and F. J. Balta Calleja. Phys. Rev. B 57, 2286, (1998).
33. X. Sun and M. Song, Macromolecular Theory and Simulations, 18, 155 (2009).
34. A. Ramakalyan, Linear circuits analysis and synthesis, Oxford university press, (2005).
35. S. Kirkpatrick, Rev. Mod. Phys. 45, 574, (1973).
36. A. Barone and G. Paternò, Physics and Applications of the Josephson Effect (John Wiley & Sons, New York, 1982
37. I. Balberg, C. H. Anderson, S. Alexander, and N. Wagner, Phys Rev. B 30, 3933, (1984).
38. L. Berhan, and A. M. Sastry, Phys. Rev. E 75, 041120, (2007).
39. Y. B. Yi, L. Berhan, and A. M. Sastry, J. Appl. Phys. 96, 1318, (2004).

Chapter 4 Electrical Properties in Carbon Nanotube/Graphite Oxide Layered Nano-Structure Hybrid Materials

4.1 Introduction

Electrically conductive films have been extensively studied due to their various potential applications, such as for microheaters [1], electrodes [2], electromagnetic interference shielding [3] and photoelectric films [4]. CNTs are widely regarded as a candidate for producing highly conductive films [5,6]. Several methods of manufacturing macroscopic pure CNT films have been reported [7-10]. However, the strength of CNT films made by the solution method [7] is not satisfactory. The application of the chemical vapor deposition (CVD) [8, 9] technique is limited by its high costs.

In a recently method, conductive MWCNT films were fabricated, in which were graphite oxide (GO) were used as a carrier [11]. GO, which consists of two dimensional oxidized graphene sheets, can be exfoliated into individual nanoplatelets (GONPs) in water with the assistance of ultrasound. GONP may contain hundreds of graphene layers. In the microsturcture of GO, hydrophilic oxygen groups are attached on the graphene sheet, and the graphene oxide shows insulating behaviour. It is believed that the MWCNT/GONP hybrid films, because of their high surface conductivity [11], may be used as high-performance transparent conductors.

Very recently, the preparation and characterization of MWCNT/GONP conductive films were reported [11]. The present aim is to report on the electrical properties and leaky capacitive behaviour of MWCNT/GONPs hybrid films. In present work, the DC and AC properties of MWCNT/GONPs film with various concentrations (p) were investigated, and the experimental data were discussed in term of equivalent circuit model. We also measured the specific capacitance, leakage current and power factor

as the function of MWCNT content, applied voltage and temperature. The specific capacitance and relatively high power factor were discussed in relation to the area of MWCNT layers and electrical properties of MWCNT percolation networks. Finally, the charging and discharging behaviours of MWCNT/GONP films were also measured. These results are important for improving the knowledge of the electrical properties of MWCNT/GONP films, understanding the dielectric properties of GONP, and opening a new way for its possible dielectric applications. This chapter was organized as follows. Section 4.2 presented the sample preparation and measurements. Section 4.3 gave the results from electrical measurements and the discussion. Section 4.4 provided a conclusion of present work.

4.2 Experimental

4.2.1 Preparation of Samples

GO was prepared from expandable graphite (EG, Chinese Qingdao Graphite Company) following the procedure mentioned in Ref. 12. 2.5g EG was mixed with 57.5 ml concentrated H_2SO_4 in ice bath (0℃) for half an hour. 7.5g $KMnO_4$ was slowly added into the mixture in order to keep the temperature of the mixture not exceeding 20℃. The mixture was then heated to 35±3℃ and kept stirring for 30 min. Dropwise addition of 115ml distilled water caused the temperature increase to 98℃. The reaction was kept at this temperature for 15 min. Finally, the oxidation reaction was terminated by adding 350 ml distilled water and 25ml 30% H_2O_2 solution. Collection of the EG oxide (EGO) by filtering and successive washing with 5% HCl aqueous solution was repeated by three times until there was no sulphate detected by $BaCl_2$ solution. The EGO was dried at 50℃ under vacuum for one week. The exfoliation of 100mg EGO in 10g DMF was conducted using ultrasonication with a power of 300W for 1 hour at room temperature to obtain stable GONP/DMF (10mg/ml) dispersion.

The MWCNTs were provided by Chengdu Institute of Organic Chemistry, Chinese Academy of Science, with 3-5 wt% hydroxyl groups (-OH) attached on the side wall. The MWCNT/DMF solution was prepared by adding MWCNTs (0.1g) to DMF (40g), followed by sonication with high power (300W) unltrasonic tip for an hour. GONP/DMF (10mg/ml) and MWCNT/DMF (2.5mg/ml) dispersion was mixed together and adjusted to have a concentration of 2.5mg/ml. The substrates used were 18.5×11.5mm glass sheets, which were thoroughly cleaned. The MWCNT/GO film was obtained by pouring the solution into a glass container with the glass substrate inside, and drying for a day at 100℃. The thickness of the film was controlled by adjusting the volume of solution used for casting. The thickness of all films with various concentrations of MWCNTs was about 8μm.

4.2.2 Measurement

The electrical resistances of samples were measured by using the four-probe method with Jandel Engineering Ltd's multi-height microposition probing system. In the measurement, a current was input from across two outer probes, and the variation of the resistance was determined by monitoring the change of the voltage across inner probes. The voltage was detected by using NI USB-6211 data acquisition (DAQ). The proper contact between probes and surface of samples was ensured to keep the testing voltage stable. AC measurements were performed using NI USB-6211 data acquisition as the source over a frequency range 10 rad/s-1M rad/s with amplitude of 50mV.

The capacitance was measured by two termination methods. A voltmeter-ammeter-wattmeter test-circuit, in which the component parts were selected with regard to the range of the capacitance to be measured, was used as the testing circuit presented in Fig.4.1. The electrical contacts were made by silver paste, and two wires were placed

over (soldering iron) the silver paste to form a two-probe measurement setup.

The microtextural characterization of the MWCNT/GO films was performed by scanning electron microscopy (SEM) and transmission electron microscopy (TEM), which is presented in Fig.4.3 and Fig. 4.4. SEM images were taken on the field emission gun scanning electron microscopy (FEGSEM) (LEO 1530 VP instrument). TEM analysis was conducted using a JEOL 2100 FX instrument. The GONP/DMF dispersions were dropped on the copper grid for imaging directly. X-ray photoelectron spectroscopy (XPS) analysis of GONP powders was performed on VG ESCALAB5 (VG Scientific Ltd. England) under 10^{-7} Torr vacuum with AlKα X-Ray source using power of 200W. Fourier transform infrared (FTIR) spectra were recorded on Mattson 3000 FTIR spectrometer using transmission mode with a 4cm^{-1} resolution over 120 scans.

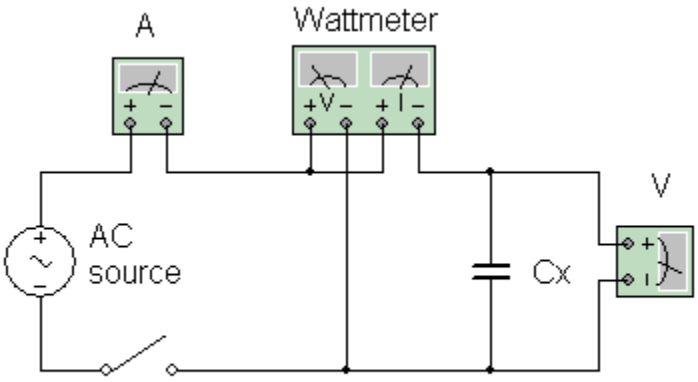

Figure 4.1 Illustration of the voltmeter-ammeter-wattmeter test-circuit used to determine the capacitance and power factor of samples in this work. C_x represents the sample.

4.2.3 Measuremental Errors

One of error sources in the measurement is due to the joule heat generated by the

testing current. As reviewed in section 2.4.1, the bulk electrical conductivity of CNT composites can be affected by the rise of local temperature [13]. In order to minimize errors induced by joule heating, the test current should be as low as possible. However, in order to achieve high quality of signal to noise ratio (SNR), the test current cannot be too low. Here, the samples were tested using a testing current of 10mA for reaching the balance between the two factors. All measurements were processed as fast as possible to minimize the effect of power dissipation in samples. The temperature of the sample was also monitored using a contact senor for evaluating the error caused by the rise of temperature, and the real-time temperature signal of the sample under testing current of 10mA is presented in Fig. 4.2. It can be observed that variation of temperature in samples is relatively low under testing current of 10mA.

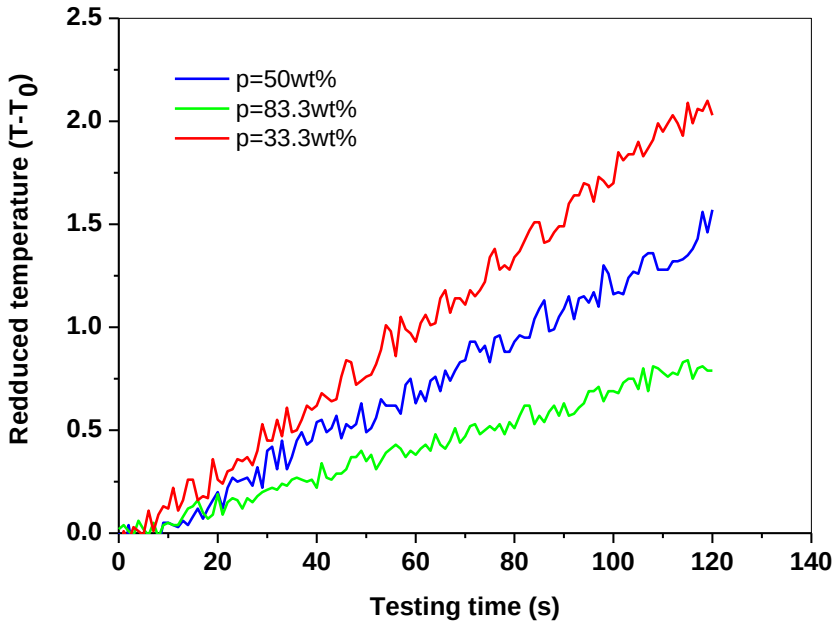

Figure 4.2 Variation of temperature in the samples versus testing time. T is the real-time temperature and T_0 is the zero-current temperature of the samples.

Another error of the measurement is induced by the contact resistance and capacitance between the electrode and the MWCNT/GONP film. In order to reduce the contact

resistance, the electrical contacts were made by silver paste. The data used was the average result of four measurements.

4.3 Results and Discussion

4.3.1 The Morphology of MWCNT/GONP Hybrid Materials

Fig. 4.3 presents the TEM images of exfoliated MWCNT-OH and GO in DMF. It can be seen that the EGO was fully exfoliated into GO nanoplatelets by ultrasonic treatment. Stankovich et al. [14] employed AFM to identify the thickness of both GO nanoplatelets in water and chemically modified GO nanoplatelets in organic solvent as $\sim$1nm. In TEM images, the thickness of GO cannot be exactly identified, but can be estimated as several nanometers from the folded edge of GO nanoplatelets in the high magnification TEM images. SEM images of the MWCNT/GO film are shown in Fig. 4.4. Clearly, it can be observed that the film has a layered structure. The SEM surface images of the MWCNT/GO film are illustrated in Fig. 4.5. It can be found that in the MWCNT/GO hybrid material of p=33.3wt%, MWCNTs tends to aggregate in a certain area. For the MWCNT/GO film with p=50 wt% and 83.3 wt%, a MWCNT percolation network can be observed in the form of entangled coils.

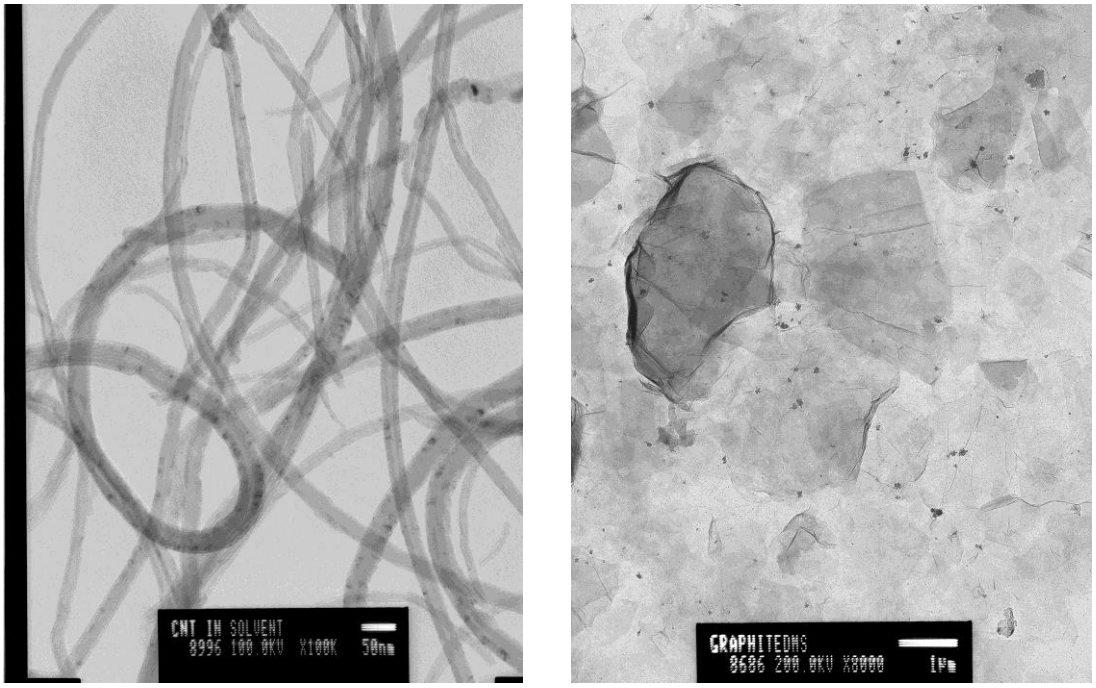

Figure 4.3 TEM images of exfoliated MWCNT-OH (left, 2.5mg/g) and GONPs (right, 10mg/g) in DMF.

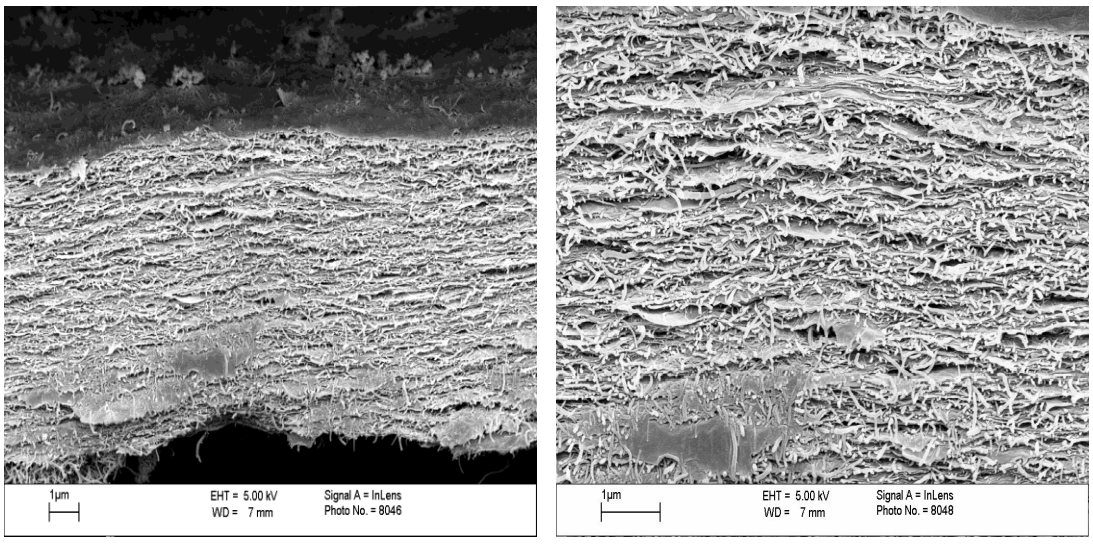

(a) (b)

Figure 4.4 Cross-sectional SEM images of the MWCNT/GONP film with p=66.6wt%.

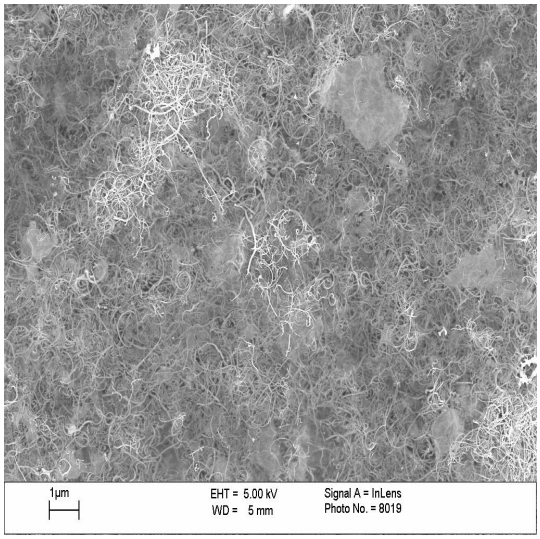
1µm
EHT = 5.00 kV
WD = 5 mm
Signal A = InLens
Photo No. = 8019

(a)

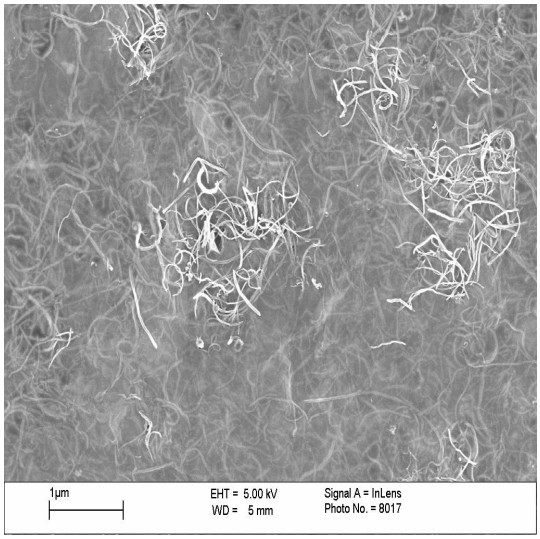
1µm
EHT = 5.00 kV
WD = 5 mm
Signal A = InLens
Photo No. = 8017

(b)

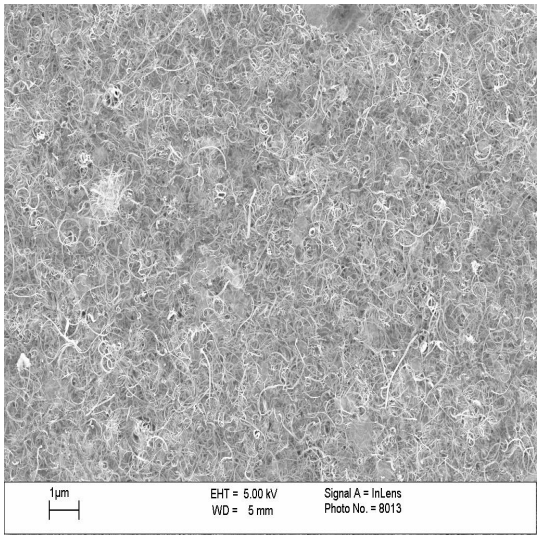
1µm
EHT = 5.00 kV
WD = 5 mm
Signal A = InLens
Photo No. = 8013

(c)

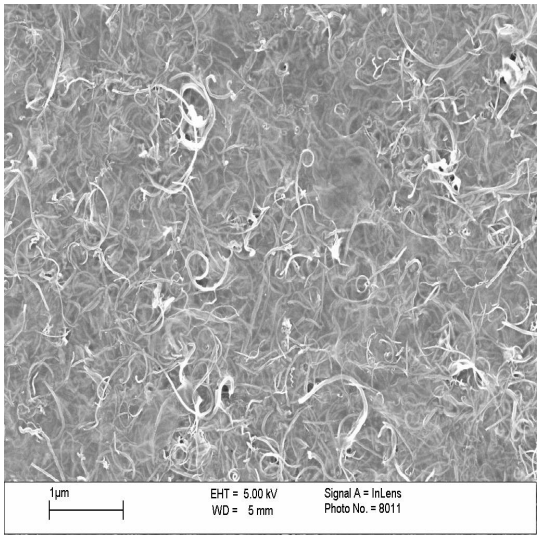
1µm
EHT = 5.00 kV
WD = 5 mm
Signal A = InLens
Photo No. = 8011

(d)

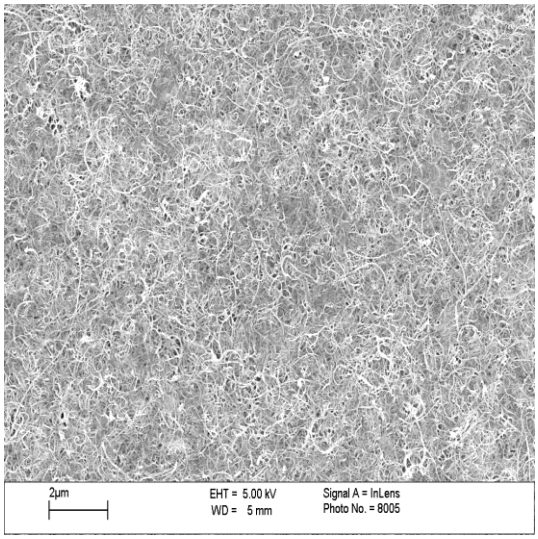
2µm
EHT = 5.00 kV
WD = 5 mm
Signal A = InLens
Photo No. = 8005

(e)

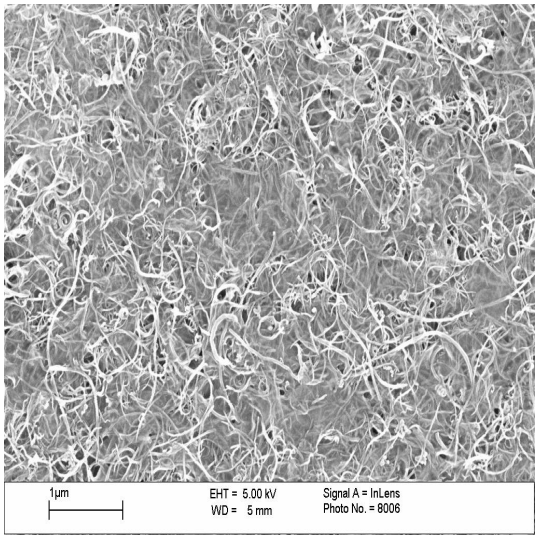
1µm
EHT = 5.00 kV
WD = 5 mm
Signal A = InLens
Photo No. = 8006

(f)

Figure 4.5 Surface SEM images of (a, b) MWCNT/GONP film with p=33.3wt%, (c, d) MWCNT/GONP film with p=50wt%, and (e, f) MWCNT/GONP with p=83.3wt%.

4.3.2 Theoretical Prediction of the Cohesive Energy and Potential in MWCNT/GONP Hybrid Materials

During forming the MWCNT/GONP film, MWCNTs were attracted to the surface of the GONP due to van der Waals interactions. The cohesive properties of graphic solids can be estimated based on the Lennard-Jones (LJ) potential, which can be expressed as follows [15]

$$u(l) = -\frac{A}{l^6} + \frac{B}{l^{12}} \tag{4.1}$$

where l is the distance between two atoms, A is the attractive constant, and B is the repulsive constant. The equivalent distance l_0 is given by [15]

$$l_0 = \left(\frac{2B}{A}\right)^{1/6} \tag{4.2}$$

LJ potential was successful in description of the cohesive properties of graphitic solids that depend on the van der Waals interactions [16]. Here, the cohesive properties were calculated by assuming a continuous distribution of atoms on the MWCNTs and GONP sheet. In another words, the MWCNTs were seen as a continuum cylinder and GONP was treated as a flat sheet with uniform mass distribution. One reason for the assumption is that the effect of correct electron distribution is not important in the calculation of the cohesive properties of graphitic solids [17]. Another reason is to simplify the calculation.

The values of LJ constants (listed in Tab. 4.1) used in present work were estimated from the universal graphitic potential given by Girifalco et al. [17]. In the present work, the potential was calculated as

$$U(R) = \oint u(l)\, ds_{CNT}\, ds_{GO} \tag{4.3}$$

where u(l) is LJ potential, l is the distance between the two elements on MWCNTs, ds_{CNT} , and on the GONP, ds_{GO}.

Table 4.1 Lennard-Jones constants used in the MWCNT/GONP hybrid film.

A (eV/Å^6)	B (eV/Å^{12})	x_0(Å)
16.9	28.0×10^3	3.85

The potential per unit length was computed for MWCNTs with a diameter of 5 nm on a square GONP with dimension of 1 μm, and are presented in Fig. 4.6 (a). In order to clearly see the variation of potential energy at the edge of GONP, the potential per unit length was also calculated on a square GONP with dimension of 10nm, which is shown in Fig. 4.6 (b). It can be seen that the potential is lowest in the central area of GONP, and increases as the MWCNT approaches the edges of the GONP. Therefore, during forming the MWCNT/GONP film, the MWCNTs intend to locate at the central area of GONP.

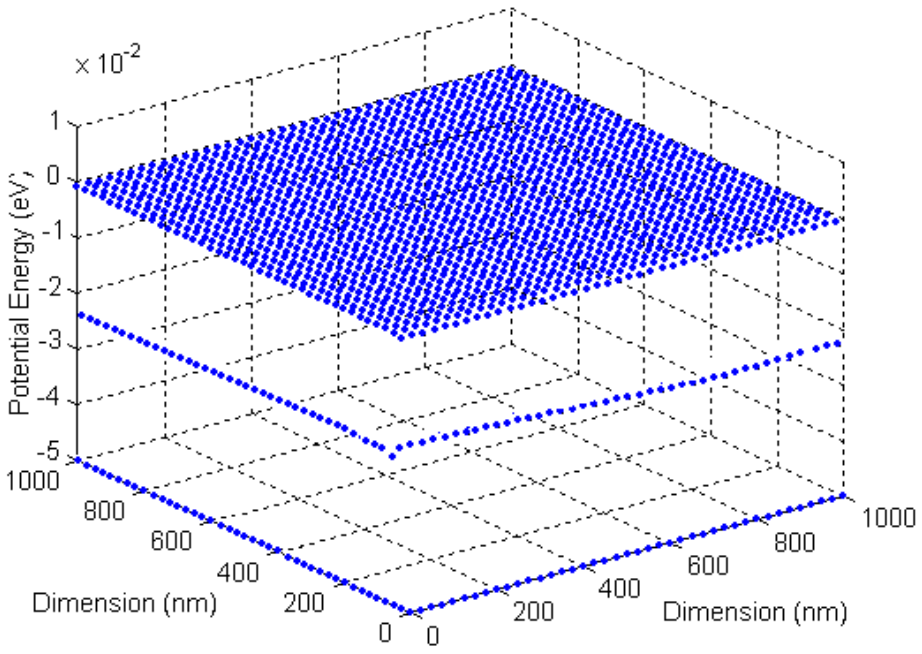

(a)

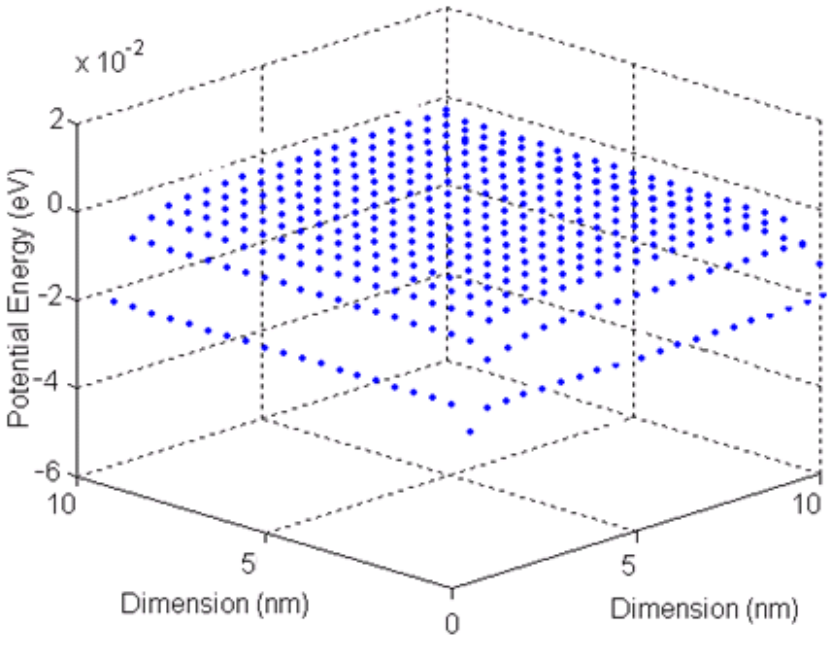

(b)

Figure 4.6 Illustration of interaction potential per length (1 Å) in MWCNT/GONP for (a) the GONP sheet with dimension of 1 μm, and (b) the GONP sheet with dimension of 10 nm.

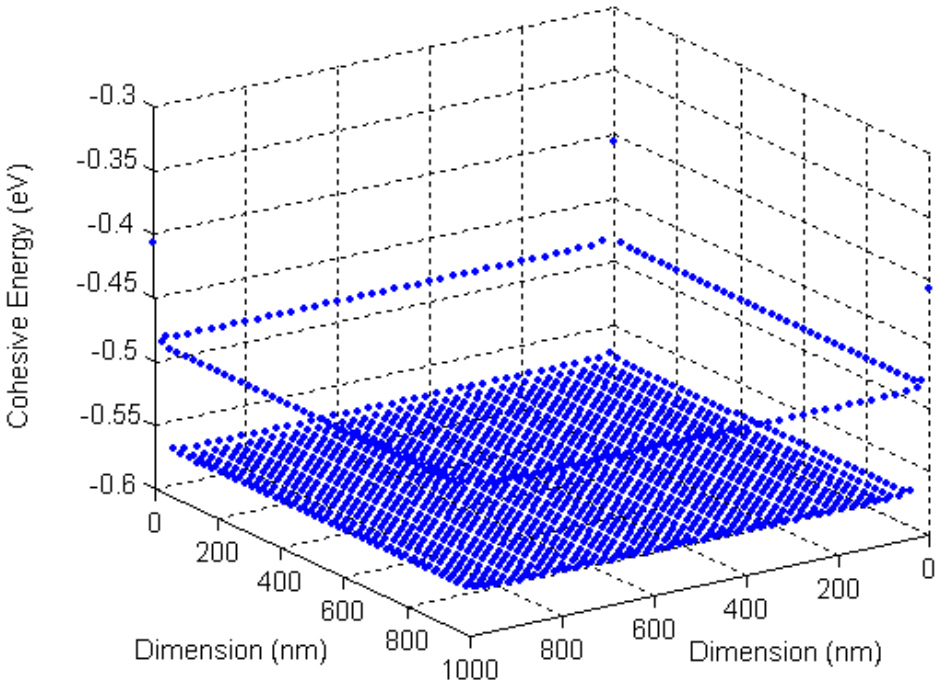

(a)

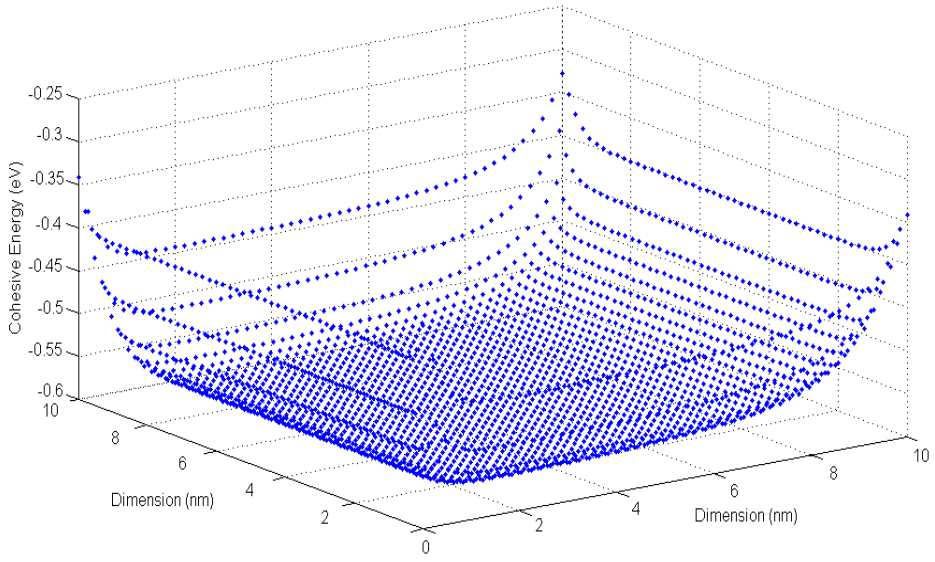

(b)

Figure 4.7 Illustration of cohesive energy per unit length (1 Å) of MWCNT (diameter of 5 nm) in the MWCNT/GONP system for (a) the GONP with the dimension of sheet with dimension of 1 μm, and (b) the GONP sheet with dimension of 10 nm.

The cohesive energy per unit length in the MWCNT/GONP systems with the GONP sheet with dimension of 1μm and 10nm are shown in Fig. 4.7. It can be found that the cohesive energy is the largest in the central area of the GONP sheet, and deceases as the MWCNT approaches the edges of GONP sheet. From this result, it can be predicted that MWCNTs tend to adhere to the central area of GONP sheet. The cohesive energy can be affected by the dimension of MWCNTs, and the cohesive energies for MWCNTs with various diameters are listed in Tab. 4.2. The results indicated that the cohesive energy increases with increasing the diameter of MWCNTs.

Table 4.2 Cohesive energies (eV/ Å) in MWCNT/GONP films.

Diameter of CNTs (nm)	Cohesive energy (eV/Å)
1	-0.3524
2	-0.4305
3	-0.4982
4	-0.5528
5	-0.5868

4.3.3 DC and Frequency-Independent AC Conductivities of MWCNT/GONP Films

The measurements of DC and AC conductivities were carried out for all MWCNT/GONP samples. The DC conductivity was calculated from the slope of the I-V curve. The DC conductivity (σ_{DC}) and frequency independent AC conductivity (σ_0) as a function of MWCNT mass fraction are presented in Fig.4.8. Agreement can be observed between the frequency-independent AC and DC conductivities, and both of them can be fitted by the same curve. The electrical conductivity of

MWCNT/GONP hybrid films can be classified into three categories, low-mass fraction ($p < 30wt\%$), mid-range ($p \sim 30wt\%$), and high-mass fraction ($p > 30wt\%$). As mass fraction increases in the low-mass fraction range, the electrical conductivity only increases slightly. When the mass fraction approaches and over the percolation threshold, the conductivity rapidly increases up to 10^{-2} S/m. The experimental data are in good agreement with the scaling law (see Fig. 4.8(b)). The percolation threshold, p_c, was found to be 29.6wt% and the exponent, t, to be 1.58. It can be noticed that p_c is much higher (nearly four orders) than CNT/polymer composites. This high percolation threshold may be partly due to the layered microstructure in the film, which can be seen from Fig4.4. Within this structure, MWCNTs are constrained to lie among GONP sheets, and the intersections between MWCNTs are reduced significantly by the insertion of GONP as a barrier in the percolation network of MWCNTs. However, this is not the only explanation for the difference of four orders of magnitude in p_c.

During the formation of the MWCNT/GONP film, MWCNTs were attracted on the surface of GONP sheets due to van der Waals interactions, and tended to locate in the central area of GONP sheets. This distribution of MWCNTs might be partly due to the low potential in the central area of GONP sheets as discussed in section 4.3.2. The intrinic un-flat edges in graphene sheets may also result in this central distribution of MWCNTs. The intrinsic ripples and warping in freestanding graphene sheets introduced by stresses located at the edge of graphene sheets have been reported by Shenoy et al. [18]. Fold edges can also be induced during the formation, and can be observed from the TEM images shown in Fig. 4.3. These act as an atomic potential barrier, repelling the MWCNTs and causing them to be distributed in the flat central area of GONP sheets. In the case of low-mass fraction, most of MWCNTs were distributed in the central area of GO sheets, and, consequently, the MWCNTs were wrapped by GONP sheets. The MWCNTs also tended to aggregate due to the attraction potential between them, and the percolation network was not formed

between the MWCNT 'aggregations'. As the mass fraction was increased to p_c, the MWCNT aggregators became larger in size than GONP sheets. The interactions between CNT aggregators on the GONP sheets compensated the stress at the edges of GONP sheets, consequently, the amplitude of the ripples was reduced. As a result, the atomic potential barrier was reduced. The interaction energy between MWCNTs was enhanced as mass faction was increased. This increased interaction energy enabled MWCNTs to overcome the atomic barriers. As the mass fraction increases over p_c, the percolation network between 'aggregation' starts to form, and, consequently, the conductivity of MWCNT/GONP hybrid materials will rapidly increase.

From the experimental results, the conductivity for the pure MWCNT film could be estimated to be 1S/m using the scaling law. This is six orders of magnitude lower than that of a single MWCNT [19]. This discrepancy is caused by the contact potential barrier to the electronic transport between MWCNTs, which results in a lower effective conductivity.

It can be seen from Fig. 4.8 (a) that, in the case of the low-mass fraction, the AC conductivity (σ_{AC}) was approximately one order of magnitude higher than the DC conductivity (σ_{DC}). However, as the mass fraction was above p_c, σ_{AC} was close to σ_{DC}. When a DC electrical field is applied on the MWCNT/GONP film, the charge carriers tunnel through the film, and the major constraint to σ_{DC} is the activation energies [20]. For AC conduction, the charge carriers scan a distance under the perturbing wave, and the limitation on σ_{AC} is the highest barrier in the scanning distance [20]. With low-mass fractions and the mass fraction is just above p_c, the AC charge carriers can only travel through small parts of the percolation networks, and do not need to overcome the highest barrier, whereas the DC charge carriers must overcome such barriers in order to transport through the entire network. As a result, $\sigma_{DC} < \sigma_{AC}$ .In the case of $p > p_c$, a percolating network is formed and the number of pathways for electron transport increases with increasing mass fraction. Electrons

mainly transport through the percolating network. It follows that σ_{DC} is expected to be close to σ_{AC} . It can be seen from Fig. 4.8(a) that σ_{DC} of the MWCNT/GONP film with mass fraction above 50wt% approached to σ_{AC}.

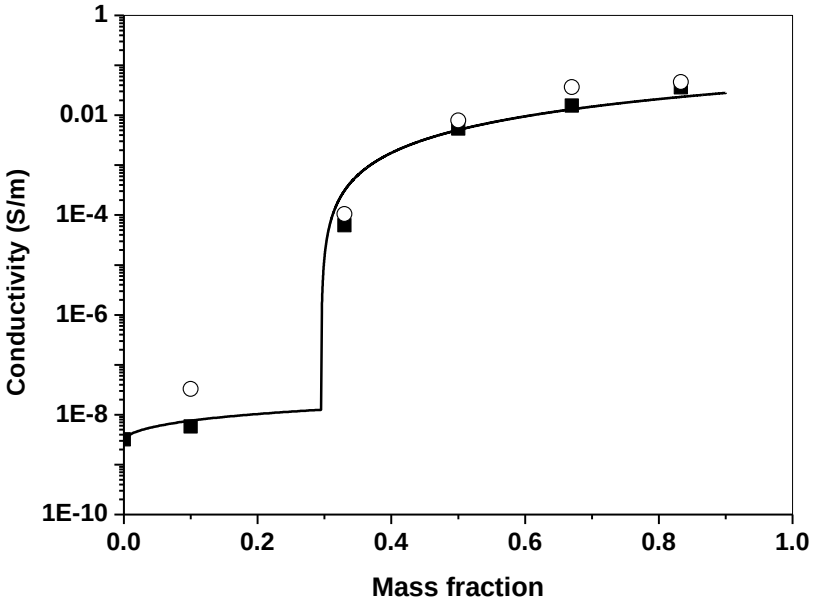

(a)

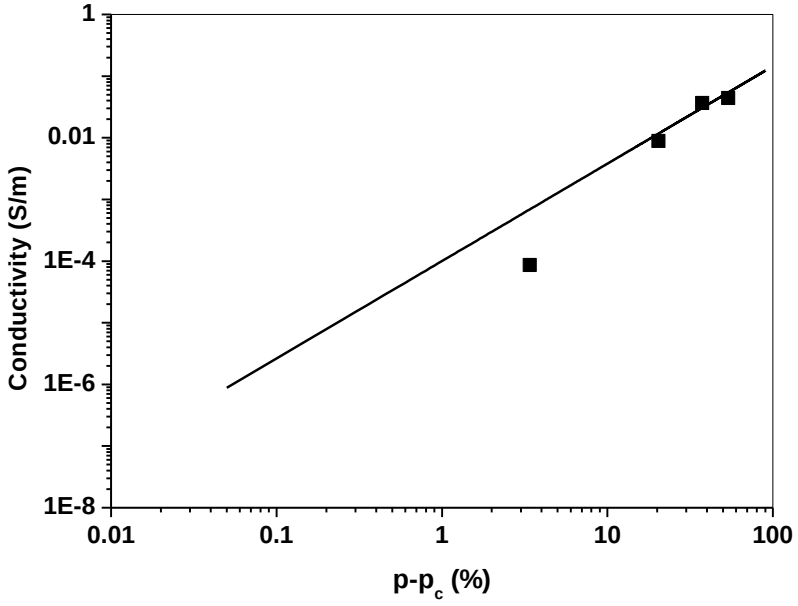

(b)

Figure 4.8 (a) Illustration of DC and AC conductivities for the MWCNT/GO NP film vs MWCNT mass fraction. (b) Logarithmic plot of conductivity versus $p - p_c$. The

solid line is a fit of DC conductivity to the percolation scaling law with $p_c = 29.6\%$ and $t = 1.58$

4.3.4 AC Behaviour of MWCNT/GONP Films

The AC conductivity of MWCNT/GONP films with various MWCNT mass fractions is presented in Fig.4.9. After the relatively small frequency independent plateau, the conductivity grows with increasing frequency, and eventually becomes stable beyond the peak at a certain frequency. In order to prove that the frequency-dependent behvaiour is not induced by the measurement, a SWCNT film was also measured. A frequency independent behaviour can be observed. For the GONP film, it always exhibited a frequency-dependent behaviour (see Fig. 4.9).

As discussed in chapter 3, the equivalent circuit has widely been employed to explain the electrical properties of various conductive composites [21]. In order to understand the frequency-dependent behaviour, an equivalent circuit model was also employed in this research. The proposed circuit model for MWCNT/GONP films is presented in Fig. 4.10. Here, the contact resistance and capacitance between electrodes and samples were neglected, and the Gaussian thermal noise was also ignored due to its zero average over a long period of time. R_e represents the equivalent resistance that depends on the DC resistance of the sample, C_e is the equivalent capacitance that can be calculated from the slope of the frequency-dependent curves shown in Fig 4.9, and L_e is the equivalent inductance between MWCNTs [22]. A complex transfer function $H(j\omega)$ [23] was used to describe the frequency-response of the voltage between the inside pair of probes. The complex transfer function of the equivalent circuit was written as follows:

$$H(j\omega) = \frac{V(j\omega)}{I(j\omega)} = \frac{1}{\frac{1}{R_e} + j\omega C_e} + j\omega L_e = \frac{R_e + j\omega L_e - \omega^2 C_e R_e L_e}{1 + j\omega C_e R_e} \qquad (4.4)$$

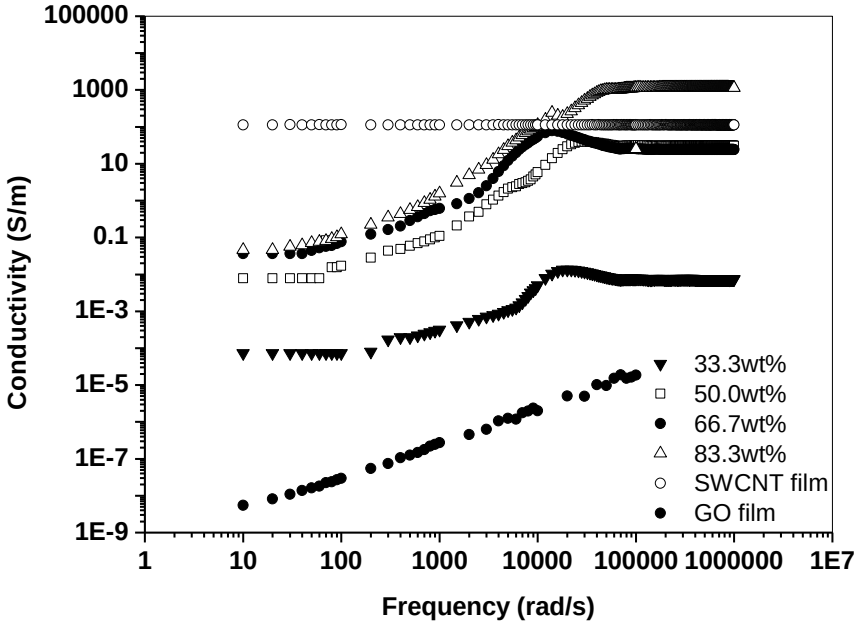

Figure 4.9 Illustration of frequency-dependent conductivity vs. MWCNT mass fraction. The tests were performed at 295K.

The effect of the inductance between MWCNTs on the conductivity is very small in the frequency range from 0 to 10^6rad/s used in the present measurement. Therefore, we only investigated the resistive and capacitive behaviour of the samples. The value of R_e and C_e were calculated from experimental results, and were listed in Tab. 4.3. It can be found that the value of C_e increases with increasing MWCNT mass fraction. This increase is due to the enlargement of the area of MWCNT 'electrodes'. In the MWCNT/GONP hybrid films, the layered MWCNTs were separated by insulating GONP sheets, and such microstructure could be seen as a nano-capacitor. These conducting MWCNT layers can be seen as 'plates of capacitors', and the GONP sheets can be treated as 'insulting separation layers'. Generally, the capacitance of a capacitor is positively proportional to the area of the electrodes. As the mass fraction of MWCNTs is increased, the area of MWCNT 'plates' will increase. As a result, the capacitance induced by the layered structure also increases. Therefore, the value of C_e is enhanced with increasing mass fraction. The value of C_e is also much higher than

that of other CNT based conductive composites [24, 25]. This high C_e could also be due to the layered micro-structure in MWCNT/GONP hybrid film.

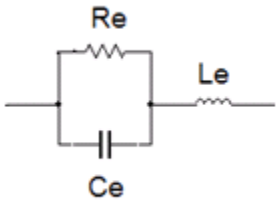

Figure 4.10 Schematic of proposed circuit model for the MWCNT/GONP films.

The critical frequency ω_0 was marked as the frequency at which the admittance reached 110% of the frequency-independent admittance. Fig. 4.11 shows ω_0 versus MWCNT mass fraction. In general, ω_0 for CNTs blending with insulating materials is scaled by the definition of correlation length [26], $\omega_c \propto (p - p_c)^{v/a}$, where v = 4/3 and a = 0.9 for a 2-D material. Therefore, for most CNT based conductive materials, ω_0 increases with increasing CNT mass fraction. Interestingly, one can clearly see that ω_0 in the MWCNT/GONP hybrid films decreases with increasing MWCNT mass fraction, and that ω_0 is also relatively low compared to other CNT-based conductive composites [25, 27]. This inverse trend could be due to the enhancement of capacitive behaviour by increasing MWCNT mass fraction. In the case of films with mid-range mass fractions, the MWCNT conducting area rapidly increases with increasing MWCNT mass fraction due to the formation of percolation network. As a result, C_e is strongly enhanced. In the case of hybrid films with high-mass fraction, the conducting area is larger than that of GONP sheets, and percolation networks are formed. The addition of more MWCNTs does not significantly increase the effective area of the 'plate of capacitor', but only increases the thickness of the conducting area and the connecting points between the 'capacitors'. Consequently, C_e is slightly enhanced and ω_0 decreases gently at the high-mass fraction. This inverse trend also can be demonstrated by using the

equivalent circuit model. ω_0 can be obtained as follows.

$$|H(j\omega)| - R_e = 0.1R_e$$

Then,

$$\omega_0 = \sqrt{\frac{0.21}{C_e^2 R_e^2}} \tag{4.5}$$

As shown in Tab. 4.3, the value of $C_e^2 R_e^2$ increases with increasing MWCNT mass fraction. Therefore, ω_0 decreases with mass fraction due to the rapid increase of C_e.

Table 4.3 Values of R_e and C_e for all the MWCNT/GONP hybrid films.

Mass fraction	R_e	C_e	$C_e^2 R_e^2$ ($\Omega^2 F^2$)
33.3%	$1.351 \times 10^4 \Omega$	4.337±0.42 μF	$(3.427 \pm 0.32) \times 10^{-3}$
50%	128	9.594±0.47 mF	1.5±0.04
66.7%	29	45.523±2.33mF	1.7±0.04
83.3%	22	70.912±3.25mF	2.4±0.05

From Fig. 4.9, it can be observed that the AC conductivity of the MWCNT/GONP hybrid films exhibits a frequency-independent behaviour again, as applied frequency is high enough. This might be due to the loss of dielectric properties for GONP insulating layer. The voltage per unit time on the GONP sheet increases with increasing applied frequency. Electrical breakdown occurs as the voltage per unit time on the GONP sheet is over the dielectric strength of the GONP sheet.

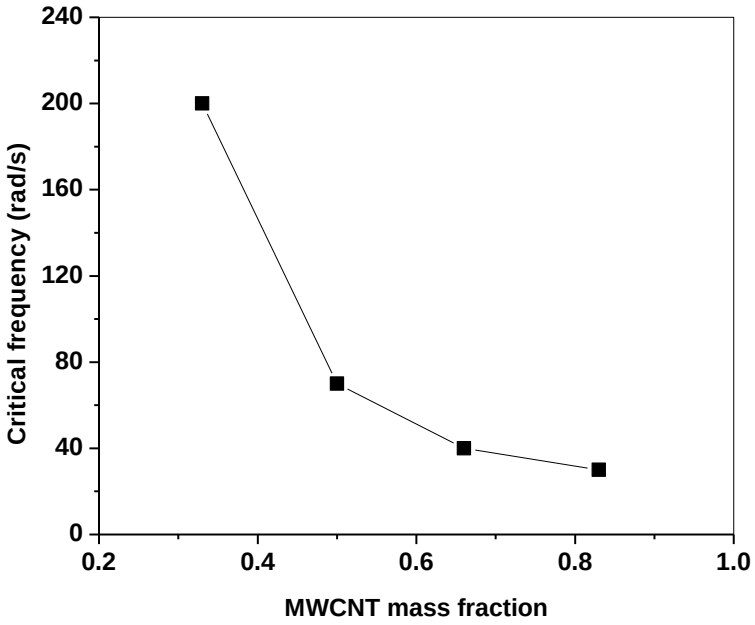

Figure 4.11 Illustration of the critical frequency vs. MWCNT mass fraction.

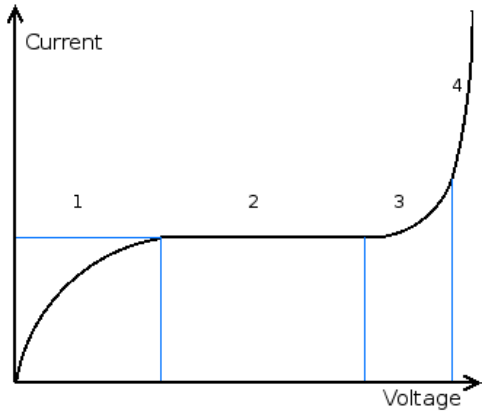

Figure 4.12 Illustration of I-V curve before breakdown [28].

Table 4.4 Values of loss frequency and saturated frequency.

Mass fraction	Loss frequency (rad/s)	Saturated frequency (rad/s)
33.3 wt%	6500	20000
50 wt%	3500	26000
66.7 wt%	1100	16000
83.3 wt%	-	18000

Before breakdown, the dielectric materials exhibit a non-linear voltage-current behaviour, which is presented in Fig. 4.12. In region 1, as applied voltage increases, the additional current can be induced by free ions that can be accelerated by the electrical field, and the electrical conductivity of the insulating material also increases [28]. Then, the current will be saturated after the applied voltage increasing to a certain level of voltage. In region 3, the current rapidly increases with applied voltages due to the ion avalanche, which can be understood by the Townsend discharge mechanism [28]. Such behaviour also can be observed from the present experimental results (shown in Fig. 4.13). Here, the frequency, at which additional current is induced and the insulating properties of GONP sheets start to decease, is concerned with loss frequency, and the frequency of the peak is called saturated frequency. These frequencies are listed in Tab. 4.4. It can be found that the loss frequency reduces with increasing mass fraction. Generally, the dielectric strength decreases with increasing the dimension of samples, because more defects are contained in the larger size of samples. As mass fraction increases, the area of MWCNT ‘electrode’ increases, and the area of GONP sheet contacted with ‘electrode’ also increases. Therefore, the loss frequency decreases with increasing MWCNT mass fraction due the increase of defects in the GONP sheets.

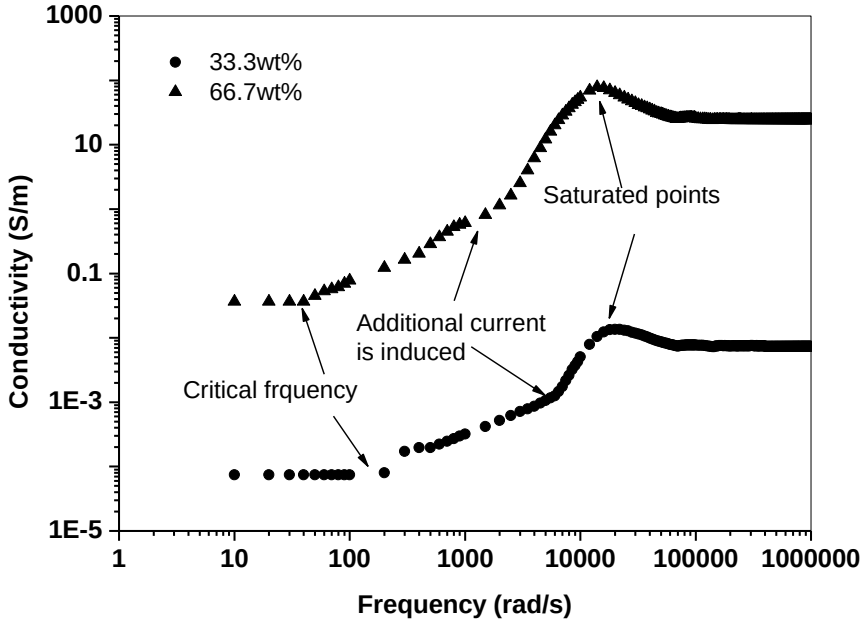

Figure 4.13 Illustration of frequency-dependent conductivity vs. MWCNT mass fraction.

4.3.5 Leaky Capacitive Behaviour in MWCNT/GONP Hybrid Films

As discussed in section 4.3.3, the MWCNT/GONP film exhibits a strong capacitive behaviour, and also possesses relatively high electrical conductivity. Therefore, it is called as leaky capacitive behaviour. Many 'leaky' capacitors have been manufactured for the enhancement of the capacity, such as supercapacitors [29], which possess extremely high capacitancs and also have relative high electrical conductivity. In this section, we will investigate the specific capacitance, leakage current and power factor of the MWCNT/GONP hybrid films.

The capacitance of MWCNT/GONP hybrid film was measured by using the voltmeter-ammeter-wattmeter test-circuit presented in Fig. 4.1. The formula stated below permit computations of the capacitance, and power factors [30],

$$C_x = \frac{I \times 10^6}{V \times 2 \cdot \pi \cdot f} \tag{4.6}$$

$$PF\% = \frac{W \times 100}{I \times V} \tag{4.7}$$

where I and V are the readings from ammeter and voltmeter, W is the reading from wattmeter, f is the frequency of AC source, PF% is power factor and C_x is capacitance of the tested sample in mF's. Fig. 4.14 shows the specific capacitance of MWCNT/GONP films as a function of MWCNT mass fraction measured under various voltages (10mV, 50mV, and 100mV) between the probes. As MWCNT mass fraction increases in the low mass fraction range, the capacitance of the film only slightly increases with mass fraction. When the mass fraction approaches and over the percolation threshold, capacitance of the films rapidly increases from 10^{-9} to 10^{-6} F with the most increase happening in the range between 30wt% to 50wt%. After mass fraction over 50wt%, the capacitance become gently rising with mass fraction again. This capacitive behaviour can be understood by using equivalent circuit model and the notion of electrolytic capacitor as follows.

As discussed in section 4.3.3, in low mass fraction range, the percolation network between MWCNT 'aggregations' is not formed. Thus, the 'nano-capacitors' constructed by MWCNT-GONP-MWCNT layered structure are isolated from each other, and electrons travel though the film mainly by tunneling conduction. The capacitance of sample is mainly caused by the 'nano-capacitors' near the electrodes. Therefore, the capacitance of the film is relatively low.

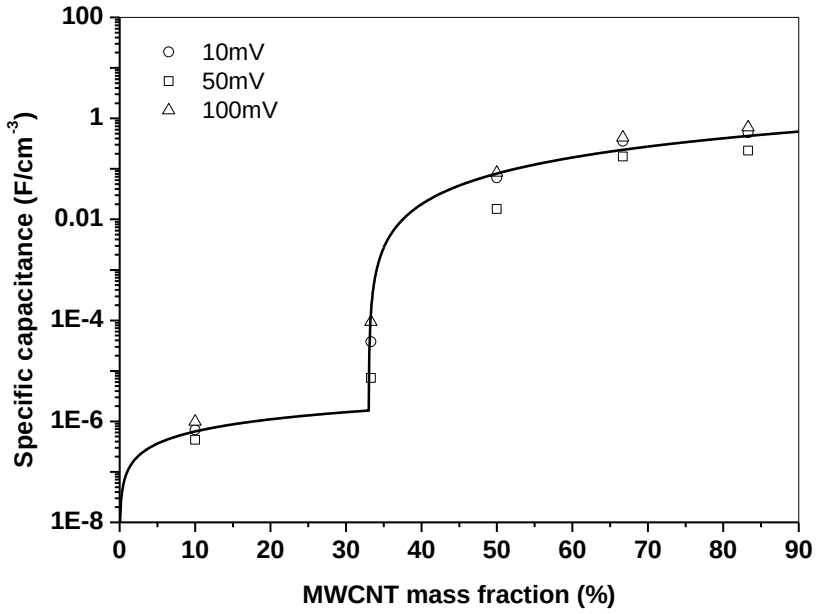

(a)

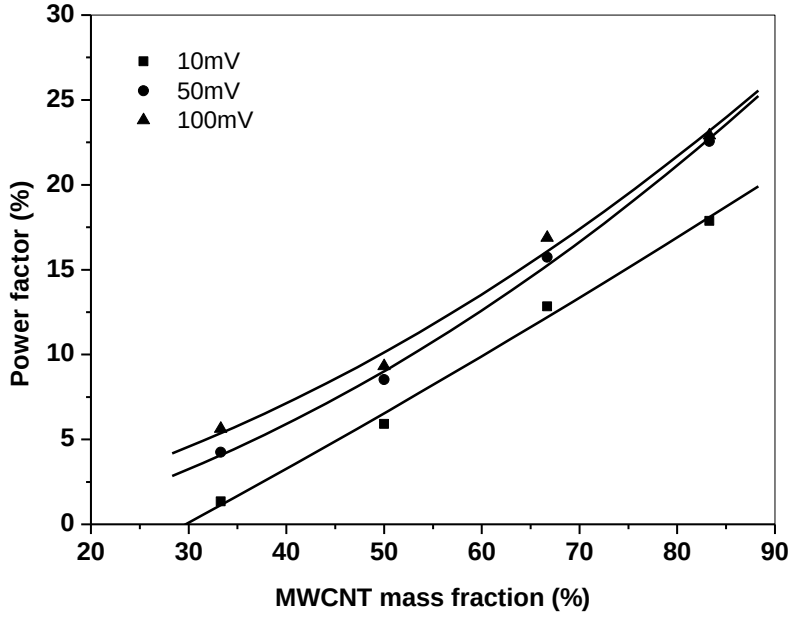

(b)

Figure. 4.14 (a) Illustration of specific capacitance for the sample as a function of various mass fractions of MWCNTs, which were measured under voltages of 10mV, 50mV and 100mV between probes. (b) Curve of the power factor versus MWCNT mass fraction. The power factors were measured with various voltages of 10 mV,

50mV, and 100mV.

While the mass fraction over p_c, the percolation network between 'aggregation' starts to form, and electrons can transport though the continuous pathway between the electrodes. As discussed in chapter 3, the CNT percolation network can be analyzed by the equivalent circuit model, in which the percolation network of MWCNTs can be treated as a resistor network. The value of resistors relates to the contact resistance between the MWCNTs. In the region of MWCNT 'electrodes', the MWCNTs strongly entangle with each other. As a result, most of resistors in the equivalent circuit are connected in parallel. Thus, the resistance of the network for MWCNT 'aggregation' is low. The equivalent resistance for the connection of the two MWCNT 'electrodes' separated by the GONP sheets may be much higher than that of 'electrodes' because of less MWCNTs contained in the pathways between the 'electrodes' and less interactions between these MWCNTs. In the equivalent circuit, the voltage difference between the two MWCNTs 'electrodes' separated by the GONP sheet is induced by that high equivalent resistance connected between these two 'electrodes'. In the present work, the partly modified MWCNTs are employed to produce MWCNT/GONP films. As a result, the potential difference between the electrodes is due to the high contact resistance and high resistance of modified MWCNT itself [31].

Here, as the mass fraction is above p_c, the MWCNT/GONP hybrid film can be considered as an 'electrolytic capacitor', in which MWCNTs play the both roles of electrolyte and in practice electrodes, and GONP sheets act as the dielectric separation. The equivalent resistance between MWCNT 'electrodes' acts as 'the resistance of the dielectric film' for electrolytic capacitors. As the percolation network is formed between the MWCNT 'electrodes', the area of 'electrode' rapidly increases by connecting the isolated 'plates' together. Consequently, in the mid-range mass fraction,

the capacitance of MWCNT/GONP films strongly increases with increasing the mass fraction due to the positive proportion of capacitance to the area of 'electrodes'. In high-mass fraction range, the percolation network is completely formed, the 'electrodes' are fully connected with each other, and the area of 'electrode' becomes, therefore, stable with increasing MWCNT mass fraction. Consequently, the curve representing the range of high MWCNT mass fraction exhibits as a plateau.

Fig. 4.14 (b) presents the power factor as a function of MWCNT mass fraction measured with various testing voltages. Similar to electrolytic capacitors, the MWCNT/GONP film with mass fraction above p_c also possesses a relatively high power factor. The power factor of the MWCNT/GONP film is much higher than that of dielectric capacitors whose power factors normally below 1% [32]. This high power factor could be induced by the high leakage current of the films due to the transport of electrons through the percolation network. It can also be found that the power factor increases with increasing MWCNT mass fraction. This increase is due to the enhancement of electrical conductivity by increasing the mass faction.

From Fig. 4.14 (a) and (b), it also can be observed that the measured capacitance and power factor depend on testing voltages. Both of measured capacitance and power factor rise with increasing the testing voltage. This influence may partly due to the enhancement of the tunneling conducting. As reviewed in section 2.3.5, the nanotubes cannot really connect with each other, and the gap between them acts as a potential barrier to internanotube tunneling. It is likely that the electrical conduction in this system is limited by tunneling between nanotubes. With the higher applied voltages, electrons possess higher energy, and the effective area that electron can access is enlarged, which can be equivalent to say that the area of 'electrodes' increases. For this reason, the measurement, which is operated with higher testing voltages, will give a high capacitance for the same sample. Another reason is that depending on the testing voltage, the film will more or less warm up, and this local temperature

fluctuation can also affect the tunneling conduction, which can be described by the fluctuation induced tunneling model [33],

$$\sigma_{DC} \propto \exp[-T_1/(T+T_0)] \tag{4.8}$$

where T is the local temperature, $T_1 = wA\varepsilon^2/8\pi\kappa$, and $T_0 = 2T_1/\pi w\chi$ with $\chi = (2mV_0/h^2)^{1/2}$, k is the Boltzmans constant, m and e is the mass and charge of electron, respectively, V_0 is the barrier height, w is the width of the gap between nanotubes and A is the area of conducting regions. With the high voltage, the energy dissipated as tunneling through the nanojuction between nanotubes is high due to the high tunneling current. Consequently, the local temperature rises up more quickly than with lower testing voltages, which enhance the tunneling conducting. For this reason, tests, which are performed with higher voltages, will cause more leakage current, which is responsible for higher power factor.

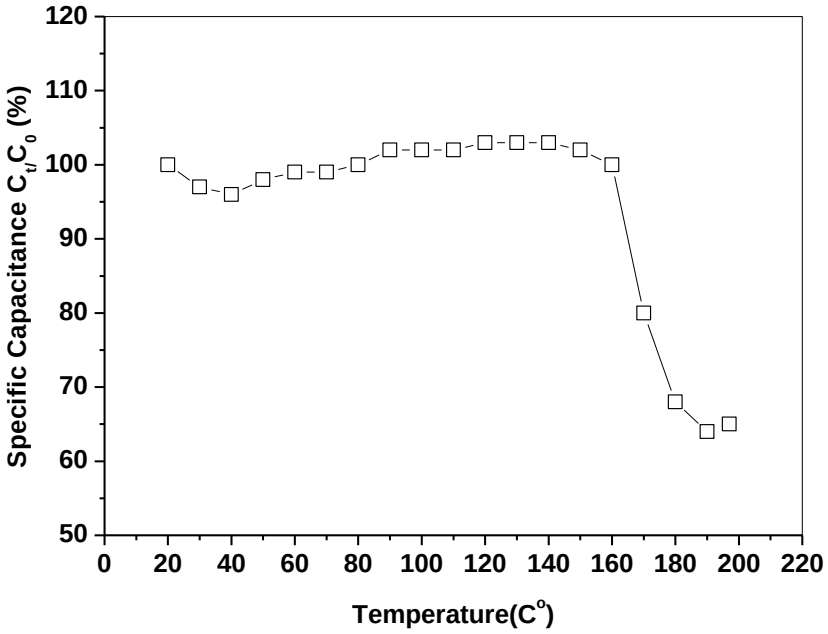

Figure 4.15 Variation of specific capacitance with temperature for MWCNT/GO film with mass fraction of 50% under testing voltage of 50mV. Samples were kept at the testing temperature for 30 min before measurement.

The effect of temperature on the capacitance may be of considerable importance for the application of capacitor. Fig.4.15 presents the specific capacitance against temperature. It can be observed that below 160℃, the capacitance gradually increases due to the expansion of the effective area of 'electrodes' and enhancement of tunneling conduction. As temperature increases over 160℃, the capacitance rapidly decreases with increasing temperature. This decrease may be due to the loss of dielectric properties of the GONP sheets.

GO is an insulator, whose conductivity depends on the oxygen content [34]. At the temperature above 160℃, the redox reactions occurs in GONP sheets, which have been reported by many groups [34]. Fig. 4.16 shows FTIR results for the GONP and thermal treated GO at 200℃ for 10 min. The peak at the position of 2356 cm^{-1}, which belongs to O-H group, decreases after heat treatment. It is different from the literature, in which decomposition of GO is known to be accompanied by a liberation of CO and CO_2 [34]. We believe that the intermediate decomposition product of GO was obtained in the present work. Fig.4.17 presents X-ray photoelectron spectroscopy (XPS) results of the GO and thermal treated GO, and also can confirm that redox reactions occurs in GO sheets. In the test, in order to remove the effect of sample charging, peak 1 was set at its standard position of 285eV. For the GO after heat treatment, the bonding energy of peak 2 and peak 3 slightly reduced by 0.3 eV and 0.15eV, and the areas of these peaks were also changed, which is presented in Tab. 4.5. This indicates that the number of C-O and C=O groups decreases after the heat treatment.

Initially, the number of sp^2 bonds in the GO is small, and these sp^2 bonds are separated by amorphous sp^3 bonds, which form high tunneling barriers between conducting sp^2 bonds. Therefore, the GO is insulating. From both FTIR and XPS results, it can be found that the oxygen content in the GO decreases after the heat

treatments. It can be reached that the number of sp^3 bonds decreases during the heat treatments, and the number of sp^2 phases increases. As the sp^2 phases start to connect between ordered rings, and switch from amorphous to 2-D percolation, the conductivity of GO increases sharply. This also is confirmed by the electrical measurement. Fig. 4.18 shows the resistivities for heat treated GO and MWCNT/GONP films at various temperatures. Both of GO and MWCNT/GONP films show a significant decrease in resistivity after the heat treatment above 160℃ due to the increase of π bonds in GO sheets.

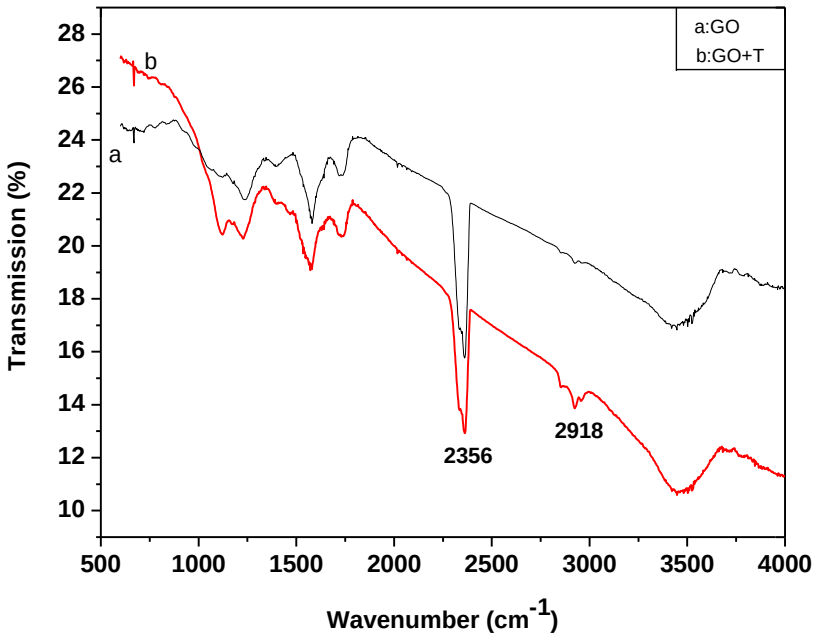

Figure 4.16 FTIR spectra of (a) GO; (b) heat treatment GO (GO+T).

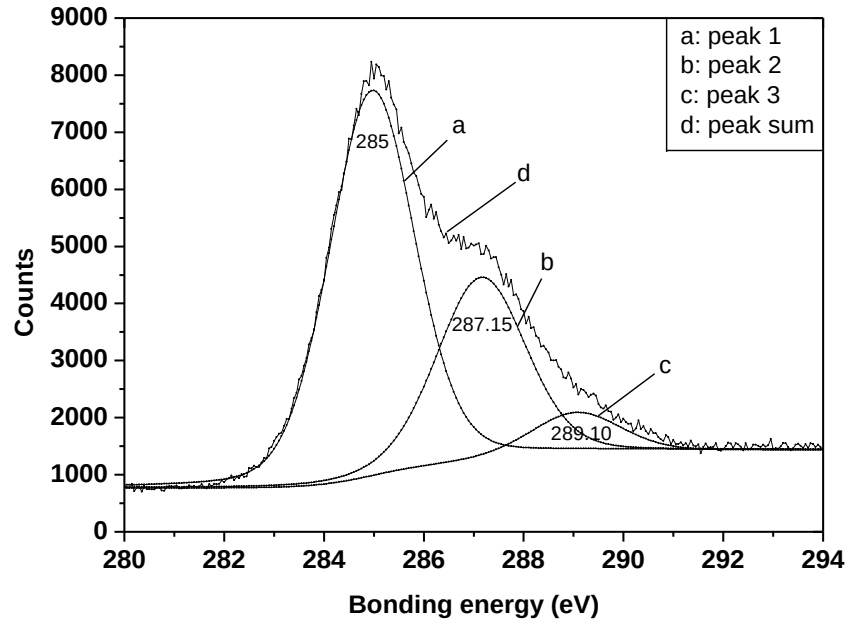

(a)

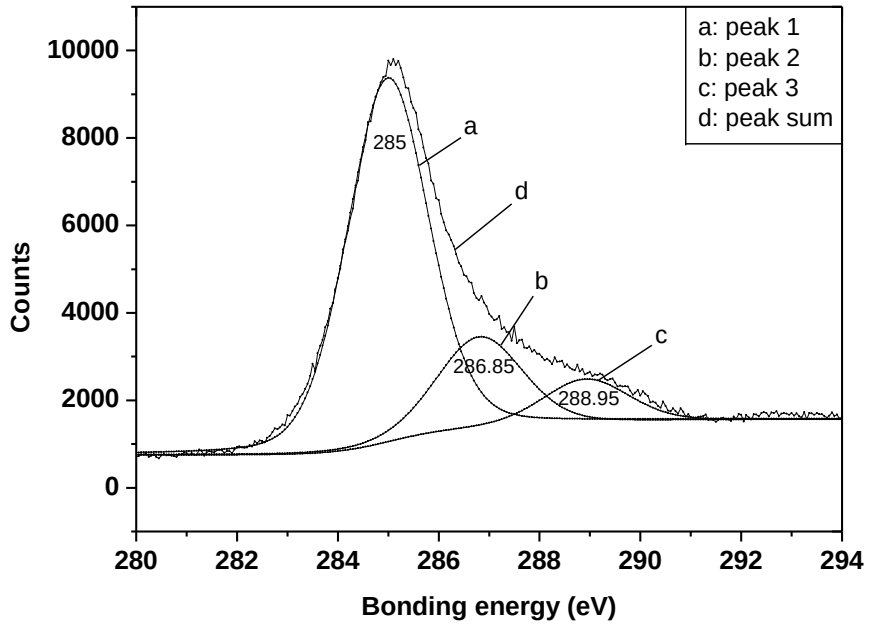

(b)

Figure 4.17, C1s spectra of (A) GO; (B) GO+T;

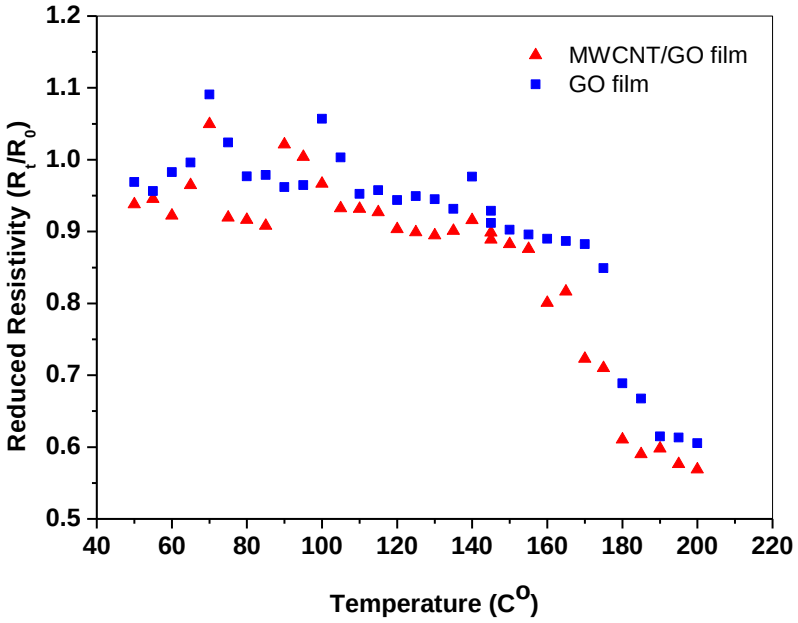

Figure.4.18 Illustration of the resistivity of heat treated GO film and the MWCNT/GONP film with the mass fraction of 50% at various temperature for 10 min. The test was performed with 50 mV using two termination method.

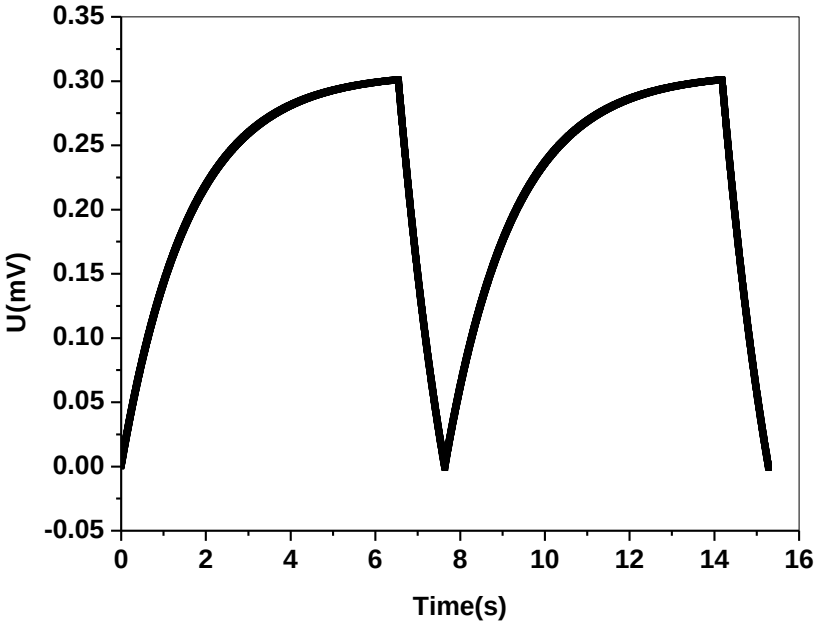

Figure 4.19 Illustration of charge-discharge galvanostatic cycling at 3×10^{-6}A, and 20℃ for the MWCNT/GONP film with MWCNT mass fraction of 50%.

Table 4.5 Position (bonding energy) and area for each peak*.

Sample	Parameters	Peak 1	Peak 2	Peak 3
(A) GO	Position (eV)	285	287.15	289.1
	Area	15899	7819	1735
(B) GO+T	Position (eV)	285	286.85	288.95
	Area	18460	4863	2331

* The position of peak 1 is consistent with C-C or C-H bonds while the position of peak 2 is consistent with C-O or C-N bonds and the position of area 3 is consistent with C=O.

Fig. 4.19 shows the galvanostatic charge and discharge curves of the sample with MWCNT mass fraction of 50%. As the film was charged, at first, the voltage of sample rised sharply to 0.18-0.2V, but the energy store in the sample at this step was small. Then, the increasing speed of voltage slowed down from 0.2V to 0.3V, and most energy was stored at this step. As the hybrid film was discharged, the voltage was rapid drop from 0.3V to 0V, which indicates the self-discharge occured in the film. The result is different from the typical electrochemical capacitors, which means no electrochemical reaction occurs as charged. The energy density of the film with MWCNT mass fraction of 50% was found to be 0.09Wh/m^{-3}.

4.4 Conclusions

Both of DC and AC conductivities of the MWCNT/GONP hybrid films were measured for selected MWCNT mass fractions of 10%, 33.3%, 50%, 66.7%, and 83.3%. As the mass fraction increases in the low mass fraction range, the DC conductivity of the film only slightly increased. When the mass fraction approached and over the percolation threshold, the DC conductivity followed the percolation scaling law. The DC conductivity rapidly increased from approximately 10^{-9}S/m of the host graphene oxide to over 10^{-1}S/m with the most increase happening in the range between 30wt% to 50wt%. The relatively high percolation threshold of

MWCNT/GONP films may be caused by the low potential energy in the central area of GONP sheet and intrinsic ripples and warping in the freestanding graphene sheets. The AC conductivity (σ_{AC}) is approximately 1 order of magnitude higher than DC conductivity (σ_{DC}) in the low mass fraction range and the mass fraction is just over p_c. For the mass fraction above the percolation threshold, σ_{AC} was close to σ_{DC}.

After the relatively small frequency independent plateau, the AC conductivity increased with increasing frequency, and the AC conductivity eventually became stable. The critical frequencies of the MWCNT/GONP hybrid films were much lower than that of other types MWCNT based composites. The equivalent circuit was employed to understand the frequency dependent conductivity. The equivalent capacitance of the MWCNT/GONP film increased with increasing the mass fraction, and decreased with increasing the applied frequency due to the loss of insulating properties of GONP sheets.

The MWCNT/GONP film showed relatively high specific capacitance ($0.192 F/cm^{-3}$ with the mass fraction of 83.3%) and power factor compared to conventional dielectric capacitors. In low MWCNT mass fraction range, the capacitance of the film only slightly increased with mass fraction. As the mass fraction approached and over the percolation threshold, capacitance of samples rapidly increases from 10^{-9} to 10^{-6} F. Both of measured capacitance and power factor can be enhanced by increasing the test voltages. Above $160C^{o}$, the redox reactions occurred in the GO sheets, and the capacitance of the MWCNT/GONP film rapidly decreases due to the loss of insulating property of GONP sheets.

References

1. O.C. Jeong and S. Konishi, Sens. Actuators A143, 97 (2008).

2. C.M. Niu, E.K. Sichel, R. Hocth and D. Moy, Appl. Phys. Lett. 70, 1480 (1997).
3. D.D.L. Chung, Carbon 39, 279, (2001).
4. R. Könenkamp, K. Boedecker, M. C. Lux-Steiner, M. Poschenrieder, F. Zenia, C. Levy-Clement, and S. Wagner, Appl. Phys. Lett. 77, 2575 (2000).
5. Y. Yamada and D.D.L Chung, Carbon 46, 1798 (2008).
6. Z. Ounaies, C. Park, K. E. Wise, E. J. Siochi, J. S. Harrison, Composites Scien. Tech. 63, 1637 (2003).
7. T. V. Sreekumar, T. Liu and S. Kumar, Chem. Mater. 15, 175 (2003).
8. L. Song, L. Ci, L. Lv, Z. Zhou, X. Yan, D. Liu, H. Yuan, Y. Gao, J. Wang, L. Liu, X. Zhao, Z. Zhang, X. Dou, W. Zhou, G. Wang, C. Wang and S. Xie, Adv. Mater. 16, 1529 (2004).
9. Y. H. Li, M. Zhao, M. Roe, D. Furniss, Y. Q. Zhu, S. R. P. Silva, J. Q. Wei, D. H. Wu and C. H. P. Poa, Small 2, 1026 (2007).
10. Z. Sun, Y.J. Li, G.Y. Chen, S.P. Lau, B.K. Tay, J.S. Chen, L.K. Cheah, Surface Rev. Lett. 8, 505 (2001).
11. D. Cai, M. Song and C. Xu, Adv. Mater. 20, 1706 (2008).
12. P. Liu, K. Gong, P. Xiao and M. Xiao, J. Mater. Chem. 10, 933 (2000).
13. W. A. deHeer, W. S. Bacsa, A. Chatelain, T. Gerfin, R. Humphrey-Baker, L. Forro, and D. Ugatre, Science 268, 845 (1995).
14. S. Stankovich, R. D. Piner, S. T. Nguyen, R. S. Ruoff, Carbon 44, 3342 (2006).
15. G. Ciccotti, D. Frenkel, and I. R. McDonald, Simulation of Liquids and Solids: Molecular Dynamics and Monte Carlo Methods in Statistical Mechanics, Amsterdam; New York; North-Holland, 1987.
16. K. Kniaz, and L. A. Lad, J. Phys. Chem. 25, 693 (2005).
17. L. A. Girifalco, M. Hodak, and R. S. Lee, Phys. Rev. B 62, 13104 (2000).
18. V. B. Shenoy, C. D. Reddy, A. Ramasubramaniam, Y. W. Zhang, Phys. Rev. Lett. 101, 245501 (2008).
19. H. Dai, E. W. Wong, and C. M. Lieber, Science 272, 523 (1996).
20. J. C. Dyre, J. Appl. Phys. 64, 2456 (1988).

21. S. Kirkpatrick, Rev. Mod. Phys. 45, 574 (1973).
22. J. J. Plombon, K. P. O'Brien, F. Gstrein, V. M. Dubin, Y. Jiao, Appl. Phys. Lett. 90, 063106 (2007).
23. A. Ramakalyan, Linear Circuit: Analysis and Synthesis, Oxford University Press, 2005.
24. L. Flandin, M. Verdier, B. Boutherin, Y. Brechet, and J. Y. Cavaille, J Polymer Science B, 37, 805 (1998).
25. B. E. Kilbride, J. N. Coleman, J. Fraysse, P. Fournet, M. Cadek, A. Drury, S. Hutzler, S. Roth, and W. J. Blau, J. Appl. Phys. 92, 4024 (2002).
26. D. Stauffer, A. Aharony, Introduction to Percolation Theory, Taylor and Francis, London, 1992.
27. D. S. Mclanlan, C. Chiteme, C. Park, K. E. Wise, S. E. Lowther, P. T. Lillehei, E. J. Siochi, and J. S. Harrison, J Polymer Scien. B 43, 3237 (2005).
28. N. E. Hill, Dielectric Properties and Molecular behaviour, Van Nostrand, 1969.
29. E. Frackwiak, K. Metenier, V. Bertagna and F. Beguin, Appl. Phys. Lett. 77, 2421 (2000).
30. A. M. Georgiev, The Electrolytic Capacitor, Crosby lockwood and son Ltd. London, 1945.
31. A. Javey, and J. Kong, Carbon Nanotube Electronics, Springer, 2009.
32. G. W. A. Dummer, Fixed capacitor, Sir Isaac Pitman&Sons Ltd. 1964.
33. P. Sheng, Phys. Rev. B 21, 2180 (1980).
34. T. P. Jeffrey, T, Belytschko, and C. S. George, J. Phys. Chem. C 111, 18099 (2007).

Chapter 5 Effect of Mechanical Deformation on Electrical Properties of SWCNT Films and Its Composites

5.1 Introduction

Unique electrical properties of CNTs have attracted enormous attention during past two decades [1-2]. As reviewed in chapter 2, significant progress and understanding have been made in this field, but many challenges still exist and limitations need to be overcome. In this chapter, the effect of mechanical deformation on the electrical properties (electrical conduction and thermoelectric power) of SWCNT based materials will be investigated.

Strain sensors are important in the science and engineering fields. Existing strain sensors offer excellent performance in terms of sensitivity and response time [3]. However, these sensors have to be connected to battery power source and signal acquisition equipment [3]. These limitations make existing strain senors impossible to be embedded into material level, and to monitor the moving structures. Recently, optical fiber was employed to develop a strain sensor, which can be embedded into material level [4]. However, the optical fiber based strain sensor is fragility and high cost, and expensive equipments are also required for acquiring strain information. Therefore, a new strain sensor is needed to overcome these limitations.

Smart materials fabricated using nanotechnology have the potential to improve the way for measuring motion in devices from nano-scale to macro-scale in size [5-7]. The CNT is the one of smart materials [7], which has received great interest due to their extraordinary electrical properties and potential applications. Due to their sensitive electronic structure as viewed in section 2.3.3, CNTs offer attractive alternatives for developing a new strain sensor [7]. In addition, integrating CNTs into polymers are currently interest in producing a strain senor [8]. As reviewed in section

2.5, many efforts have been made for developing novel strain sensors based on CNT films and CNT/polymer composites. However, these studies directly related the intrinsic sensitive band structure to bulky electrical properties of CNT mat or composites without considering the change of intertube barriers during deformation. As reviewed in section 2.3.5, the large contact resistance can be induced by the unavoidable gaps between CNTs, and plays a dominant role in the electrical conduction in disordered CNT systems. The variation of the intertube barrier regions can result in the change of contact resistance and the topology of the equivalent circuit of the CNTs systems. The deviation from the linear trend, which was observed in these studies, is also not clearly understood. In addition, both of electrical properties and sensing behaviours of CNT based films are also strongly dependent on the electrical types of CNTs [9, 10].

Thermoelectric power (TEP) of a material is concerned with the amplitude of an induced thermoelectric voltages responding to the temperature difference in the material. TEP always refers to the seebeck effect, Peltier effect and the Thomson effect [11], and is extremely sensitive to the change of electronic structure at the Fermi energy [12] in a material. TEP is employed to fabricate all heat engines that are used for converting thermal energy to electrical power. In recently, TEP is employed in cooling applications such as portable refrigerators, and electronic component coolers.

Materials fabricated using nanotechnology show the capability to enhance thermoelectric phenomena, which have attracted much attention recently due to their potential for thermoelectric applications. Among several possible smart materials, CNTs have received a great deal of interest from researchers. As reviewed in section 2.3.6, there have been a number of experimental efforts to measure TEP of the individual nanotube, CNT ropes and macroscopic CNT ‘mat’ [13-18]. The large value of TEP of semiconducting nanotubes was also observed, which is induced by the

Schottky barriers at SWCNT-electrode junction. TEP of crystalline ropes of SWCNTs was measured by Hone et al. [13]. They stated that TEP was large and holelike at relatively high temperature and reduced to zero as temperature approach to zero.

The modifications of TEP, which were resulted by intertube barrier regions and the change of Fermi level, were also investigated by many research groups. Small et al. [18] measured the TEP of individual SWCNT in mesoscopic scales. They reported that TEP can be modified by the gate electric field, and it was well correlated to the electrical conductance of SWCNTs according to the Mott formula. The extremely sensitive TEP to gas exposure history was explored by Bradley et al.[14]. They reported that the positive TEP of CNTs was induced by the exposure to air or oxygen, and TEP of SWCNT crossed zero and changed the sign as sample was degassed. Romero et al. [17] measured the TEP of SWCNT film in vaccum. Their results indicate that the total TEP of SWCNT film is negative in vaccum and the metallic nanotubes give a dominant contribution. TEP can also be affected by the barrier regions. Baxendal et al. [16] reported that the strongly positive TEP of randomly oriented CNT mat was induced by the intertube regions. In these studies, CNTs may be subjected to various mechanical deformations, which may correlate to the changes in the electronic structure of CNTs and intertube barriers regions, and a variation of TEP can be induced. However, the effect of mechanical deformation on the TEP of CNT based materials has not been explored yet.

This chapter was organized as follows. Section 5.2 presented the sample preparation and measurements. Section 5.3 investigated the strain sensing behaviours of the SWCNT films and SWCNT/PVA composites with consideration of contribution from intertube gaps. Section 5.4 explored the effect of mechanical deformations on TEP of SWCNT films with various thicknesses. Section 5.5 provided a conclusion of present work.

5.2 Experimenal

5.2.1 Preparation of Samples

Macroscopic SWCNT films were supplied by Li et al. [19] using chemical vapor deposition (CVD) method. A circular gas-flow stabilizer was introduced in the quartz reaction tube, which help the formation of a uniform and high quality film on the stainless-steel film collector situated downstream of the reaction tube. The thickness of SWCNT film can be controlled by adjusting the reaction time. The films deposited on the collector are technically free standing and can be easily manipulated. The average density of the film is $\approx 1.8 \pm 2.0 \mathrm{gcm}^{-3}$.

A 10 wt% SWCNT/PVA composite was selected. The SWCNT/PVA film was prepared as follows. 5% by weight PVA (Fisher Scientific Ltd), water solution (adding 5 g of PVA to 95 g distill water) was prepared with assistance of magnetic stirrer for 1h at 80℃. Purified SWCNTs (0.5g, Chengdu Institute of Organic Chemistry, Chinese Academy of Science) was dissolved in distill water (99.5g) by the assistance of strong ultrasonic treatment (300W) for 1h at room temperature. The PVA/water (5%) and SWCNTs/water (0.5%) dispersion was mixed by ultrasonic treatment for 30 min at room temperature. Then, the mixture was pour into a glass container, and put in the oven at 40℃ for one week to obtain dried SWCNT/PVA film with thickness estimated about 100μm.

The sensing films (SWCNT films with thickness of 450nm and 1900nm, and SWCNT/PVA film) were adhered onto a SiO_2 substrate by using high strength epoxy for perfect strain transfer, and the sample has dimensions of $10\mathrm{mm} \times 5\mathrm{mm}$, which is presented in Fig. 5.1. Then, the SiO_2 substrate with sensing film was adhered to an aluminum specimen ($50\mathrm{mm} \times 10\mathrm{mm} \times 0.5\mathrm{mm}$) by high strength epoxy to ensure that no slippages occurs between the specimen and SiO_2 substrate.

Figure 5.1 Images of SWCNT film on the SiO_2 substrate adhered to aluminum specimen.

5.2.2 Measurement of Electrical Conduction in Deformed SWCNT Based Materials

In the static measurement, the electrical resistance of all samples was measured by using the four-probe method. A constant current was input from across two outer probes, and the variation of the resistance was determined by monitoring the change of the voltage across inner probes. The voltage was monitored by a digital multimeter (DM25 Rapitset). The SWCNT films were tested using a 50 mA current, and the SWCNT/PVA film was examined using a 10 mA current. The proper contact between probes and surface of samples was ensured to keep the testing voltage stable. The load was held for few seconds until the stable voltage readings were observed. The displacement in the specimens was induced by the equipment presented in Fig.5.2.

Dynamic measurement was conducted by applying rectangular tensile-relaxed cycle loading pattern with various strain amplitudes (0.3% and 0.5%) and periods (10s and 20s), and loading rate is 3% s^{-1}. The electrical resistance of all samples was measured by two terminations methods. In order to reduce error, Wheatstone circuit was used as testing circuit presented in Fig. 5.3. The SWCNT films were tested using 1V driving

voltage, and SWCNT/PVA composites were examined using 5V driving voltage for Wheatstone bridge. The electrical contacts were made by silver paste, and two wires were placed over (soldering iron) the silver paste to form a two-probe measurement setup. The real-time voltage changes under cycle loading were sampled at 1Hz using a data acquisition (DAQ, NI USB-6211, National Instrument Company). All measurements were performed at room temperature. The temperature of all samples was also measured for evaluating the errors caused by the rise of temperature using a contact temperature sensor.

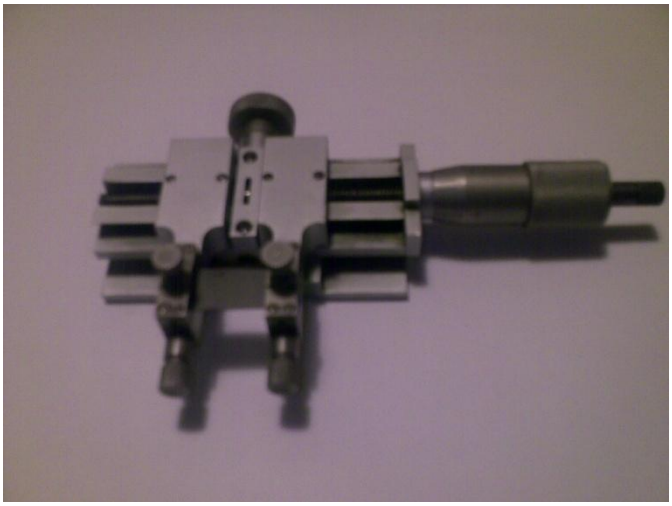

Figure 5.2 Images of the instrument for deformation.

One error source of the measurement is due to the joule heat generated by the testing current. As reviewed in section 2.5, the resistance in deformed CNT film exponentially decayed during sampling of resistance. Therefore, in order to minimize errors induced by joule heating, the test current should be as low as possible. However, the test current cannot be too low to achieve high quality signal to noise ratio (SNR). In order to reach the balance between the two factors, SWCNT films were tested with a 50 mA current, and the SWCNT/PVA film was examined with a 10 mA current. In order to reduce the error cause by the electrical heating, the testing time was also kept being as short as possible. The temperature of the samples versus testing time is presented in Fig. 5.4. From the figure, it can be found that the variation of local

temperature is relatively low at the testing current of 20 mA, and the errors caused by joule heating can be neglected.

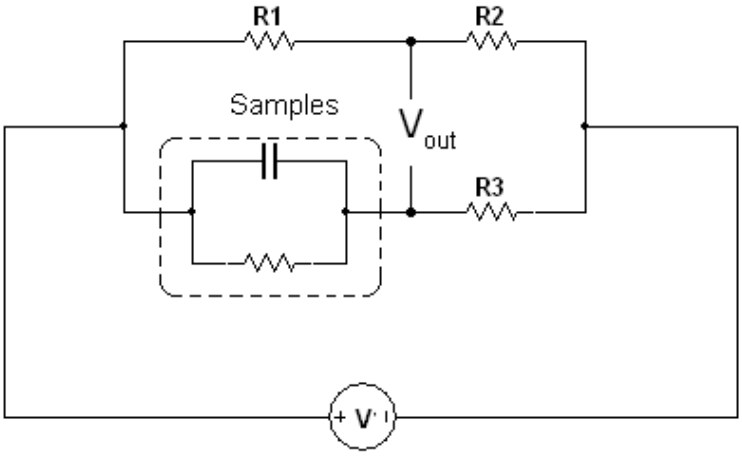

Figure 5.3 Schematic of testing circuit (Wheatstone bridge). Sample was modeled by connecting a resistor and a capacitor in parallel.

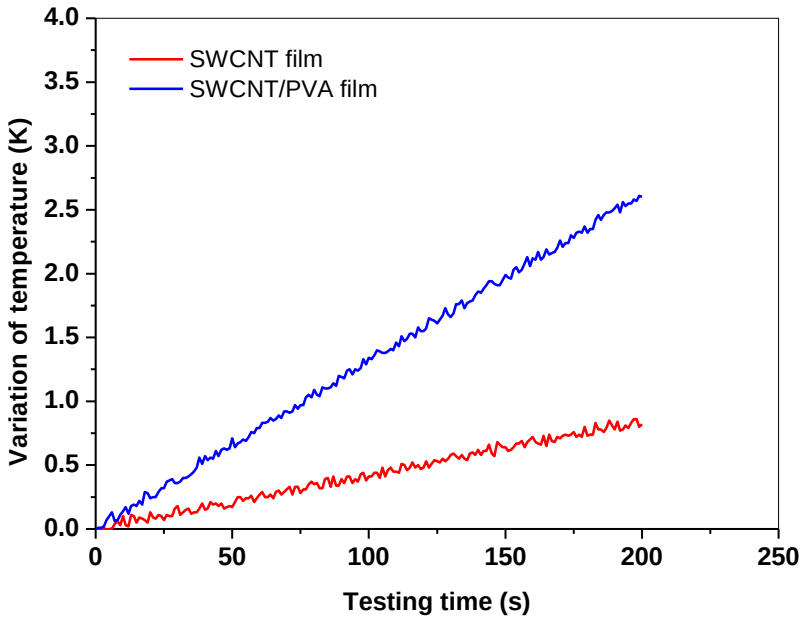

Figure 5.4 Variation of the temperature in samples versus testing time with testing current of 20 mA.

Another error source of the measurement is due to the resistance caused by the change of the distance between two probes. In this measurement, the tensile strains were of the order of 0.1%, and the changes in the dimensions of the film will be small. The variation of resistance induced by the change of the distance between two probes could be neglected.

Error can also be induced by contact resistance in the dynamic measurement. In order to reduce the contact resistance, the electrical contacts were made by silver paste. We also measured the resistance by multi-point and multi-measurement, and the data used here is the average result of four measurements.

5.2.3 Measurement of TEP in Deformed SWCNT Based Materials

The circuit for TEP measurement is presented in Fig. 5.5. Heating source, which is comprised of a ceramic-coated resistor, was placed at one end of the SWCNT film, which was employed as a heater to induce the temperature difference along the sample. The temperatures of both ends were monitored by sensing units, which consist of a contact temperature sensor. The temperature of the heater was adjusted by the control circuit. If the temperature of the sample is higher than the target one, the DAQ will send a signal to the voltage control switch to cut off the power of heating source. Otherwise, the DAQ will send a signal to switch on the power of the heater. In order to avoid the damage of epoxy adhesive strength due to high temperature, the sample temperature was varied over the range of $280\mathrm{K} < T < 380K$. In the testing circuit (shown in Fig.5.5), the current source was only used for the measurement of electrical conductivities. The conductivity of the sample was measured by the conventional four probes method (described in section 5.2.2) at a frequency of 100Hz and the electrical contact was made by silver paste. Two Cu leads were attached to the edges of the SWCNT film with silver paste for measuring TEP of the sample. The thermoelectric voltage across the sample was amplified and monitored by a voltmeter.

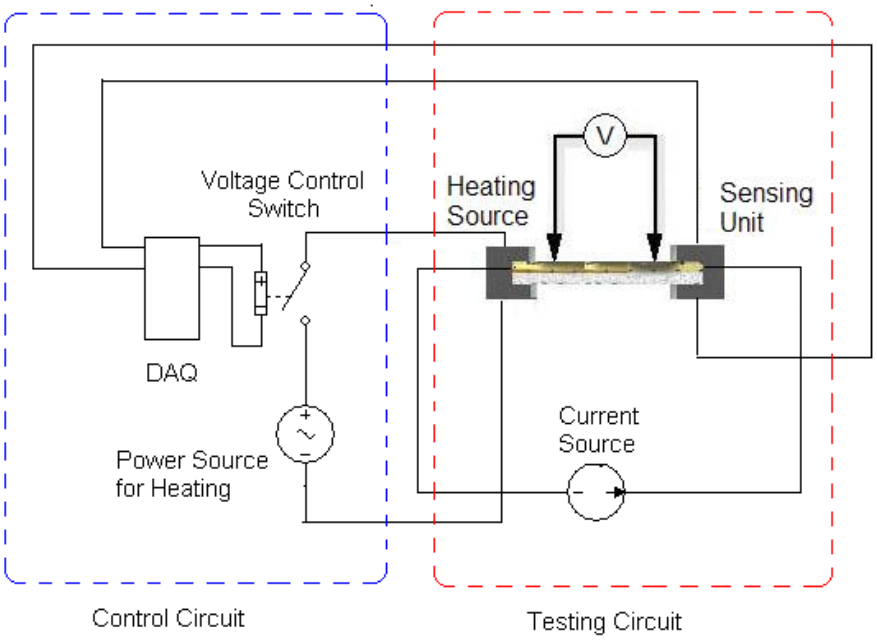

Figure 5.5 Schematic of circuit for TEP measurement. DAQ is the data acquisition equipment.

One error source of the measurement is caused by the heat transfer between two sensing units via radiation and air conduction. The radiation thermal conductance can be expressed as [20]

$$G_{rad} = \sigma(T_s + T_h)\left(T_s^2 + T_h^2\right)F_{h-s}A \quad (5.1)$$

where G_{rad} is the radiation thermal conductance, T_h is the temperature of the end with heating source, T_s is the temperature of the other end, F_{h-s} is the view factor between two adjacent senors, and A is the surface area of the sensors. It can be estimated that $F_{h-s}A \approx 1.3\text{cm}^2$, and G_{rad} is in the order of 10^{-6} W/K, which is much smaller than the thermal conductance of SWCNT films, and can be neglected.

Temperature fluctuation caused by air flow is another error source for the measurement. In order to avoid this, these samples were placed in a closed space, and

data used here were the average of five measurements. TEP were measured using different types of leads to avoid errors induced by the Cu leads used.

5.3 Effect of Deformation on Electrical Conduction in SWCNT Films and Its Composites

Fig. 5.6 (a) presents optical images of the SWCNT films with various thicknesses. The thickness of SWCNT film can be controlled by adjusting the reaction time. The SEM image of the surface of the film is presented in Fig. 5.6 (b), a SWCNT network can be observed in the form of mechanically entangled coils. The Raman spectrum of the SWCNT film (presented in Fig. 5.7) was evaluated by using Renishaw 2000 spectrometer with a laser excitation wavelength of 785 nm and spectrometer resolution of 4 cm^{-1}. The Raman peak at 235.91cm^{-1} suggested that SWCNTs with a diameter of 0.95nm were dominant in the film [19]. Two Raman bands appeared at 422.51cm^{-1} and 843.06cm^{-1} in the intermediate region, which indicated that the armchair-type SWCNTs were dominant in the film [19]. The low intensity ratio of D-band (1300.5cm^{-1}) to G-band (1590.3cm^{-1}) revealed that there was very little amorphous carbon in the film.

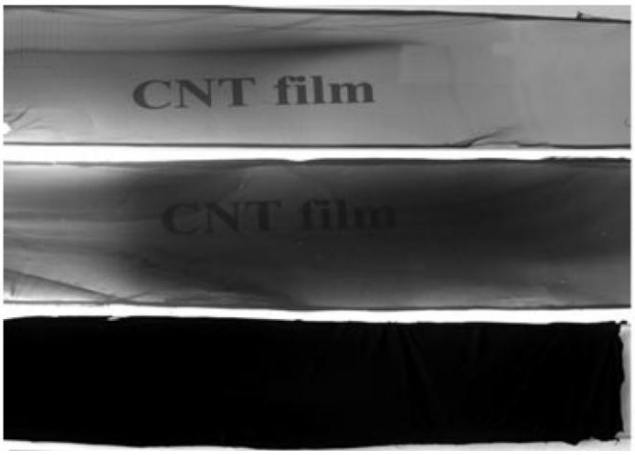

(a)

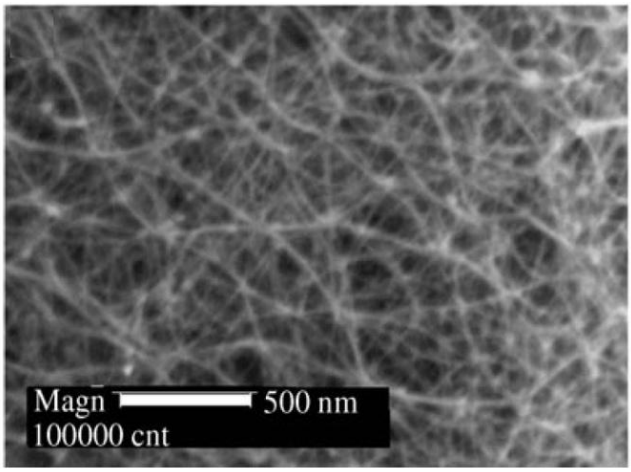

(b)

Figure 5.6 (a) Optical image illustrating SWCNT films with various thicknesses. Top film: thickness of 450nm. Middle film: thickness of 850nm. Bottom film: thickness of 1900nm. (b) Surface SEM image of SWCNT film.

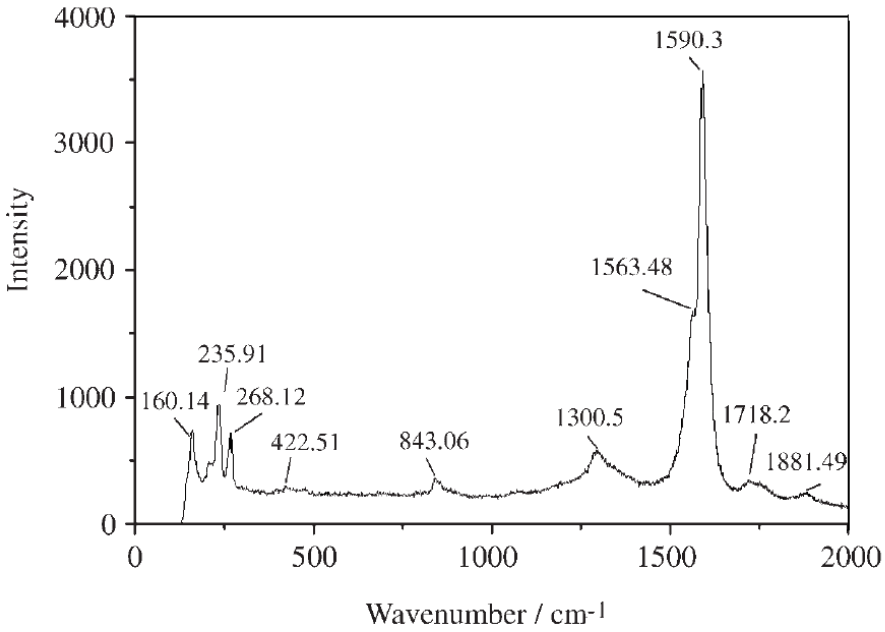

Figure 5.7 Raman spectrum of the SWCNT films using an excitation wavelength of 785 nm [19].

The resistance of the film measured by four-point probe method is given by [21]

$$R = \frac{V}{I} C\left(\frac{a}{d}, \frac{d}{s}\right) \quad (5.2)$$

where V is the voltage measured from two inner probes, I is the testing current across the outer two probes, and $C\left(\frac{a}{d}, \frac{d}{s}\right)$ is a factor that depends on the dimension of the tested film (a is the length of the film, d is the width, and s is the distance between the probes). For clarity, the reduced resistance was used for presenting the change of electrical resistance in deformed films, and it is expressed as the ratio of measured resistance (R) in a deformed film to its zero-strain resistance (R_0). In this work, we measured the SWCNT/PVA film with various thicknesses (40μm-300μm), and they exhibited nearly the same sensing behaviour. Therefore, we only presented the results of SWCNT/PVA film with the thickness of 100μm.

The change of the reduced resistance with respect to the applied strain for each sample is presented in Fig.5.8. The data shown in Fig. 5.8 are the average value of four measurements. In this experiment, the slope of the curve represents the sensitivity. The sensitivity of strain sensor is defined as the gage factor (S_g), which is the ratio of the change of electrical resistance to the tensile strain (ε_t). S_g can be expressed as follow [22]:

$$S_g = \frac{\Delta R}{\varepsilon_t} \quad (5.3)$$

where $\Delta R = \frac{R - R_0}{R_0}$, and R_0 is the resistance of the zero-strain film. The S_g of each sample is listed in Tab. 5.1. Clearly, the strain response of the thin SWCNT film (450nm) exhibits higher sensitivity than that of other two films.

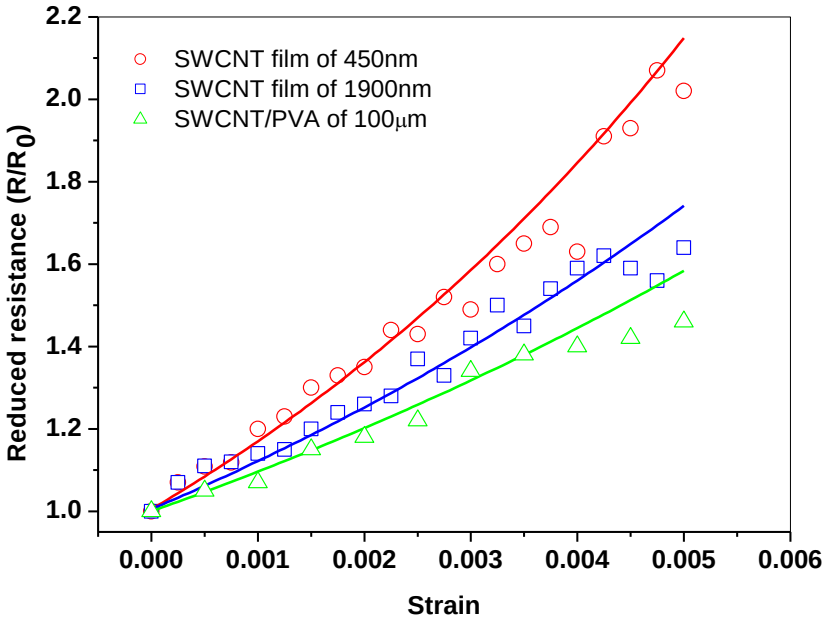

Figure 5.8 Variation of reduced resistance with tensile strain for SWCNT/PVA film and SWCNT films with various thicknesses of 450nm and 1900nm at 280K. The solid lines are the fitting ones from Eq. 5.8 with parameters listed in Tab.5.2.

Table 5.1 Gage factors for the SWCNT films (450nm and 1900 nm) and SWCNT/PVA composite film (100μm).

Samples	Gage factor
SWCNT film (450nm)	194±8
SWCNT film (1900nm)	148±4
SWCNT/PVA	87±4

For the heterogeneous systems comprising the electrical pathways formed by conducting fibers, the electrical conductance can be modeled by using an equivalent circuit [23], which was discussed in chapters 3 and 4. In the equivalent circuit model, the junctions between SWCNTs can be normally modeled as a resistor R connecting with a capacitor C in parallel. Here, we only focus on DC conductance of the SWCNT systems. Therefore, the junctions were treated as an equivalent resistor adding to the equivalent circuit, and its resistance related to the contact resistance. The equivalent

circuit of SWCNT network was composed by placing resistors (attributed to junctions and SWCNT itself) in parallel or series, and electrical properties can be obtained by analyzing the circuit. As discussed in section 3.4, the complex resistor networks can be finally boiled down to a single equivalent resistor, whose value (R_t) can be presented by

$$R_t = n \cdot (R_{CNT} + R_c) \tag{5.4}$$

where n is a constant that depends on the topology of equivalent circuit, R_{CNT} is the resistance of SWNCT, and R_c is the contact resistance. From the literature [24], the individual SWCNT possesses extremely high electrical conductivity, which is in the order of $10^4 - 10^7 S/m$ [24], and the contact resistance induced by the intermolecular junction ranges from $10^5\Omega$ to $10^7\Omega$ [25]. Therefore, $R_{CNT} \ll R_c$, as a result, the total resistance of the SWCNT film or the SWCNT composite film is dominated by the barrier regions, and Eq. 5.4 can be rewritten as:

$$R_t = n \cdot R_c \tag{5.5}$$

The conduction in CNT network is commonly described by fluctuation induced tunneling model (FIT) [26]. FIT model has the following form,

$$\begin{aligned} \sigma &= \sigma_0 \exp[-T_1/(T + T_0)] \\ T_1 &= wA\varepsilon_0^2/8\pi k \\ T_0 &= A\varepsilon_0^2/4\pi^2\chi k \end{aligned} \tag{5.6}$$

where w is the width of the tunneling gap, A is the area of the capacitance formed by the tunneling junction, V_0 is the height of barrier, m is the mass of electrons, $\varepsilon_0 = 4V_0/ew$, and $\chi = (2mV_0/h^2)^{1/2}$. Here, it is assumed that no slippage occurs between the neighboring nanotubes in the low strain regime. The effect of strain on

the local morphology can be separated into two components: the variation of barrier width, $\Delta w = w \cdot \varepsilon_t \sin\beta$ and the change of the area of intermolecular junction due to the elongation of CNTs, $\Delta A = A \cdot \varepsilon_t \cos\beta$, where β is the angle between the uniaxial strain and the orientation of barrier. By considering an image force correction to a rectangular barrier, the FIT model for the deformed CNT systems can be rewritten as [27]

$$\sigma = \sigma_0 \exp\left[c \cdot \varepsilon_t - \frac{1.48T_1}{T+T_0} + \frac{0.02T_1T_0}{(T+T_0)^2}\right] \tag{5.7}$$

where c is a constant, T_1 and T_0 are the parameters, which can be determined from zero-strain FIT model, Eq. 5.5. Here, T_1 and T_0 can be obtained by fitting Eq. 5.6 to the temperature variation data, which is presented in Fig. 5.9. For a given size of sample, the resistance is negatively proportional to the conductivity, and Eq. 5.6 can be rewritten as

$$R = R'_0 \exp\left[-c \cdot \varepsilon_t + \frac{1.48T_1}{T+T_0} - \frac{0.02T_1T_0}{(T+T_0)^2}\right] \tag{5.8}$$

Here, we write Eq. 5.8 in a simple form as

$$R = R'_0 \exp\left[-c \cdot \varepsilon_t + F\right] \tag{5.9}$$

where R'_0 relates to the zero-strain resistance, and F is a constant for the given temperature. The experimental data were well fitted by Eq. 5.9 with parameters listed in Tab. 5.2, and the fitting lines are presented in Fig. 5.8. It can be found that the variation of the sensitivity is mainly caused by parameter c in Eq. 5.9. It can be considered that c is related to the orientation of the barrier regions, slippages between CNTs and the topology of the equivalent circuit.

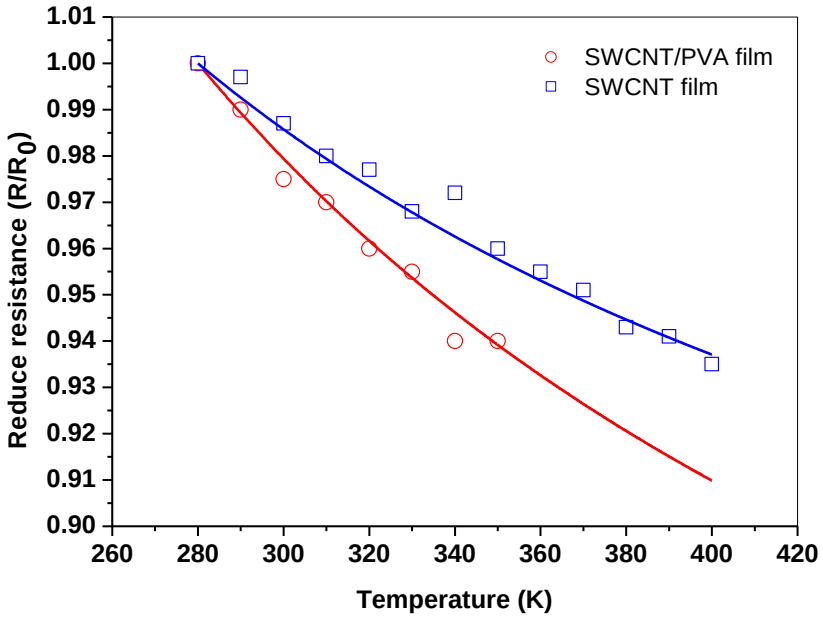

Figure 5.9 Variation of reduced resistance with temperature for SWCNT and SWCNT/PVA films. The solid lines are the fitting ones from Eq. 5.9 with parameters presented in Tab.5.2.

As mentioned in section 2.3.5, the contact resistance is dominant in the disorder CNT system, and it is mainly affected by the width of intertube barriers, the angle between nanotubes, and the contact area [25]. In present work, the strain level is low, $\varepsilon \leq 0.5\%$. Therefore, the variation of contact resistance due to the changes of the angles and contact area between CNTs are so small that the changes can be neglected. If the orientation of barrier region is parallel to the direction of strain, the width of barrier region will not be changed by strain ($\beta = 0$, then $\Delta w = w \cdot \varepsilon_t \sin\beta = 0$), and the corresponding contact resistance is approximately unchanged. Therefore, the variation of resistance in deformed CNT bundles with strain is mainly caused by the intrinsic sensitive properties of CNTs (as reviewed in section 2.3.3). The samples used were comprised of randomly oriented SWCNT systems. As the thickness of samples increases, the disorder SWCNT network turns from a 2-D system to a 3-D dimensional one. It was supposed that the number of transport routes, which are

consisted of resistors caused by the barriers oriented to strain, increased with increasing the dimension of the sample, and these routes could be weakly affected by the strain and possess relatively low electrical resistance. As a stress is applied on the sample, the current tends to transport through these routes. Therefore, it can be concluded that the sensitivity of thick SWCNT film is lower than that of thin SWCNT film (as presented in Fig 5.8).

Table 5.2. Fitting parameters of Eq.5.9. F was calculated from Eq. 5.8 by using the T_1 and T_0 obtained from Fig. 5.9.

Thickness	c	F	T_1 (K)	T_0 (K)
450 nm (SWCNT)	-75	0.307	62.8	5.8
1900nm (SWCNT)	-58	0.307	62.8	5.8
100μm (SWCNT/PVA)	-44	0.475	93.2	10.4

As the applied strain was approximately above 0.4%, the thick SWCNT film (1900nm) and SWCNT/PVA sample presented a deceasing sensitivity. This decease of sensitivity indicates the strain dependent nature of current path. The decline in sensitivity occurs as current is rerouted due to the slippages between SWCNTs. The rearrangement of the entangled points, which can strongly affect the transport routes, can also be caused by the slippages. The corresponding variation of electrical resistance to the rearrangement is partly un-recoverable.

In order to confirm the occurrence of the slippages between SWCNTs and observe the 'viscoelastic' nature of the electrical pathways in SWCNT network, the recovery measurements were performed. Fig. 5.10 (a) and (b) present the time dependent recovery behaviour of these three specimens with strains of 0.3% and 0.6%, respectively. The unrecoverable resistances of samples are shown in Fig 5.10 (c). It can be noted that the electrical recovery behaviour is similar to the recovery characteristics of polymers. Both recovery behaviours are time dependent, which are

normally concerned with viscoelastic behaviour. Therefore, we modified Voigt-Kelvin model [29] to describe the current recovery behaviour, namely

$$R(t) = R_m(\varepsilon) + R_d \exp(-t/\tau) \tag{5.10}$$

where $R_m(\varepsilon)$ is the un-recoverable resistance induced by the slippages between SWCNTs, R_d is the original resistance of the deformed sample, τ is a constant at the given strain.

The best fit achieved with Eq. 5.10 is presented as solid lines in Fig 5.10 (a) and (b), and the fitting parameters are listed in Tab. 5.3. It can be observed that the resistance of 450nm SWCNT film immediately recovered to zero-strain value as the stress was removed at the both strain levels (elastic strain response), and other samples exhibited time dependent recovery behaviour ('viscoelastic' strain response), which was enhanced with increasing the strain level. The unrecoverable resistance can be observed for the SWCNT/PVA and 1900nm SWCNT films at the strain of 0.6% due to the rearrangement of entangled points between SWCNTs. The different recovery behaviours of two SWCNT films indicate that more slippages occur with increasing thickness. Since the epoxy provides a strong bonding, which prevents slippages between SWCNTs, to the SWNCTs near the interface between SiO_2 substract and the SWCNT film. Therefore, the thin SWCNT film (450nm) exhibited 'elastic' sensing behaviour. As thickness increases, the simple mechanical bonding is dominant in the region relatively far from the strong bonding interface. Therefore, slippages occur in the thick SWCNT film, which exhibited 'viscoelastic' sensing behaviour. Here, all measurements were conducted in the elastic displacement range of aluminum specimen. Thus, the measured 'viscoelastic' behaviour was not resulted by the aluminum specimens.

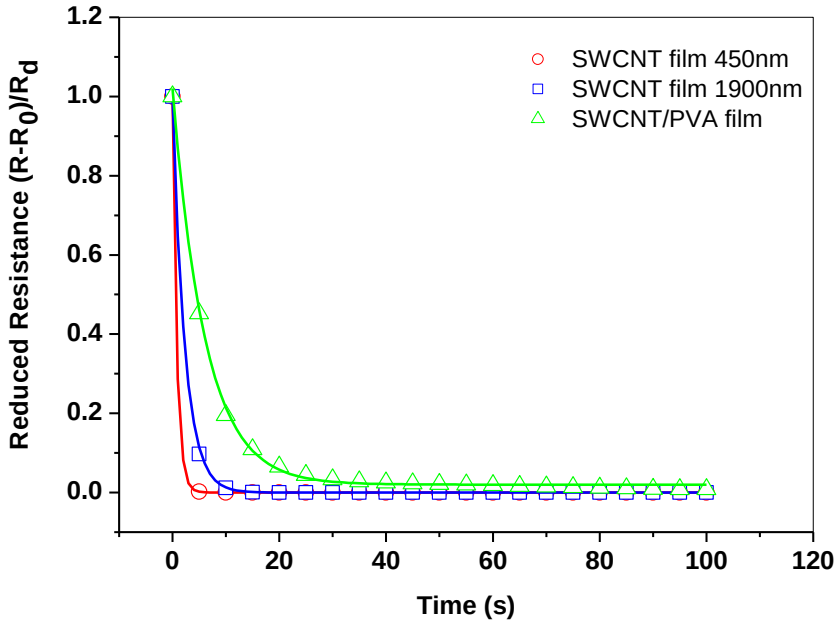
Reduced Resistance (R-R0)/Rd
Time (s)
SWCNT film 450nm
SWCNT film 1900nm
SWCNT/PVA film
1.2
1.0
0.8
0.6
0.4
0.2
0.0
0
20
40
60
80
100
120

(a)

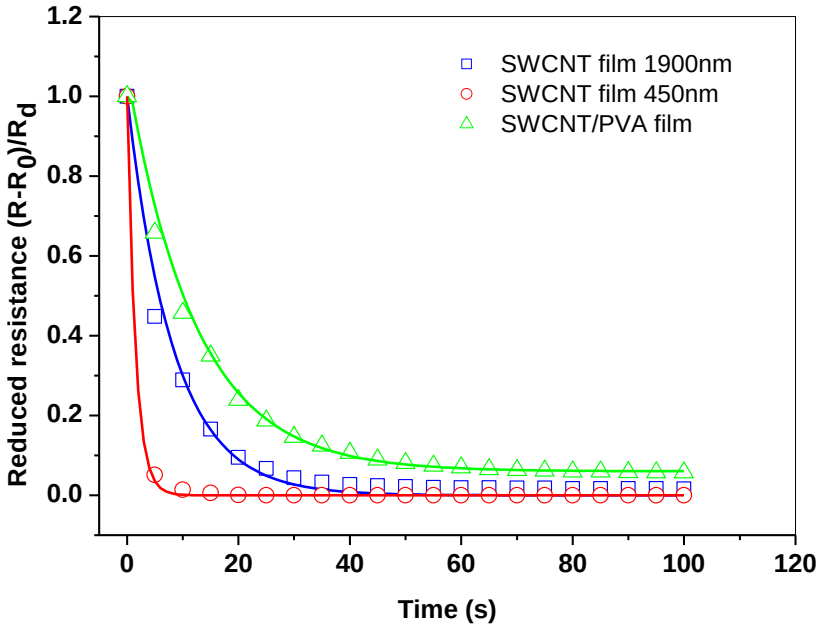
Reduced resistance (R-R0)/Rd
Time (s)
SWCNT film 1900nm
SWCNT film 450nm
SWCNT/PVA film
1.2
1.0
0.8
0.6
0.4
0.2
0.0
0
20
40
60
80
100
120

(b)

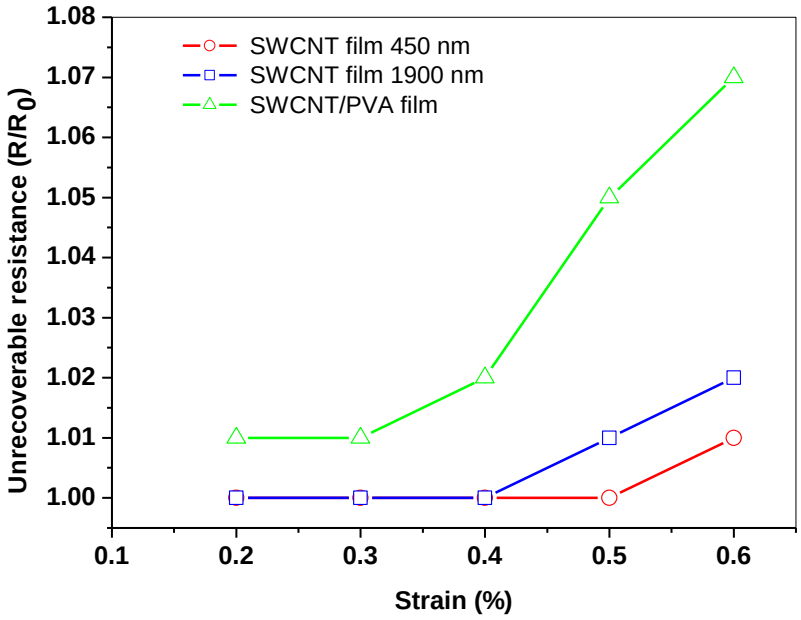

(c)

Figure 5.10 Recovery behaviour of resistance with deformations (a) 0.3% and (b) 0.6%. Solid lines are the fitting ones by Eq. 5.10 with parameters listed in Tab. 5.3. (c) illustration of unrecoverable resistance with applied strain.

Table 5.3 Fitting parameters of Eq.5.10.

Thickness	R_m/R_d	τ
Strain of 0.3%		
450nm	0	0.7
1900nm	0	2.1
100μm (SWCNT/PVA)	0.021	6.2
Strain of 0.6%		
450nm	0	1.6
1900nm	0.016	5.2
100μm (SWCNT/PVA)	0.063	13.4

Dynamic measurements are also necessary to develop a SWCNT based strain sensor. In practical situation, where loading is often periodic, in order to give a precise sensibility, the overall response of the sensor should be well predicted and controlled. The 'viscoelastic' nature of SWCNT network can also be manifested by a dynamic strain measurement, which is presented in Fig. 5.11. It can be seen that SWCNT film with thickness of 450nm always exhibits an 'elastic' response to the dynamic load. The resistance is unchanged in each loading phase. The SWCNT/PVA composite film displays a 'viscoelastic' response. The resistances gradually increase with the number of loading cycles experienced as presented in Fig 5.12 (b), and the 'viscoelastic' behaviour is intensified with increasing the strain level put into the equipment. As the strain level increased from 0.3% to 0.5%, the response of the SWCNT film with a thickness of 1900nm varies from 'elastic' to 'viscoelastic' behaviour, and the 'viscoelastic' behaviour was also enhanced as increasing the strain level as shown in Fig. 5.12 (a). From Fig 5.12, it also can be found that the average reduced resistance increases with decreasing the period of the dynamic loading pattern. Due to the 'viscoelastic' nature of strain response, the resistance induced by the deformation cannot be recovered immediately. If the recovery time decreases, the residual resistance at the end of each cycle will increase. Therefore, the 'viscoelastic' response was enhanced with decreasing the period of loading pattern as shown in Fig. 5.11 (a) and (c).

The resistance of the sample under periodic strain can be predicted as that resistance caused by the applied strain added to the residual resistance at the end of previous recovery phase, namely,

$$R(t) = R'_r \exp[-c \cdot \varepsilon_t + F] + R'_d \exp(-t/\tau) \quad (5.11)$$

where R'_r is the residual resistance at the end of previous recovery phase and R'_d is the resistance at the end of previous loading phase. The first term in Eq. 5.11

represents the resistance induced by applied strain, and the second term demonstrates the residual resistance.

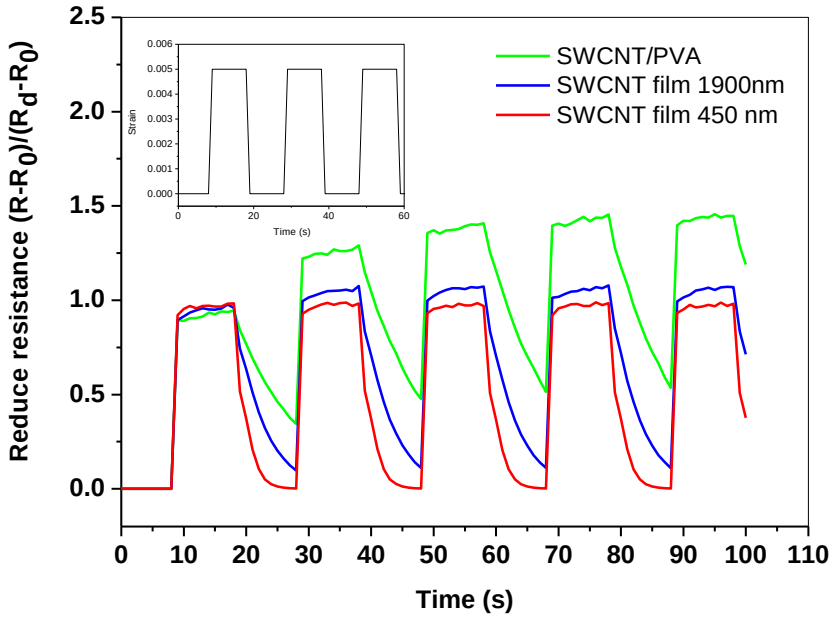

(a)

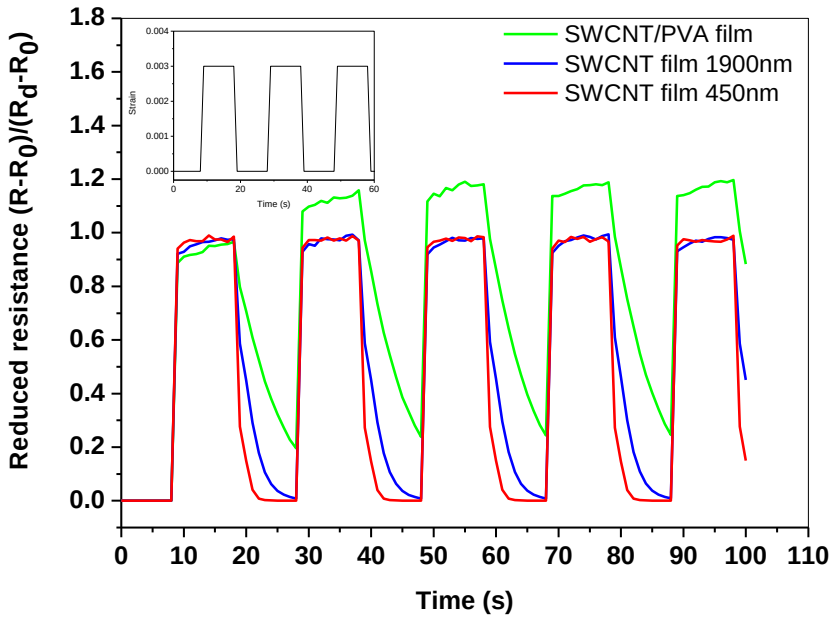

(b)

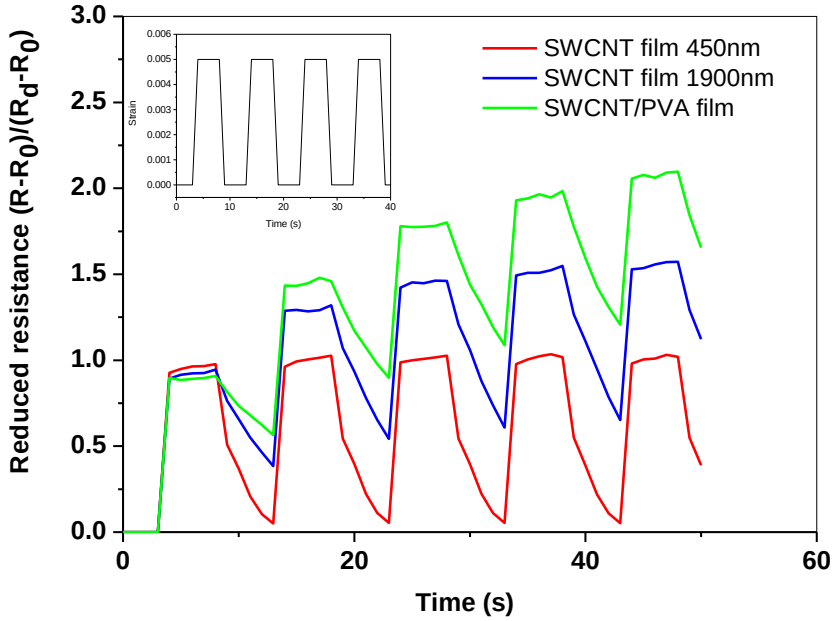

(c)

Figure 5.11 Response of SWCNT based films to the dynamic strain put into the equipment with various periods and strain level. (a) period of 20s and strain of 0.5%, (b) period of 20s and strain of 0.3%, and (c) period of 10s and strain of 0.5%. The inset are the applied intermittent strain signal.

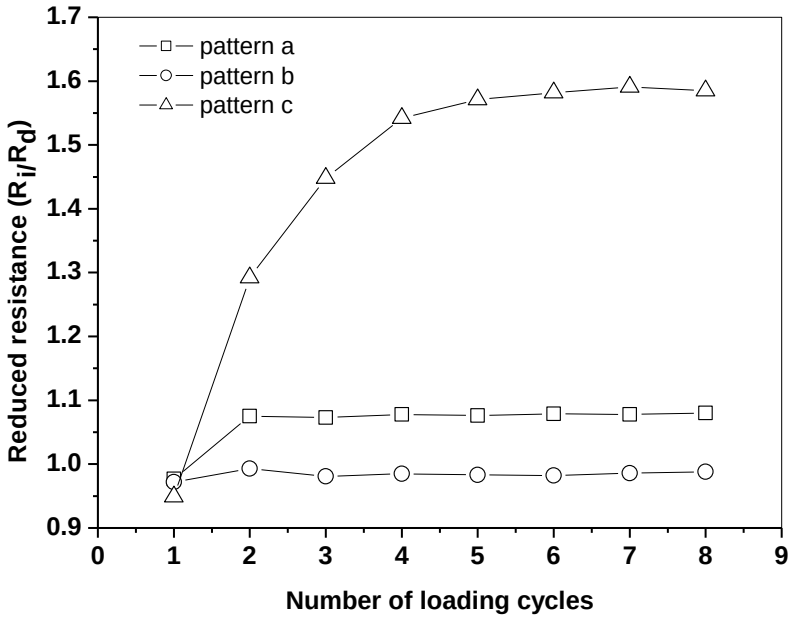

(a)

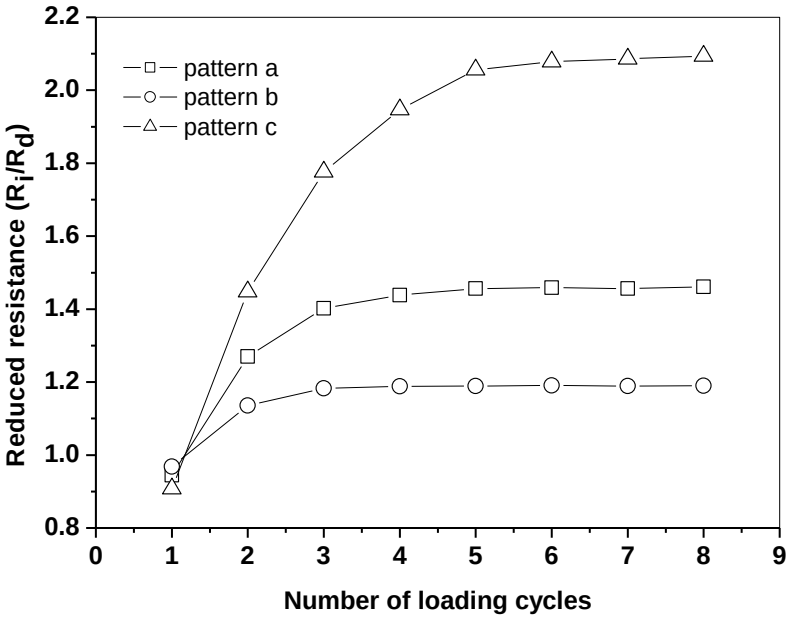

(b)

Figure 5.12 Illustration of average reduced resistance (R_i/R_d) against the number of loading pattern experienced for (a) SWCNT film (1900nm), and (b) SWCNT/PVA tested under various loading patterns: (a) period of 20s and strain of 0.5%, (b) period of 20s and strain of 0.3%, and (c) period of 10s and strain of 0.5%. R_i is the average resistance in loading cycle i, and R_d is the resistance of the static deformed films.

From Fig 5.12, it can also be observed that the most increase in average reduced resistance occurs in first few loading phases. After saturated point, at which the trend of resistance turn from increase to be stable with loading phases experienced, the strain response of 'viscoelastic' samples shows 'pseudo-elastic' behaviour. This may indicate that rearrangement of electrical routes weakly affect the strain response after the saturated point.

For the dynamic measurement, the strain sensitivity can be expressed as [22]

$$S_d = \frac{\Delta R_{peak\ -peak}\ /R_0}{\varepsilon} \quad (5.12)$$

where $\Delta R_{peak-peak}$ is the amplitude of the peak, and R_0 is the resistance of zero-strain samples.

The dynamic strain sensitivity of the SWCNT film with a thickness 1900nm and the SWCNT/PVA film is listed in Tab. 5.4. By comparing these results in Tab. 5.4 to the static sensitivity in Tab. 5.1, it can be found that the dynamic sensitivity of samples with 'elastic' strain response is nearly the same as their static sensitivity. The dynamic sensitivity of the films with 'viscoelastic' strain response is lower than their static sensitivity. The more 'viscoelastic' behaviour the films exhibit, the lower sensitivities they have.

Table 5.4. Dynamic sensitivitiy of SWCNT and SWCNT/PVA films.

Sample	Pattern 1	Pattern 2	Pattern 3
SWCNT film (450 nm)	188±5	190±4	186±6
SWCNT film (1900nm)	135±3	140±2	131±3
SWCNT/PVA	74±3	76±2	70±4

The 'viscoelastic' behaviour of SWCNT film with a thickness of 1900nm and the SWCNT/PVA film can also be indicated by their relaxation behaviour, which are presented in Fig.5.13. The SWCNT film at an applied strain of 0.3% is nearly 'elastic', and its resistance is nearly unchanged with time elapsing. The gradual drop of the resistance is resulted by the relaxation of SWCNTs in the SWCNT/PVA film. The samples with the higher strain level showed stronger relaxation behaviours.

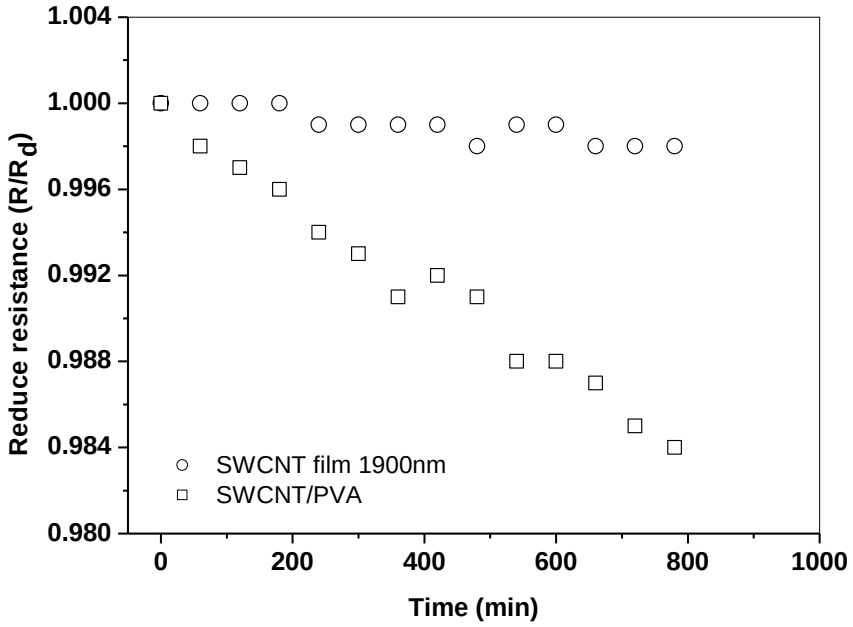

(a)

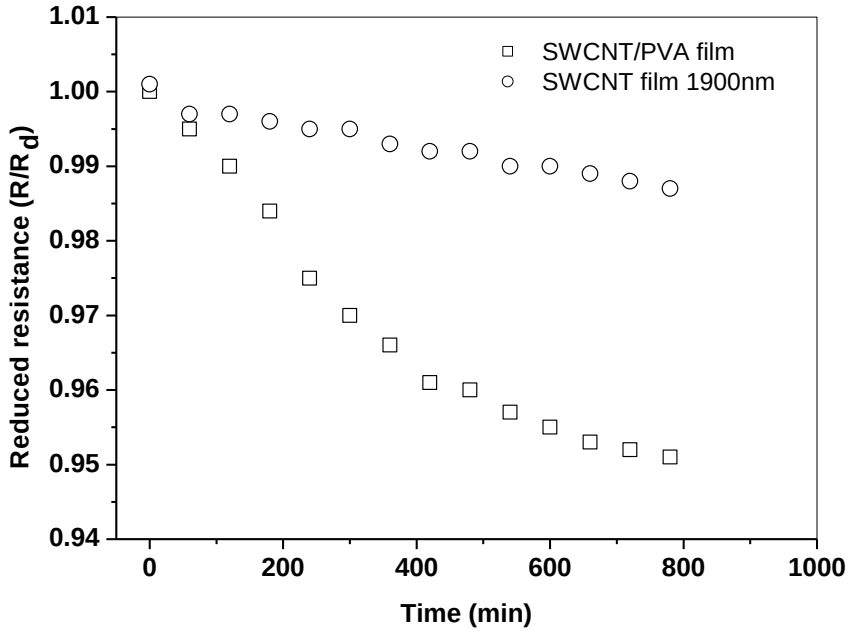

(b)

Figure 5.13. Relaxation behavior of SWCNT/PVA and SWCNT film with a thickness of 1900nm at the various strains of: (a) 0.3% and (b) 0.5%.

5.4 Strain Dependent Thermoelectric Power of SWCNT Films

The variation of TEP with the applied strain is presented in Fig. 5.15 for the SWCNT films with various thicknesses. It should be noted that the data are for oxygen-doped samples under ambient condition. For the SWCNT film with a thickness of 450nm, TEP gradually decreases with increasing strain from 0% to 0.15%, and as strain is above 0.15%, TEP turns to rapidly increase with increasing strain. Here, we defined critical strain as the strain at the turning point. The curve of the film with thickness of 1900nm presented a similar trend to that of the 450 nm-thickness film, but its curve exhibited a weakly increase of TEP as strain was beyond the turning point. The effect of strain on TEP could be interpreted by using Nordheim-Gorter relation and FIT model.

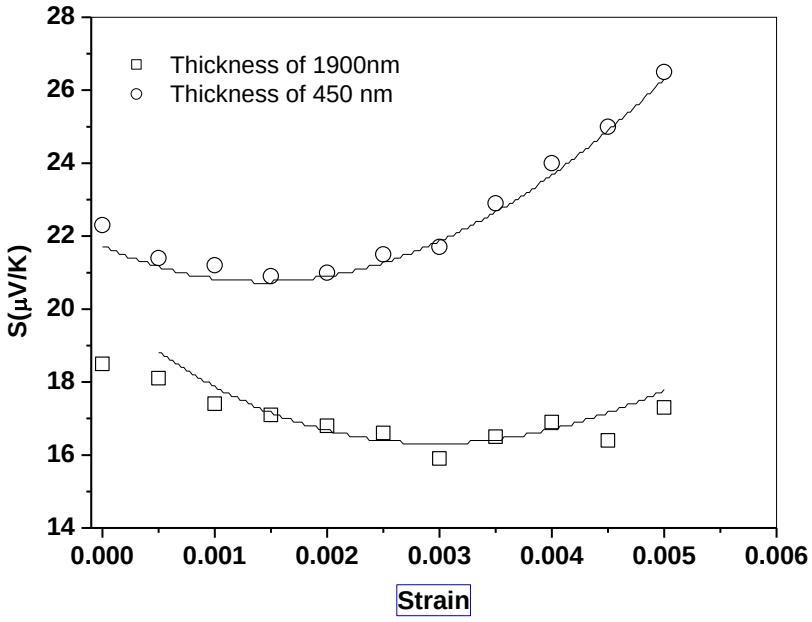

Figure 5.15 Variation of TEP with uniaxial strain for the SWCNT films with the thickness of 850nm and 1900nm, respectively. The solid lines are the fitting ones by Eq. 5.25 with parameters presented in Tab.5.5. The measurements were performed at 280K.

Generally, TEP for a homogeneous system can be calculated via the Boltzman transport equation using the standard Mott formula [30]:

$$S = \frac{\pi^2 k^2 T}{3e} \frac{d\ln \sigma(E)}{dE}\Big|_{E_F} \tag{5.13}$$

where *k* is the Boltzman constant, T is temperature, e is electronic charge, and $\sigma(E)$ is a conductivity-like function of electronic energy E. The heat current intends to transfer through the smallest distance between conductors, which is same as the principle of electrical transport [31]. In the present work, it was assumed the heat current has the same pathway as electrical current.

For a heterogeneous system, in which current transport through the pathways formed by fibers, TEP can be obtained by analogs of Nordheim-Gorter rule for diffusion TEP due to the different scattering mechanisms [30]. As reviewed in section 2.3.6, TEP of a SWCNT film can be written as the sum of the conductance-weighted contribution from metallic and semiconducting SWCNT paths, which are approximately treated as connecting with each other in parallel, namely,

$$S = \frac{\sigma_1}{\sigma} S_1 + \frac{\sigma_2}{\sigma} S_2 \tag{5.14}$$

where S_1 and S_2 are TEPs for metallic and semiconducting pathways, and the total conductance is the sum of the conductance of two paths, $\sigma = \sigma_1 + \sigma_2$.

It was expected that there were no slippages between the nanotubes, when strain was low (discussed in section 5.3). As reviewed in section 2.3.3, the electronic states of a SWCNT allowed by the Born-von Karman boundary condition were predicted lie on the parallel lines, which are perpendicular to the radius of SWCNT [10]. In the undeformed SWCNT, the BZ is the hexagonal with the Fermi point k_F at the vertices (k_V). Near k_F, the electronic states can be described by linear relationship, $|k - k_F|$.

The density of states (DOS) for deformed SWCNTs can be expressed by [10]:

$$\mathrm{DOS}(\epsilon) \propto [\epsilon^2 - (\vartheta - \Delta k_F)^2]^{-1/2} \tag{5.15}$$

where ϑ is related to the type of SWCNTs. As reviewed in section 2.3.3, when the uniaxial strain is applied on a SWCNT, k_F is driven away from k_V along the direction with an angle of 3θ (chiral angle) from the axis that is perpendicular to the allowed state lines. The tensile strain induced band gap is largest for zigzag SWCNTs and zero for armchair SWCNTs.

For a one-band system in a 1-D conductor, the Seebeck coefficient can be derived as [11],

$$S = -\frac{k}{e}\left(\frac{3F_{1/2}}{F_{-1/2}} - \zeta\right) \tag{5.16}$$

where F_i is Fermi-Dirac function, and ζ is the reduced Fermi level relative to the band edge for electrons and holes. The Fermi-Dirac function F_i is given by

$$F_i = \int_0^\infty \frac{x^i}{e^{(x-\zeta)}+1}\,dx \tag{5.17}$$

Assuming the absence of the phonon-drag effect at the temperature of measurement performed, by using the free electron approximation [30], Eq. 5.16 in the phonon scattering regime can be rewritten as follows:

$$S = -\frac{k}{e}\left(\frac{|\lambda|}{T} - \zeta\right) \tag{5.18}$$

where λ is the gap temperature measured from the Fermi level to the band edge. Here, we assume an activated form for the uniaxially deformed non-armchair SWCNTs,

$\lambda \propto (\vartheta - C\varepsilon_t)^{1/2}$, where C is determined by the types of SWCNTs. The conductivity of a deformed non-armchair SWCNT can be generally expressed as [33],

$$\sigma = n_0 q\mu \cdot \exp\left(\frac{-E_g}{2kT}\right) \tag{5.19}$$

where n_0 relates to temperature, T, reduced Fermi level and effective masses of electrons and holes, q is charge of carriers, μ is the mobility of charge carriers, and E_g is the energy between the conduction and valence band. Here, we assume the mobility of charge carriers is unchanged with strain due to the lack of experimental knowledge. E_g can be generally written as $E_g \propto \vartheta - C\varepsilon_t$.

Previous studies [13, 17] have tacitly assumed that the total conductance of a CNT mat is dominated by metallic channels, and the electronic states of armchair do not change with deformation. Then, the general expression of total TEP can be derived from Eq. 5.14, namely

$$S_{tot} = A + \left[B(\vartheta - C\varepsilon_t)^{1/2}\right]\exp\left[-D(\vartheta - C\varepsilon_t)\right] \tag{5.20}$$

where A, B, C, D are constants. A is related to TEP of metallic nanotubes, B, C, D is related to the types of CNTs in the sample. The first and second terms represent the weighted contribution of armchair and non-armchair TEPs, respectively. Eq. 5.20 can give a good fitting to the experimental data of deformed CNT bundles, because barrier regions are oriented and perpendicular to the strain direction. In this case, the total TEP is entirely determined by CNT pathways with no contributions from the barrier regions. However, in randomly oriented SWCNT films, the effect of barriers can be not neglected. A strongly positive TEP of the SWCNT film can be observed from the experimental data presented in Fig. 5.15. This strongly positive TEP may be partly due to the randomly oriented barrier between SWCNTs.

The total TEP of the random SWCNT film can be modeled by parallel pathways interrupted by the series-connected barrier. For the random systems, the electrical transport is dominated by the electron transfer between large conducting regions rather than by hopping between localized states. TEP of the 1D conduction can be approximately expressed by [33]

$$S = \frac{-\pi^2 k^2 T}{3e} \frac{1}{\sigma} \frac{d\sigma}{dE}\Big|_{E_f} \tag{5.21}$$

Although Eq. 5.21 was originally obtained from bulk systems, it is still valid in 1D conduction [18]. The conductivity of the barrier region can be expressed using the FIT model [26],

$$\begin{aligned} \sigma &= \sigma_0 \exp[-T_1/(T+T_0)] \\ T_1 &= wA\varepsilon_0^2/8\pi k \\ T_0 &= A\varepsilon_0^2/4\pi^2 \chi k \end{aligned} \tag{5.22}$$

where w is the width of the tunneling gap, A is the area of the capacitance formed by the tunneling junction, V_0 is the height of barrier, m is the mass of electron, $\varepsilon_0 = 4V_0/ew$, and $\chi = (2mV_0/h^2)^{1/2}$. The effect of strain on the local morphology can be divided into two components: variation of the barrier width, $\Delta w = w \cdot \varepsilon_t \cos\beta$ and the change of the area of capacitance due to the stretch of CNTs, $\Delta A = A \cdot \varepsilon_t \sin\beta$. By considering an image force correction to a rectangular barrier, the FIT, model can be rewritten as [27]

$$\sigma = \sigma_0 \exp[c \cdot \varepsilon_t - \frac{1.48T_1}{T+T_0} + \frac{0.02T_1 T_0}{(T+T_0)^2}] \tag{5.23}$$

where c is a constant, T_1 and T_0 are the parameters, which can be determined from zero-strain FIT model, Eq. 5.22. Here, we rewrite Eq. 5.23 in a simple form,

$\sigma = \sigma_0 \exp[c \cdot \varepsilon_t + F]$.

For the system comprising the SWCNT electrical pathways intermittently broken by the random oriented barrier between nanotubes, Eq. 5.14 can be rewritten as

$$S = \frac{R_1}{R} S_1 + \frac{R_2}{R} S_2 \tag{5.24}$$

where R_1 is the resistance of SWCNTs, R_2 is the resistance of the barrier regions, the total resistance of the film is composed of these two terms, $R = R_1 + R_2$, S_1 and S_2 represent TEP of the SWCNTs and barrier regions, respectively. Then, the total TEP of SWCNT films with the consideration of the contribution of the barrier regions can be obtained from Eqs. 5.20 and 5.23 as follows,

$$S = A' \exp[c \cdot \varepsilon_t + F] + \left[B'(\vartheta - C\varepsilon_t)^{1/2}\right] \exp[-D'(\vartheta - C'\varepsilon_t)] \exp[c \cdot \varepsilon_t + F] + E' \exp[-c \cdot \varepsilon_t - F] \tag{5.25}$$

where A'-E' are constants. The first and second terms in Eq. 5.25 represent the weighted contributions of armchair and non-armchair nanotubes, and the third term is the contribution of the barrier region.

The experimental data can be fitted with Eq. 5.25 by a procedure that F can be calculated from Eqs. 5.22 and 5.23, B, C' C, D, and ϑ have physically reasonable values, and c can be determined by fitting the Eq. 5.23 to the actual conductance of the deformed film, which is presented in Fig. 5.8. The parameters for the best fits with Eq. 5.25 to the experimental results are given in Tab. 5.5, and the fitting lines presented as solid ones in Fig. 5.15. The parameter $(\vartheta - C'\varepsilon_t)$ indicates the variation of the energy gap for non-armchair nanotubes with the applied strain. D' reveals the distribution of types of non-armchair SWCNTs in the film, and the high value of D'

means narrow distribution for types of nanotubes in the film. Generally, the conductance of the fiber filled systems decreases with increasing the applied strain. Therefore, the sign of parameter c is negative.

The measured TEP of deformed SWCNT films can be well described in term of the present model. The increase of the TEP above the critical strain is resulted by introducing the positive term of the contribution from the barrier regions. The barriers also can induce the additional carrier scattering associated with the perturbation in the longitude transport pathway. Therefore, DOS of electron was enhanced in the SWCNT film due to the intertube barriers [30]. These factors might result in the positive term of barrier regions. Form Fig.5.15, it can also be observed that the effect of the barriers deceases with increasing the thickness of film. As the thickness increases, the SWCNT network turns from a 2-D to a 3-D system, and the number of possible transport routes, in which the orientation of the barrier is perpendicular to strain, increases. As strain is applied on the film, the current tends to transport through these routes, which are weakly affected by the strain. Therefore, the influence of strain on TEP of SWCNT film fast vanishes as the thickness of film increases.

Table 5.5. Best fitting parameters by Eq.5.25.

Thickness (nm)	A' (μV/k)	B' ($\mu V/keV^{1/2}$)	C (eV)	C' (eV)	D' (eV^{-1})	E' (μV/K)	Θ (eV)	c	F
450	-0.05	424	14.66	14.38	1.5	11.2	0.18	-152	-0.307
1900	-0.21	821	12.22	12.13	1.2	5.8	0.13	-117	-0.307

Further evidence for the present analysis was obtained from the temperature variation of deformed SWCNT films shown in Fig.5.16. The experimental results can be modeled by using Eq. 2.43, and the fitting parameters are listed in Tab.5.6. It can be observed that the positive contribution (E) from barrier regions increases with increasing the applied strain due to the enhancement of the barrier regions in the deformed SWCNT film.

Table 5.6 Best fitting parameters of Eq.2.43. The value of A', D and λ used in present work are from the calculated value given in ref.15 .

Strain	A'	B'	C' (μV/k)	D(μV/k)	E(μV/$k^{3/2}$)	λ(K)
0%	-6×10^{-6}	623	3×10^{-5}	0.05	0.21	201
0.4%	-6×10^{-6}	636	3×10^{-5}	0.05	0.32	201
0.5%	-6×10^{-6}	648	3×10^{-5}	0.05	0.45	201

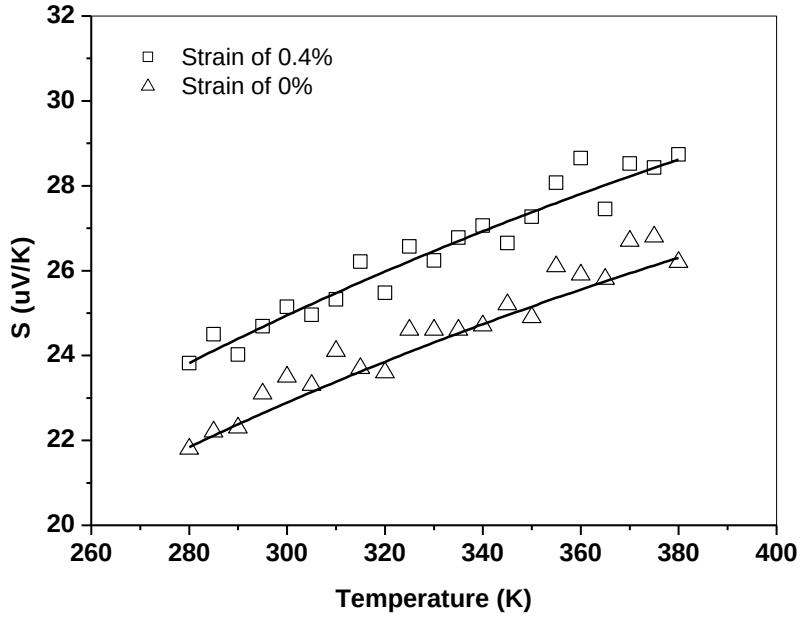

Figure 5.16. Variation of TEP with temperature for the SWCNT film with a thickness of 450nm under different strains level (0%, and 0.4%), and the solid lines are the fitting ones with parameters presented in Tab.5.6.

5.5 Conclusions

In conclusions, the variations of the resistance of CNT films and composites with strain are mainly resulted from the change of random oriented intertube barriers due to the deformation. Experimental results showed that SWCNT/PVA film exhibited 'viscoelastic' behaviour, and the SWCNT film with a thickness of 1900nm displayed

'viscoelastic' behaviour at high strain, and 'elastic' behaviour at low strain. These two films could not represent the applied strain in a dynamic load test, and they are not suitable for developing a strain sensor. The SWCNT film with a thickness of 450nm always presented 'elastic' response to static and dynamic strain due to its 2-D structure and the stronger epoxy interfacial bonding, and it is suitable for developing a strain sensor.

An electrical model of SWCNT strain sensor was derived from the FIT model for describing the resistance induced by the change of random oriented intertube barriers. The model gave a good fit to the strain-response. The 'viscoelastic' response was well descried by the modified Voigt-Kelvin model, which can be used for correcting resistance drift, and predicting the repeatability of sensors.

TEP of deformed SWCNT films with various thicknesses was measured. A positive increase of TEP was induced by the applied strain, and the increase became weak as increasing the thickness of SWCNT films. The experimental results were fitted by a derived numerical model in terms of a variation of Nordheim-Gorter relation and FIT model. The numerical model showed a proper interpretation of strain-dependent TEP. The increase of TEP above the critical strain resulted from the contribution of the barrier regions, and the effect of barrier regions decreases with increasing the thickness of the film. The temperature variations of TEP with strain were also examined.

References

1. J.C. Charlier, X. Blasé, and S. Roche, Rev. Mod. Phys. 79, 677 (2007).
2. J. W. Mintmire, B. I. Dunlap, and C. T. White, Phys. Rev. Lett. 68, 631 (1992).
3. R. Ljubisa, Sensor Technology and Devices, Boston London Artech house, 1994.
4. K. T. V. Grattan, and B. T. Meggit, Optical Fiber Sensing Technology, Dordrecht

London Kluwer Acadamic, 1999.

5. Y. Li, X. Qiu, F. Yang, X. Wang and Y. Yin, Nanotechnology 19, 165502 (2008).
6. J. Zhou, Y. Gu, Y. Hu, W. Mai, P. H. Yeh, G. Bao, A. K. Sood, D. L. Polla, and Z. L. Wang, Appl. Phys. Lett. 94, 191103 (2009).
7. Q. Zhao, M. D. Frogley, and H. D. Wagner, Compos. Sci. Technol. 62, 147 (2002).
8. N. Muto, Y. Arai, S. G. Shin, Compos. Sci. Technol.61, 875 (2001).
9. J. W. Mintmire and C. T. White, Phys. Rev. Lett. 81, 2506 (1998).
10. L. Yang, and J. Han, Phys. Rev. Lett. 85, 154 (2000).
11. D. D. Pollock, Thermoelectricity Theory Thermometry Tool, ASTM Special Technical Publication 852, 1985.
12. G. Mahan, Solid State Phys. 51, 81 (1998).
13. J. Hone, I. Ellwood, M. Muno, A. Mizel, M. L. Cohen, A. Zettl, A. G. Rinzler, and R. E. Smalley, Phys. Rev. Lett. 80, 1042 (1998).
14. K. Bradley, S. H. Jhi, G. Collins, J. Hone, M. L. Cohen, S. L. Louie, and A. Zettl, Phys. Rev. Lett. 85, 4361 (2000).
15. M. Baxendal, K. G. Kim, and G. A. J. Amaratunga, Phys. Rev. B 61, 12705 (2000).
16. G. U. Sumanasekera, B. K. Pradhan, H. E. Romero, K. W. Adu, and P. C. Eklund, Phys. Rev. Lett. 89, 166801 (2002).
17. H. E. Romero, G. U. Sumanasekera, G. D. Mahan, and P. C. Eklund, Phys. Rev. B 65, 205410 (2002).
18. J. P. Small, K. M. Perez, and P. Kim, Phys. Rev. Lett. 91, 256801 (2003).
19. Y. H. Li, Y. M. Zhao, M. Roe, D. Furniss, Y. Q. Zhu, S. Ravi, P. Silva, J. Q. Wei, D. H. Wu, and C. H. Patrick Poa, Small 2, 1026 (2006).
20. L. Shi, D. Li, C. Yu, W. Jang, D. Kim, Z. Yao, P. Kim, and A. Majumdar, J. Heat Transfer 125, 881 (2003).
21. F. M. Smits, Bell Syst. Tech. J. 5, 711 (1958).
22. J. W. Dally and W. F. Riley, Experimental Stress Analysis 3rd edn, New York: McGraw-Hill, 1990.

23. S. Kirkpatrick, Rev. Mod. Phys. 45, 574 (1973).

24. T. W. Ebbessen, H. J. Lezec, H. Hiura, J. W. Bennett, H. F. Ghaemi, and T. Thio, Nature 382, 54 (1996).

25. A. Buldum and J. P. Lu, Phys. Rev. B 63, 161403 (2001).

26. P. Sheng, Phys. Rev. B 21, 2180 (1980).

27. E. K. Sichel, P. Sheng, J. I. Gittleman, and S. Bozowski, Phys. Rev. B 24, 6131, 1981.

28. R. Saito, G. Dresselhaus, and M. S. Dresselhaus, Physical Properties of Carbon Nanotubes, Imperial College Press, 1998.

29. A. W. Birley, B. Hawork, J. Batchelor, Physics of Plastics, Oxford University Press, 1991.

30. R. D. Bernard, Thermoelectricity in Metals and alloys, Taylor&Francis, 1992.

31. H. Zhong, and J. R. Lukes, Phys. Rev. B 74, 125402 (2003).

32. S. S. Li, Semiconductor Physical Electronics, Springer, 2006.

33. M. Cutler and N. F. Mott, Phys. Rev. 181, 1336 (1969).

Chapter 6 Conclusions and Future Work

6.1 Conclusions

This project mainly investigated the electrical properties of CNT based materials. The DC and AC properties of CNT/polymer composites were explored based on the equivalent circuit model. A continuum model was constructed by introducing effective tunneling conduction for predicting the DC conductivity of CNT/polymer composites. The influence of the microstructure in CNT/polymer composites on DC conductivity was assessed particularly for CNT/PE, CNT/PI and CNT/PVA composites. Results revealed that both of percolation threshold and the DC conductivity can be affected by the polymer matrix and tortousity of CNTs. Contact resistance have a significant influence on the DC conductivity, but do not affect the percolation threshold. The simulated results suggested that CNTs might not be an effective filler to improve the conductivity of polymers unless the contact resistance can be significantly reduced.

The AC properties of CNT/polymer nanocomposites were also studied by using the continuum model, and it was found that the AC properties were also strongly affected by the local morphology in the CNT/polymer composites. In the case of composites with high mass fraction, the curl curliness of MWCNTs only had a weak influence on the AC conductivity of the nanocomposite. In the mid-range mass fraction, with increasing curl ratio of MWCNTs, the AC conductivity, interestingly, became frequency-dependent in low frequency range, which was properly explained based on the linear circuit theory. Both of AC conductivity and critical frequency can be significantly affected by the size of CNTs clusters.

In order to develop a more reasonable and quantified method for the prediction of AC conductivity, a series numerical formulas were derived by using a numerical

capacitively and resistively junction model. An equivalent RC circuit with simple definition of the values of contact resistance and average mutual capacitance for CNT/polymer nanocomposites was introduced in this work. Theoretical results were in good agreement with experimental data, and successfully predicted the effect of the morphology on the AC properties.

The electrical properties of MWCNT/GO hybrid films were measured. It was found that MWCNT/GO films possessed much higher percolation threshold than that of MWCNT/polymer composites, which may be caused by the low potential energy in the central area of GO sheet and intrinsic ripples and warping in the freestanding graphene sheets. As the mass fraction approached and over the percolation threshold, the DC conductivity of MWCNT/GO hybrid films also followed the percolation scaling law. The critical frequencies of the MWCNT/GO hybrid films were much lower than other MWCNT/polymer composites. As frequency increased to a certain level, the loss of dielectric properties for GO insulating layer occurred. The MWCNT/GO film showed relatively high specific capacitance ($0.192\,\mathrm{F/cm^{-3}}$ with the mass fraction of 83.3%) and power factor compared to conventional dielectric capacitors. Both of measured capacitance and power factor can be enhanced by increasing the testing voltages. Above $160C^{o}$, the redox reactions occurred in the GO sheets, and the capacitance of the MWCNT/GO film rapidly decreases due to the loss of insulating property of the GO sheets.

The sensing behaviours of SWCNT and SWCNT/PVA films were examined, and understood by introducing a modified Voigt-Kelvin model. It was found that SWCNT/PVA film exhibited ‘viscoelastic’ behaviour, and the SWCNT film with a thickness of 1900nm presented ‘viscoelastic’ behaviour at high strain, and ‘elastic’ behaviour at low strain. The SWCNT film with a thickness of 450nm always presented ‘elastic’ response to static and dynamic strain, which is suitable for developing a strain sensor.

Finally, TEP of deformed SWCNT films with various thicknesses was measured. The results revealed that a positive increase of TEP can be induced by the applied strain, and the increase became weak as increasing the thickness of SWCNT films. A numerical model in terms of a variation of Nordheim-Gorter relation and FIT model was developed, and gave a proper interpretation of varied TEP with strain. From the numerical model, it was reached that the increase of TEP above the critical strain resulted from introduced the positive term of the contribution from the barrier region, and the effect of barrier region decreased with increasing the thickness of the film.

6.2 Recommendations to Future Research

Outcomes of this project has led us to improve the knowledge of the electrical properties of CNT based materials, and design better CNT devices and CNT/polymer composites. In the aspect of the conductive CNT/polymer composites, our results revealed that the contact resistance was one of the main limitations for the improvement of the electrical conductivity. In order to significantly enhance electrical conductivity, the contact resistance must be maximally reduced. This strategy could be implemented as we could induced suitable dopants adhered to the sidewall of CNTs, which can create excess charge carriers and increase the conductivity of CNT based materials.

Although extensive efforts have been made to develop CNT based strain sensors, the repeatability and reliability of the sensor are still being challenge. Results of this work suggested that the 'viscoelastic' sensing behaviour could be caused by the slippages between CNTs. In order to improve the the repeatability and reliability of the CNT sensors, the slippages must be prevented. This strategy could be implemented as we could use very thin CNT films as sensing layer and adhere it to the substrate using polymers with high adhesive strength, which can prevent the slippages between CNTs.

The research on the MWCNT/GO hybrid film is still in its early stage. The exciting results found in this stage drive us to dig out more applications of this new nanomaterial as electronic and energy storage devices.

Appendix A

(1) Program Flow Chart For Generating Miscrostructure of CNT Composites

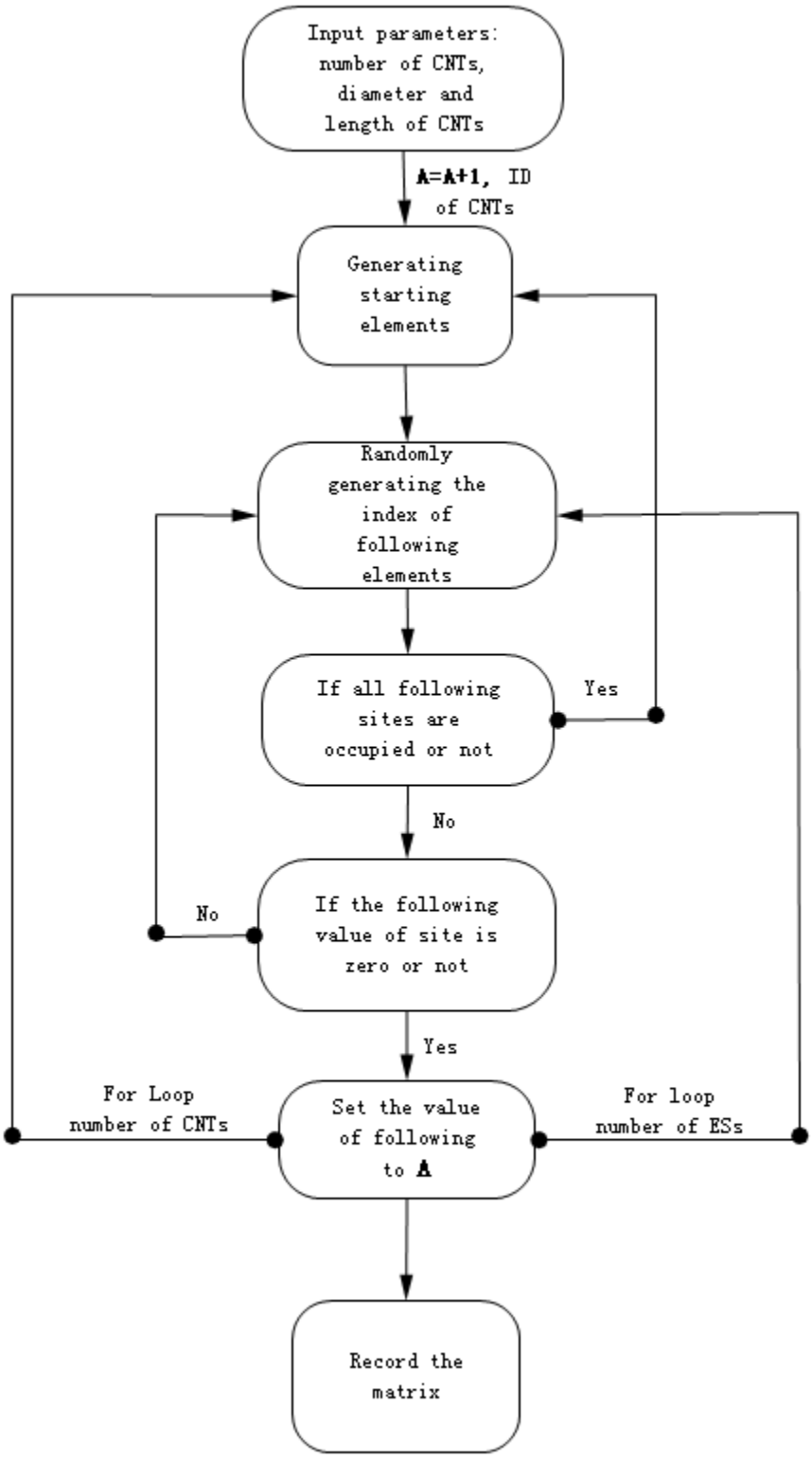

(2) Program Flow Chart For Generating DC SPICE Input File

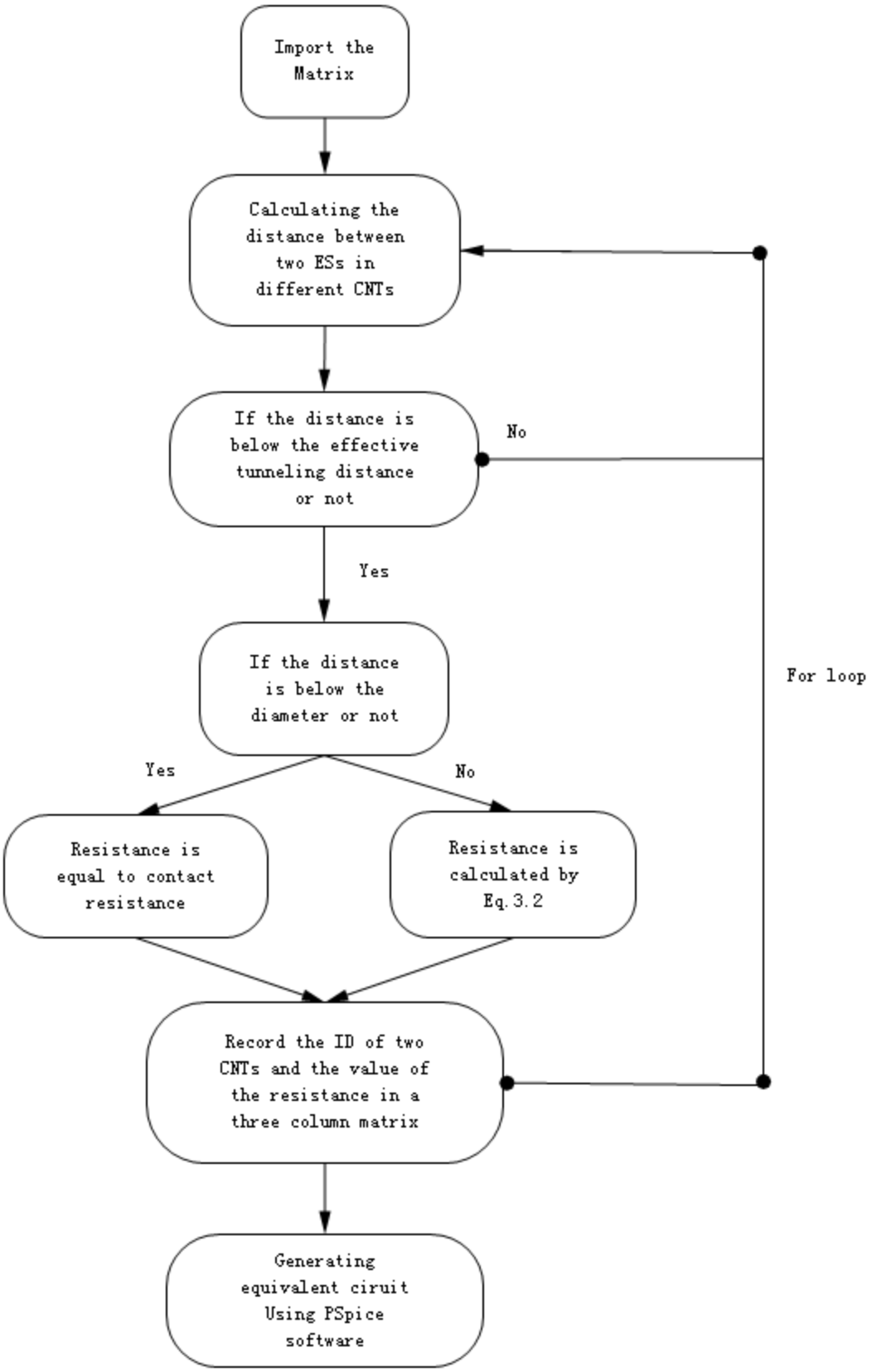

(3) Program Flow Chart For Generating AC SPICE Input File

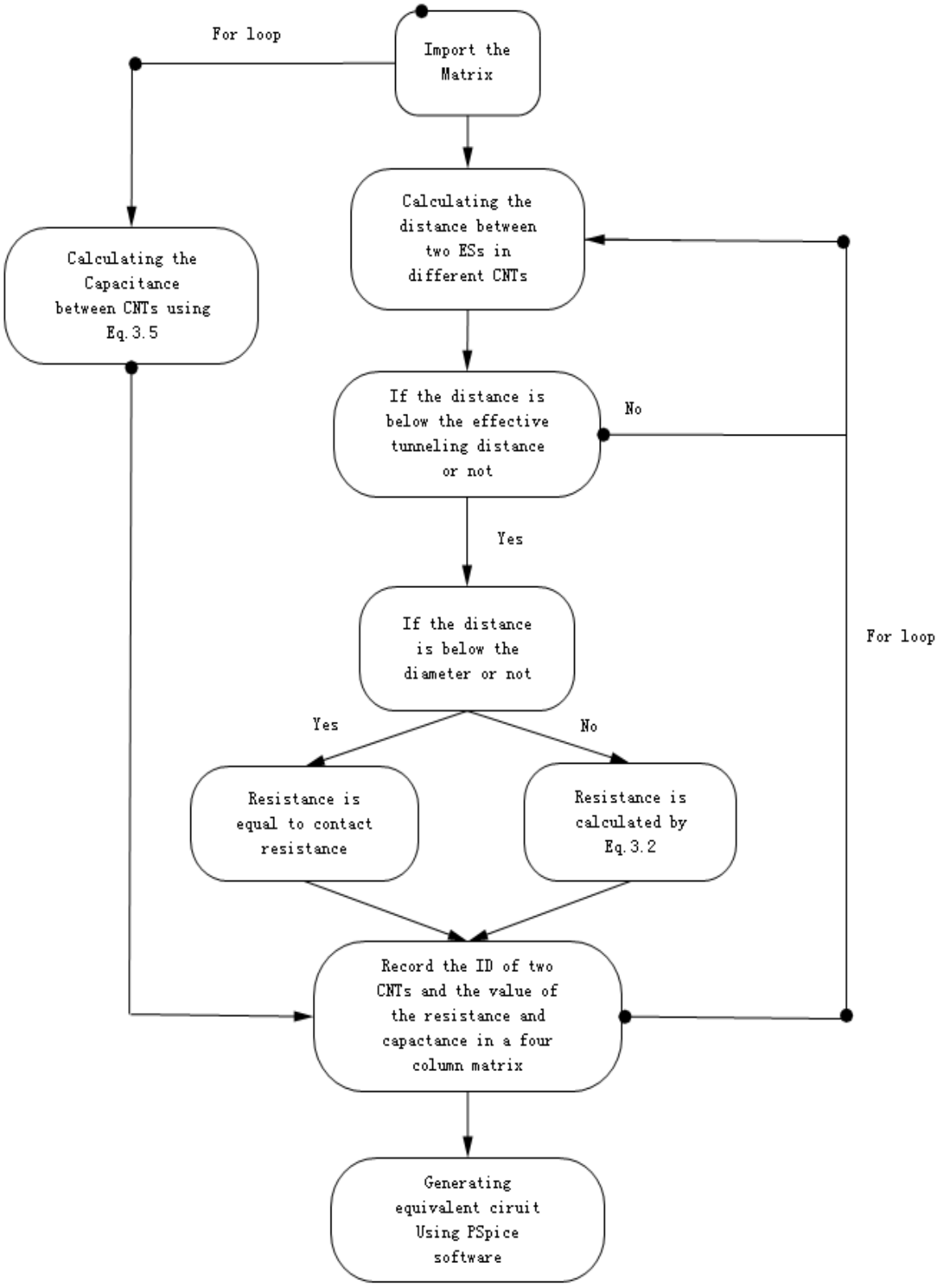

Program for Generating 2-D Microstructure (starting element)

```
% Build matrix    model of CNTs in polymers
% input L=length of CNTs
%            d=dimension
%            N=number of CNTs
%output    mothermatrix for computing following variables
%             orientation=orien
%             volume percent=volp
%             number of intersection=numsect
%Notes: build a model of cnts in polymers by using matrix, the
%            elements display polymers equal to zero, and cnts equal
%            to 1. The cnts distribution determine by rand matrix.
global mothermatrix;
a=160000;% size of polymer&cnt composites, the given volume V
mothermatrix=zeros(a,a); % bulid mother matrix
N=1000;
d=1;
L=5000;
elenum=round(L/d); % number of elements needed for single CNT
starnumpre=rand(1,N).*a; % determine the starting position of CNT
starnum=round(starnumpre);
rejust=0;
aindex=0;%ORIENTATION
accnum=0;% presetting account for the unitary length ORIENTATION
orienlength=100;
orienangle=zeros(1,round(elenum/orienlength)*N); % build the matrix to store the orietation
angle ORIENTATION
```

```
% first loop
for indxm=1:length(starnum)% loop to build cnt, indxm is the column index
    i=starnum(1,indxm);% rows index
    j=round(rand(1,1).*a);%column index
    tubecurve=rand(1,elenum); % random array to make a adjustment

    revi=i;
    revj=j;
    m=0;
    accnum=0; %ORIENTATION
    rowsac=0; % counter ORIENTATION
    colomnac=0; % counter ORIENTATION
    posize=4; %size of position matrix control the shape of cnts
    upward=zeros(1,posize);
    downward=zeros(1,posize);
    forward=zeros(1,posize);
    backward=zeros(1,posize);

    % adjustment part
 if tubecurve(1,1)<0.25 % move forwad
    % to adjust the previous position
    i=i+1;
    rowsac=rowsac+1;% count for i change ORIENTATION
 elseif   tubecurve(1,1)>0.25& tubecurve(1,1)<0.5 % move backward

        i=i-1;
        rowsac=rowsac-1;% count for i change ORIENTATION
 elseif   tubecurve(1,1)>0.5& tubecurve(1,1)<0.75 % move up

      j=j+1;
```

```
        colomnac=colomnac+1;% count for j change ORIENTATION
elseif  tubecurve(1,1)>0.75 % move down
        j=j-1;
        colomnac=colomnac-1;%count for j change ORIENTATION
end

% second loop
 for n=2:elenum

      % COMPUTING ORIENTATION
      accnum=accnum+1; %account for the length to computing the orientation
      if accnum>orienlength
            aindex=aindex+1;
            orienangle(1,aindex)=atand(abs(colomnac)/abs(rowsac));% record the orienangle
            accnum=0; % reset
            colomnac=0; % reset
            rowsac=0;% reset

      end
      % end of computing orientation

      % counter and index for the unrepeatable adjustment
      m=m+1;
      if m>posize;
            m=m-posize;
      end

     if tubecurve(1,n)<0.25&sum(backward(1,:))>0
       rejust=rand(1,1);
     if rejust<0.33
```

```
            revi=i;
            i=i-1;
            rowsac=rowsac-1;% ORIENTATION
        elseif rejust>0.33&rejust<0.66
            revj=j;
            j=j+1;
            colomnac=colomnac+1;%ORIENTATION

        elseif rejust>0.66
            revj=j;
            j=j-1;
            colomnac=colomnac-1; %ORIENTATION
        end
        continue
          end

if tubecurve(1,n)>0.25&tubecurve(1,n)<0.5&sum(forward(1,:))>0
        rejust=rand(1,1);
        if rejust<0.33
            revi=i;
            i=i+1;
            rowsac=rowsac+1;%ORIENTATION
        elseif rejust>0.33&rejust<0.66
            revj=j;
            j=j+1;
            colomnac=colomnac+1;%ORIENTATION
        elseif rejust>0.66
            revj=j;
            j=j-1;
            colomnac=colomnac-1;%ORIENTATION
```

```
        end
        continue
end

if tubecurve(1,n)>0.5&tubecurve(1,n)<0.75&sum(upward(1,:))>0
        rejust=rand(1,1);
        if rejust<0.33
                revi=i;
                i=i-1;
                rowsac=rowsac-1;%ORIENTATION
        elseif rejust>0.33&rejust<0.66
                revi=i;
                i=i+1;
                rowsac=rowsac+1;%ORIENTATION
        elseif rejust>0.66
               revj=j;
                j=j-1;
                colomnac=colomnac-1; %ORIENTATION
        end
        continue
end

if tubecurve(1,n)>0.75&sum(downward(1,:))>0
        rejust=rand(1,1);
        if rejust<0.33
                revi=i;
                i=i-1;
                rowsac=rowsac-1;%ORIENTATION
        elseif rejust>0.33&rejust<0.66
```

```
            revi=i;
            i=i+1;
            rowsac=rowsac+1;%ORIENTATION
        elseif rejust>0.66
             revj=j;
             j=j+1;
             colomnac=colomnac+1;%ORIENTATION
        end
        continue
end

if tubecurve(1,n)<0.25&sum(backward(1,:))==0 % move forwad
         % to adjust the previous position
            revi=i;
            i=i+1;
            rowsac=rowsac+1;%ORIENTATION

elseif tubecurve(1,n)>0.25& tubecurve(1,n)<0.5&sum(forward(1,:))==0 % move backward
             revi=i;
             i=i-1;
             rowsac=rowsac-1;%ORIENTATION

elseif tubecurve(1,n)>0.5& tubecurve(1,n)<0.75&sum(upward(1,:))==0%move up

             revj=j;
             j=j+1;
             colomnac=colomnac+1;%ORIENTATION
elseif tubecurve(1,n)>0.75&sum(downward(1,:))==0 % move down
             revj=j;
             j=j-1;
```

```
        colomnac=colomnac-1;%ORIENTATION
        end
% end of adjustment

% position unrepeatable in 100 elements
if revi<i
        forward(1,m)=1;
elseif revi>=i
                forward(1,m)=0;
end

if revi>i
        backward(1,m)=1;
elseif revi<=i
        backward(1,m)=0;
end

if revj<j
        downward(1,m)=1;
elseif revj>=j
        downward(1,m)=0;
end

if revj>j
        upward(1,m)=1;
elseif revj<=j
        ypward(1,m)=0;
end

%boundary condition
```

```
            if i>a
                i=i-a+1;
            end
            if j>a
                j=j-a+1;
            end
            if j<1
                j=j+a-1;
            end
            if i<1
                i=i+a-1;
            end
            mothermatrix(i,j)=1;% elements of cnt equal to one
        end % end of second
    end % end of first
    imshow(~mothermatrix)
    whos mothermatrix
    average=sum(orienangle(1,:))/aindex
    orien=cosd(average)
    aindex
```

Program for Generating 3-D Film Structure

```
% Build matrix    model of CNTs in polymers
    % input L=length of CNTs
    %            d=dimension
    %            N=number of CNTs
    %output    mothermatrix for computing following variables
    %             orientation=orien
```

```
%              volume percent=volp
%              number of intersection=numsect
%Notes: build a model of cnts in polymers by using matrix, the
%              elements display polymers equal to zero, and cnts equal
%              to i. The cnts distribution determine by rand matrix.
global mothermatrix;
a=160000;% size of polymer&cnt composites
b=10000;% thickness of Polymer&cnt composites
mothermatrix=zeros(a,a,b); % bulid mother matrix
N=400;
ID=0; %ID of CNTs
d=1;
L=1000;
elenum=round(L/d); % number of elements needed for single CNT
starnumpre=rand(1,N).*a; % determine the starting position of CNT
starnum=round(starnumpre);
rejust=0;
aindex=0;%ORIENTATION
accnum=0;% presetting account for the unitary length ORIENTATION
orienlength=100;
orienangle=zeros(1,round(elenum/orienlength)*N); % build the matrix to store the
orietation angle ORIENTATION


% first loop
for indxm=1:length(starnum)% loop to build cnt, indxm is the column index
    i=starnum(1,indxm);% rows index
    j=round(rand(1,1).*a);%column index
    k=round(rand(1,1).*b);%k index
    tubecurve=rand(1,elenum); % random array to make a adjustment
    ID=ID+1;
```

```
revi=i;
revj=j;
revk=k;
m=0;
accnum=0; %ORIENTATION
rowsac=0; % counter ORIENTATION
colomnac=0; % counter ORIENTATION
kac=0;% K orientation
posize=4; %size of position matrix control the shape of cnts
%set up
upward=zeros(1,posize);
downward=zeros(1,posize);
forward=zeros(1,posize);
backward=zeros(1,posize);
leftward=zeros(1,posize);
rightward=zeros(1,posize);

% adjustment part
 if tubecurve(1,1)<=0.166667 % move forwad
% to adjust the previous position
i=i+1;
rowsac=rowsac+1;% count for i change ORIENTATION
elseif tubecurve(1,1)>0.167& tubecurve(1,1)<=0.333 % move backward

    i=i-1;
    rowsac=rowsac-1;% count for i change ORIENTATION
elseif tubecurve(1,1)>0.333& tubecurve(1,1)<=0.5 % move up

  j=j+1;
  colomnac=colomnac+1;% count for j change ORIENTATION
```

```
elseif tubecurve(1,1)>0.5& tubecurve(1,1)<=0.667 % move down
        j=j-1;
        colomnac=colomnac-1;%count for j change ORIENTATION
elseif tubecurve(1,1)>0.667& tubecurve(1,1)<=0.833 % move rightward
          k=k+1;
          kac=kac+1;% count for i change ORIENTATION
elseif tubecurve(1,1)>0.833& tubecurve(1,1)<=1 % move left
        k=k-1;
        kac=kac-1;% count for k change ORIENTATION
end

% second loop
 for n=2:elenum
      COMPUTING ORIENTATION
      accnum=accnum+1; %account for the length to computing the orientation
      if accnum>orienlength
          aindex=aindex+1;
          orienangle(1,aindex)=atand(((abs(colomnac)).^2+(abs(kac)).^2).0.5/abs(rowsac));
          % record the orienangle
          accnum=0; % reset
          colomnac=0; % reset
          rowsac=0;% reset
          kac=0;%reset

      end
      % end of computing orientation

      % counter and index for the unrepeatable adjustment

      m=m+1;
```

```
 if m>posize;
       m=m-posize;
 end

 if tubecurve(1,n)<=0.167&sum(backward(1,:))>0
rejust=rand(1,1);
if rejust<=0.2
      revi=i;
      i=i-1;
      rowsac=rowsac-1;% ORIENTATION
elseif rejust>0.2&rejust<=0.4
      revj=j;
      j=j+1;
      colomnac=colomnac+1;%ORIENTATION

elseif rejust>0.4&rejust<=0.6
      revj=j;
      j=j-1;
      colomnac=colomnac-1; %ORIENTATION

elseif rejust>0.6&rejust<=0.8
      revk=k;
      k=k+1;
      kac=kac+1;%ORIENTATION

elseif rejust>0.8&rejust<=1
      revk=k;
      k=k-1;
      kac=kac-1; %ORIENTATION
end
```

```
        continue
          end


    if tubecurve(1,n)>0.167&tubecurve(1,n)<=0.333&sum(forward(1,:))>0
        rejust=rand(1,1);
        if rejust<=0.2
            revi=i;
            i=i-1;
            rowsac=rowsac-1;% ORIENTATION
        elseif rejust>0.2&rejust<=0.4
            revj=j;
            j=j+1;
            colomnac=colomnac+1;%ORIENTATION

        elseif rejust>0.4&rejust<=0.6
            revj=j;
            j=j-1;
            colomnac=colomnac-1; %ORIENTATION

        elseif rejust>0.6&rejust<=0.8
            revk=k;
            k=k+1;
            kac=kac+1;%ORIENTATION

        elseif rejust>0.8&rejust<=0.1
            revk=k;
            k=k-1;
            kac=kac-1; %ORIENTATION
        end
        continue
```

```
end


if tubecurve(1,n)>0.333&tubecurve(1,n)<=0.5&sum(upward(1,:))>0
    rejust=rand(1,1);
    if rejust<=0.2
        revi=i;
        i=i-1;
        rowsac=rowsac-1;% ORIENTATION
    elseif rejust>0.2&rejust<=0.4
        revj=j;
        j=j+1;
        colomnac=colomnac+1;%ORIENTATION

    elseif rejust>0.4&rejust<=0.6
        revj=j;
        j=j-1;
        colomnac=colomnac-1; %ORIENTATION

    elseif rejust>0.6&rejust<=0.8
        revk=k;
        k=k+1;
        kac=kac+1;%ORIENTATION

    elseif rejust>0.8&rejust<=0.1
        revk=k;
        k=k-1;
        kac=kac-1; %ORIENTATION
    end
    continue
end
```

```
if tubecurve(1,n)>0.5&tubecurve<=0.667&sum(downward(1,:))>0
    rejust=rand(1,1);
    if rejust<=0.2
        revi=i;
        i=i-1;
        rowsac=rowsac-1;% ORIENTATION
    elseif rejust>0.2&rejust<=0.4
        revj=j;
        j=j+1;
        colomnac=colomnac+1;%ORIENTATION

    elseif rejust>0.4&rejust<=0.6
        revj=j;
        j=j-1;
        colomnac=colomnac-1; %ORIENTATION

    elseif rejust>0.6&rejust<=0.8
        revk=k;
        k=k+1;
        kac=kac+1;%ORIENTATION

    elseif rejust>0.8&rejust<=0.1
        revk=k;
        k=k-1;
        kac=kac-1; %ORIENTATION
    end
    continue
end
```

```
if tubecurve(1,n)>0.667&tubecurve<=0.883&sum(leftward(1,:))>0
    rejust=rand(1,1);
     if rejust<=0.2
          revi=i;
          i=i-1;
          rowsac=rowsac-1;% ORIENTATION
     elseif rejust>0.2&rejust<=0.4
          revj=j;
          j=j+1;
          colomnac=colomnac+1;%ORIENTATION

     elseif rejust>0.4&rejust<=0.6
          revj=j;
          j=j-1;
          colomnac=colomnac-1; %ORIENTATION

     elseif rejust>0.6&rejust<=0.8
          revk=k;
          k=k+1;
          kac=kac+1;%ORIENTATION

     elseif rejust>0.8&rejust<=0.1
          revk=k;
          k=k-1;
          kac=kac-1; %ORIENTATION
     end
     continue
end

if tubecurve(1,n)>0.883&tubecurve<=1&sum(rightward(1,:))>0
```

```
        rejust=rand(1,1);
          if rejust<=0.2
                revi=i;
                i=i-1;
                rowsac=rowsac-1;% ORIENTATION
          elseif rejust>0.2&rejust<=0.4
                revj=j;
                j=j+1;
                colomnac=colomnac+1;%ORIENTATION

          elseif rejust>0.4&rejust<=0.6
                revj=j;
                j=j-1;
                colomnac=colomnac-1; %ORIENTATION

          elseif rejust>0.6&rejust<=0.8
                revk=k;
                k=k+1;
                kac=kac+1;%ORIENTATION

          elseif rejust>0.8&rejust<=0.1
                revk=k;
                k=k-1;
                kac=kac-1; %ORIENTATION
          end
          continue
    end


    if tubecurve(1,n)<=0.167&sum(backward(1,:))==0 % move forwad
```

```
% to adjust the previous position
    revi=i;
    i=i+1;
    rowsac=rowsac+1;%ORIENTATION

elseif tubecurve(1,n)>0.167& tubecurve(1,n)<=0.333&sum(forward(1,:))==0
% move backward
        revi=i;
        i=i-1;
        rowsac=rowsac-1;%ORIENTATION

elseif tubecurve(1,n)>0.333& tubecurve(1,n)<=0.5&sum(upward(1,:))==0%move up

     revj=j;
     j=j+1;
    colomnac=colomnac+1;%ORIENTATION
elseif tubecurve(1,n)>0.5&tubecurve<=0.667&sum(downward(1,:))==0 % move down
     revj=j;
     j=j-1;
     colomnac=colomnac-1;%ORIENTATION
elseif tubecurve(1,n)>0.667& tubecurve(1,n)<=0.883&sum(rightward(1,:))==0%move right

     revk=k;
     k=k+1;
    colomnac=colomnac+1;%ORIENTATION
elseif tubecurve(1,n)>0.883&sum(leftward(1,:))==0 % move left
     revk=k;
     k=k-1;
     colomnac=colomnac-1;%ORIENTATION
```

```
end
% end of adjustment

if revi<i
    forward(1,m)=1;
elseif revi>=i
        forward(1,m)=0;
end

if revi>i
    backward(1,m)=1;
elseif revi<=i
    backward(1,m)=0;
end

if revj<j
    downward(1,m)=1;
elseif revj>=j
    downward(1,m)=0;
end

if revj>j
    upward(1,m)=1;
elseif revj<=j
    upward(1,m)=0;
end

if revk<k
    leftward(1,m)=1;
elseif revk>=k
```

```
        leftward(1,m)=0;
    end


    if revk>k
        rightward(1,m)=1;
    elseif revk<=k
        rightward(1,m)=0;
    end


    %Monte C boundary condition
            if i>a
                i=i-a+1;
            end
            if j>a
                j=j-a+1;
            end
            if j<1
                j=j+a-1;
            end
            if i<1
                i=i+a-1;
            end
            if k>a
                k=k-a+1;
            end
            if k<1
                k=k+a-1;
            mothermatrix(i,j,k)=ID;% elements of cnt equal to a integer
     end % end of second
```

```
end % end of first
imshow(~mothermatrix)
whos mothermatrix
average=sum(orienangle(1,:))/aindex
orien=cosd(average)
aindex
```

Core Program for Generating DC SPICE

```
%       compute the electrical conduction
% Input: mothermatrix and idmatrix
% Output: index of the nearest elements and the distance between the
%           nearest elements
% Notes: Sub-function of main. Four parts of this function:
%           find the elements equal to one, store the index of each element
%           build up the matrix of the distance bewteen the CNTs, find the min
%           -distance elements.

idindex=0; % idindex is the index of matrixi and matrixj
idindexa=0;% the index of matrixi and matrixj used in the third loop
ID=0; % id is the identification of each cnt
matrixi=zeros(N, elenum); % the matrix store the i of the each cnt, one row one cnt
matrixj=zeros(N, elenum); % the matrix store the j of the each cnt, one row one cn
matrixk=zeros(N, elenum); % the matrix store the k of the each cnt, one row one CNT
distance=zeros(elenum, elenum);
eledistance=zeros(1,elenum);
icolindex=0;%colomn index pf matrixi
icolindexa=0;
```

```
jcolindex=0;%colomn index of matrixj
kcolindex=0;
indexmini=0;
indexminj=0;
indexmink=0;
h=0;%count
l=0;%count in final part
zerocounter=0;%count for overlap point

% build up the matrix to store the position of cnts
for idindex=1:N
    ID=ID+1;
    [indexi,indexj,indexk]=find(idmatrix=ID);%import microsturcture matix
    matrixi(idindex,:)=indexi.'; % copy by rows
    matrixj(idindex,:)=indexj.'; % copy by rows
    matrixk(idindex,:)=indexk.';%
end
% end of build up the matrix of CNTs

for idindex=1:N % first loop
    for icolindex=1:elenum % second loop
        for idindexa=1:N % third loop
            if idindex==idindexa
                continue
            end
                for icolindexa=1:elenum    % fourth loop

eledistance(idindexa,icolindexa)=((matrixi(idindex,icolindex)-matrixi(idindexa,icolindexa)).^2+(ma
trixj(idindex,icolindex)-matrixj(idindex,icolindexa)).^2+(matrixk(idindex,icolindex)-matrixk(idindex
,icolindexa)).^2).^1/2;
```

```
if eledistance<d;%d should be set a value
    zerocounter=zerocounter+1;
end
if elecdistance<effectdis
  %runing calculation program based on Eq.3.2, In order to minimize the calculation
    loop,here we used a matrix of calculated value of tunneling resistance, it only need to
    find the responding value from the matrix.
    a=a+1;
c(1,a)=idindex;% record the ID of nanotubes as nodes in SPICE
c(2,a)=icolindex;% record the ID of nanotubes as nodes in SPICE
c(3,a)=Rtunneling;% from the tunneling matrix, value of tunneling resistance
                        end %end of fourth loop
              end % end of third loop

[indexmini,indexminj,indexmink]=find(eledistance<=effdistance);% should be set a value.

for loopnum=1:length(indexmini) % recording tunneling index
    h=h+1;
    mini(1,h)=matrixi(idindexa,indexminj);
    minj(1,h)=matrixj(idindexa,indexminj);
    mink(1,h)=matrixk(idindexa,indexminj)
    minio(idindex,h)=matrixi(idindex,icolindex);
    minjo(idindex,h)=matrixj(idindex,icolindex);
    minko(idindex,h)=matrixk(idindex,icolindex);
    tunnelingdistance(idindex,h)=eledistance(idindex,icolindex);% record the min-distance
                end    %end of condition more
          end % end of second loop
  end % end of first loop
ss='nodes                nodes                resistance';
```

```
fid=fopen('SPICE.dat','w');
fprintf(fid,'%s\n',ss);
fprintf(fid,'%c\n','');
fprintf(fid,'%10.1f        %10.1f        %10.2f\n',c);
fclose(fid)
```

Core Program for Generating AC SPICE

```
%        compute the electrical conduction
% Input: mothermatrix and idmatrix
% Output: index of the nearest elements, tunneling matrix and the distance between the
%        nearest elements
% Notes: Sub-function of main. Four parts of this function:
%        find the elements equal to one, store the index of each element
%        build up the matrix of the distance bewteen the CNTs, find the min
%        -distance elements.

idindex=0; % idindex is the index of matrixi and matrixj
idindexa=0;% the index of matrixi and matrixj used in the third loop
ID=0; % id is the identification of each cnt
matrixi=zeros(N, elenum); % the matrix store the i of the each cnt, one row one cnt
matrixj=zeros(N, elenum); % the matrix store the j of the each cnt, one row one cn
matrixk=zeros(N, elenum); % the matrix store the k of the each cnt, one row one CNT
distance=zeros(elenum, elenum);
eledistance=zeros(1,elenum);
icolindex=0;%colomn index pf matrixi
icolindexa=0;
jcolindex=0;%colomn index of matrixj
kcolindex=0;
indexmini=0;
```

```
indexminj=0;
indexmink=0;
h=0;%count
l=0;%count in final part
zerocounter=0;%count for overlap point

% build up the matrix to store the position of cnts
for idindex=1:N
    ID=ID+1;
    [indexi,indexj,indexk]=find(idmatrix=ID);%import microsturcture matix
    matrixi(idindex,:)=indexi.'; % copy by rows
    matrixj(idindex,:)=indexj.'; % copy by rows
    matrixk(idindex,:)=indexk.';%
end
% end of build up the matrix of CNTs

for idindex=1:N % first loop
    for icolindex=1:elenum % second loop
        for idindexa=1:N % third loop
            if idindex==idindexa
                continue
            end
                for icolindexa=1:elenum    % fourth loop

eledistance(idindexa,icolindexa)=((matrixi(idindex,icolindex)-matrixi(idindexa,icolindexa)).^2+(ma
trixj(idindex,icolindex)-matrixj(idindex,icolindexa)).^2+(matrixk(idindex,icolindex)-matrixk(idindex
,icolindexa)).^2).^1/2;

    if eledistance<d;%d should be set a value
        zerocounter=zerocounter+1;
```

```
end
if elecdistance<effectdis
%runing calculation program based on Eq.3.2, In order to minimize the calculation
 loop,here we used a matrix of calculated value of tunneling resistance, it only need to find
 the responding value from the matrix.
 a=a+1;
c(1,a)=idindex;% record the ID of nanotubes as nodes in SPICE
c(2,a)=icolindex;% record the ID of nanotubes as nodes in SPICE
c(3,a)=Rtunneling;% from the tunneling matrix, value of tunneling resistance
c(4,a)=capacitance(idindex, icolindex);
                end %end of fourth loop
          end % end of third loop
    end % end of second loop
end % end of first loop
ss='nodes                nodes                resistance                capacitance';
fid=fopen('SPICEAC.dat','w');
fprintf(fid,'%s\n',ss);
fprintf(fid,'%c\n','');
fprintf(fid,'%10.1f      %10.1f      %10.2f      %10.8f\n',c);
fclose(fid)
```

Core Program for Computing Capacitance

```
L=0;
l=0;
% set the initial value
a(1,1)=1;
a(1,2)=1;
b(1,1)=1;
b(1,2)=1;
```

```
i=0;
k=0;
for idindex=1:N % first loop
        for icolindex=1:elenum % second loop
  L=L+1;
  if L=100;
     i=i+1;

length(1,i)=orietationangle(1,idindex)*((matrixi(idindex,icolindex)-matrixi(a(1,1),a(1,2))).^2+(matr
ixj(idindex,icolindex)-matrixj(a(1,1),a(1,2)))).^2+(matrixk(idindex,icolindex)-matrixk(a(1,1),a(1,2)))
).^2).^1/2
                y1=(idindex-a(1,1))/2;
                y2=(icolindex-a(1,2))/2;
                a(1,1)=idindex;
                a(1,2)=icolindex;
                areaa(1,i)=length(1,i)*d;
                for idindexa=1:N % third loop
                    if idindex==idindexa % avoiding computing for same CNT
                       continue
                    end
                for icolindexa=1:elenum    % fourth loop
                     if l=100;
                        j=j+1;

length(1,i)=orietationangle(1,idindex)*((matrixi(idindex,icolindex)-matrixi(b(1,1),b(1,2))).^2+(mat
rixj(idindex,icolindex)-matrixj(b(1,1),b(1,2)))).^2+(matrixk(idindex,icolindex)-matrixk(b(1,1),b(1,2)
))).^2).^1/2
% orientationangle was computed from program for generating microstructure.
                        areab(1,j)=length(1,i)*d;
                        x1=(idindexa-b(1,1))/2;
```

```
                                x2=(icolindexa-b(1,2))/2;

distance=((matrixi(x1,x2)-matrixi(y1,y2).^2+(matrixj(x1,x2)-matrixj(y1,y2))).^2+(matrixk(x1,x2)-m
atrixk(y1,y2))).^2).^1/2
                                b(1,1)=idindexa;
                                b(1,2)=icolindexa;
                                capacitancea(1,j)=dielecon*min(areaa(1,i),areab(1,j))/distance;
                            end % end of if
                        end % end of Fourth loop
                        end % end of Third loop
                        end% end of if
                    end % end of Second loop
                capacitance(1,idindex)=sum(capcitancea(1,:));
        end % end of First loop
        ss=' capacitance';
        fid=fopen('capc.dat','w');
        fprintf(fid,'%s\n',ss);
        fprintf(fid,'%c\n','');
        fprintf(fid,'%10.8f \n',capciatance);
        fclose(fid)
```

Appendix B

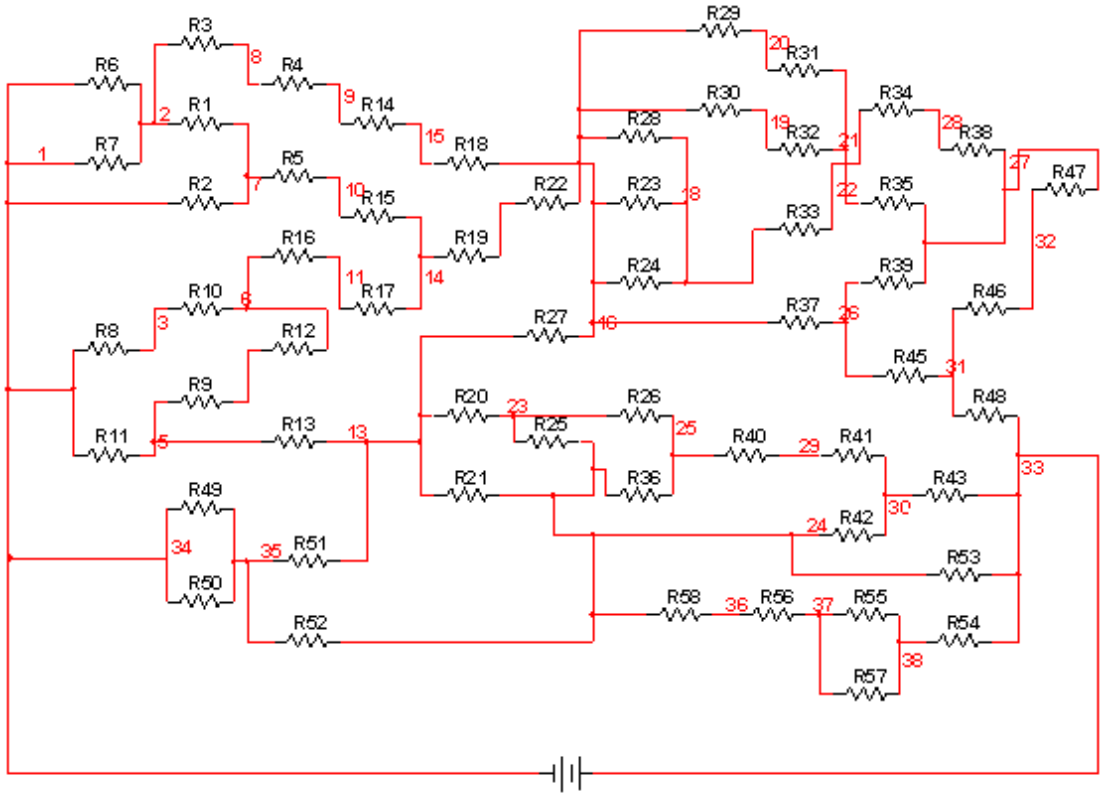

Equivalent circuit for the microstructure presented in Fig. 3.3

The connecting matrix of the microstructure presented in Fig. 3.4

Element	Node i	Node j	Value (Ω)
R1	1	2	5×10^5
R2	2	3	5×10^5
R3	2	3	4.32×10^6
R4	3	7	5×10^5
R5	4	5	5×10^5
R6	5	6	5×10^5
R7	5	6	5×10^5
R8	6	3	7.81×10^6

List of Publications

Xinxin Sun and Mo Song, "Highly Conductive Carbon Nanotube/Polymer Nanocomposites Achievable?", **Macromolecular Theory and Simulations,** 18, 2009, pp 155-161.

Xinxin Sun and Mo Song, " Numerical Simulation on AC Properties of Carbon Nanotube/Polymer Composites", **Macromolecular Theory and Simulations,** ***Accepted*****.**

Xinxin Sun and Mo Song, "Theoretical Estimation of Elastic Proprties for Single-Walled Carbon Nanotubes", **Abstract Booklet of Micro and Nanotechnology 2005**, IoM Communications, London, 2005, p 8.

Jie Jin, Xinxin Sun, Mo Song**,** and Gang Zhou, "Carbon Nanotube Strain Sensors for Damage Detection and Monitoring in Composite Aerostructures", **The International Conference on Smart Materials and Nanotechnology**, Harbin, China, 2007, p 104.